

POLITECNICO DI TORINO

CORSO DI LAUREA MAGISTRALE IN INGEGNERIA MECCANICA

Dipartimento di Ingegneria Meccanica e Aerospaziale



Enhancement and Evaluation of a Vertical Vehicle Dynamics Controller

Relatore:

Prof. Enrico Galvagno

Correlatori:

Prof. Dr.-Ing. Markus Lienkamp

Erik Enders

Candidata:

Giulia Bonelli

Ottobre 2020

The present thesis work was developed within the Italdesign Special Mobility Program of 6 months in Munich at TUM (Technische Universität München). The whole project, in terms of resources and outcomes, has been carried out at BMW AG in Munich.

Enhancement and Evaluation of a Vertical Vehicle Dynamics Controller

Wissenschaftliche Arbeit zur Erlangung des Grades

Master of Science (M.Sc.)

an der Fakultät für Maschinenwesen der Technischen Universität München

Betreut von Prof. Dr.-Ing. Markus Lienkamp
Erik Enders, M.Sc.
Lehrstuhl für Fahrzeugtechnik

Eingereicht von Giulia Bonelli, B.Sc.
Via Monginevro 56
10141 Turin

Eingereicht am 28.09.2020

Master's thesis

Enhancement and Evaluation of a Vertical Vehicle Dynamics Controller

With regard to highly automated and autonomous driving, there is a shift in priorities in the driving dynamics design of passenger cars. To this day, the design is characterized by the conflict of objectives between comfort and safety/sportiness, where the vehicles must achieve certain target values depending on the vehicle class and the respective brand image. However, with the elimination of the driving task, less attention will be paid to the driving experience of a vehicle in the future and new comfort requirements will be added, for example with regard to the performance of secondary activities. It must therefore be possible for semi-automated vehicles to have different vehicle characteristics depending on the state of automation. The aim of the work is the enhancement and evaluation of a vertical vehicle dynamics controller. First, the existing controller should be tested in simulation for different parametrizations in well-defined scenarios. Second, the controller should be enhanced by a logic to coordinate the modal controller and the skyhook controller. The enhanced controller should be tested again in the same scenarios and the results should be compared to the controller before, where either skyhook or modal control was active. Suitable objective metrics need to be used and tested for the evaluation of the simulation results. Sound engineering practice and suitable statistical methods need to be applied in this thesis work. The results need to be evaluated, analyzed and critically discussed in this thesis work. The following key points must be processed:

- Literature research on the state of the art
- Familiarization with vertical vehicle dynamics control and objectification methods
- Development/Enhancement of the controller
- Carrying out simulations to test and compare the controller
- Evaluation, analysis and discussion of the results
- Identify future research topics based on this thesis work

The written thesis work should document the individual work steps in a clear and concise form. The candidate acknowledges to carry out the study work independently and to reference any scientific tools or resources he/she uses. The submitted work remains the property of the chair as examination material and may only be made available to third parties with the consent of the chair holder.

Prof. Dr.-Ing. M. Lienkamp

Issued: _____

Supervisor: Erik Enders, M. Sc.

Handed in: _____

Geheimhaltungsverpflichtung

Frau: **Bonelli, Giulia**

Gegenstand der Geheimhaltungsverpflichtung sind alle mündlichen, schriftlichen und digitalen Informationen und Materialien, die der Unterzeichner vom Lehrstuhl oder von Dritten im Rahmen seiner Tätigkeit am Lehrstuhl erhält. Dazu zählen vor allem Daten, Simulationswerkzeuge und Programmcode sowie Informationen zu Projekten, Prototypen und Produkten.

Der Unterzeichner verpflichtet sich, alle derartigen Informationen und Unterlagen, die ihm während seiner Tätigkeit am Lehrstuhl für Fahrzeugtechnik zugänglich werden, strikt vertraulich zu behandeln.

Er verpflichtet sich insbesondere:

- derartige Informationen betriebsintern zum Zwecke der Diskussion nur dann zu verwenden, wenn ein ihm erteilter Auftrag dies erfordert,
- keine derartigen Informationen ohne die vorherige schriftliche Zustimmung des Betreuers an Dritte weiterzuleiten,
- ohne Zustimmung eines Mitarbeiters keine Fotografien, Zeichnungen oder sonstige Darstellungen von Prototypen oder technischen Unterlagen hierzu anzufertigen,
- auf Anforderung des Lehrstuhls für Fahrzeugtechnik oder unaufgefordert spätestens bei seinem Ausscheiden aus dem Lehrstuhl für Fahrzeugtechnik alle Dokumente und Datenträger, die derartige Informationen enthalten, an den Lehrstuhl für Fahrzeugtechnik zurückzugeben.

Besondere Sorgfalt gilt im Umgang mit digitalen Daten:

- Für den Dateiaustausch dürfen keine Dienste verwendet werden, bei denen die Daten über einen Server im Ausland geleitet oder gespeichert werden (Es dürfen nur Dienste des LRZ genutzt werden (Lehrstuhlaufwerke, Sync&Share, GigaMove).
- Vertrauliche Informationen dürfen nur in verschlüsselter Form per E-Mail versendet werden.
- Nachrichten des geschäftlichen E-Mail Kontos, die vertrauliche Informationen enthalten, dürfen nicht an einen externen E-Mail Anbieter weitergeleitet werden.
- Die Kommunikation sollte nach Möglichkeit über die (my)TUM-Mailadresse erfolgen.

Die Verpflichtung zur Geheimhaltung endet nicht mit dem Ausscheiden aus dem Lehrstuhl für Fahrzeugtechnik, sondern bleibt 5 Jahre nach dem Zeitpunkt des Ausscheidens in vollem Umfang bestehen. Die eingereichte schriftliche Ausarbeitung darf der Unterzeichner nach Bekanntgabe der Note frei veröffentlichen.

Der Unterzeichner willigt ein, dass die Inhalte seiner Studienarbeit in darauf aufbauenden Studienarbeiten und Dissertationen mit der nötigen Kennzeichnung verwendet werden dürfen.

Datum:

Unterschrift: _____

Erklärung

Ich versichere hiermit, dass ich die von mir eingereichte Abschlussarbeit selbstständig verfasst und keine anderen als die angegebenen Quellen und Hilfsmittel benutzt habe.

Garching, den 28.09.2020

Giulia Bonelli, B. Sc.

Table of contents

Abbreviations	V
Formula Symbol	VII
1 Introduction	1
1.1 Motivation and aim of the work	1
1.2 Structure of the work	2
2 Basics	5
2.1 Vehicle Suspensions	5
2.2 Passive suspensions: ride comfort and road-holding	7
2.3 The full vehicle model	9
2.3.1 Twist mode	10
2.3.2 State space approach and equations	11
2.4 Objectification methods for ride comfort	16
2.4.1 ISO 2631.....	16
2.4.2 Other approaches	17
2.5 Ride safety estimation	18
2.6 Road roughness classification	19
2.7 The controller	20
2.7.1 Skyhook principle.....	20
2.7.2 Modal analysis and modal controller theory.....	21
2.7.3 P controller: extended Skyhook	23
2.7.4 R controller.....	24
3 State of the art	27
3.1 Switching strategies	27
3.1.1 Anytime control with two controllers.....	27
3.1.2 Neural networks and coordinated control strategies.....	27
3.1.3 Crone suspension switching algorithm	28
3.2 Adaptive control of active and semi-active suspensions	28
3.3 Suspension oriented Skyhook control	29

3.4	Criticism of the state of the art.....	30
4	Method.....	33
4.1	Scientific news value	33
4.2	Development environment	33
4.3	Test scenarios	35
4.4	Kalman Filter.....	38
4.5	Coordination logic.....	41
4.5.1	Adaptive gain	42
4.5.2	Ride comfort	44
4.5.3	Road-holding	46
4.5.4	Suspensions constraint.....	48
4.5.5	Gain correction.....	50
4.6	Modified P controller.....	51
4.7	Simulation results	52
4.7.1	Adaptive gain results.....	52
4.7.2	Heave	54
4.7.3	Pitch.....	55
4.7.4	Roll.....	57
4.7.5	Overall comfort perception.....	58
4.7.6	Dynamic wheel loads.....	59
4.7.7	Thresholds tuning potential.....	60
5	Results.....	63
5.1	Experimental setup	63
5.2	Measurements processing	64
5.3	Experimental results with P and R controllers	70
5.4	Comparison with the full vehicle model.....	73
5.5	Experimental results with modified P controller and coordination logic	76
5.6	Sensitivity analysis on modified P controller	82
5.7	Coordination logic at different speeds.....	86
6	Discussion	89
7	Summary and Outlook	91
	List of figures	i
	List of tables.....	vii
	References	ix

Appendix xv

Abbreviations

AB	Aschheim, one way
A-C-A-C	Profile with 2 roughness classes, A and C
ADMA	Automotive Dynamic Motion Analyzer
BA	Aschheim, way back
BACE	BMW Autocoding Environment
C	Profile with class C roughness
CD	Test track in proximity to Freising
FnP	Freising to Pulling
ISO	International Organization for Standardization
MIMO	Multiple Input Multiple Output
MnF	Massenhausen to Fürholzen
P	Proportional or Extended Skyhook controller
PS	Power Spectrum
PSD	Power Spectral Density
R	State feedback controller with pole placement
RMS	Root Mean Square
SAE	Society of Automotive Engineers

Formula Symbol

Latin Symbols

In the following, formula symbols are displayed in their general form. The most frequently used are provided with the index j , which is specified in a separate table.

Symbol	Unit	Description
\mathbf{A}	-	System matrix
a_{ISO}	m/s ²	Overall acceleration value according to ISO 2631
\mathbf{B}	-	Input matrix
B	m/sam- ples	Sampling interval
b_j	m	Track widths
b_{eng}	m	Distance of the engine mountings from the x-axis
\mathbf{C}	-	Output matrix
c_j	N/m	Stiffness
c_v	-	Coefficient of variation
\mathbf{D}	-	Feedthrough matrix
\mathbf{D}_j		Damping matrix
\mathbf{D}^*	-	Desired damping matrix in the R controller
$\Delta\mathbf{D}^*$	-	Difference between the desired damping matrix and the actual damping matrix
$d_{Bo,max}$	Ns/m	Maximum body damping rate
$d_{Bo,min}$	Ns/m	Minimum body damping rate
D_j	-	Damping rate over critical damping
d_j	Ns/m Ns/rad	Damping rate
$d_{sky}, d_{sky,j}$	Ns/m Ns/rad	Skyhook damping rate
$\widehat{\mathbf{D}}_{Bo}$	-	Body damping matrix not considering the engine
\mathbf{E}	-	External matrix

\mathbf{e}	-	Vector error input to the P controller
\mathbf{F}	-	Prefilter matrix to the R controller
$f_{0,j}$	Hz	Undamped eigenfrequency
$F_{\text{dyn,check}}$	-	Boolean variable for road-holding
$F_{\text{dyn},j}$	N	Dynamic wheel load computed with measured signals
\mathbf{F}_{ext}	-	External force vector
F_j	N	Force
f_j	Hz	Eigenfrequency
$\mathbf{F}_{\text{modal},j}$	-	Modal forces vector
$F_{\text{pass},j}$	N	Passive part of the damping force
$\mathbf{F}_{\text{susp,d}}$	N	Total suspensions damping force
$\mathbf{F}_{\text{susp,d},j}$	N	Total suspensions damping force at the four corners
$\mathbf{F}_{u,j}$	N	Semi-active part of the suspension force
F_z	N	Dynamic wheel load for quarter car model
$F_{z_{w,j},\text{dyn}}$	N	Dynamic wheel load for the full vehicle model
$\tilde{F}_{z_{w,i,j},\text{dyn}}$	N	Online estimation of dynamic wheel loads with Kalman Filter
$F_{z_{w,j},\text{stat}}$	N	Static wheel load
$\mathbf{F}_{z_{w},\text{dyn}}$	-	Dynamic wheel loads vector
G_d	m^3	PSD of the vertical displacement
$G_{\text{Fdyn,fr}}$	-	Dynamic wheel load gain, front right
$G_{\text{Fdyn,fl}}$	-	Dynamic wheel load gain, front left
$G_{\text{Fdyn,max}}$	-	Maximum between $G_{\text{Fdyn},i,j}$ with $i \in \{f, r\}, j \in \{r, l\}$
$G_{\text{Fdyn,rl}}$	-	Dynamic wheel load gain, rear left
$G_{\text{Fdyn,rr}}$	-	Dynamic wheel load gain, rear right
G_{PS}	-	Gain from the online PS estimation in the frequency range of 0-5 Hz
G_R	-	Adaptive gain
$G_{\text{sus,def}}$	-	Suspension deflection gain
\mathbf{h}	-	Vertical road displacement vector
\mathbf{I}	-	Identity matrix

i_j	-	Transmission ratio
J	-	Optimization index
$J_{eng,xx}$	kg m ²	Roll inertia moment of the engine
$J_{Bo,t}$	kg m ²	Twist inertia moment of the body
J_{xx}	kg m ²	Roll inertia moment of the body
J_{yy}	kg m ²	Pitch inertia moment of the body
K^+	-	Coordination logic
K_j		Stiffness matrix
K^*	-	Desired stiffness matrix
ΔK^*	-	Difference between the desired stiffness matrix and the actual one
K_P	-	Gain matrix of the P controller
$K_{P,\alpha}$	-	Gain matrix of the Modified P controller
$K_{P,j}$	Ns/m Ns/rad	P factor of the P controller
$K_{P,\alpha,j}$	Ns/m Ns/rad	P factor of the modified P controller
\hat{K}_{Bo}	-	Body stiffness matrix not considering the engine
k_j	-	Percentage of static wheel load
L	m	Length of a road profile
l_f	m	Distance from the front axle to the centre of gravity
l_r	m	Distance from the rear axle to the centre of gravity
l_{eng}	m	Distance of the engine from the x axis
M_j	-	Mass matrix
$M_{Bo,w}$	-	Body mass distributed on the four corners
\hat{M}_{Bo}	-	Mass matrix not considering the engine mass
M_j	Nm	Torque
m	-	Number of actuators
m_j	kg	Mass
N	-	Measurement inputs
n	-	System degrees of freedom
n	cycles/m	Spatial frequency

Formula Symbol

n_0	cycles/m	Conventional spatial frequency
$PS_{\ddot{z}_{Bo,ISO}}$	$(m/s^2)^2$	Online power spectrum estimation of $\ddot{z}_{Bo,ISO}$ via windowing
$PS_{\ddot{z}_{Bo, ISO,0-5 Hz}}$	$(m/s^2)^2$	$PS_{\ddot{z}_{Bo,ISO}}$ limitation to the frequency range of the body eigenfrequency 0-5 Hz
PS_{trans}	-	Boolean variable that corrects the adaptive gain accounting for the delay in the power spectrum estimation
p	-	Poles position
\mathbf{R}	-	Feedback matrix
sus_{th}	m	Suspension deflection threshold to overcome to obtain $G_{sus,def}$
t	s	Time
th_{def}	-	Threshold for the gain in suspension deflection
th_{dyn}	-	Threshold for G_{Fdyn}
th_{Fdyn}	N	Threshold for dynamic wheel load
th_{PS}	-	Threshold for G_{PS}
th_{ratio}	-	Threshold for power spectrum estimation
th_{xdef}	m	Threshold for suspension deflection
\mathbf{T}	-	Transformation matrix
ΔT	s	Time interval
t_0	s	Initial time
t_e	s	Final time
t_{Bo}	rad	Position of the body in twist mode
\dot{t}_{Bo}	rad/s	Angular rate of the body in twist mode
\ddot{t}_{Bo}	rad/s ²	Angular acceleration of the body in twist mode
\mathbf{u}	-	Input or control vector
\mathbf{u}_{MP}	-	Control vector from the Modified P controller at the four corners
$\mathbf{u}_{MP,modal}$	-	Modal control vector from the Modified P controller
\mathbf{u}^*	-	Modal control vector from the R controller
$\mathbf{u}_{R,g}^*$	-	Modal control vector from the R controller with the coordination logic
\mathbf{u}_P	-	Control vector from the P controller at the four corners
$\mathbf{u}_{P,modal}$	-	Modal control vector from the P controller
$\mathbf{u}_{P,modal,g}$	-	Modal control vector from the P controller with the coordination logic

\mathbf{u}_R	-	Control vector from the R controller at the four corners
\mathbf{u}_{eng}	-	Control vector for the engine disturbances
\mathbf{v}	-	Measurement noise covariance
v_x	m/s	Vehicle speed
\mathbf{w}	-	Process noise covariance
W_j	m/rad	Weightings
x	-	Independent variable of the lookup tables
\mathbf{x}	-	State variable vector
\mathbf{y}	-	Output vector
y	-	Dependent variable of the lookup tables
\mathbf{y}_{set}	-	Set signal for P controller
$\ddot{z}_{B0,ISO}$	m/s ²	Overall acceleration value for the coordination logic
z_j	m	Position in heave mode
\dot{z}_j	m/s	Velocity in heave mode
\ddot{z}_j	m/s ²	Acceleration in heave mode
Δz_j	m	Relative position in heave mode
$\Delta \dot{z}_j$	m/s	Relative velocity in heave mode
$\widetilde{\Delta z}_{susj}$	m	Kalman Filter estimated suspension deflection through double discrete-time integration

Greek symbols

Symbol	Unit	Description
α_j	-	Proportional factor in the modified P controller
β	rad	Randomly generated angle
$\boldsymbol{\eta}$	-	Vector of modal coordinates
θ_{B0}	rad	Position of the body in pitch mode
$\dot{\theta}_{B0}$	rad/s	Velocity of the body in pitch mode
$\ddot{\theta}_{B0}$	rad/s ²	Acceleration of the body in pitch mode
λ_i	-	Eigenvalue
μ	variable	Mean
σ	variable	Standard deviation
τ	-,N,m	Time constant in exponential laws
φ_j	rad	Position in roll mode
$\dot{\varphi}_j$	rad/s	Velocity in roll mode
$\ddot{\varphi}_j$	rad/s ²	Acceleration in roll mode
$\boldsymbol{\Psi}$	-	Eigenvector matrix
ω_j	rad/s	Natural frequency

Subscripts

Symbol	Description
arb	Anti-roll bar
Bo	Body
eng	Engine
f	Front
fl	Front left
fr	Front right
k	Kalman filter
opt	Optimal
r	Rear
rl	Rear left
rr	Rear right
ro	Road
sys	System
sus	Suspension
T	Tyre
w	Wheel

1 Introduction

Autonomous driving allows vehicle occupants to perform secondary activities. This becomes possible especially from Level 3 of automation, which, according to SAE definitions [1, p. 2], corresponds to conditional automation, as the task of monitoring the driving environment is performed by the system and not by the driver. Among the consequences, there are greater demands on driving comfort.

Vertical vehicle dynamics control is an important aspect in the improvement of semi-active or active suspensions and one of its aim is combining driving safety and driving comfort. The existing conflict between safety and comfort is objective of several research works and especially with passive suspensions, it cannot be completely solved. Fully active suspensions can adjust their behaviour depending on the driving situation but they present negative aspects as the lack of safety and higher costs [2, p. 1120]. Consequently, semi-active suspensions have been improved in terms of technology and controlling algorithms. The current research focuses on the enhancement of the vertical vehicle dynamics with semi-active suspensions by means of suitable controlling logics.

1.1 Motivation and aim of the work

The present thesis work has the objective of improving a modal vertical vehicle dynamics control system in terms of resolution of the conflict between driving safety and driving comfort. The latter becomes significant when considering autonomous driving where vehicle occupants are allowed to perform secondary activities. This leads to an increasing attention towards road excitations and the direction and frequency dependence of comfort perception.

Ride safety and ride comfort are goals that can be achieved independently by using a specific type of controller. For example, a Skyhook controller [3] can be used with the purpose of ideally suspend the sprung mass by means of a virtual damper connected to an inertial reference in the sky. Skyhook control does not consider the wheel dynamics though, and therefore it only is suitable for improving driving comfort. An opposite approach is represented by a Groundhook controller [4], which uses a fictitious damping element between the wheel and the ground, leading to an optimization of road-holding. An example of combination between these two approaches is performed by checking the relative suspension deflection that allows the definition of two variable damping coefficients representing, respectively, the fictitious damper connected to the sky or to the ground [5]. Another combination method is derived for active suspensions by means of a suitable control law accounting for both groundhook and skyhook dampers [6].

There are several applicable approaches to analyse vehicle dynamics. A multibody system approach [7], explores the dynamic behaviour of either rigid or flexible interconnected bodies by simulating their relative movements. Each subsystem is modelled with accuracy but some

evaluations cannot be performed as, for example, the independent adjustment of stiffness and damping characteristics of the body vehicle in each desired spatial direction.

The current research uses a different approach with the assumption of rigid body and takes over an existing work [8]. Its aim was adjusting the dynamic behaviour of the body in the modal coordinates of heave, pitch and roll by means of a transformation matrix which led to the definition of a supplementary eigenmode, the twist mode. KARLE defines two control logics to achieve decoupling, each one mainly pursuing either ride comfort or road-holding [8]. In order to take account of driving safety, a modal controller (R) is implemented. On the other hand, from a comfort perspective, an extended skyhook control with twist mode (P) is used. The aim of this thesis work is to enhance the above mentioned controllers by means of a suitable coordination logic between the two. Not only does the latter need to assure the system stability, but it also should provide a better overall vehicle performance.

Different analyses are conducted in this work and different methods are presented in order to improve the existing controllers. Either stochastic road measurements and artificially generated ones are used to test the logic in different scenarios and suitable objectification methods are employed to evaluate the results in terms of driving comfort. An appropriate estimation of a driving safety index is also performed.

A linear vehicle model is implemented in a simulation environment and at the beginning, it is tested with different driving scenarios, either using the modal controller or the skyhook controller. A sensitivity analysis is also conducted. Secondly, the coordination logic is developed in order to reduce the distance between the two conflicting objectives. The enhanced controller is tested again and the results are compared with the ones obtained previously. Finally, the developed logic is tested in a real vehicle which is equipped with continuously adjustable semi-active actuators. In the simulation environment, fully active suspensions can also be simulated.

1.2 Structure of the work

An overview of the work structure is given (Figure 1.1). In Section 1.1, the motivation of the work is presented and goals are defined. In Chapter 2, the needed theoretical background is summarised. This includes a focus on suspensions types, the full vehicle model equations, the objectification methods for ride comfort, road-holding estimation and road roughness classification. The equations of the existing controllers are also described.

At the same time, a research on the state of the art regarding the possibility of coordinating two different controllers has been conducted and presented in Chapter 3. In addition, an overview of some vertical vehicle dynamics controlling approaches is given. Criticism on the state of the art is performed (Section 3.3). This directly leads to the development of a new method which is presented in Chapter 4. The results of the experimental tests in the vehicle are shown in Chapter 5 and discussed in Chapter 6. Comments on the developed logic as well as a summary of the work with possible future projects are given in Chapter 7.

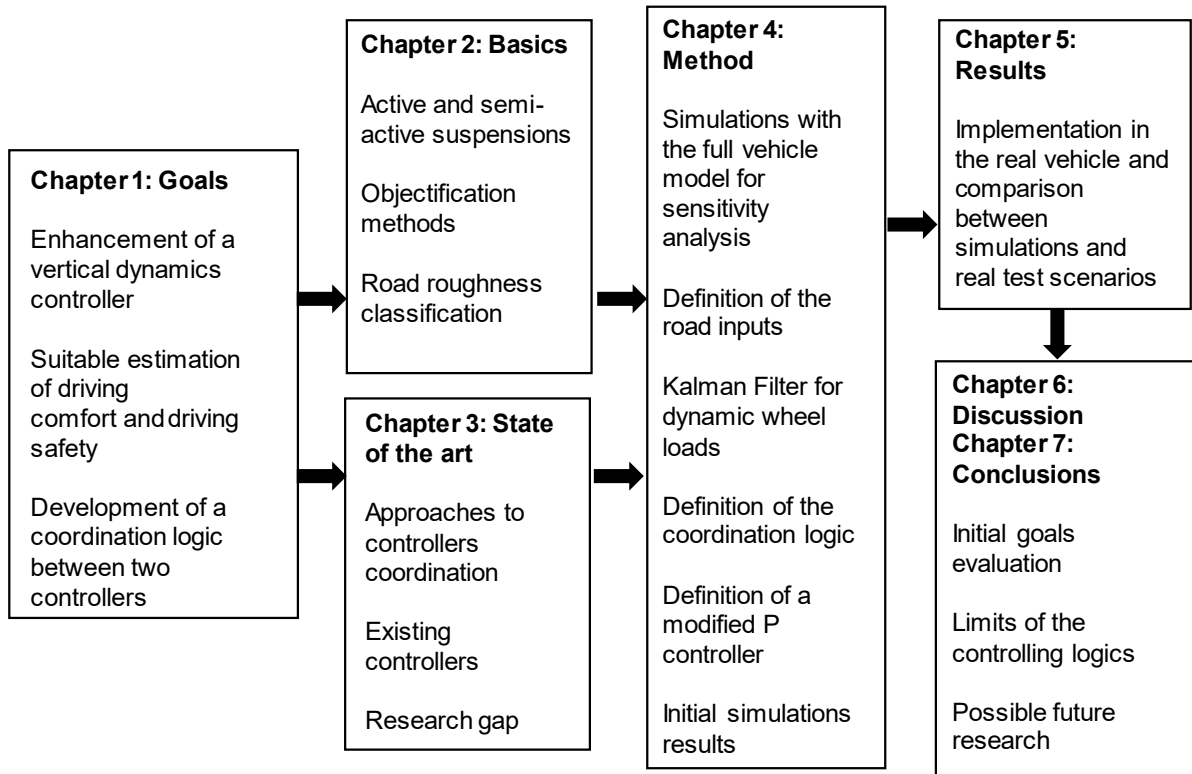


Figure 1.1: Structure of the work

2 Basics

This chapter contains the fundamental theoretical principles which are needed in order to develop the coordination logic between the two controllers and to reach a general enhancement of the vehicle performances. Firstly, an overview on suspensions is given (Section 2.1), then some considerations are made on road-holding and ride comfort in passive suspensions (Section 2.2). The full vehicle model implemented in the simulation environment is described (Section 2.3). In Section 2.4, objectification methods for ride comfort are presented. In Section 2.5, an appropriate method for road-holding estimation is shown and in Section 2.6, the road roughness classification approach employed in this work is displayed. Finally, the existing controllers are analysed (Section 2.7).

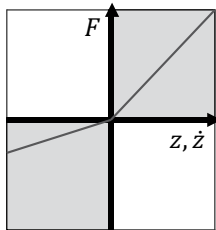
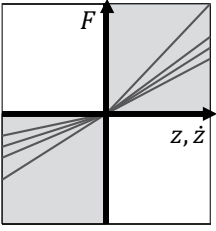
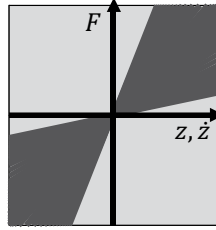
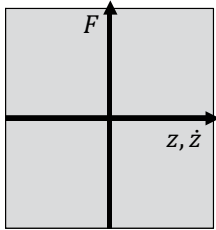
2.1 Vehicle Suspensions

Suspensions connect the vehicle body to the wheels in order to allow a relative motion between them. In their simplest form, they consist of an elastic element, a damping element and a set of mechanical connections to link the sprung mass to the unsprung masses. The spring carries the body mass and isolates it from the induced road disturbances and therefore has a role in comfort. The damper is involved in both driving safety and driving comfort. Its tasks are the body damping and the limitation of wheel oscillations, directly referable to driving safety as, a non-bouncing wheel is the requirement for road-contact forces transfer. In other words, a suspension is a low pass filter that should isolate the vehicle from the short wavelength features deriving from the deterioration of road surfaces. It should ideally allow the vertical movements of the wheels to follow the vertical road profile, while assuring the maintenance of the body at a fixed height [9]. Being driving comfort and driving safety, two opposite goals, it is easy to understand why passive suspensions have been partially substituted with semi-active or fully active ones. The latter require a consistent power absorption and present safety issues management [2, pp. 1120-1121]. A possible compromise is represented by semi-active suspensions, also known as variable damping suspensions. The main difference between active and semi-active suspensions is that the first ones can introduce energy to the system. Regardless of the semi-active control systems implemented, in case of some control failure, semi-active suspensions would work just as passive ones, which makes them more reliable. A classification of electronically controlled suspensions according to the required energy, the controlled variable and the control bandwidth is shown (Table 2.1, [10, p. 15]). Further details on this, can be found in literature [2, p. 1121], [11, p. 1356].

There are different available technologies for semi-active suspensions. Electromechanical actuators, equipped with servo-valves controlled in current where the latter corresponds to a certain opening of the valves' cross section. Magneto-rheological and electro-rheological dampers in which fluids can change their viscosity by means of a magnetic or electric field.

The control strategy enhanced and implemented in this work is applied to semi-active suspensions with electrohydraulic dampers controlled by an electric current varying from 0 A to 1.8 A. These values respectively correspond to minimum damping and maximum damping with the valve completely open. The dynamic properties of the actuators are neglected in the simulation model. Inverse look-up tables are used to obtain the control current by checking the relative velocity of the dampers. This corresponds to a certain desired damping force. In the model, tests can be carried out by using either real actuators properties or by simulating fully active suspensions with no limitations to the deliverable force. Additional information on the suspensions set-up is given in Appendix G.

Table 2.1: Suspension classification [10, p. 25]

System	Force range	Control variable	Energy demand [W]	Control bandwidth [Hz]
passive		-	-	-
adaptive		Damping ratio	10-20	1-5
semi-active		Damping ratio	10-20	30-40
fully-active		Force	5000-10000	20-30

2.2 Passive suspensions: ride comfort and road-holding

In order to focus on the conflict between road-holding and ride comfort, a concise analysis of a quarter car model with passive suspensions has been conducted. In Appendix B, the quarter car model as well as the parameter adaptation from the full vehicle model to the simplified one are presented. Quarter car model represent a monovalent passive suspension, whose damping coefficient and stiffness can be tuned. Suspensions should provide ride comfort by means of a soft setup for the spring and the damper while on the other hand, they should assure driving safety which requires a stiff configuration.

In order to account for driving comfort and road-holding, two transfer functions are calculated respectively as \ddot{z}_{B0}/z_{r0} and $(F_z/c_T)/z_{r0}$. Driving comfort is obtained when the vertical acceleration of the sprung mass is minimized while, road-holding can be achieved when the vertical force transmitted to the ground does not oscillate so as to guarantee the correct manoeuvrability of the vehicle. In Figure 2.1, the transfer functions are shown with the vehicle in the passive configuration and using a quarter car model with a focus on the effect of the damping coefficient. They are smoothed with a moving average filter with a span of 15 samples. The road disturbance input is a stochastic road measurement and the vehicle speed on the path is constant and equal to 100 km/h. Further details on this aspect are given in Section 4.3. The transfer functions shown in Figure 2.1, are then compared with the ones obtained with different values of the suspension damping coefficient. The obtained results are represented in Figure 2.2 and are comparable to their theoretical formulation [12, p. 16]. The correspondence between the values in Figure 2.2 and the optimal passive damping coefficient as calculated in Appendix B, is shown (Table B.1). Figure 2.2 clearly highlights the conflict between road-holding and ride comfort in passive suspensions. The latter have fixed damping and stiffness coefficients that need to represent a compromise between the two objectives. When it comes to ride comfort, at low damping rates, there is a large peak at the body eigenfrequency (around 1 Hz) and a smaller one at the wheel hop eigenfrequency (around 10 Hz). At the same time, not only the body and the wheels eigenfrequencies should be taken into account, but also other significant frequency ranges as for example, the one that goes from 4 Hz to 8 Hz, as it is the most effective on human perception of ride comfort. Consequently, when it comes to generally minimizing the sprung mass vertical acceleration in the frequency range between 0 and 20 Hz, a low damping coefficient could be chosen (d_{B0}) displaying particular attention at the consequences on the body eigenfrequency peak. An opposite behaviour is experienced if considering road-holding, where significantly high peaks are found with low damping rates at the wheel hop eigenfrequency. It is important to limit the vertical force oscillations as this results in the possibility of developing lateral forces on the ground and consequently guaranteeing an appropriate manoeuvrability of the vehicle in terms of steering and braking. For this purpose, an higher damping coefficient could be used ($2d_{opt}$). A compromise between the two, could be represented by $1.25d_{opt}$ which corresponds to a damping ratio of 0.4773. An extended analysis on this topic is performed in [13, pp. 255-258]. The influence of other design parameters, such as suspension stiffness, on ride comfort and road-holding is investigated. There are many attempts of optimization of the suspensions parameters in literature in passive configuration. For example, the suspension of a two degrees of freedom vehicle, travelling on a randomly generated road is optimized with respect to both road-holding and ride comfort in [14]. In conclusion, passive suspensions can only provide fixed vehicle performances that cannot be adjusted depending on the driving situation.

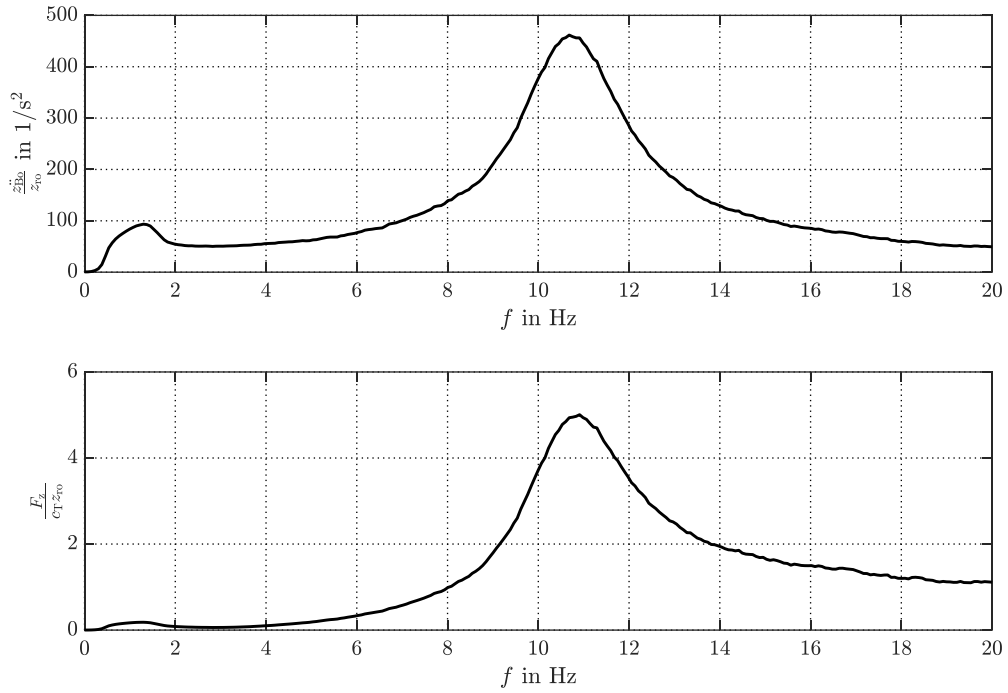


Figure 2.1: Transfer functions for vehicle passive configuration

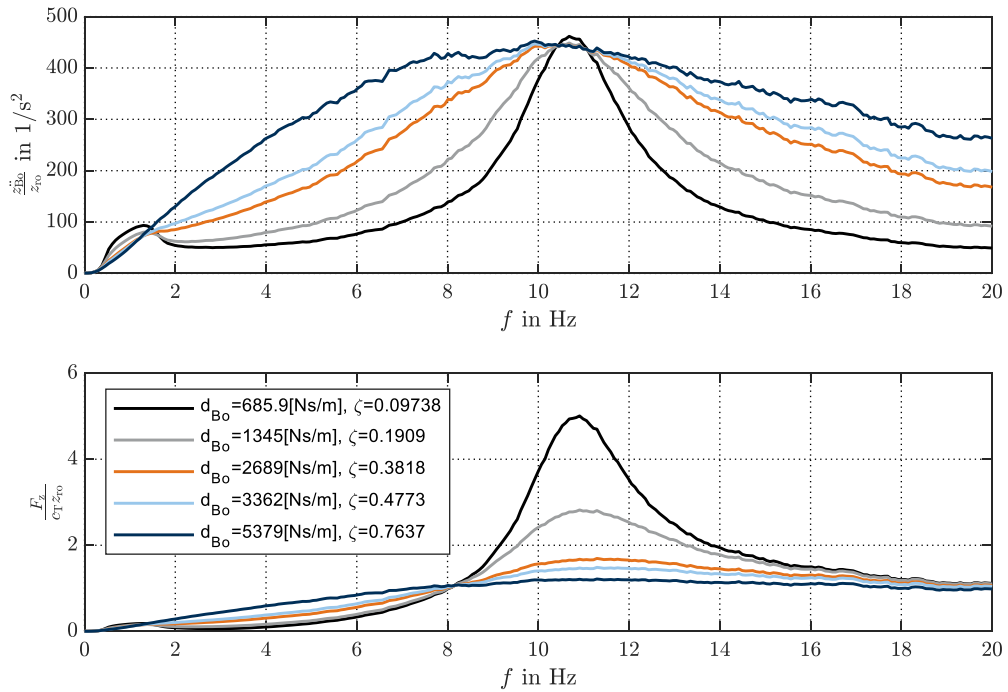


Figure 2.2: Transfer functions for vehicle passive configuration with different damping rates

2.3 The full vehicle model

The full vehicle model (Figure 2.3, [8, p. 6]) presents the following degrees of freedom: heave of the four wheels, the body eigenmodes of heave, pitch and roll and heave and roll of the engine unit, which has been modelled as a separate mass. The last degree of freedom is of twist and belongs to the body. Further explanations on the twist mode will be given in Section 2.3.1.

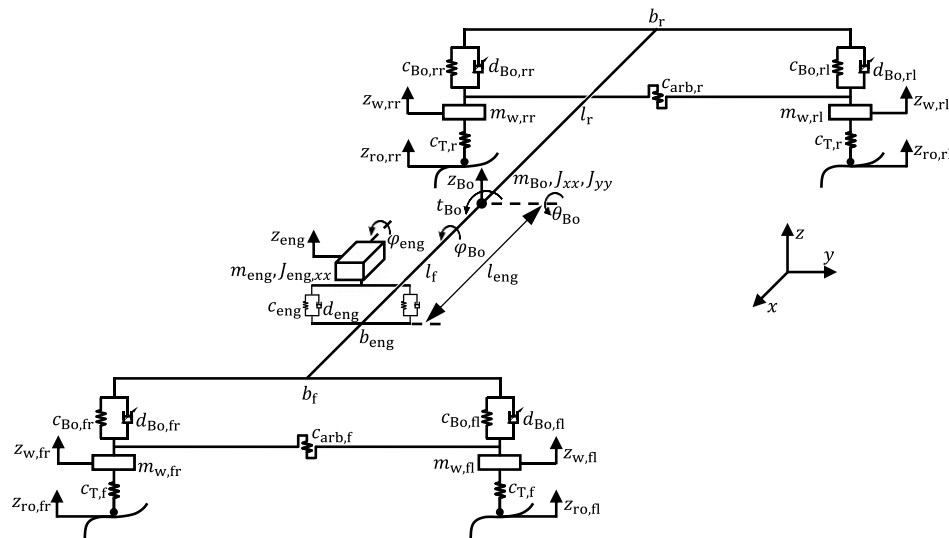


Figure 2.3: Full vehicle model [8, p. 6]

The following assumptions have been made :

- Linear spring

The spring behaviour can be considered linear in the working range around the rest static position of $-0.1 \text{ m} \leq \Delta z \leq 0.1 \text{ m}$.

- Linear damper

The damper passive component has a working range of $-1 \text{ m/s} \leq \Delta \dot{z} \leq 1 \text{ m/s}$, and can be considered linear. The active component is non-linear and it is added to the first one.

- Centre of gravity for pitch and roll

The movements of pitch and roll happen, respectively, around the pitch centre and roll axis. In the model they are assumed to be placed in the centre of gravity. Furthermore, non-diagonal terms of inertia moments for pitch and roll are neglected.

- Small angle

In the working range of $\pm 10^\circ$, it is assumed that $\sin x \approx x$ and $\cos x \approx 1$, with an error that is under the 2 %.

- Rigid wheel suspension

The wheels are assumed to perform an ideal vertical movement, with the neglect of toe and camber angles as well as viscoelastic effects.

- Linear tyre

The tyre is approximated by a linear spring and its damping can be neglected [15].

- Constant installation ratio from the wheels to the suspensions

The installation ratio from the wheels to the suspensions is assumed to be constant in the suspensions deflection range. Further explanations on this aspect are given in Appendix G. Forces exchanged between the road and the wheels, the wheels and the body and the body and the engine are considered to be acting in vertical direction.

- Rigid body

The vehicle is modelled as a rigid body in the frequency range of interest, 0-20 Hz.

- Linear behaviour of the engine mounts

The engine mounts modelled as a linear spring and damper with stiffness and damping respectively of 600 N/mm and 6 Ns/mm. This is a simplifying assumption because they are made of an elastomeric material which shows a changing behaviour in the frequency range of 0-30 Hz when excited with sinusoidal excitations of different amplitudes.

- Constant vehicle speed

All the simulations are conducted by considering an uniform straight motion. All possible loads transfers due to driving manoeuvres such as steering, braking and accelerating are neglected as the focus is on road induced vertical movements, namely on vertical vehicle dynamics.

2.3.1 Twist mode

The twist mode corresponds to the torsional movement around the longitudinal axis of the vehicle. It is introduced in order to guarantee the solvability of the system of equations of the vehicle model, which would be not determined. The idea is to distribute the actuating force resulting from the active element of the semi-active suspension, on the four corners of the vehicle, where mono-valent vertical wheel suspensions are placed. The body modes of heave, pitch and roll are indeed sufficient to calculate three suspensions forces for a rigid body. The forth, belonging to the last mono-valent vertical wheel suspension causes an over-determined system. This problem can be solved by means of a pseudo-inverse matrix [16]. Instead of using the pseudo-inverse approach, a forth degree of freedom for the body has been introduced, the twist of the structure, t_{Bo} , leading to the solvability of the system of equations with the definition of a square transformation matrix. A moment of inertia for the twist mode, $J_{Bo,t}$, has been calculated without having a physical correspondence by means of a certain damping and stiffness of the body and a certain damping ratio for the twist mode $D_{t_{Bo}}$. As there is no possibility of estimating such an inertia moment, the following synthetic formula has been used, assuming a passive damping ratio for twist mode, $D_{t_{Bo}} = 0.1$.

$$J_{Bo,t} = \frac{\left(\frac{d_{t_{Bo}}}{2D_{t_{Bo}}}\right)^2}{c_{t_{Bo}}} = 991 \text{ kgm}^2 \quad (2.1)$$

This leads to the definition of an undamped natural frequency with the following:

$$f_{0,t} = \sqrt{\frac{c_{t_{Bo}}}{J_{Bo,t}}} \frac{1}{2\pi} = 1.46 \text{ Hz} \quad (2.2)$$

The introduction of the twist mode also aims at the reduction of the wheel excitation without influencing the other modes.

2.3.2 State space approach and equations

In order to solve the equations of the full vehicle model described above, a state space approach has been used. The general form of the state space model is [17, p. 18]:

$$\dot{\mathbf{x}} = \mathbf{A}\mathbf{x} + \mathbf{B}\mathbf{u} + \mathbf{E}\mathbf{z} \quad (2.3)$$

$$\mathbf{y} = \mathbf{C}\mathbf{x} + \mathbf{D}\mathbf{u} \quad (2.4)$$

The state vector is:

$$\mathbf{x} = \begin{pmatrix} z_w \\ x_{Bo} \\ x_{eng} \\ \dot{z}_w \\ \dot{x}_{Bo} \\ \dot{x}_{eng} \end{pmatrix} \quad (2.5)$$

The degrees of freedom of the wheels are:

$$\mathbf{z}_w = \begin{pmatrix} z_{w,fr} \\ z_{w,fl} \\ z_{w,rl} \\ z_{w,rr} \end{pmatrix} \quad (2.6)$$

Therefore x_{Bo} , having introduced the twist mode, is defined as it follows:

$$\mathbf{x}_{Bo} = \begin{pmatrix} z_{Bo} \\ \theta_{Bo} \\ \varphi_{Bo} \\ t_{Bo} \end{pmatrix} \quad (2.7)$$

and for the engine:

$$\mathbf{x}_{eng} = \begin{pmatrix} z_{eng} \\ \varphi_{eng} \end{pmatrix} \quad (2.8)$$

The input vector is:

$$\mathbf{u} = \mathbf{u}_R + \mathbf{u}_p + \mathbf{u}_{eng} = \mathbf{F}_u = \begin{pmatrix} F_{u,fr} \\ F_{u,fl} \\ F_{u,rl} \\ F_{u,rr} \end{pmatrix} \quad (2.9)$$

And the external input vector is:

$$\mathbf{z} = \begin{pmatrix} z_{ro} \\ F_{ext} \end{pmatrix} \quad (2.10)$$

The output vector is:

$$\mathbf{y} = \begin{pmatrix} \dot{z}_{Bo} \\ \dot{\theta}_{Bo} \\ \dot{\phi}_{Bo} \\ \dot{t}_{Bo} \end{pmatrix} = \dot{\mathbf{x}}_{Bo} \quad (2.11)$$

The system matrices used in the state space equations are:

$$\mathbf{A} = \begin{bmatrix} \mathbf{0} & \mathbf{I} \\ \mathbf{M}_{sys}^{-1} \mathbf{K}_{sys} & \mathbf{M}_{sys}^{-1} \mathbf{D}_{sys} \end{bmatrix} \quad (2.12)$$

$$\mathbf{B} = \begin{bmatrix} \mathbf{0}_{10 \times 4} \\ \mathbf{M}_w^{-1} \\ -\mathbf{M}_{Bo}^{-1} \mathbf{T} \\ \mathbf{0}_{2 \times 4} \end{bmatrix} \quad (2.13)$$

$$\mathbf{C} = [\mathbf{0}_{4 \times 14} \quad \mathbf{I}_4 \quad \mathbf{0}_{4 \times 2}] \quad (2.14)$$

$$\mathbf{D} = \mathbf{0} \quad (2.15)$$

$$\mathbf{E} = \begin{bmatrix} \mathbf{0}_{10 \times 6} & \\ \mathbf{M}_w^{-1} \mathbf{K}_T & \mathbf{0}_{4 \times 2} \\ \mathbf{0}_{4 \times 6} & \\ \mathbf{0}_{2 \times 4} & \mathbf{M}_{eng}^{-1} \end{bmatrix} \quad (2.16)$$

The system mass matrix is defined as:

$$\mathbf{M}_{sys} = \begin{bmatrix} \mathbf{M}_w & 0 & 0 \\ 0 & \mathbf{M}_{Bo} & 0 \\ 0 & 0 & \mathbf{M}_{eng} \end{bmatrix} \quad (2.17)$$

With \mathbf{M}_w , as the mass matrix for the four wheels, \mathbf{M}_{Bo} , as the body mass matrix excluding the contribution of the engine, \mathbf{M}_{eng} , as the engine mass matrix:

$$\mathbf{M}_w = \begin{bmatrix} m_{w,fr} & 0 & 0 & 0 \\ 0 & m_{w,fl} & 0 & 0 \\ 0 & 0 & m_{w,rl} & 0 \\ 0 & 0 & 0 & m_{w,rr} \end{bmatrix} \quad (2.18)$$

$$\mathbf{M}_{Bo} = \begin{bmatrix} m_{Bo} - m_{eng} & 0 & 0 & 0 \\ 0 & J_{yy} - m_{eng} l_{eng}^2 & 0 & 0 \\ 0 & 0 & J_{xx} - J_{xx,eng} & 0 \\ 0 & 0 & 0 & J_{Bo,t} \end{bmatrix} \quad (2.19)$$

$$\mathbf{M}_{eng} = \begin{bmatrix} m_{eng} & 0 \\ 0 & J_{xx,eng} \end{bmatrix} \quad (2.20)$$

The system stiffness matrix \mathbf{K}_{sys} is calculated as a combination of the wheel stiffness matrix \mathbf{K}_T , the suspension stiffness matrix \mathbf{K}_{sus} , the engine stiffness matrix \mathbf{K}_{eng} and the matrix that accounts for the anti-roll bar, \mathbf{K}_{arb} . The multiplication factor of the latter results from the fact that

a roll moment is equally supported by the left and the right wheel. The complete relationship between \mathbf{K}_{sys} and the other matrices is shown in Appendix C.

$$\mathbf{K}_{\text{sys}} = \begin{bmatrix} -\mathbf{K}_{w,w} & \mathbf{K}_{w,\text{Bo}} & \mathbf{0} \\ \mathbf{K}_{\text{Bo},w} & -\mathbf{K}_{\text{Bo},\text{Bo}} & \mathbf{K}_{\text{Bo},\text{eng}} \\ \mathbf{0} & \mathbf{K}_{\text{eng},\text{Bo}} & -\mathbf{K}_{\text{eng},\text{eng}} \end{bmatrix} \quad (2.21)$$

$$\mathbf{K}_{\text{T}} = \begin{bmatrix} c_{\text{T},\text{fr}} & 0 & 0 & 0 \\ 0 & c_{\text{T},\text{fl}} & 0 & 0 \\ 0 & 0 & c_{\text{T},\text{rl}} & 0 \\ 0 & 0 & 0 & c_{\text{T},\text{rr}} \end{bmatrix} \quad (2.22)$$

$$\mathbf{K}_{\text{sus}} = \begin{bmatrix} c_{\text{Bo},\text{fr}} & 0 & 0 & 0 \\ 0 & c_{\text{Bo},\text{fl}} & 0 & 0 \\ 0 & 0 & c_{\text{Bo},\text{rl}} & 0 \\ 0 & 0 & 0 & c_{\text{Bo},\text{rr}} \end{bmatrix} \quad (2.23)$$

$$\mathbf{K}_{\text{eng}} = \begin{bmatrix} 2c_{\text{eng}} & 0 \\ 0 & \frac{c_{\text{eng}}b_{\text{eng}}^2}{2} \end{bmatrix} \quad (2.24)$$

$$\mathbf{K}_{\text{arb}} = \frac{1}{2} \begin{bmatrix} c_{\text{arb},\text{f}} & -c_{\text{arb},\text{f}} & 0 & 0 \\ -c_{\text{arb},\text{f}} & c_{\text{arb},\text{f}} & 0 & 0 \\ 0 & 0 & c_{\text{arb},\text{r}} & -c_{\text{arb},\text{r}} \\ 0 & 0 & -c_{\text{arb},\text{r}} & c_{\text{arb},\text{r}} \end{bmatrix} \quad (2.25)$$

The system damping matrix \mathbf{D}_{sys} is obtained from the wheel damping matrix \mathbf{D}_{T} , the passive damping matrix of the suspensions \mathbf{D}_{sus} and the damping matrix of the engine in the eigenmodes of heave and roll, \mathbf{D}_{eng} . The complete relationship between \mathbf{D}_{sys} and the other matrices is shown in Appendix C. The damping rates of the wheels are considered negligible.

$$\mathbf{D}_{\text{sys}} = \begin{bmatrix} -\mathbf{D}_{w,w} & \mathbf{D}_{w,\text{Bo}} & \mathbf{0} \\ \mathbf{D}_{\text{Bo},w} & -\mathbf{D}_{\text{Bo},\text{Bo}} & \mathbf{D}_{\text{Bo},\text{eng}} \\ \mathbf{0} & \mathbf{D}_{\text{eng},\text{Bo}} & -\mathbf{D}_{\text{eng},\text{eng}} \end{bmatrix} \quad (2.26)$$

$$\mathbf{D}_{\text{T}} = \begin{bmatrix} 0 & 0 & 0 & 0 \\ 0 & 0 & 0 & 0 \\ 0 & 0 & 0 & 0 \\ 0 & 0 & 0 & 0 \end{bmatrix} \quad (2.27)$$

$$\mathbf{D}_{\text{sus}} = \begin{bmatrix} d_{\text{Bo},\text{fr}} & 0 & 0 & 0 \\ 0 & d_{\text{Bo},\text{fl}} & 0 & 0 \\ 0 & 0 & d_{\text{Bo},\text{rl}} & 0 \\ 0 & 0 & 0 & d_{\text{Bo},\text{rr}} \end{bmatrix} \quad (2.28)$$

$$\mathbf{D}_{\text{eng}} = \begin{bmatrix} 2d_{\text{eng}} & 0 \\ 0 & \frac{d_{\text{eng}}b_{\text{eng}}^2}{2} \end{bmatrix} \quad (2.29)$$

Once that the modal components, namely a force for the heave mode and moments for pitch, roll and twist are computed in the control block, a transformation matrix leads to the calculation of the real forces acting at the four corners of the vehicle:

$$\begin{pmatrix} F_{z,Bo,sus} \\ M_{\theta,Bo,sus} \\ M_{\varphi,Bo,sus} \\ M_{t,Bo,sus} \end{pmatrix} = \begin{bmatrix} 1 & 1 & 1 & 1 \\ -l_f & -l_f & l_r & l_r \\ \frac{b_f}{2} & \frac{b_f}{2} & \frac{b_r}{2} & -\frac{b_r}{2} \\ -\frac{b_f}{2} & \frac{b_f}{2} & -\frac{b_r}{2} & \frac{b_r}{2} \end{bmatrix} \begin{pmatrix} F_{fr} \\ F_{fl} \\ F_{rl} \\ F_{rr} \end{pmatrix} \quad (2.30)$$

$$\mathbf{F}_{\text{modal,sus}} = \mathbf{T}\mathbf{F}_{\text{sus}} \quad (2.31)$$

Where the transformation matrix is:

$$\mathbf{T} = \begin{bmatrix} 1 & 1 & 1 & 1 \\ -l_f & -l_f & l_r & l_r \\ \frac{b_f}{2} & \frac{b_f}{2} & \frac{b_r}{2} & -\frac{b_r}{2} \\ -\frac{b_f}{2} & \frac{b_f}{2} & -\frac{b_r}{2} & \frac{b_r}{2} \end{bmatrix} \quad (2.32)$$

The suspensions forces at the four corners of the vehicle, \mathbf{F}_{sus} can be split into a passive linear component for the suspension damping and stiffness and the actuating force of the semi-active actuators, \mathbf{F}_u .

$$\mathbf{F}_{\text{sus}} = -(\mathbf{D}_{\text{sus}}\Delta\dot{\mathbf{z}}_{\text{sus}} + \mathbf{K}_{\text{sus}}\Delta\mathbf{z}_{\text{sus}} + \mathbf{F}_u) \quad (2.33)$$

The relative movement between the body and the wheels is calculated with:

$$\Delta\mathbf{z}_{\text{sus}} = \mathbf{z}_{\text{Bo}} - \mathbf{z}_{\text{w}} \quad (2.34)$$

Where:

$$\mathbf{z}_{\text{Bo}} = \begin{pmatrix} z_{\text{Bo,fr}} \\ z_{\text{Bo,fl}} \\ z_{\text{Bo,rl}} \\ z_{\text{Bo,rr}} \end{pmatrix} = \mathbf{T}^T \mathbf{x}_{\text{Bo}} = \begin{bmatrix} 1 & -l_f & -\frac{b_f}{2} & -\frac{b_f}{2} \\ 1 & -l_f & \frac{b_f}{2} & \frac{b_f}{2} \\ 1 & l_r & \frac{b_r}{2} & -\frac{b_r}{2} \\ 1 & l_r & -\frac{b_r}{2} & \frac{b_r}{2} \end{bmatrix} \begin{pmatrix} z_{\text{Bo}} \\ \theta_{\text{Bo}} \\ \varphi_{\text{Bo}} \\ t_{\text{Bo}} \end{pmatrix} \quad (2.35)$$

The force that accounts for the anti-roll bar contribution is calculated as it follows:

$$\mathbf{F}_{\text{arb}} = -\mathbf{K}_{\text{arb}}\Delta\mathbf{z}_{\text{sus}} \quad (2.36)$$

The equations of motion of the wheels are summarized as:

$$\mathbf{M}_{\text{w}}\ddot{\mathbf{z}}_{\text{w}} = -(\mathbf{F}_{\text{sus}} + \mathbf{F}_{\text{arb}}) + \mathbf{F}_{\text{ro}} \quad (2.37)$$

The force vector representing the solicitation generated by the road irregularities is \mathbf{F}_{r0} and its formulation is the following:

$$\mathbf{F}_{r0} = -\mathbf{K}_T \Delta \mathbf{z}_{w,rel} \quad (2.38)$$

Where $\Delta \mathbf{z}_{w,rel}$ corresponds to the relative displacement between the wheels and the road input.

$$\Delta \mathbf{z}_{w,rel} = \begin{pmatrix} z_{w,fr} \\ z_{w,fl} \\ z_{w,rl} \\ z_{w,rr} \end{pmatrix} - \begin{pmatrix} z_{ro,fr} \\ z_{ro,fl} \\ z_{ro,rl} \\ z_{ro,rr} \end{pmatrix} = \mathbf{z}_w - \mathbf{z}_{ro} \quad (2.39)$$

The equations of motion of the engine are:

$$\mathbf{M}_{eng} \ddot{\mathbf{x}}_{eng} = \mathbf{F}_{eng} + \mathbf{F}_{ext} \quad (2.40)$$

The vector \mathbf{F}_{eng} considers the forces acting between the engine and the body. The engine is fixed to the body with two engine mounts symmetrically placed with respect to the longitudinal axis of the vehicle.

$$\mathbf{F}_{eng} = -(\mathbf{D}_{eng} \Delta \dot{\mathbf{x}}_{rel,eng} + \mathbf{K}_{eng} \Delta \mathbf{x}_{rel,eng}) \quad (2.41)$$

\mathbf{F}_{ext} is not considered in this work but could account for external disturbances.

$$\mathbf{F}_{ext} = 0 \quad (2.42)$$

The relative displacement between the engine and the body is defined as it follows:

$$\Delta \mathbf{x}_{rel,eng} = \mathbf{x}_{eng} - \mathbf{T}_{eng}^T \mathbf{x}_{Bo} \quad (2.43)$$

$\Delta \dot{\mathbf{x}}_{rel,eng}$ can be derived from Eq. (2.43). The engine transformation matrix \mathbf{T}_{eng} is:

$$\mathbf{T}_{eng} = \begin{bmatrix} 1 & 0 \\ -l_{eng} & 0 \\ 0 & 1 \\ 0 & 0 \end{bmatrix} \quad (2.44)$$

The heave engine force and roll engine moment can be derived from the modal coordinates using the engine transformation matrix:

$$\mathbf{F}_{modal,eng} = \begin{pmatrix} F_{z,Bo,eng} \\ M_{\theta,Bo,eng} \\ M_{\phi,Bo,eng} \\ M_{t,Bo,eng} \end{pmatrix} = \mathbf{T}_{eng} \mathbf{F}_{eng} = \begin{bmatrix} 1 & 0 \\ -l_{eng} & 0 \\ 0 & 1 \\ 0 & 0 \end{bmatrix} \begin{pmatrix} F_{z,eng} \\ M_{\phi,eng} \end{pmatrix} \quad (2.45)$$

The equations of motion of the body are the following:

$$\begin{pmatrix} m_{B_0} \ddot{z}_{B_0} \\ J_{yy} \ddot{\theta}_{B_0} \\ J_{xx} \ddot{\phi}_{B_0} \\ J_{B_0,t} \ddot{t}_{B_0} \end{pmatrix} = \mathbf{F}_{\text{modal,sus}} + \mathbf{F}_{\text{modal,arb}} - \mathbf{F}_{\text{modal,eng}} \quad (2.46)$$

$$\mathbf{M}_{B_0} \ddot{\mathbf{x}}_{B_0} = \mathbf{T}(\mathbf{F}_{\text{sus}} + \mathbf{F}_{\text{arb}}) - \mathbf{T}_{\text{eng}} \mathbf{F}_{\text{eng}} \quad (2.47)$$

2.4 Objectification methods for ride comfort

When it comes to ride comfort, suitable objectification methods are required in order to correlate the subjective feelings of a vehicle occupant and a representative physical quantity. Ride comfort can be defined as the comfort experienced by vehicle occupants from stationary oscillations when the vehicle travels on a road with vertical irregularities [13, p. 248]. Especially in automated and autonomous driving, the perception of comfort changes significantly because the occupants perform secondary activities. An overview on the objectification methods for ride comfort is given in [18]. In order to evaluate driving comfort, the Root Mean Square (RMS) of the accelerations of the body eigenmodes is always calculated to have an immediate feedback on driving comfort. RMS values are also estimated online via a sliding window method. The latter, consists of a window of specified length which moves over the data sample by sample and the RMS value is computed over the data in the window. Another method implemented in this work, is the online estimation of the Power Spectrum (PS) of acceleration signals. Further details on this will be given in Section 4.5.2.

ISO-2631 [19], BS 6841 [20] and VDI-2057 [21], [22], are some of the possible objectification methods for ride comfort. In this work, ISO-2631 is used. Other approaches from science are the methods of RERICHA [23], CUCUZ [24], KLINGER [25] and HENNECKE. A general overview of such methods is given as it follows.

2.4.1 ISO 2631

ISO 2631 has the aim of measuring whole-body vibrations to take account of health, comfort and perception in the frequency range from 0.5 Hz to 80 Hz, and of motion sickness from 0.1 Hz to 0.5 Hz. The SAE [26] has identified the range between 4 and 8 Hz as the most sensitive for human bodies. The procedure described in [19], is applicable when accelerations at certain supporting surfaces can be measured. The required surfaces where translational and rotational accelerations must be measured are seat, backrest and foot. Transducers should be located at the interface between the body and the source of its vibration.

For the sake of this work, a simplifying assumption is made as direct measurements at the interfaces points are not available in real vehicle tests and neither are they fictitiously estimated in simulations. Vertical acceleration in z-direction, as well as rotational accelerations around x- and y-axes (Figure 2.3), which respectively correspond to the accelerations of the eigenmodes of heave, roll and pitch, are supposed to be measured in the centre of gravity. These acceleration

signals are weighted in the frequency domain according to health, comfort, perception and motion sickness. An overall weighted RMS of an acceleration, a_{ISO} can be calculated. A weakness of this approach is that it underestimates the sensitivity to horizontal vibrations in multi-axial vibration [27]. In Table 2.2, the correlation between a_{ISO} and comfort perception is displayed [19, p. 25].

Table 2.2: Comfort perception [19, p. 25]

a_{ISO} in m/s^2	Perception description
< 0,315	Not uncomfortable
0,315 – 0,63	A little uncomfortable
0,5 – 1	Fairly uncomfortable
0,8 – 1,6	Uncomfortable
1,25 – 2,5	Very uncomfortable
> 2	Extremely uncomfortable

2.4.2 Other approaches

VDI 2057 was first introduced in 1987 [21], displaying his own method but was adapted later to ISO 2631 which was published in 1997, [22]. This procedure considers some additional measurement points but still calculates a weighted vibration parameter whose value is correlated to the subjective comfort perception. BS 6841 has a similar approach to the others but neglects the measurements at the backrest in y and z-direction and uses a different weighting function [20]. Other possible approaches in the objectification of ride comfort are the ones from RERICHA [23], CUCUZ [24], KLINGER [25] and HENNECKE, all based on ISO 2631. RERICHA additionally considers the steering wheel vibration by means of its angular acceleration, CUCUZ also takes into account single obstacles as a source of vibration, KLINGER increases the considered degrees of freedom at multiple interfaces and pays significant attention to stochastic roads and engine vibration while, HENNECKE only refers to pitch and roll. GRIFFIN states that different factors such as seating discomfort and noise affect the judgments on ride comfort [28] and also outlines some of the limitations of the standard methods. General factors regarding comfort or discomfort in sitting are identified in [29]. They include environment, posture, aesthetics, space, convenience and social or organizational parameters. Further details on chairs tests, in order to assess sitting comfort are given in [30].

Two experimental studies are conducted in literature in order to investigate the differences in the cited objectification methods [18]. The studies show that there is a considerable difference in comfort perception between attentive and inattentive occupants as the latter tend to increase their body movements. In certain driving situations, an accentuated movement of the head can be observed which results in a reduced driving comfort. Additionally, inattentive occupants are more susceptible to centripetal accelerations [31]. An extended version of ISO 2631 is presented by considering the head as a measurement point and it is proved that it leads to an enhancement in the objectification of driving comfort [32]. This new setup of body measurement system, including the head, is designed in [33].

2.5 Ride safety estimation

When it comes to vertical dynamics, ride safety is provided by the suspensions as long as forces can be transferred between the tires and the road. This leads to the vehicle manoeuvrability in terms, for example, of steering and braking.

In this thesis work, the following criteria on the dynamic wheel loads RMS value is chosen to evaluate driving safety [34, p. 20]:

$$\|F_{z_{w,ij,dyn}}\|_{\text{rms}} \leq \frac{F_{z_{w,ij,stat}}}{3} \quad (2.48)$$

with $i \in \{f, r\}, j \in \{r, l\}$. The static wheel loads are computed as it follows:

$$F_{z_{w,fj,stat}} = g(m_{Bo} \frac{l_r}{2l} + m_{w,fj}) \quad (2.49)$$

$$F_{z_{w,rj,stat}} = g(m_{Bo} \frac{l_f}{2l} + m_{w,rj}) \quad (2.50)$$

In [35, p. 2] dynamic wheel loads calculation is presented for a quarter car model. In the simulation model, dynamic wheel loads are derived offline with:

$$F_{z_{w,dyn}} = M_w(\ddot{z}_w - g) + M_{Bo,w}(\ddot{z}_{Bo} - g) \quad (2.51)$$

with:

$$\ddot{z}_w = \begin{pmatrix} \ddot{z}_{w,fr} \\ \ddot{z}_{w,fl} \\ \ddot{z}_{w,rl} \\ \ddot{z}_{w,rr} \end{pmatrix} \quad (2.52)$$

$$\ddot{z}_{Bo} = \begin{pmatrix} \ddot{z}_{Bo,fr} \\ \ddot{z}_{Bo,fl} \\ \ddot{z}_{Bo,rl} \\ \ddot{z}_{Bo,rr} \end{pmatrix} = \begin{bmatrix} 1 & -l_f & -\frac{b_f}{2} & -\frac{b_f}{2} \\ 1 & -l_f & \frac{b_f}{2} & \frac{b_f}{2} \\ 1 & l_r & \frac{b_r}{2} & -\frac{b_r}{2} \\ 1 & l_r & -\frac{b_r}{2} & \frac{b_r}{2} \end{bmatrix} \begin{pmatrix} \ddot{z}_{Bo} \\ \ddot{\theta}_{Bo} \\ \ddot{\phi}_{Bo} \\ \ddot{t}_{Bo} \end{pmatrix} = T^T \ddot{x}_{Bo} \quad (2.53)$$

$$M_{Bo,w} = \begin{bmatrix} m_{Bo} \frac{l_r}{2l} & 0 & 0 & 0 \\ 0 & m_{Bo} \frac{l_r}{2l} & 0 & 0 \\ 0 & 0 & m_{Bo} \frac{l_f}{2l} & 0 \\ 0 & 0 & 0 & m_{Bo} \frac{l_f}{2l} \end{bmatrix} \quad (2.54)$$

Eq. (2.54) shows how to refer the vehicle body mass to the four wheels, with an equilibrium around the centre of gravity. Eq. (2.51) is used as a reference for the online estimation of the dynamic wheel loads which is needed in the switching logic between the controllers and it is performed by using a Kalman filter, as described in Section 4.4. In simulations, the acceleration

due to gravity is neglected as the full vehicle model equations are derived from the static deflection of the body and the wheels.

2.6 Road roughness classification

A significant aspect of this work, is the possibility of testing the enhanced controller with different roads inputs, at least in a preliminary phase, when the logic is being developed. In addition to the availability of a few stochastic road measurements, artificially generated road inputs are needed. In order to correlate the results of the simulations in terms of comfort or road-holding to the road input, ISO 8608 is used [36]. It prescribes a general method to classify road roughness, using the Power Spectral Density (PSD) of the vertical road displacement as well as its spatial frequency. Spatial frequency, n , is measured as cycles/m while the PSD of the vertical displacement G_d in m^3 . The general procedure used in this work to generate random but classifiable profiles is presented. The method showed in [37] is followed. The conventional spatial frequency value is $n_0 = 0.1$ cycles/m. Depending on the road class, from A to H, a corresponding PSD value $G_d(n_0)$ can be identified [36]. The PSD of the vertical displacement, representing the road profile is:

$$G_d(n) = G_d(n_0) \left(\frac{n}{n_0}\right)^{-2} \quad (2.55)$$

Being N , the number of measurements inputs, and being L , the length of the longitudinal coordinate of the road profile x , the sampling interval B , can be estimated, as well as the spatial resolution Δn and the maximum spatial frequency, n_{max} :

$$B = \frac{L}{N} \quad (2.56)$$

$$\Delta n = \frac{1}{L} \quad (2.57)$$

$$n_{max} = N\Delta n \quad (2.58)$$

Therefore, the spatial frequency for an artificial road profile can be calculated as a vector $\Delta n \leq n \leq N\Delta n$, with spatial resolution Δn . Through some mathematical passages, the following expression for a random but classifiable road input can be obtained for the road vertical displacement, $h(x)$:

$$h(x) = \sum_{i=0}^N \sqrt{2\Delta n G_d(i\Delta n)} \cos(2\pi i\Delta n x + \beta) \quad (2.59)$$

Where β , is a randomly generated angle within 0 and 2π . In order to account for the differences between the left and right paths, the role of the coherence between parallel roads has been investigated. According to [38], when two parallel tracks are needed, a second correlated random profile may be generated in a similar way to the first. In order to do that, the cross spectral density and the cross phase angles, between the two parallel tracks, have to be known. This leads to the definition of an ordinary coherence function. In this work, the assumption of complete correlation between the parallel tracks is made (unitary coherence) in order to simplify the

generation of the artificial profiles. The difference between the two paths is therefore obtained by means of a phase angle, shifting the first one with respect to the second one. Further approaches to define an appropriate coherence function, can be found in [39], [40].

2.7 The controller

In this chapter, the existing controller (Figure 2.4 [41]) is presented as developed in [8]. It consists of a modal state feedback controller (R) and of an extended skyhook controller with twist mode (P). The controller also presents a feedforward compensation for engine and drivetrain vibrations, which is neglected in this work. The R controller is inspired by the Lotus Modal Control [42] and includes a pole placement by deciding the values of the eigenfrequencies and damping ratios for the considered modes, namely heave, pitch, roll and twist. The P controller is based on the skyhook principle [3], which is extended to the whole vehicle by selecting a P value representing a skyhook inertial damping for each direction of movement. The more comfortable P controller does not consider the wheels dynamics and therefore, it is not suitable for road-holding. On the other hand, the R controller limits the dynamic wheel loads variations but, entails higher body accelerations values because it shows the dynamics of a passive system in each eigenmode. In the existing model, the two controllers can only be used separately by manually disabling one of the two. This has led to the necessity of developing a suitable coordination logic (K^+) that could possibly enhance the existing controller and achieve better vehicle performances in terms of resolution of the conflict between driving safety and driving comfort.

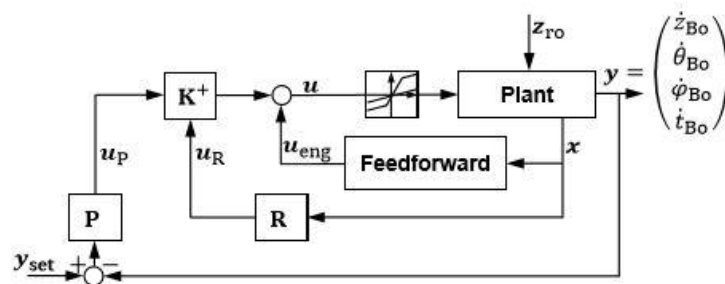


Figure 2.4: Vertical dynamics controller [8, p. 33]

First of all, an overview on the Skyhook principle is given (Section 2.7.1). The theoretical principles of modal analysis and modal controller theory are shown (Section 2.7.2). Finally, the P controller (Section 2.7.3) and the R controller (Section 2.7.4) are presented.

2.7.1 Skyhook principle

Skyhook controller was developed in 1974 by Karnopp [3]. In its simplest form, the Skyhook controller isolates the motion of the mass from the ground motion. The body is suspended via a virtual damper, d_{sky} and the actual damping force is controlled by the adjustment of the damping ratio d_{Bo} (Figure [43, p. 31]). The latter depends indeed, on the relative speed of the body to the wheels and on the direction of the damper displacement.

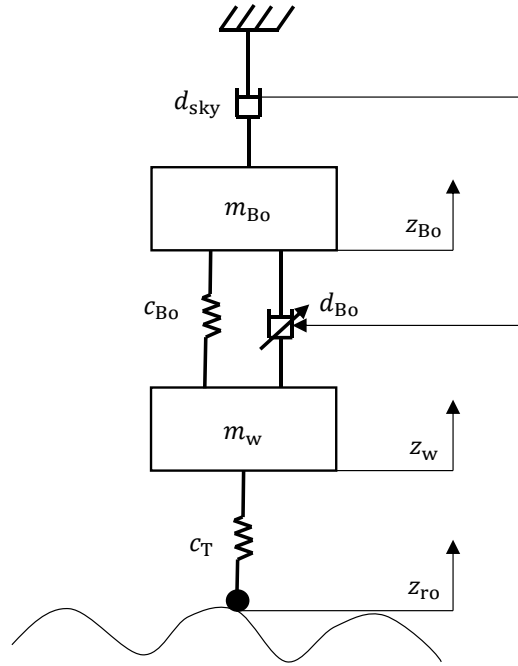


Figure 2.5: Skyhook principle on quarter car suspension [43, p. 31]

The equations representing the Skyhook control of a quarter car vehicle are the following [43]:

$$d_{B0} = \begin{cases} d_{B0,max} & \text{if } \frac{d_{sky}\dot{z}_{B0}}{\dot{z}_{B0} - \dot{z}_w} > d_{B0,max} \\ \frac{d_{sky}\dot{z}_{B0}}{\dot{z}_{B0} - \dot{z}_w} & \text{if } d_{B0,min} < \frac{d_{sky}\dot{z}_{B0}}{\dot{z}_{B0} - \dot{z}_w} \leq d_{B0,max} \\ d_{B0,min} & \text{if } \frac{d_{sky}\dot{z}_{B0}}{\dot{z}_{B0} - \dot{z}_w} \leq d_{B0,min} \end{cases} \quad (2.60)$$

The range of variation of d_{B0} depends on the kind of semi-active suspension used and can correspond to the valve opening controlling current or to the properties of an electro-rheological fluid.

2.7.2 Modal analysis and modal controller theory

Modal analysis is the study of the dynamic properties of a system in the frequency domain and it allows to define its eigenfrequencies and eigenmodes which represent the way the system vibrates. For a second order mechanical system of n degrees of freedom, the following modal analysis can be performed, where \mathbf{y} is the vector containing the system degrees of freedom, \mathbf{M} is the positive definite, real and diagonal mass matrix, \mathbf{K} is the positive semidefinite or definite, real, symmetric stiffness matrix, \mathbf{D} is the positive semidefinite or definite, real, symmetric damping matrix and \mathbf{F} is the external force vector. The property of the symmetry is always valid when natural systems are examined.

$$\mathbf{M}\ddot{\mathbf{y}} + \mathbf{D}\dot{\mathbf{y}} + \mathbf{K}\mathbf{y} = \mathbf{F} \quad (2.61)$$

When considering an undamped and unforced system, meaning $\mathbf{F} = \mathbf{D} = 0$, the existence of synchronous solutions can be demonstrated. This leads to the definition of the eigenvalue problem:

$$(\mathbf{K} - \omega^2 \mathbf{M})\mathbf{y}_0 = 0 \quad (2.62)$$

Which can be solved by:

$$\det(\mathbf{K} - \omega^2 \mathbf{M}) = 0 \quad (2.63)$$

Eigenvalues can be calculated by means of the following:

$$\omega_i^2 = \lambda_i \quad (2.64)$$

with $i = 1 \dots n$. In general, a modal direct transformation can be performed, where $\boldsymbol{\eta}$ represents the vector of the modal coordinates of the system and $\boldsymbol{\Psi}$ is the matrix containing the autovectors of the undamped modal system, as columns:

$$\mathbf{y} = \boldsymbol{\Psi}\boldsymbol{\eta} \quad (2.65)$$

Substituting Eq. (2.65) in Eq. (2.61) and pre-multiplying for the transposed matrix $\boldsymbol{\Psi}^T$, with $\mathbf{F} = 0$, the following is obtained:

$$\boldsymbol{\Psi}^T \mathbf{M} \boldsymbol{\Psi} \ddot{\boldsymbol{\eta}} + \boldsymbol{\Psi}^T \mathbf{D} \boldsymbol{\Psi} \dot{\boldsymbol{\eta}} + \boldsymbol{\Psi}^T \mathbf{K} \boldsymbol{\Psi} \boldsymbol{\eta} = \mathbf{0} \quad (2.66)$$

The symmetry of the stiffness and mass matrix leads to the property of orthogonality which decouples the equation for mass and stiffness terms.

$$\mathbf{M}_r \ddot{\boldsymbol{\eta}} + \boldsymbol{\Psi}^T \mathbf{D} \boldsymbol{\Psi} \dot{\boldsymbol{\eta}} + \mathbf{K}_r \boldsymbol{\eta} = \mathbf{0} \quad (2.67)$$

Where \mathbf{M}_r and \mathbf{K}_r are diagonal matrices. The complete decoupling can be achieved by manipulating the damping matrix, for example with proportional damping. A completely decoupled system, cannot be obtained though, in the full vehicle model presented in Section 2.3. This is due to some asymmetries like the different values of the suspension stiffness between the front and rear or the position of the centre of gravity which is not centred with respect to the longitudinal axis.

For MIMO systems (Multiple Input Multiple Output), a central control can be implemented with complete decoupling of the equations through state feedback. The idea behind the state feedback approach is that all state variables can be measured or at least estimated. The state vector is always returned to the control block. The control input \mathbf{u} , is obtained by the difference between a set signal, prefiltered with \mathbf{F} and a feedback signal multiplied by the controller matrix (Figure 2.6). A comparison on different state feedback controller design methods is performed in [44].

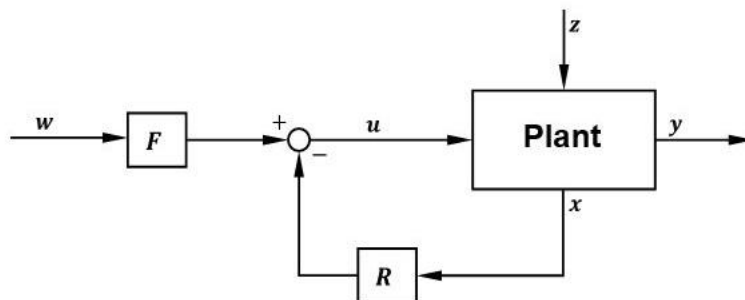


Figure 2.6: State feedback controller

The control variable enters the plant with the following expression:

$$\mathbf{u} = -\mathbf{R}\mathbf{x} + \mathbf{F}\mathbf{w} \quad (2.68)$$

The desired transfer function must be diagonal to generate decoupled equations. In order to achieve that, the number of controlled variables must be equal to the number of actuators. This is the reason why the twist mode is introduced. An extended explanation on modal control laws is given in [45]. In order to apply a modal control law, a reduced set of degrees of freedom is chosen as controlled variables. Being $n_R < n$, the number of degrees of freedom of the system chosen as the controlled variables (with n , the total number of degrees of freedom), and being m , the number of the actuators implemented in order to control the plant, the following rules are valid. If $m = n_R$, the problem is determined, the transformation matrix from modal coordinates to the actuators directions is invertible. If $m > n_R$, the problem is over-determined and a pseudo-inverse matrix needs to be adopted. This filters the measurement noise in a least square sense. If $m < n_R$, the problem is under-determined and a state observer is required to estimate the missing measurements. In the full vehicle model (Section 2.3), with the assumption of a rigid body, the dynamic behaviour could be described by the body heave, roll and pitch motions. This would lead to three controllable variables and four actuators placed at the corners of the vehicle via the semi-active suspensions and would require the usage of a pseudo-inverse approach which has been substituted by the introduction of a new degree of freedom for the body motion. The R controller whose mathematical model is presented in Section 2.7.4, finds its basis in [46], where a feedback controller has been implemented in order to separately tune heave, pitch and roll motions of a vehicle body via decoupling of the model equations. Decoupling is achieved with a state feedback controller whose control law consists of a gain multiplying the feedback state vector. There are two gain matrices, one for stiffness and one for damping. They both result in the difference between the desired stiffness and damping matrices and the true ones. The desired dynamics is defined with diagonal matrices which guarantees decoupling. The equations of motion in the directions of heave, pitch and roll can be obtained and the real actuating forces are entered in the model with a transformation matrix considering the real points of application of the forces. The described approach, shows a non-quadratic matrix for modal transformation that cannot be inverted as the system is over-determined.

2.7.3 P controller: extended Skyhook

The Skyhook principle presented in Section 2.5.1, can be identified as a proportional (P) controller. It could be extended to the whole vehicle by implementing it on each of the four corners. In this work though, the Skyhook principle has been applied to the modal coordinates of heave, pitch, roll and twist. This can be achieved by means of a $K_{P,i}$ proportional factor, being $i \in [z_{B_0}, \theta_{B_0}, \varphi_{B_0}, t_{B_0}]$ (Figure 2.7) and by using the transformation matrix. In the extended Skyhook control, the $K_{P,i}$ values correspond to the d_{sky} of Figure 2.5.

The P controller block, is fed by an error e , generated as the difference between a set, \mathbf{y}_{set} and a feedback \mathbf{y} as in Eq. (2.70). The set signal is always equal to zero, meaning that the body velocity in the different modes is required to be null (Eq. (2.69)). The feedback signals are the velocities of the body in each direction of movement.

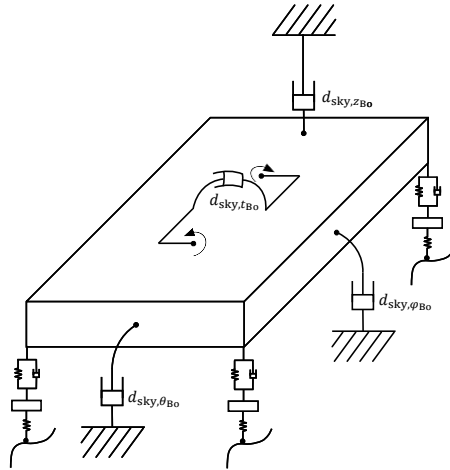


Figure 2.7: Extended Skyhook controller with twist mode [8, p. 39]

$$\mathbf{y}_{\text{set}} = \mathbf{0} \quad (2.69)$$

$$\mathbf{e} = \mathbf{y}_{\text{set}} - \mathbf{y} \quad (2.70)$$

The so calculated error is multiplied by a K_P gain, which can be set to a different value for each modal direction.

$$\mathbf{u}_{P,\text{modal}} = \mathbf{K}_P \mathbf{e} = -\mathbf{K}_P \mathbf{y} \quad (2.71)$$

Where \mathbf{K}_P is:

$$\mathbf{K}_P = \begin{bmatrix} K_{P,z_{B0}} & 0 & 0 & 0 \\ 0 & K_{P,\theta_{B0}} & 0 & 0 \\ 0 & 0 & K_{P,\varphi_{B0}} & 0 \\ 0 & 0 & 0 & K_{P,t_{B0}} \end{bmatrix} \quad (2.72)$$

In order to compute the input actuating force from the P controller, the modal transformation matrix is used:

$$\mathbf{u}_P = -\mathbf{T}^{-1} \mathbf{u}_{P,\text{modal}} = \mathbf{T}^{-1} \mathbf{K}_P \mathbf{y} \quad (2.73)$$

2.7.4 R controller

The R controller, in terms of system controllers classification, is a state feedback with pole placement. The latter is desired as it means directly deciding the location of the eigenvalues of the system. As a matter of fact, the R controller allows to choose the desired stiffness, via the desired undamped natural frequencies, and damping, via the damping ratios, for the four body degrees of freedom (Figure 2.8, [8, p. 34]). The input vector \mathbf{u}_R is calculated after a retransformation of the modal coordinates into the direction of action of the four actuators at the vehicle corners. The present work does not aim at achieving a perfect decoupling between the modes, as done in [8]. Consequently, the values of the spring stiffness, c_i , and of the damping coefficients, d_i are tuned in an optimal sense, being $i \in [z_{B0}, \theta_{B0}, \varphi_{B0}, t_{B0}]$, to achieve the best road-holding or ride comfort. Further explanations on this are given in Appendix F.

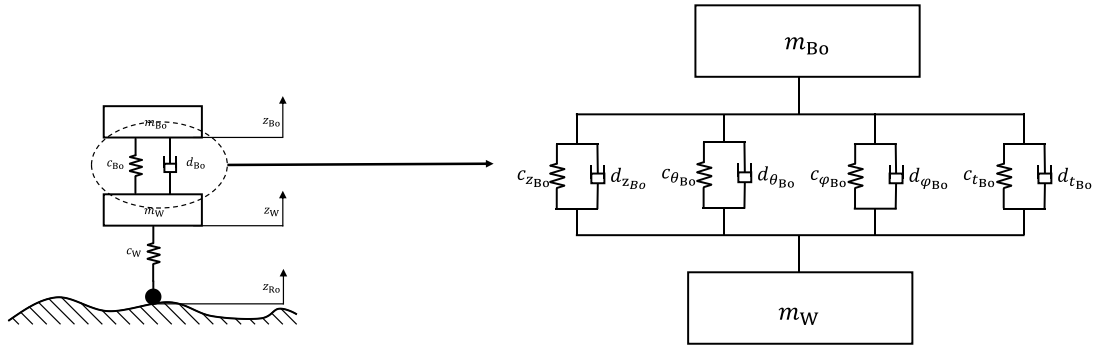


Figure 2.8: R controller [8, p. 34]

In the derivation of the control law, only the body movements are taken into account while the movements of the engine are neglected. This derives from the assumption that the eigenfrequencies of the body are of an order of magnitude lower than the ones of the engine and that the vehicle shows a rigid body behaviour. The state space equations for the full vehicle change as it follows:

$$\hat{\mathbf{K}}_{\text{Bo}} = \mathbf{T}(\mathbf{K}_{\text{sus}} + \mathbf{K}_{\text{arb}})\mathbf{T}^T \quad (2.74)$$

$$\hat{\mathbf{D}}_{\text{Bo}} = \mathbf{T}\mathbf{D}_{\text{sus}}\mathbf{T}^T \quad (2.75)$$

$$\hat{\mathbf{M}}_{\text{Bo}} = \begin{bmatrix} m_{\text{Bo}} & 0 & 0 & 0 \\ 0 & J_{yy} & 0 & 0 \\ 0 & 0 & J_{xx} & 0 \\ 0 & 0 & 0 & J_{\text{Bo},t} \end{bmatrix} \quad (2.76)$$

The body dynamics can be seen as the difference between the desired one and the passive suspensions dynamics as it follows:

$$\mathbf{M}_{\text{Bo}}\ddot{\mathbf{x}}_{\text{Bo}} = -(\hat{\mathbf{D}}_{\text{Bo}}\Delta\dot{\mathbf{x}}_{\text{Bo}} + \hat{\mathbf{K}}_{\text{Bo}}\Delta\mathbf{x}_{\text{Bo}}) + \mathbf{u}^* \quad (2.77)$$

But it can also be expressed as an immediate derivation of equations from Figure 2.8.

$$\mathbf{M}_{\text{Bo}}\ddot{\mathbf{x}}_{\text{Bo}} = -(\mathbf{D}^*\Delta\dot{\mathbf{x}}_{\text{Bo}} + \mathbf{K}^*\Delta\mathbf{x}_{\text{Bo}}) \quad (2.78)$$

Where \mathbf{D}^* and \mathbf{K}^* are diagonal matrices and give place to decoupled equations. Eq. (2.78), shows the dynamics of a passive system.

$$\mathbf{D}^* = \begin{bmatrix} d_{z_{\text{Bo}}} & 0 & 0 & 0 \\ 0 & d_{\theta_{\text{Bo}}} & 0 & 0 \\ 0 & 0 & d_{\phi_{\text{Bo}}} & 0 \\ 0 & 0 & 0 & d_{t_{\text{Bo}}} \end{bmatrix} \quad (2.79)$$

$$\mathbf{K}^* = \begin{bmatrix} c_{z_{\text{Bo}}} & 0 & 0 & 0 \\ 0 & c_{\theta_{\text{Bo}}} & 0 & 0 \\ 0 & 0 & c_{\phi_{\text{Bo}}} & 0 \\ 0 & 0 & 0 & c_{t_{\text{Bo}}} \end{bmatrix} \quad (2.80)$$

And with $\Delta\mathbf{x}_{\text{Bo}}$:

$$\Delta\mathbf{x}_{\text{Bo}} = \mathbf{T}^{-T}\Delta\mathbf{z}_{\text{sus}} = \mathbf{x}_{\text{Bo}} - \mathbf{T}^{-T}\mathbf{z}_{\text{w}} \quad (2.81)$$

From Eq. (2.77) and Eq. (2.78) the following is derived:

$$\begin{aligned} \mathbf{u}^* &= -(\mathbf{D}^* \Delta \dot{\mathbf{x}}_{B_0} + \mathbf{K}^* \Delta \mathbf{x}_{B_0}) + (\widehat{\mathbf{D}}_{B_0} \Delta \dot{\mathbf{x}}_{B_0} + \widehat{\mathbf{K}}_{B_0} \Delta \mathbf{x}_{B_0}) \\ &= -(\Delta \mathbf{D}^* \Delta \dot{\mathbf{x}}_{B_0} + \Delta \mathbf{K}^* \Delta \mathbf{x}_{B_0}) \end{aligned} \quad (2.82)$$

$$\Delta \mathbf{D}^* = \mathbf{D}^* - \widehat{\mathbf{D}}_{B_0}; \quad \Delta \mathbf{K}^* = \mathbf{K}^* - \widehat{\mathbf{K}}_{B_0} \quad (2.83)$$

Eq. (2.83) can be expressed via the state space variables, underlining the two effects of the control law, on the body and on the wheels:

$$\mathbf{u}^* = -(\Delta \mathbf{D}^* \dot{\mathbf{x}}_{B_0} + \Delta \mathbf{K}^* \mathbf{x}_{B_0}) + \Delta \mathbf{D}^* \mathbf{T}^{-T} \dot{\mathbf{z}}_w + \Delta \mathbf{K}^* \mathbf{T}^{-T} \mathbf{z}_w \quad (2.84)$$

To obtain the actual control law of the actuators, the transformation matrix is used:

$$\begin{aligned} \mathbf{u}_R &= -\mathbf{T}^{-1} \mathbf{u}^* = \mathbf{T}^{-1} (\Delta \mathbf{D}^* \dot{\mathbf{x}}_{B_0} + \Delta \mathbf{K}^* \mathbf{x}_{B_0}) - \mathbf{T}^{-1} (\Delta \mathbf{D}^* \mathbf{T}^{-T} \dot{\mathbf{z}}_w + \Delta \mathbf{K}^* \mathbf{T}^{-T} \mathbf{z}_w) \\ &= -\mathbf{R} \mathbf{x} \end{aligned} \quad (2.85)$$

Matrix \mathbf{R} is shown in Appendix B. In the simulation model, Δz_{sus} and $\Delta \dot{z}_{\text{sus}}$ are used as input variables as they can be directly measured in the real vehicle. The control law is modified as it follows:

$$\mathbf{u}_R = \mathbf{T}^{-1} \Delta \mathbf{D}^* \mathbf{T}^{-T} \Delta \dot{\mathbf{z}}_{\text{sus}} + \mathbf{T}^{-1} \Delta \mathbf{K}^* \mathbf{T}^{-T} \Delta \mathbf{z}_{\text{sus}} \quad (2.86)$$

When it comes to the wheels dynamics, the following applies:

$$\mathbf{M}_w \ddot{\mathbf{z}}_w = \mathbf{D}_{\text{sus}} \Delta \dot{\mathbf{z}}_{\text{sus}} + (\mathbf{K}_{\text{sus}} + \mathbf{K}_{\text{arb}}) \Delta \mathbf{z}_{\text{sus}} - \mathbf{K}_T \mathbf{z}_{w,\text{rel}} + \mathbf{u}_R \quad (2.87)$$

Neglecting the road excitation, $\mathbf{z}_{r_0} = 0$, and the body movements, ($\mathbf{x}_{B_0} = \dot{\mathbf{x}}_{B_0} = 0$), and substituting Eq. (2.86) in Eq. (2.87), the controlled wheels dynamics is derived:

$$\mathbf{M}_w \ddot{\mathbf{z}}_w = -(\mathbf{T}^{-1} \mathbf{D}^* \mathbf{T}^{-T} \dot{\mathbf{z}}_w + (\mathbf{T}^{-1} \mathbf{K}^* \mathbf{T}^{-T} + \mathbf{K}_T) \mathbf{z}_w) \quad (2.88)$$

The stiffness behaviour is decoupled as \mathbf{K}_T is a diagonal matrix and the secondary diagonal elements can be neglected due to the high stiffness values of the tyres. The damping terms show a coupled behaviour depending on the deviation between the desired damping values in the body eigenmodes: the greater, the higher the coupling in the wheels.

3 State of the art

This chapter presents a concise overview of the state of the art in the switching between different controllers techniques (Section 3.1) and in adaptive controllers applied to active or semi-active suspensions (Section 3.2). An overview on suspension oriented Skyhook control is given (Section 3.3). In Section 3.4 a criticism to the state of the art is conducted.

3.1 Switching strategies

In this section, switching strategies between controllers are presented. These include anytime control algorithm, artificial neural network and coordinated control strategies as well as Crone suspension switching algorithm. In [47], it is shown how switching between a finite number of controllers can be used to improve closed loop performances.

3.1.1 Anytime control with two controllers

In computer science, an example of event-triggered anytime control with two controllers is found in [48]. In embedded control systems, computational resources are usually shared and random data packets losses as well as unavailability of process variables can happen. Anytime algorithms have been taken into account especially for real time systems. Such an anytime algorithm presents two control policies requiring a different amount of processor resources to calculate the input to the control unit. The switching between the two controllers is realized comparing a certain process variable to a significant threshold. Linear control algorithms are transformed to anytime control algorithms by switching between controllers of different order.

3.1.2 Neural networks and coordinated control strategies

In the field of artificial intelligence, artificial neural network (ANN) attempts to imitate the human brain logic. ANN finds one of its possible applications in power transmission [49], with the aim of coordinating three control laws with a genetic algorithm capable of tuning some system parameters and minimizing some performance indices.

A coordinated system is a model built on different hierarchical levels in which a coordinator at the highest level is in charge of managing subsystems at the lowest levels. This is achieved by means of a suitable control law that needs to ensure a proper interaction between the lower level subsystems. An example of overall coordinated controller is found in [50], with the purpose of ensuring power sharing between a renewable and a dispatchable source of energy. An adaptive neuro-fuzzy inference system (ANFIS) based coordinated controller is presented in [51]. Its aim is to enhance the stability and reliability of a multiterminal high voltage direct current system

(MTDC) in combination to a series of PI controllers. Other examples of coordinated controllers in the energy field can be found in [52], [53], [54]. A coordinated control strategy is proposed in order to combine different goals in a full vehicle model [55]. A coordination between two families of controllers, high order sliding mode and backstepping controllers is achieved. The aim of the work is to globally control the chassis with respect to active steering, differential braking and active suspensions. Both normal and critical driving situations are considered and when entering from the first scenario to the second one, a smooth switching in control parameters of the active suspension is performed. A threshold is defined, and a stability factor is used for the switching condition.

3.1.3 Crone suspension switching algorithm

CRONE is the French acronym of “suspension `a Comportement Robuste d’Ordre Non Entier” [56], and consists of a traditional suspension configuration where the spring and the damper are substituted by an hydropneumatic system. These systems are called multi-mode systems as they are provided with a switching law to choose between different modes. Usually, those switching laws depend on a driver’s input. In [57] a switching law between an hard and a soft mode is analysed depending on the driver’s action on the steering wheel. Two architectures are available whose difference is due to additional air volumes to the principal one. The main objective of this system is to solve the dilemma between road-holding and ride comfort.

3.2 Adaptive control of active and semi-active suspensions

Adaptive control is a control method that consists of an adaptation of the controller to the system varying conditions by changing a set of parameters and eventually the control law. In [58] an example of adaptive control for vehicle active suspensions with unknown nonlinearities is presented. A prescribed performance function is used into the control design to stabilize heave and pitch motions and an adaptive law is implemented in order to achieve a parameter estimation. In [59], a traffic condition based fuzzy controller for active suspension is designed. Two fuzzy controllers for front and rear suspensions are implemented and tuned by considering two optimization objectives, namely a ride comfort index and the maximum suspension travel. Adaptive nonlinear active suspension control, based on a road classifier with a modified super-twisting algorithm is shown in [60]. In an offline phase, optimised control parameters are estimated and provided to a probabilistic neural network (PNN) for training. In an online phase, PNN determines the road level and the corresponding control parameters which are supplied to a nonlinear controller providing the active contribution of the suspension. A control law for a semi-active suspension is extended from the conventional skyhook control, and the controller gains are scheduled for various frequency regions of road disturbances by means of road-frequency adaptive controller [61]. In addition, several adaptive controller approaches are presented in order to detect the driving state and consequently schedule the controller parametrization [34].

In adaptive control theory, the multiple model approach can be found. This leads to an improved efficiency in adaptive systems. A large number of models can be used at every simulation time step. In [62] a multiple model switching controllers using H_∞ control for systems with large uncertainties is carried out. In switching based control, a set of candidate controllers for some

corresponding multiple models is chosen and the main controller switches between the set of candidate, according to online measurements. The H_∞ control theory is used to develop single candidate controllers. An example of its application to active suspension systems is given in [63].

3.3 Suspension oriented Skyhook control

In literature, there are several examples of suspension oriented skyhook control. These approaches have been mainly applied to quarter car models with semi-active dampers. A simple method for skyhook damper control is presented in [64] and applied to continuously adjustable dampers.

Another possibility is a suspension oriented skyhook control which is compared to an H_∞ control in a quarter car model [65]. With reference to Figure 3.1 [65, p. 108], the following control law was designed:

$$\mathbf{u} = -d_{\text{sky}}\dot{z}_{B_0} + \alpha d_{\text{sky}}\dot{z}_w \quad (3.1)$$

Where d_{sky} represents the damping of the link to the sky and α the percentage of the damping d_{sky} used for the suspension.

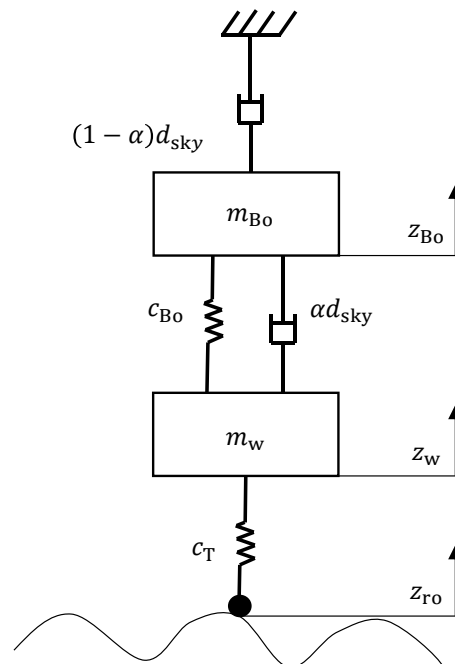


Figure 3.1: Quarter car model with suspension oriented Skyhook controller

In [66], some practical aspects of the same approach are carried out and conclusions are made on the better efficiency on the H_∞ control despite the easier adjustability of the skyhook approach. In [67] a study on the dynamic jerk caused by the change in the damping force is developed by means of an adjustable damping factor depending on the relative velocity between the sprung and the unsprung masses. In [68], the \mathbf{u} input force is estimated by minimizing a J index with

linear quadratic control. The J index takes into account limitations on the suspension deflection. This approach is compared to the classic Skyhook approach where:

$$\mathbf{u} = -d_{\text{sky}}\dot{\mathbf{z}}_{\text{Bo}} \quad (3.2)$$

In this case the quarter car vehicle is designed with a virtual prototype so that full vehicle manoeuvres can be simulated. In [69], optimal suspensions for quarter car models are analysed. A performance index accounting for tire and suspension deflection is formulated. In [70], an optimal skyhook control for semi-active suspensions is developed. The control law is the same of Eq. (3.1). A weighted cost function is designed and it is minimized to obtain an optimal value for both d_{sky} and α . In [71], Eq. (3.1) is modified as it follows and the control law is addressed to as *modified Skyhook control*.

$$\mathbf{u} = C_{\text{max}}\alpha(\dot{\mathbf{z}}_{\text{Bo}} - \dot{\mathbf{z}}_{\text{w}}) + (1 - \alpha)\dot{\mathbf{z}}_{\text{w}} \quad (3.3)$$

With:

$$C_{\text{max}} = C_{\text{p}} + C_{\text{s}} \quad (3.4)$$

$$\alpha = \frac{C_{\text{p}}}{C_{\text{max}}} \quad (3.5)$$

Where C_{p} and C_{s} are, respectively, the passive and Skyhook damping rates and C_{max} is the physical limit on the performance of the damper. BESINGER approach [71] was taken and implemented in a more complex model but applied with quarter car model equations only on the four vehicle corners [72]. A different approach implemented the skyhook control law of Eq. (3.1) by modifying and extending it, to a 7 degrees of freedom vehicle model to control heave, pitch and roll [73]. Conclusions on optimal α values or on a way of combining the different proposed control laws were not drawn though. The above mentioned approaches are transformed and enhanced in order to develop a *modified P controller* (Section 4.6).

3.4 Criticism of the state of the art

The R modal controller, manages to efficiently control the wheel dynamics. With respect to [46], where the wheels were not considered in the control law, the R control provides better driving safety. In the modal space though, this results in the dynamics of a passive system and entails higher acceleration values that results in uncomfortable driving perceptions. Of course the difference with a passive suspension is the possibility of tuning the body modes of heave, pitch, roll and twist individually and variably. On the other hand, the more comfortable P controller alone, does not account for the wheels dynamics and can imply dangerously high dynamic wheel loads. This leads to the necessity of a suitable coordination logic between the two controllers.

From the concise overview on the state of the art, it is clear that the idea of switching between two different controllers has not been sufficiently explored yet, especially in the field of semi-active and active suspension control and with the aim of combining safety and comfort. The definition of an appropriate coordination logic directly implies an online estimation of some variables of interest that can possibly represent ride comfort as well as road-holding. The control

logic must combine the R and the P controller in an adaptive way depending on the simulation scenario.

As a consequence, aspects from adaptive control theory are considered as well as switching controller approaches. Classic adaptive controllers, in their simplest form, adjust the controller parameters in a continuous way as a consequence of an online identification of model variables changing in time, but do not necessarily imply the use of multiple controllers especially displaying two different objectives. At the same time, switching strategies between controllers do not seem to be applied to active and semi-active suspensions, and the attempts of coordinated controllers refers to vehicle subsystems that are not considered in this work, as the focus is on vertical dynamics.

On the other hand, suspension oriented Skyhook approaches have always been developed for quarter car models and even when applied to more complex models they would anyway consider only heave, pitch and roll of the body. In addition, their main field of interest has always been magneto-rheological dampers and not electrohydraulic ones.

4 Method

This chapter describes the procedures and the methods that have been used in the enhancement of the vertical dynamics controller. From the criticism to the state of the art, the scientific news value of the work is presented (Section 4.1). The development environment (Section 4.2) as well as test scenarios (Section 4.3) are described. The development of four Kalman filters to estimate the dynamic wheel loads is carried out (Section 4.4). The coordination logic design is derived (Section 4.5) and a modified P controller is presented (Section 4.6). Finally, simulations results are shown (Section 4.7).

4.1 Scientific news value

From the criticism of the state of the art, the scientific news value of the work can be immediately derived. First of all, P and R controllers were designed in [8] to achieve decoupling and consequently a variable tuning in the body eigenmodes. They could only be used separately by manually activating one of the two before starting a simulation. The P controller alone is more suitable where road excitations, whose profile is smaller than the suspension travel, are simulated. In those cases, the Skyhook principle can compensate the solicitation and provide high comfort without incurring into road-holding issues. With larger excitations the R controller is preferable even though it reduces comfort perception due to its passive dynamics in the modal space. In this work, P and R controllers are tuned to achieve respectively optimal comfort and optimal road-holding with the minimization of the accelerations RMS values as well as of dynamic wheel loads. The feedforward compensation for engine dynamics is neglected in this work. A strong novelty is a coordination logic, K^+ . This removes the necessity of manually choosing the controller in the simulation as K^+ directly adjusts the overall control law depending on the driving simulation. This results in an optimal exploitation of both controllers strengths. Secondly, a modified P controller is developed. Its effectiveness is compared with the coordination logic one. A novelty with respect to [65], is that in this work, the modified Skyhook principle is applied to the full vehicle model and not to a quarter car one. Electrohydraulic dampers are implemented and not magneto-rheological ones. There have been attempts of extending this modified principle to a seven degrees of freedom vehicle model, but in none of these cases the twist mode was considered.

4.2 Development environment

The implementation of the model is performed in the object-oriented environment MatLab/Simulink. The advantage of using a simulation model relies in the possibility of making adjustments and modifications, as well as conducting relatively fast sensitivity analysis, without incurring in

additional costs or efforts. Only when the logic is fully optimized in the simulation environment, it can be tested in the real vehicle where further improvements can be performed. The simulation model consists mainly of three parts (Figure 4.1). The controllers block, which consists of the P controller, the R controller, the coordination logic between the two, and of a transformation block which transforms the desired modal force and moments from the controllers into the active or semi-active forces at the four suspensions corners. The real forces estimator block, which contains inverse lookup tables that represent the actuator properties. A specific actuator model is not implemented and its dynamics is neglected, but real actuator force limits can be considered. There is a manual switch in the block that allows to perform simulations without considering the actuator force constraints and can result in ideal actuators or in a sense, active ones. Actuators are not physically placed in correspondence of the wheels and therefore an installation ratio, assumed constant in the working range, must be taken into account in terms of moments equilibrium. The total semi-active suspension force, only considering its damping component, and referred to the wheels, $F_{\text{susp,d},ij}$, is expressed as it follows:

$$F_{\text{susp,d},ij} = i_i F_{\text{susp,d}} \quad (4.1)$$

with $i \in \{f, r\}$, $j \in \{r, l\}$ and where $F_{\text{susp,d}}$ is the semi-active damping dissipative component occurring at the physical position of the shock absorbers (Appendix G). The plant model block manages the resolution of the state space equations for the chosen full vehicle model. It receives the input from the controllers, eventually considering the actuators limitations, and the input from the road, in terms of vertical displacement. As the road input is usually not known a-priori in real life tests, an estimator has been implemented in order to correctly compute the variables that are needed for the coordination logic (Section 4.5). From the plant block, the state space vector is calculated at each time step and fed as an input to the controller block. In the testing phase of the logic, the plant model block is substituted with the real vehicle, equipped with standard sensors in order to measure the inputs to the controllers block.

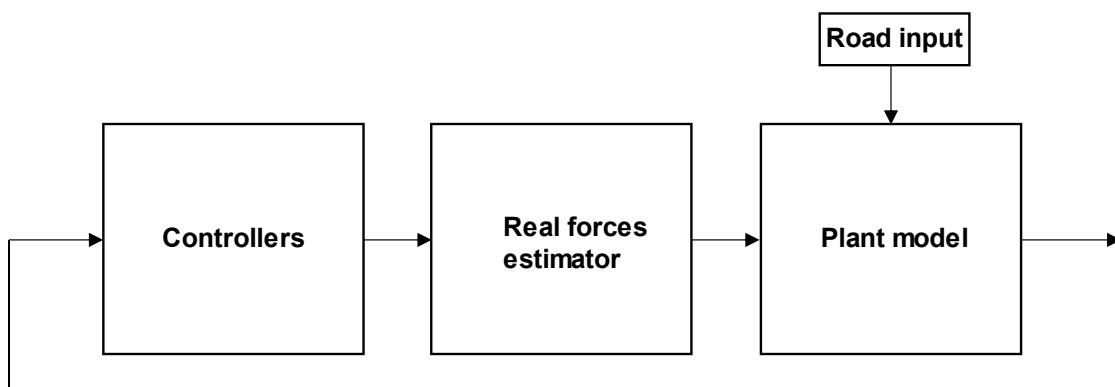


Figure 4.1: Simulation model

4.3 Test scenarios

In order to test the simulation model during the development phase of the coordination logic and to enhance the controller, different test scenarios are employed in this work. Two stochastic profiles from Munich area are available. They were recorded by means of a laser profilometer and the right and left tracks were obtained from the scan of the surface as a function of the trackwidth and the centre line of the vehicle on the road. Measurements were available in five columns, respectively representing the longitudinal coordinate going from 0 to the length of the recorded path and the road displacements in vertical direction for each wheel. A third order pass-band from 0.1 Hz to 25 Hz Butterworth filter has been used to cut off the low frequency components of the measured road profiles, specifically below 0.1 Hz and the highest ones, above 25 Hz. The Butterworth filter shows a smooth passband and a smooth increase in stopband attenuation. The attenuation in the stopband rises by $-20n$ dB/decade or $-6n$ dB/octave where n represents the number of poles and the filter order [74, 245]. The measured road profiles are addressed as MnF and FnP, respectively representing paths from Massenhausen to Fürholzen and Freising to Pulling. The dependence of the amplitude, for real road profiles, to frequency can be observed (Figure 4.2, 4.3).

Within the scope of this work, either the power spectrum or the power spectral density are always computed to elaborate the simulations results. WELCH's method is used [75], [76]. The spectrum is limited in the frequency range from 0.1 Hz to 20 Hz. Windowing is always performed to process simulation results with a hanning window of variable length. The resulting PS or PSD is usually furthermore smoothed by means of a moving average filter with a span that varies depending on the simulation.

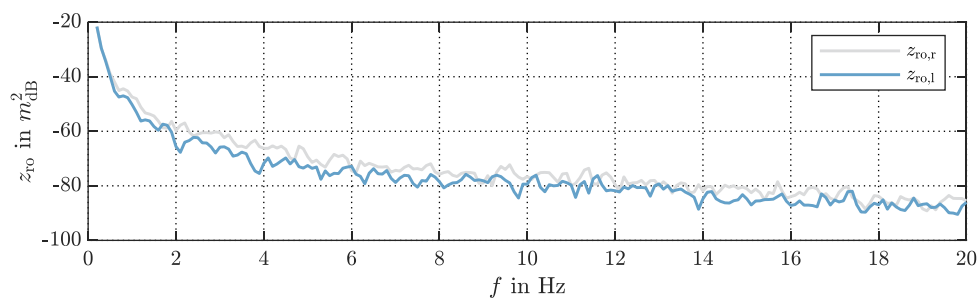


Figure 4.2: MnF, 100 km/h, Bandpass-filter 0.1-25 Hz

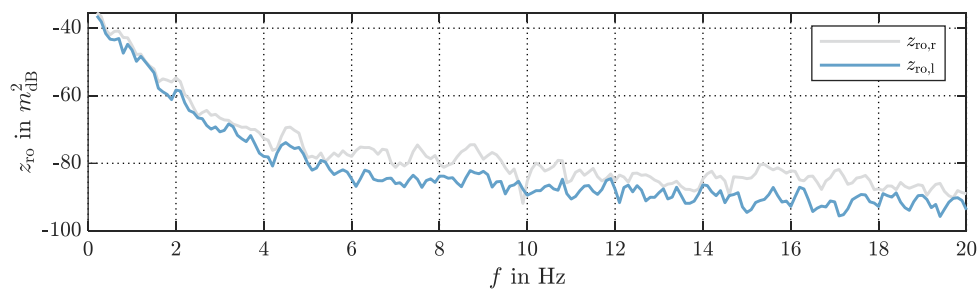


Figure 4.3: FnP, 100 km/h, Bandpass-filter 0.1-25 Hz

As well as stochastic road profiles, artificially generated ones are employed in this work. A single obstacle is modelled in order to simulate a road bump. The obstacle is assumed to be driven on with the right side of the vehicle. Figure 4.4, shows the shape of the bump.

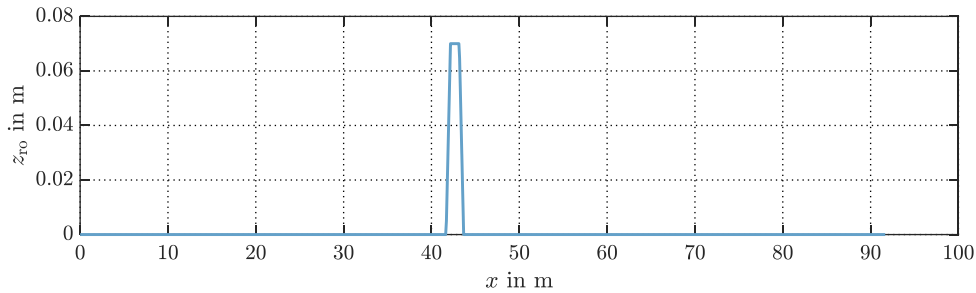


Figure 4.4: Single Obstacle, 30 km/h

The method displayed in Section 2.6, is used to generate fictitious profiles, classifiable by road roughness, following ISO 8608 prescriptions. A test profile is derived where four sections can be distinguished in terms of road roughness in a sequence that is A-C-A-C according to [36]. This road is especially suitable for the development of the coordination logic. Sections with a low roughness class (A) can be controlled by the more comfortable P controller because dynamic wheel loads are not dangerously high. On the other hand, sections with high roughness class (C) should be managed with the safer R controller that would account for the wheels dynamics. The coordination logic has to be able to detect changes in terms of induced vibrations on the vehicle, at the interface of the sections in order to correctly combine the two controllers. Figure 4.5, shows the A-C-A-C test profile.

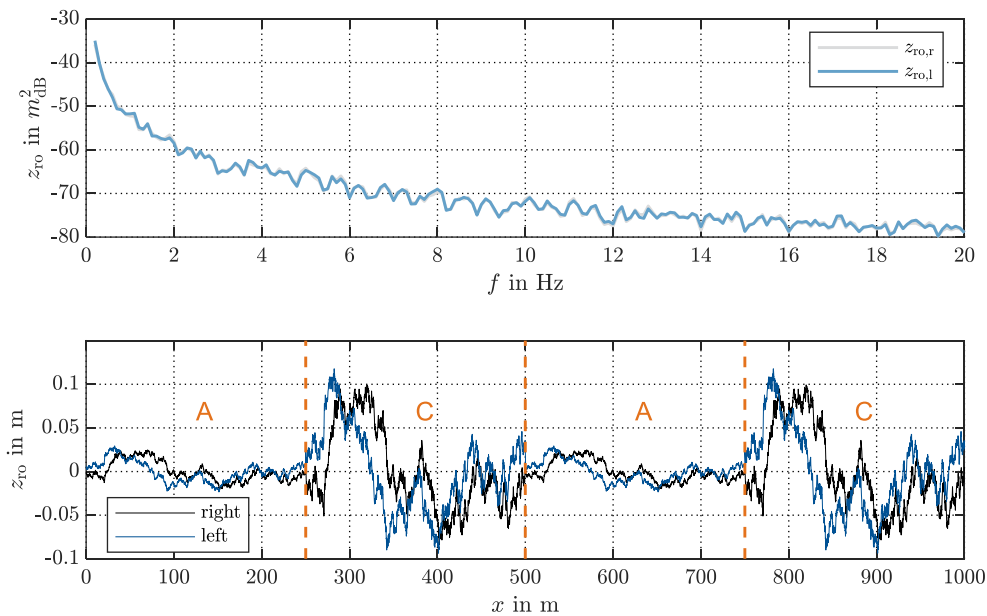


Figure 4.5: A-C-A-C profile, 100 km/h

An artificially generated road profile with C roughness is used as well (Figure 4.6) and tested with different vehicle speeds to analyse their influence on the vehicle dynamics. A road in very poor conditions can result in acceptable dynamic wheels loads if the vehicle speed is sufficiently low. Finally, a garage road profile (Garage) is modelled (Figure 4.7). It is designed as an horizontal path of 5 m followed by a downhill whose angle can be changed in the simulations. The depth is of -2 m. An horizontal path of 10 m is found at the lowest height and the entire path is

mirrored. Vehicle speed is equal to 20 km/h. The road profile displays some random A class roughness on the horizontal paths. This road has been used because it reveals another down side of the P controller.

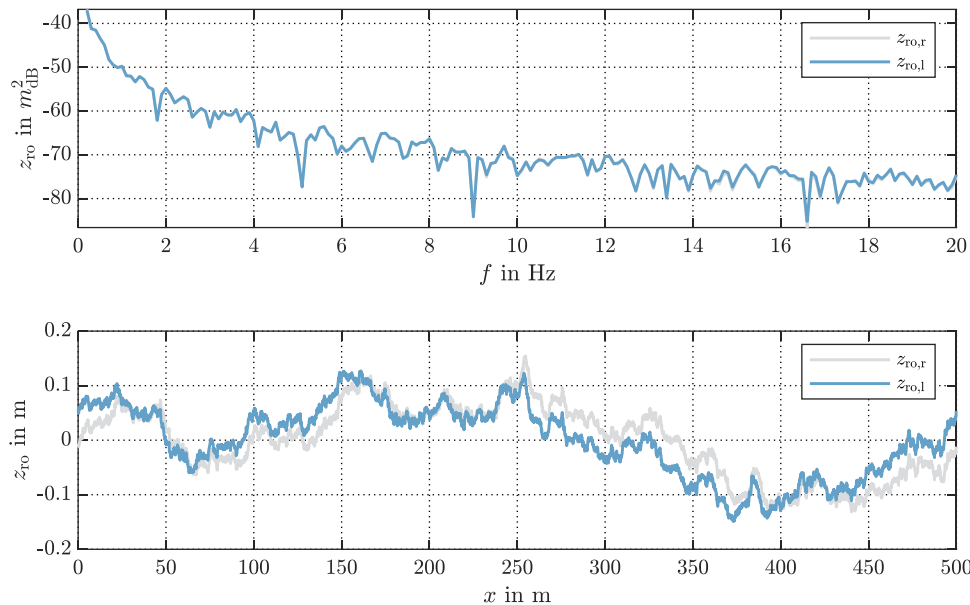


Figure 4.6: C profile, 80 km/h

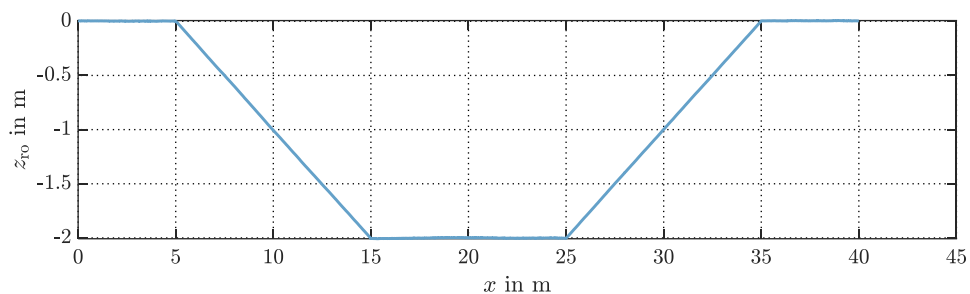


Figure 4.7: Garage, 20 km/h

The skyhook principle is built to level the body so that it does not resent of the road irregularities. If the vehicle descends on a path as in the garage simulation, the P controller would cause an undesired body elevation at the beginning of the slope in the active suspension configuration (Figure 4.8).

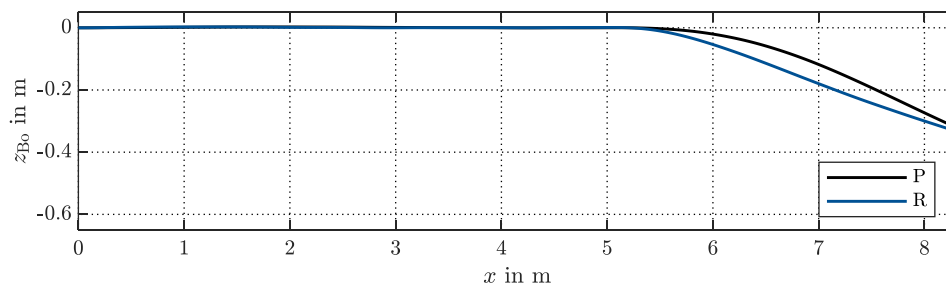


Figure 4.8: Garage, 20 km/h, z_{Bo} with P and R controller

This is visible in the simulation model as no constraint in the suspension travel is implemented. A simple constraint model to suspension deflection was developed and applied to the same simulation of Figure 4.8. The elevation of the body is reduced (Figure 4.9). In Appendix D, the constraint model is presented. The coordination logic should take into account those type of situations as well and prefer the use of the R controller.

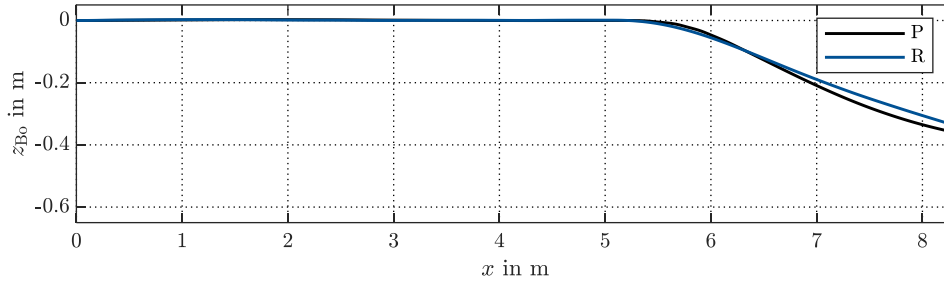


Figure 4.9: Garage, 20 km/h, z_{Bo} with P and R controller and a constraint in the suspension travel

4.4 Kalman Filter

As shown in Section 2.4, an important aspect of the coordination logic development is an appropriate estimation of dynamic wheel loads. Eq. (2.51), shows a way of calculating the desired quantity. Two main limitations are involved in this formula. First of all, in order to use the criteria of Eq. (2.48), the RMS of the dynamic wheel loads must be computed implying the knowledge of the function of interest over the interval of time considered. This means that it can only be computed offline, after having run a simulation in the model. This problem can be solved by using a *moving RMS* function consisting of a window of specified length which moves over the data. By using an appropriate window length, this procedure has proved to be sufficiently accurate. The second problem with dynamic wheel loads calculation is that it implies the resolution of the state space equations presented in Section 2.2. When it comes to the simulation model, this is always possible as the strong assumption of knowing the road input disturbance is made. In real life tests, road inputs are always unknown. Therefore, accelerations can only be measured and eventually filtered for their correct estimation. This consideration has led to the necessity of implementing a Kalman filter with the objective of estimating the wheels vertical accelerations as well as the body accelerations at the four corners of the vehicle. The employed method is presented as it follows. In Appendix E, general equations for Kalman filters are shown. The idea is to develop a robust estimator against sensor noise and modelling errors in the equations. An example of Kalman filtering in semi-active suspension control is shown in [77], where the focus is on the estimation of the vertical velocities of the body and of the damper in a quarter car model. Another possible application of Kalman filtering can be found in [78], where it is used to indirectly estimate bridge deterioration by means of the evaluation of the dynamic tyre forces. In [79], a road roughness estimation based on a discrete extended Kalman filter with unknown input is designed. General procedures for observers synthesis can be found in [80].

Figure 4.10, shows a quarter car vehicle suspension with semi-active dampers. This model is applied to the four vehicle corners and consequently, four Kalman filters are used for the sake of this work. Another possibility could have been to extend the Kalman filter to the 10 degrees of freedom of the full vehicle model. This choice would have complicated the equations by considering roll, pitch and twist of the body as well as the engine modes of heave and roll, without a

significant improvement in the results. It has been demonstrated to be sufficiently accurate despite the simplifying assumption.

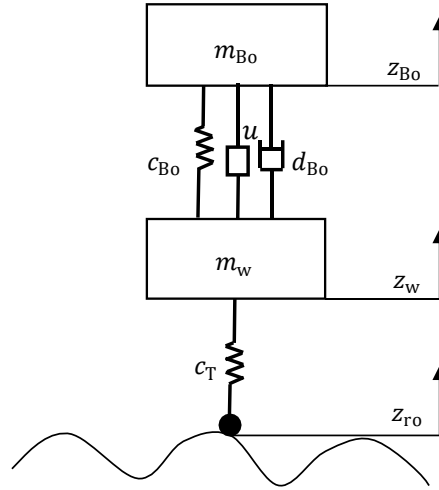


Figure 4.10: Quarter car model of semi-active suspensions

A second important assumption that has been made for the implementation of this Kalman filter, is the non-knowledge of the road input which is consequently neglected in the equations ($z_{r0} = 0$). This is taken into account by the process noise covariance w . Uncertainties on the measurement process, depending in real tests on the employed sensors, are considered in v . Further explanations on this are given in Appendix E. The following equations apply in the state space form:

$$\dot{x} = A_k x + B_k u + w \quad (4.2)$$

$$y = C_k x + D_k u + v \quad (4.3)$$

Where:

$$A_k = \begin{bmatrix} 0 & 1 & 0 & 0 \\ -c_{B0}/m_{B0} & -d_{B0}/m_{B0} & c_{B0}/m_{B0} & d_{B0}/m_{B0} \\ 0 & 0 & 0 & 1 \\ c_{B0}/m_w & d_{B0}/m_w & -(c_{B0} + c_T)/m_w & -d_{B0}/m_w \end{bmatrix} \quad (4.4)$$

$$B_k = \begin{bmatrix} 0 \\ -1/m_{B0} \\ 0 \\ 1/m_w \end{bmatrix} \quad (4.5)$$

$$C_k = \begin{bmatrix} -c_{B0}/m_{B0} & -d_{B0}/m_{B0} & c_{B0}/m_{B0} & d_{B0}/m_{B0} \\ c_{B0}/m_w & d_{B0}/m_w & -(c_{B0} + c_T)/m_w & -d_{B0}/m_w \end{bmatrix} \quad (4.6)$$

$$D_k = \begin{bmatrix} -1/m_{B0} \\ 1/m_w \end{bmatrix} \quad (4.7)$$

The state space vector, the observer vector and the control vector are respectively:

$$\mathbf{x} = [\mathbf{z}_{B0} \quad \dot{\mathbf{z}}_{B0} \quad \mathbf{z}_w \quad \dot{\mathbf{z}}_w]^T \quad (4.8)$$

$$\mathbf{y} = [\ddot{\mathbf{z}}_{B0} \quad \ddot{\mathbf{z}}_w]^T \quad (4.9)$$

$$\mathbf{u} = \mathbf{F}_{u_{ij}} \quad (4.10)$$

with $i \in \{f, r\}, j \in \{r, l\}$. It must be noted that the contribution of the damping force is split into its passive and semi-active components. The aim of the designed Kalman filter is to correctly estimate the observer vector \mathbf{y} . For each time step of the simulation model, it is calculated and finally used to compute the dynamic wheel loads. Four Kalman filters are implemented and therefore, four wheels accelerations are calculated. Four body accelerations in vertical direction, neglecting the eigenmodes of pitch, roll and twist are estimated as well at the four vehicle corners. The online estimation of the dynamic wheel load is performed as it follows:

$$\tilde{F}_{z_{w,ij,dyn}} = m_{B0,ij} \tilde{\ddot{z}}_{B0,ij} + m_{w,ij} \tilde{\ddot{z}}_{w,ij} \quad (4.11)$$

with $i \in \{f, r\}, j \in \{r, l\}$. Eq. (4.11) is obtained from Eq. (2.51) where the body acceleration in vertical direction is derived from the four body eigenmodes while this formulation is taken from a quarter car model that only considers vertical direction. This results in a general underestimation of the dynamic wheel loads. As the aim of this estimation is to implement an appropriate switching logic between the controllers with the possibility of detecting changes in the vibrations induced from the road, is considered acceptable. In order to fictitiously reproduce a measurement process in the simulation environment, a band-limited white noise is added to the accelerations of the body and of the wheels, calculated from the resolution of the state space equations of the full vehicle model in the plant. This results in the measurement vector \mathbf{y} . The latter and the control vector with the semi-active damping forces, are given as an input to the Kalman filters. These provide the estimate of the state vector and of the measurement vector. The estimated measurement vector is of interest to calculate online dynamic wheel loads. An overview of the method is shown (Figure 4.11).

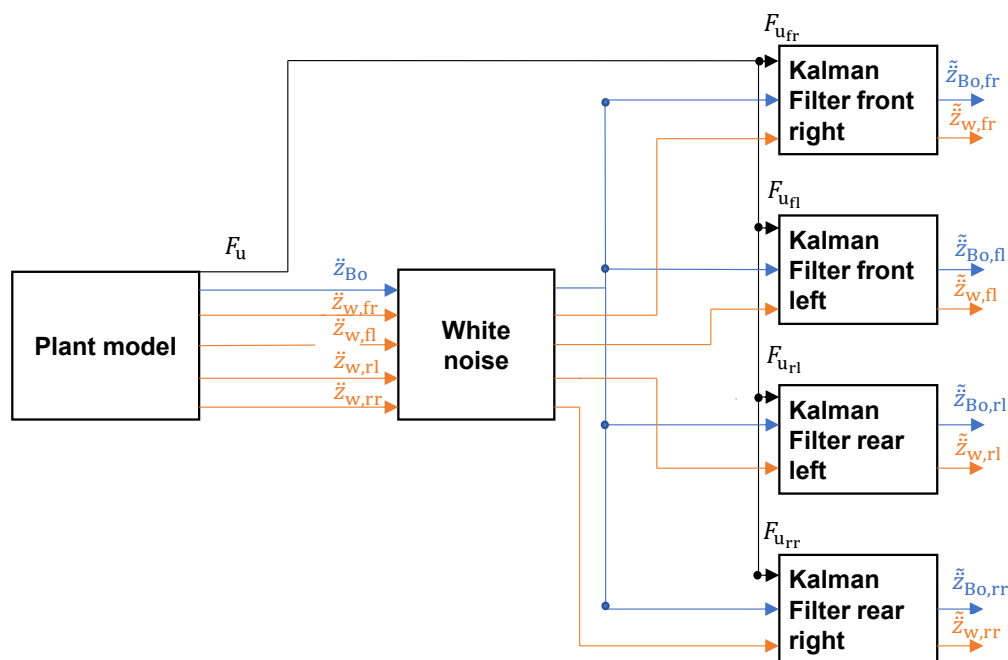


Figure 4.11: Kalman filters overview

Eq. (2.48) becomes:

$$\left\| \tilde{F}_{z_{w,ij,dyn}} \right\|_{\text{rms}} \leq k_i F_{z_{w,ij,stat}} \quad (4.12)$$

Where k_i represents a percentage of the static load and can be tuned depending on the desired dynamics. Two examples of estimation are reported. The first one (Figure 4.12) represents an initial attempt of filtering in order to estimate the vertical acceleration of the body at the front right corner. The synthetic expression, “true y” refers to the variable \ddot{z}_{B_0} , calculated from the state space model of the full vehicle and given as an input to the filter after having added some white noise. On the other hand, “estimated y” refers to the output of the filter, as the estimated vertical acceleration of the body on the front right corner, $\tilde{\ddot{z}}_{B_0,fr}$.

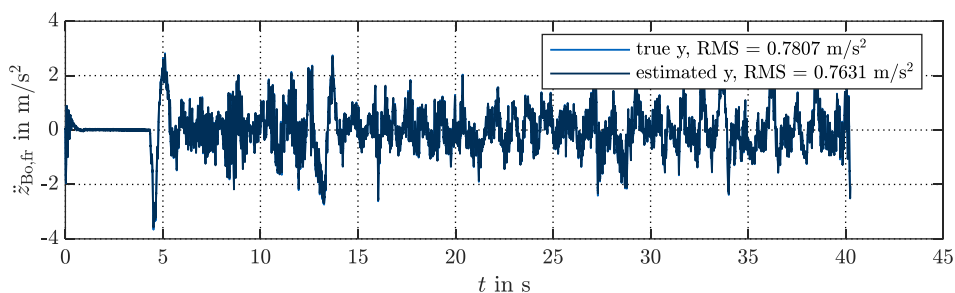


Figure 4.12: Untuned Kalman filter simulation

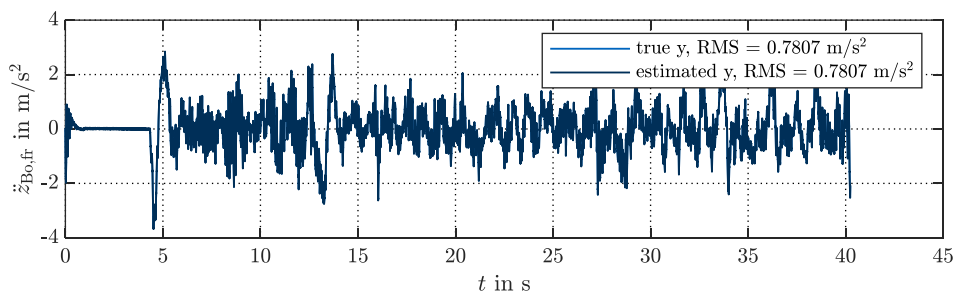


Figure 4.13: Tuned Kalman filter simulation

The second simulation (Figure 4.13) represents an optimized version of the filter having appropriately tuned the process and measurement noises. The mentioned simulations have been performed with the stochastic road profile MnF and with a constant vehicle speed of 100 km/h.

4.5 Coordination logic

One of the objectives of this work is to develop a suitable coordination logic, addressed in the controller synthesis with K^+ (Figure 2.4). Its aim is to combine two differently oriented controllers for continuously adjustable semi-active dampers: the modal R controller and the extended P controller with twist mode, respectively focused on road-holding and ride comfort. The general procedure for the development of an adaptive gain is presented (Section 4.5.1). The different aspects of the coordination logic are described in terms of ride comfort (Section 4.5.2), road-holding (Section 4.5.3) and suspensions constraints (Section 4.5.4). A correction to the adaptive gain is also made (Section 4.5.5). A modified version of the P controller is developed in Section 4.6 and it is used as a comparison for the coordination logic. Finally, some results with the semi-

active configuration are shown and compared to the ones obtained with the single controllers (Section 4.7).

4.5.1 Adaptive gain

Initial attempts of coordination have been conducted. These involved the calculation of a suitable variable that would be compared, for each time step, to a significant threshold. This would lead to the activation of either the P or the R controller and the deactivation of the other one. Such an approach entails a hard switch between the controllers. With some simulation setups, this would result in optimal switching. With very poor road conditions, the R controller would always be active and instead, with a good roughness class or lower vehicle speeds, the more comfortable P controller would be present. Issues were found when simulation parameters provided uncertainties in comfort or road-holding classification, causing a continuous switch between the controllers since the controlled variable was oscillating around the threshold. This approach was the most immediate as the controllers were thought to work separately and be manually activated before the start of a new simulation but it revealed itself as inefficient. This led to the definition of a different approach by means of an adaptive gain. The basic idea of such a gain is the appropriate online calculation of a G_R factor so that:

$$\mathbf{u}_{R,g}^* = \mathbf{u}^* G_R \quad (4.13)$$

$$\mathbf{u}_{P,modal,g} = \mathbf{u}_{P,modal}(1 - G_R) \quad (4.14)$$

Eq. (2.73) and Eq. (2.85) become:

$$\mathbf{u}_P = -\mathbf{T}^{-1} \mathbf{u}_{P,modal,g} \quad (4.15)$$

$$\mathbf{u}_R = -\mathbf{T}^{-1} \mathbf{u}_{R,g}^* \quad (4.16)$$

By the definition of a gain to weight the control laws, the continuous switching between the controllers is avoided. G_R is a real gain so that $0 < G_R < 1$ and assures the co-presence of both P and R controllers, in all possible working conditions. It is defined as “adaptive” as it has been designed to detect significant changes in comfort, road-holding or suspensions deflection and to adapt its value in an optimal way. Examples of adaptive gain synthesis, respectively in the field of renewable energies and in acoustics can be found in [81], [82]. An adaptive gain to combine road-holding and ride comfort is designed in [83] as a function of the body sprung mass. There are many examples of adaptive control laws applied in the field of semi-active suspensions as reported in Section 3.2, but a strategy to coordinate two control laws with an adaptive gain has not been explored yet. For an appropriate definition of the gain, the calculation of auxiliary gains and variables is needed. These gains are combined in order to define, for each time step, a unique value for G_R . The definition of the auxiliary gains is given in detail in Section 4.5.2, 4.5.3 and 4.5.4. The coordination between them, in order to obtain a value for G_R is summarised in Figure 4.14 and with Eq. (4.17). The idea is to compute, for each time-step of the simulation, the gains of interest: $G_{Fdyn,max}$ and the sum between G_{PS} and $G_{sus,def}$ and, by means of a switching condition, deciding which one is the output and becomes G_R , the adaptive gain that multiplies the control laws (Figure 4.14).

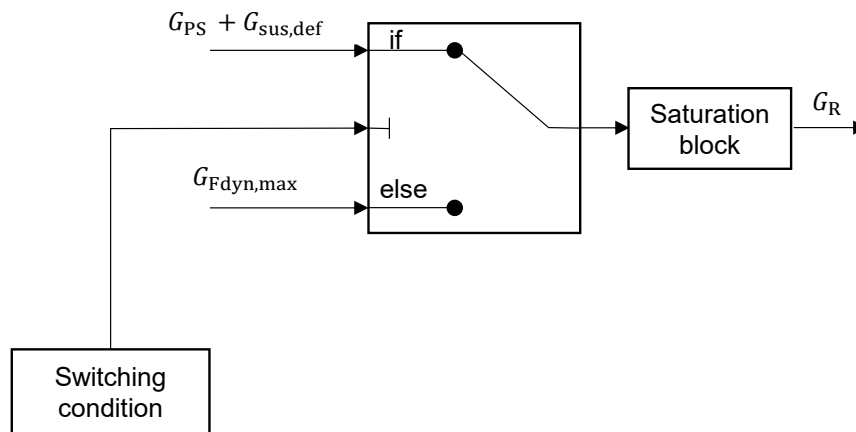


Figure 4.14: Adaptive gain logic

The switching condition (Figure 4.15), consists in meeting two requirements simultaneously: the boolean variable $F_{dyn,check}$ must be equal to 1 and $G_{PS} < G_{Fdyn,max}$. The boolean variable $F_{dyn,check}$ represents the accomplishment of the condition expressed by Eq. (4.12) on all four wheels. This always assures an acceptable level of road-holding. Switching from $G_{Fdyn,max}$ to $G_{PS} + G_{sus,def}$ entails weighting more the P controller rather than the R and results in lower accelerations. This switching is only possible if there is convenience to do that, namely $G_{PS} < G_{Fdyn,max}$ so that the percentage of usage of the R controller becomes lower, and at the same time, if the RMS of the estimated dynamic wheel loads is below a certain threshold on each vehicle corner. A saturation block is needed to ensure that $G_R \leq 1$.

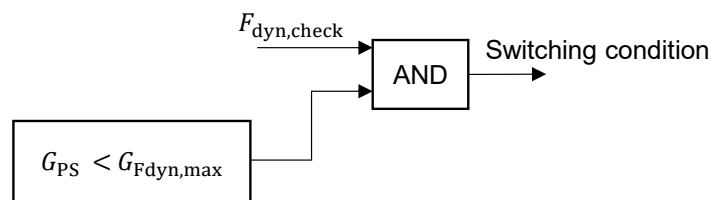


Figure 4.15: Switching condition

$$G_R = \begin{cases} G_{PS} + G_{sus,def} & \text{if } F_{dyn,check} = 1 \wedge G_{PS} < G_{Fdyn,max} \\ 1 & \text{if } G_{PS} + G_{sus,def} > 1 \\ G_{Fdyn,max} & \text{else} \end{cases} \quad (4.17)$$

The definition of the adaptive gain G_R is obtained by taking into account different aspects: ride comfort (Section 4.5.3), road-holding (Section 4.5.4) and a constraint in the suspensions deflection (Section 4.5.5). The general procedure consists of using several lookup tables which are built previously and with laws obtained by the analysis of the initial simulations. These lookup tables return, for each time-step, a value for the different auxiliary gains and through some corrections and conditions which must be respected, G_R is computed.

4.5.2 Ride comfort

The evaluation of ride comfort has the aim of computing the gain G_{PS} . In order to achieve this goal, different approaches were considered at first. The most immediate would have consisted in the calculation of the RMS values of the accelerations signals, as they are strongly correlated with the perception of comfort. The limit to such approach is the difficulty in adapting it to variable simulation conditions. A threshold should have been defined to compare the computed RMS, and there was no possibility to detect a single value that could work in all simulation scenarios. Therefore, a different solution was found. A power spectrum estimation is conducted online (Eq. (4.22)). For this, the *Spectrum Estimator* Simulink block is used. It returns as output, the power spectrum of the input signal, using Welch's method of averaged modified periodograms. The block buffers the input data into overlapping segments whose length can be specified as well as the amount of data overlap between consecutive segments. The input is chosen to be an overall acceleration signal, $\ddot{z}_{Bo,ISO}$ and the power spectrum is performed in the range going from 0 to 20 Hz, which is the one of interest. The acceleration, $\ddot{z}_{Bo,ISO}$ is obtained by combining the acceleration signals of the body in heave, pitch and roll following the prescription of ISO 2631 when combining vibrations in more than one direction [19, p. 12].

$$\ddot{z}_{Bo,ISO} = \left(\ddot{z}_{Bo}^2 W_k^2 + \ddot{\theta}_{Bo}^2 W_{e,\theta}^2 + \ddot{\varphi}_{Bo}^2 W_{e,\varphi}^2 \right)^{\frac{1}{2}} \quad (4.18)$$

The weightings are equal to [19, p. 15]:

$$W_k = 1 \quad (4.19)$$

$$W_{e,\theta} = 0.4 \text{ m/rad} \quad (4.20)$$

$$W_{e,\varphi} = 0.63 \text{ m/rad} \quad (4.21)$$

The online power spectrum estimation of $\ddot{z}_{Bo,ISO}$ is conducted with a sliding hanning window of 2 s of width and 50% of overlap between two segments.

$$PS_{\ddot{z}_{Bo,ISO}} = \frac{1}{2T} |\mathcal{F}(\ddot{z}_{Bo,ISO}(t)(\omega))|^2 \quad (4.22)$$

The power spectrum, $PS_{\ddot{z}_{Bo,ISO}}$ is further elaborated. The frequency range between 0 and 5 Hz is chosen and the power spectrum, limited to this frequency range is obtained and named $PS_{\ddot{z}_{Bo,ISO},0-5 \text{ Hz}}$ (Figure 4.16). The range of 0-5 Hz is chosen as it contains the body eigenfrequency. An examples of the power spectrum estimation at a certain time step is shown for the MnF road input at 100 km/h (Figure 4.17).

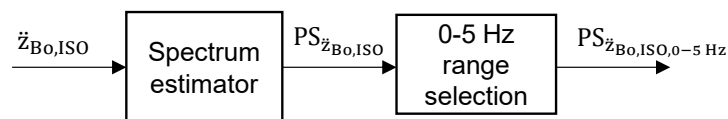


Figure 4.16: $PS_{\ddot{z}_{Bo,ISO},0-5 \text{ Hz}}$

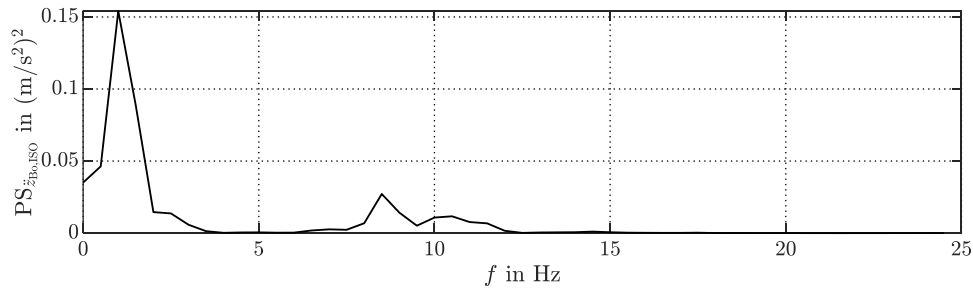


Figure 4.17: Power spectrum online estimation at a certain time step

The mean value of $PS_{z_{Bo},ISO,0-5\text{ Hz}}$ is derived and divided by the *moving maximum* of the same mean value. This ratio, which always lies between 0 and 1, is computed in order to obtain an esteem of the perceived comfort level in an objective way and without the necessity of defining any thresholds and it represents the input for a lookup table which returns a value for G_{PS} (Figure 4.18).

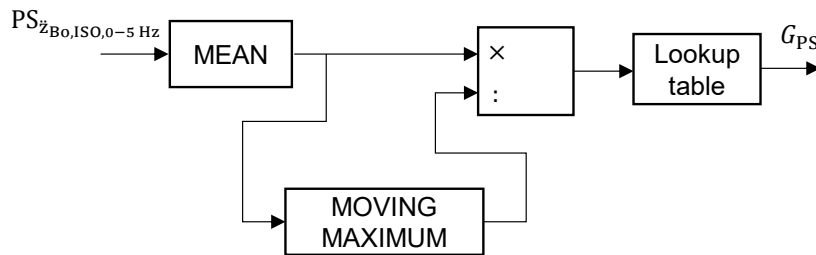


Figure 4.18: G_{PS}

The moving maximum returns a value which is the maximum calculated over a sliding window of 2 s of width. This means that its estimation becomes more precise when a sufficient number of data points are available. In other terms, the ratio between the mean value of $PS_{z_{Bo},ISO,0-5\text{ Hz}}$ and its moving maximum, gains accuracy as the simulation time goes on. Its aim is identifying when the power spectrum in the range of 0-5 Hz and estimated at a certain time step, becomes significant with respect to the entire simulation time. As showed in Figure 4.18, the ratio enters a lookup table which returns G_{PS} . The equation accounting for this lookup table is, in its general form:

$$y = 1 - e^{-\frac{x}{\tau}} \quad (4.23)$$

Where $y = G_{PS}$ and $x = \frac{\text{mean}(PS_{z_{Bo},ISO,0-5\text{ Hz}})}{\text{movingmax}(\text{mean}(PS_{z_{Bo},ISO,0-5\text{ Hz}}))}$ and τ is chosen in order to obtain $G_{PS} = \text{th}_{PS}$ when $x = \text{th}_{\text{ratio}}$. Figure 4.19, shows a possible trend of G_{PS} . Using such an exponential law assures that in case of poor driving comfort, the P controller would be weighted more than the R controller. Both th_{PS} and th_{ratio} can be tuned and adjusted.

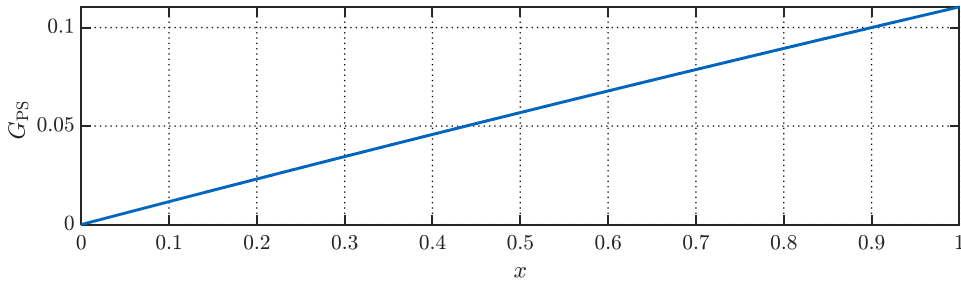


Figure 4.19: Lookup table for G_{PS}

Figure (4.20) and (4.21) show the estimation, over the simulation time, of the ratio x . In the first case, the A-C-A-C profile is employed and x is shown. Its estimation becomes more precise from the second section (C). In case of an inverted profile starting with a C section of road roughness, namely C-A-C-A, the estimation is more accurate because the denominator of x is closer to the overall maximum of the PS mean, already at the beginning of the simulation, as the first section implies less comfort for the vehicle occupants.

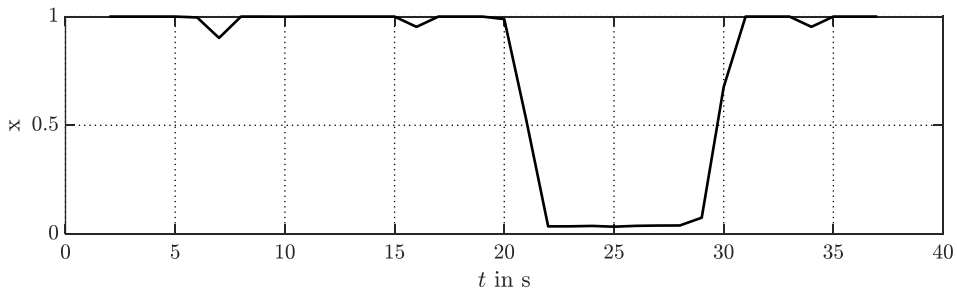


Figure 4.20: x for A-C-A-C profile

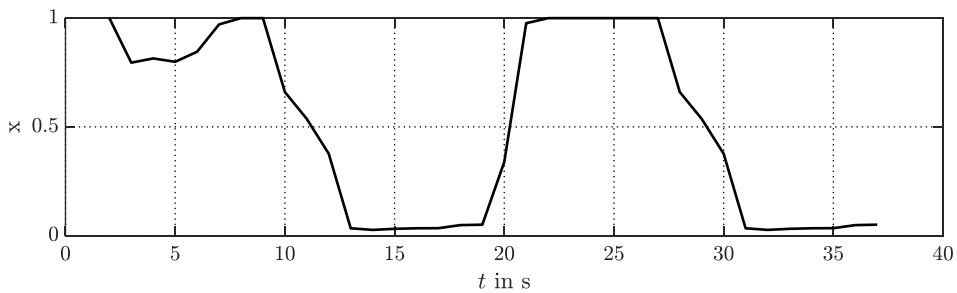
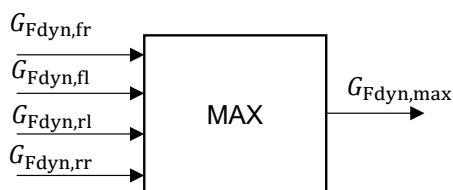


Figure 4.21: x for C-A-C-A profile

It is known that the frequency range of most human sensitivity to comfort lies between 4 and 8 Hz [19]. Several attempts were made with this frequency range but better results in terms of overall comfort estimation with $\ddot{z}_{Bo,ISO}$ have been achieved in the 0-5 Hz range.

4.5.3 Road-holding

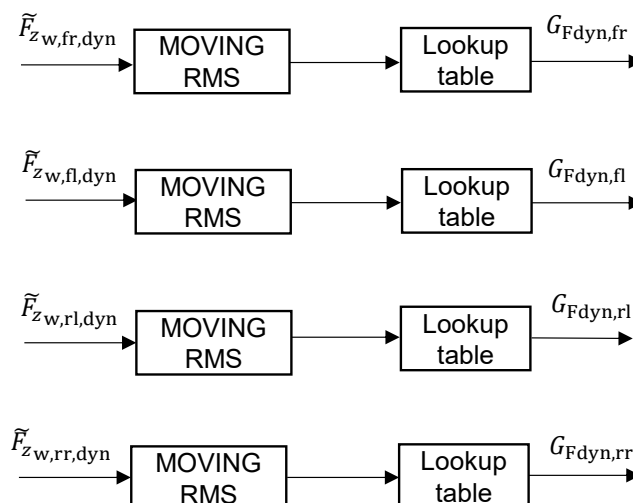
The auxiliary gain that accounts for road-holding is $G_{Fdyn,max}$ which is obtained as the maximum between $G_{Fdyn,ij}$ with $i \in \{f, r\}, j \in \{r, l\}$ (Figure 4.22).

Figure 4.22: $G_{Fdyn,max}$

In Section 4.4, a method for the estimation of dynamic wheel loads, $\tilde{F}_{z_{w,ij,dyn}}$ has been designed. Their moving RMS is computed online via a sliding window of 2 s of length and the input for the lookup tables is obtained (Figure 4.23). This results in four gains $G_{Fdyn,ij}$, each accounting for one vehicle corner. The maximum value between the four is chosen to guarantee that the R controller output is weighted with the highest value.

In the switching condition, an additional control on dynamic wheel loads is performed via $F_{dyn,check}$ which becomes equal to 1 when all four conditions of Figure 4.24 are fulfilled. The thresholds of the switching condition can be tuned depending on the desired overall dynamics via k_i . The latter is usually set to 0.35 but it can be increased in order to generally reproduce a dynamic behaviour which is closer to the one obtained with the pure P controller.

The general equation for the lookup tables in Figure 4.25, is the same as Eq. (4.23). In this case $y = G_{Fdyn,ij}$, $x = movingRMS(\tilde{F}_{z_{w,ij,dyn}})$ and τ is chosen in order to obtain $G_{Fdyn,ij} = th_{dyn}$ when $x = th_{Fdyn}$, with $i \in \{f, r\}, j \in \{r, l\}$. Both th_{dyn} and th_{Fdyn} can be tuned.

Figure 4.23: $G_{Fdyn,ij}$

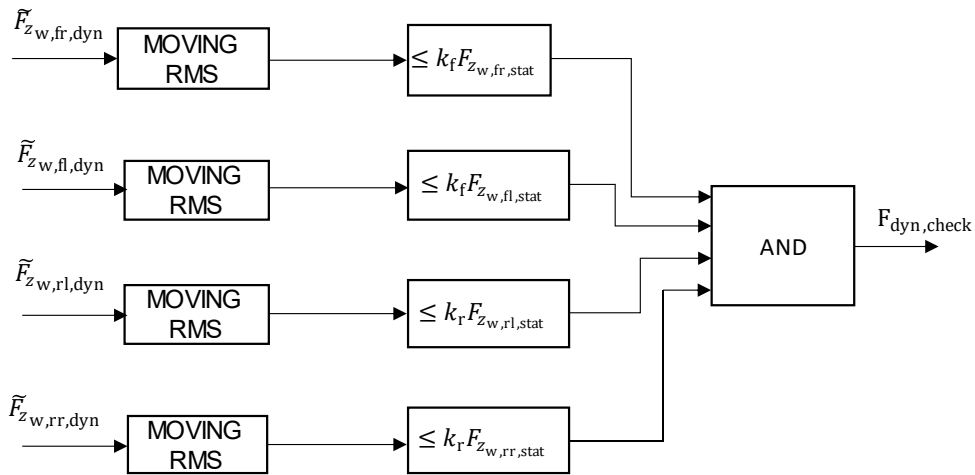


Figure 4.24: $F_{dyn,check}$

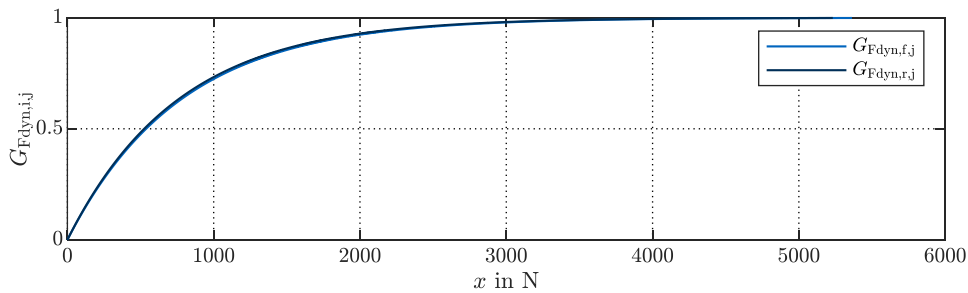
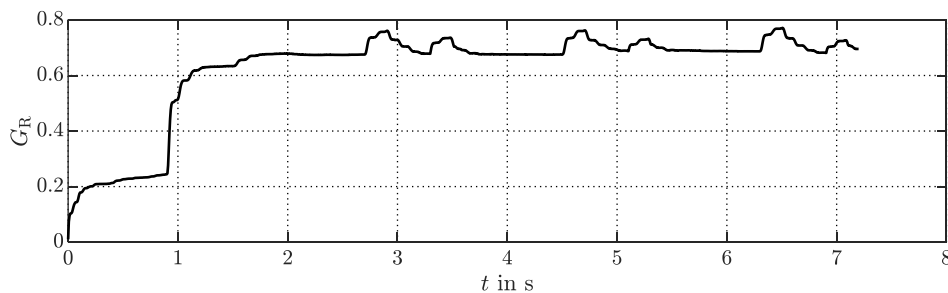
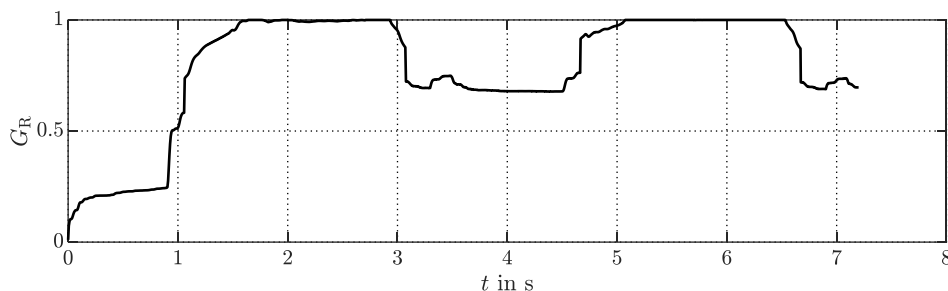


Figure 4.25: $G_{Fdyn,i,j}$

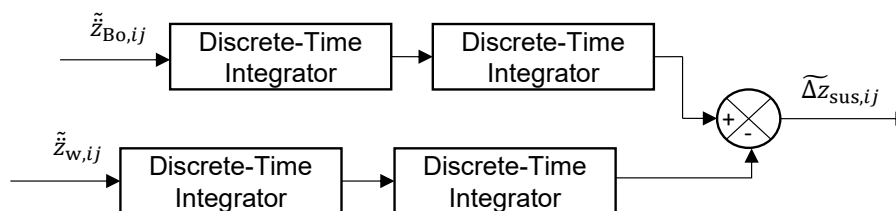
4.5.4 Suspensions constraint

Logics described in Section 4.5.2 and 4.5.3 manage to cover for a wide range of simulation setups. They are thought to work on the safety side but can eventually switch to more comfortable configurations when there is a prevalence of the extended Skyhook controller on the modal one, namely when G_R approaches to zero. There are some road scenarios where ride safety is always guaranteed because dynamic wheel loads are low and therefore the P controller is prevailing even if it is not desired. Examples are single obstacles, bumps or the road input presented in Section 4.3 with the garage road simulation. In this case, the P controller tends to level the body so that it does not resent of the road irregularities because of the skyhook principle. When descending down into the deep, the P controller would cause an undesired body elevation at the beginning of the slope in the active suspension configuration (Figure 4.8).

By neglecting the additional logic of Figure 4.14, where $G_{sus,def}$ is added to G_{PS} , the resulting G_R for the garage simulation would be the one in Figure 4.26, where the R controller would not be sufficiently predominant in the overall control law. Figure 4.27, shows G_R with the additional logic taking account of suspensions deflection.

Figure 4.26: G_R for garage simulation without $G_{\text{sus,def}}$ Figure 4.27: G_R for garage simulation with $G_{\text{sus,def}}$

This results in the necessity of defining some additional variables to detect similar behaviours. If the road input was known, an immediate shift towards the R controller would be performed. As this is not achievable, the suspension travel is considered. In the garage simulation Δz_{sus} reaches significantly high values, of the magnitude of half a meter. With other road inputs, artificially generated and measured ones, Δz_{sus} lies between ± 0.1 m. This is why Δz_{sus} is taken as a reference variable to detect the presence of slopes as in the garage simulation. In the real vehicle, Δz_{sus} is known since it is measured with standard sensor equipment. In the simulation model, it could be consequently taken directly, from the state space equation resolution block. In this case it is taken from the Kalman filter by double integration of the accelerations signals. The integrator blocks are time-discrete. Integrating a measured signal can always lead to inaccuracies in real life tests but in this simulation environment, it has proved to be accurate. Figure 4.28, shows the described procedure where $\tilde{z}_{\text{Bo},ij}$ and $\tilde{z}_{\text{w},ij}$ are the outputs of the four Kalman filters, with $i \in \{f, r\}, j \in \{r, l\}$.

Figure 4.28: $\tilde{\Delta z}_{\text{sus},ij}$

The variable $\tilde{\Delta z}_{\text{sus},ij}$ is obtained and $G_{\text{sus,def}}$ can be computed (Figure 4.29). The output of the block in Figure 4.29, is $G_{\text{sus,def}}$ if the maximum between the absolute values of $\tilde{\Delta z}_{\text{sus},ij}$ overcomes the threshold sus_{th} , otherwise it is equal to zero. The threshold is set initially to 0.10 m. This value is chosen by observing the variability of Δz_{sus} with different road inputs but it is a

reasonable choice in the constraint of the suspension stroke. For example, in [60] it is set to 0.08 m .

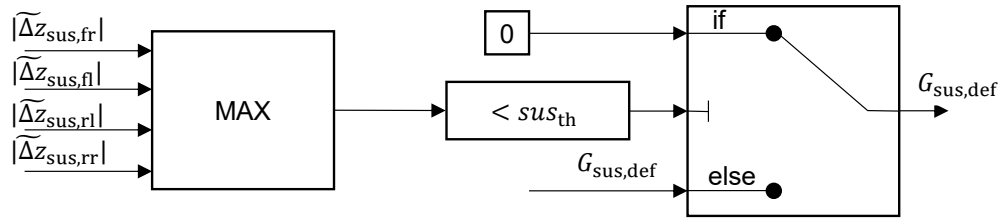


Figure 4.29: $G_{sus,def}$

At each time-step of the simulation $G_{sus,def}$ is obtained by means of a lookup table (Figure 4.30).

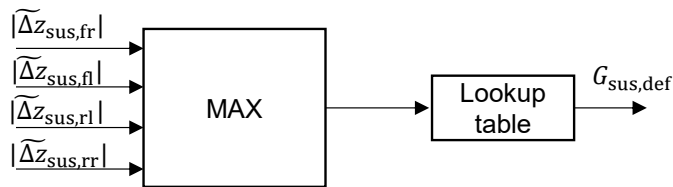


Figure 4.30: $G_{sus,def}$ logic

Eq. 4.23 holds where $y = G_{sus,def}$, $x = \max(|\tilde{\Delta z}_{sus,ij}|)$ and τ is chosen in order to obtain $G_{sus,def} = th_{def}$ when $x = th_{xdef}$. Both th_{def} and th_{xdef} can be tuned. Figure 4.31 shows a possible trend of $G_{sus,def}$.

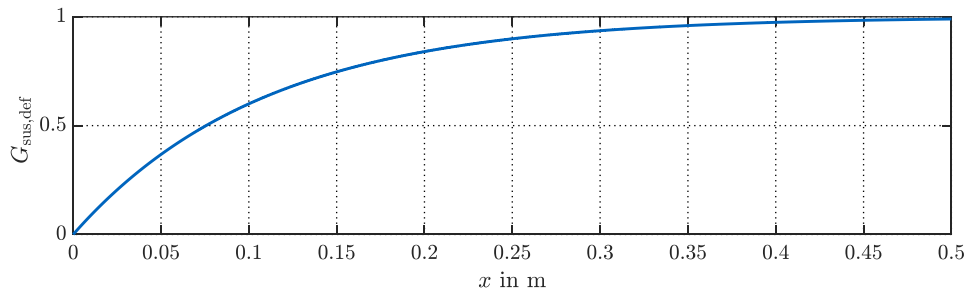
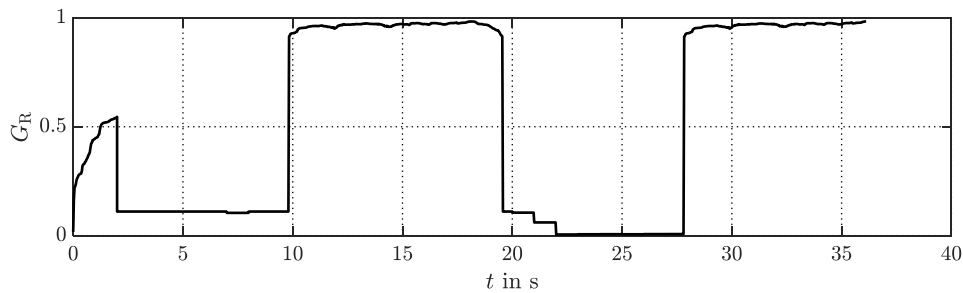


Figure 4.31: $G_{sus,def}$

4.5.5 Gain correction

An additional correction is introduced in order to account for an initial transitory where the power spectrum has not been computed yet. Such a delay depends on the windowing, which in the simulations is set to 2 s. This entails that, in the first 2 s of the simulations, the adaptive gain value would always be equal to $G_{Fdyn,max}$, weighting more the R controller and eventually overestimating the necessary road-holding. Figure 4.32 shows the adaptive gain G_R for the A-C-A-C profile with its transitory until 2 s.

Figure 4.32: G_R without gain correction

Consequently a correction is added to the resulting G_R (Figure 4.14). If both the boolean variables $F_{\text{dyn,check}}$ and PS_{trans} are equal to 1, G_R is directly set to 0.1, weighting the P controller as a 90% of the total control force. When $F_{\text{dyn,check}} = 1$, dynamic wheel loads on all four wheels are below the chosen thresholds. This results in the possibility of using the more comfortable P controller as the request on road-holding is respected. On the other hand, PS_{trans} is a logic variable, that becomes equal to 1 when the following applies:

$$\sum \text{PS}_{\dot{z}_{\text{Bo,ISO}}} == 0 \quad (4.24)$$

If Eq. (4.24) is verified, $\text{PS}_{\text{trans}} = 1$. The overview of the gain correction logic is given in Eq. (4.25).

$$G_R = \begin{cases} 0.1 & \text{if } F_{\text{dyn,check}} \wedge \text{PS}_{\text{trans}} = 1 \\ G_R & \text{if } F_{\text{dyn,check}} \vee \text{PS}_{\text{trans}} = 0 \end{cases} \quad (4.25)$$

4.6 Modified P controller

One of the objectives of this work is to generally improve the vertical vehicle dynamics controller for semi-active and active suspensions (Figure 2.4), taking into account road-holding and ride comfort. This can be achieved by means of the coordination logic described in Section 4.5, but other strategies can be considered. A modified P controller is designed with the aim of substituting both P and R controllers so not to necessitate any coordination logic as well. The R controller entails higher accelerations values because the vehicle displays the dynamics of a passive system as shown by Eq. (2.78). On the other hand, the P controller does not consider the wheels dynamics and therefore provides higher dynamic wheel loads. The modified P controller law is described as it follows:

$$\mathbf{u}_{\text{MP,modal}} = \mathbf{K}_{\text{P},\alpha} [(\alpha_i - 1)\dot{\mathbf{x}}_{\text{Bo}} - \alpha_i \Delta \dot{\mathbf{x}}_{\text{Bo}}] \quad (4.26)$$

Where $\mathbf{K}_{\text{P},\alpha}$, α_i and $\Delta \dot{\mathbf{x}}_{\text{Bo}}$ are:

$$\mathbf{K}_{\text{P},\alpha} = \begin{bmatrix} \mathbf{K}_{\text{P},\alpha,z_{\text{Bo}}} & 0 & 0 & 0 \\ 0 & \mathbf{K}_{\text{P},\alpha,\theta_{\text{Bo}}} & 0 & 0 \\ 0 & 0 & \mathbf{K}_{\text{P},\alpha,\varphi_{\text{Bo}}} & 0 \\ 0 & 0 & 0 & \mathbf{K}_{\text{P},\alpha,t_{\text{Bo}}} \end{bmatrix} \quad (4.27)$$

$$\boldsymbol{\alpha}_i = \begin{bmatrix} \alpha_{z_{B_0}} \\ \alpha_{\theta_{B_0}} \\ \alpha_{\varphi_{B_0}} \\ \alpha_{t_{B_0}} \end{bmatrix} = \begin{bmatrix} \alpha_h \\ \alpha_p \\ \alpha_r \\ \alpha_t \end{bmatrix} \quad (4.28)$$

$$\Delta \dot{\mathbf{x}}_{B_0} = \mathbf{T}^{-T} \Delta \dot{\mathbf{z}}_{\text{sus}} = \dot{\mathbf{x}}_{B_0} - \mathbf{T}^{-T} \dot{\mathbf{z}}_w \quad (4.29)$$

With $i \in \{h, p, r, t\}$ or equally, $i \in \{z_{B_0}, \theta_{B_0}, \varphi_{B_0}, t_{B_0}\}$. Eq. (4.26) transforms into:

$$\mathbf{u}_{\text{MP,modal}} = \mathbf{K}_{P,\alpha} [-\dot{\mathbf{x}}_{B_0} + \boldsymbol{\alpha}_i \mathbf{T}^{-T} \dot{\mathbf{z}}_w] \quad (4.30)$$

In order to calculate the input actuating force from the modified P controller, the modal transformation matrix is used:

$$\mathbf{u}_{\text{MP}} = -\mathbf{T}^{-1} \mathbf{u}_{\text{MP,modal}} \quad (4.31)$$

These α_i lie between 0 and 1. When $\alpha = 0$, the P controller is obtained. Increasing values for α implies a shift to a suspension oriented controller, that results, in general, in lower dynamic wheel loads and higher accelerations. From this, Eq. (2.9) can be modified as it follows:

$$\mathbf{u} = \begin{cases} \mathbf{u}_{\text{MP}} \\ \mathbf{u}_p + \mathbf{u}_r \end{cases} \quad (4.32)$$

Where \mathbf{u}_p and \mathbf{u}_r are taken from Eq. (4.15) and Eq. (4.16), the feedforward compensation term for engine vibrations is neglected and the switch between the modified P controller and the coordination logic is performed manually before the start of a simulation.

4.7 Simulation results

Simulation results are presented in this section. Details on the parametrization of the controllers are given in Appendix F. At first, adaptive gains for each road input are shown (Section 4.7.1). Secondly, an analysis on the body eigenmodes of heave (Section 4.7.2), pitch (Section 4.7.3) and roll (Section 4.7.4) is conducted with different simulation scenarios. Results for the overall acceleration value according to ISO 2631 are shown (Section 4.7.5). Dynamic wheel loads are also examined (Section 4.7.6). Simulation results are displayed in the same figures with different controller settings. Pure P and R controllers are tested and compared with the addition of the coordination logic. Simulations with the modified P controller are displayed as well. Results for the adaptive gain are always shown in the time domain and can be compared with the corresponding road inputs (Section 4.7.1). Accelerations signals as well as dynamic wheel loads are shown in the frequency domain with a logarithmic y-axis, for the two stochastic profiles of MnF and Fnp, and for the artificially generated one, A-C-A-C. Their PSD is computed with a hanning window of 1 s of width in the frequency range from 0.1 and 20 Hz. Four significant digits are used for all simulation results while three are employed for experimental measurement tests.

4.7.1 Adaptive gain results

In the following, results for the adaptive gain G_R are presented. Figure 4.33 shows its trend in time for the A-C-A-C profile, with vehicle speed equal to 100 km/h. The effectiveness of the

coordination logic is displayed as, at the interface between the two road sections, there is a shift in the prevailing controller. In terms of driving comfort, as expected, it is improved with the simulation time. In the third section, which corresponds to an A roughness class, G_R becomes lower with respect to the first section. The adaptive gains for the stochastic road inputs of MnF and FnP are also shown (Figure 4.34, 4.35).

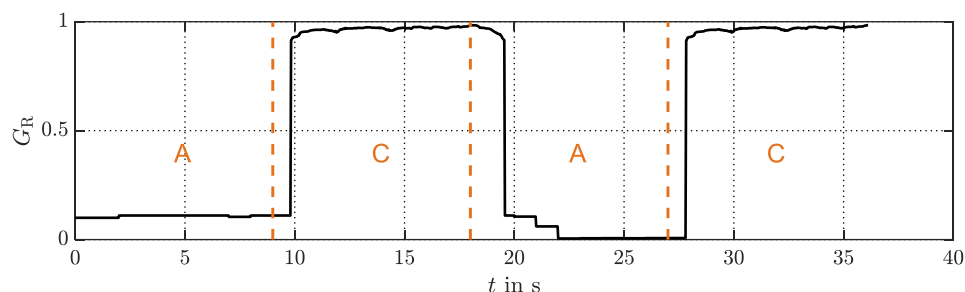


Figure 4.33: G_R for A-C-A-C profile, 100 km/h

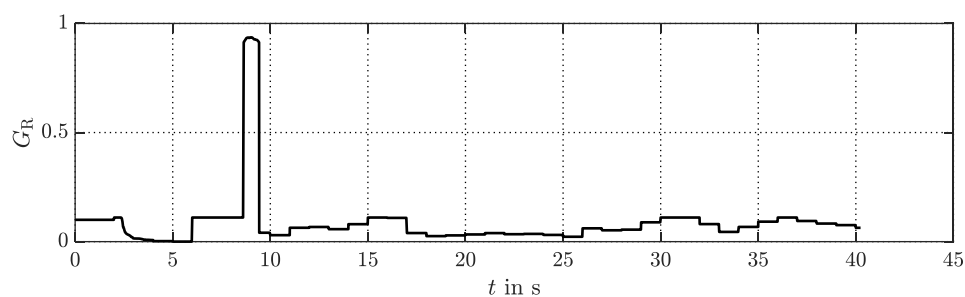


Figure 4.34: G_R for MnF, 100 km/h

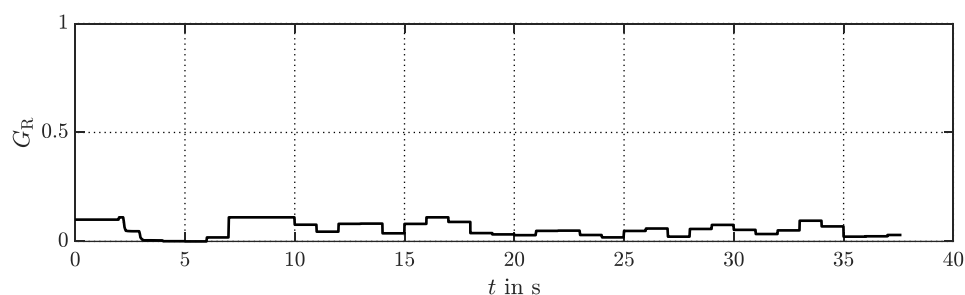


Figure 4.35: G_R for FnP, 100 km/h

Figure 4.36 shows the adaptive gain for the C profile, with vehicle speed of 80 km/h. In this case, the R controller is predominant over the whole simulation time.

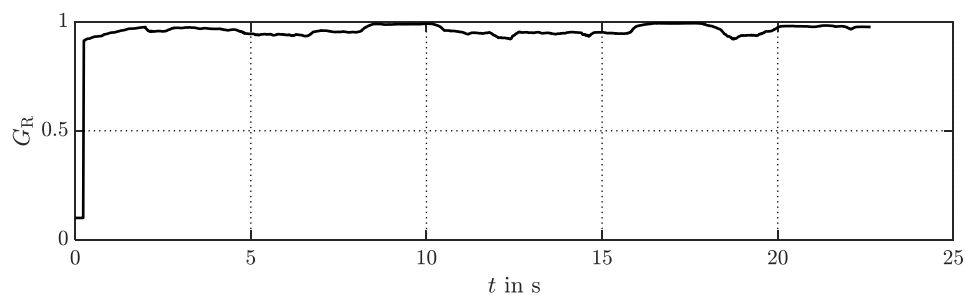


Figure 4.36: G_R for C profile, 80 km/h

When simulating a single obstacle occurring at 5 s and on the right wheels of the vehicle whose speed is 100 km/h, the coordination logic detects the bump and shifts towards the safer R controller (Figure 4.37).

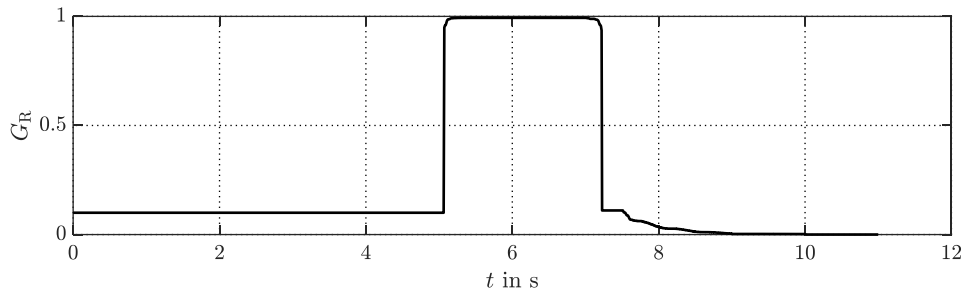


Figure 4.37: G_R for single obstacle, 100 km/h

4.7.2 Heave

In the following, the influence of the controllers on the acceleration of the body for the eigenmode of heave, \ddot{z}_{B_0} is analysed. The most comfortable behaviour in terms of lowest RMS value, is reached with the modified P controller for both stochastic road inputs (Figure 4.38, 4.39). In both cases, the four controllers display a similar behaviour until 4 Hz. At the latter, a local minimum of the R controller is found for the FnP profile. From 4 Hz to the wheel eigenfrequency, the P controller and the adaptive gain guarantee the lowest PSD, followed by the modified P controller and the R controller which shows the highest peak between 8 and 10 Hz. From 10 to 13 Hz, the R controller shows the lowest PSD, followed by the modified P controller. The behaviour from 13 Hz to 20 Hz, resembles the one described for the range between 4 Hz to the wheel eigenfrequency. For the artificially generated profile, the most comfortable RMS value is reached with the pure P controller, followed by the modified P controller, and the adaptive gain. The latter shows a similar dynamic behaviour to the R controller in the whole frequency range considered. This is due to the employed thresholds for the coordination logic in terms of maximum dynamic wheel loads. These thresholds can be tuned so to obtain a closer behaviour to the pure P controller. The lowest PSD values are reached with the pure P controller that shows a local maximum at the wheel eigenfrequency that it is shifted towards higher frequencies with respect to the R controller and the adaptive gain. The modified P controller displays a similar behaviour.

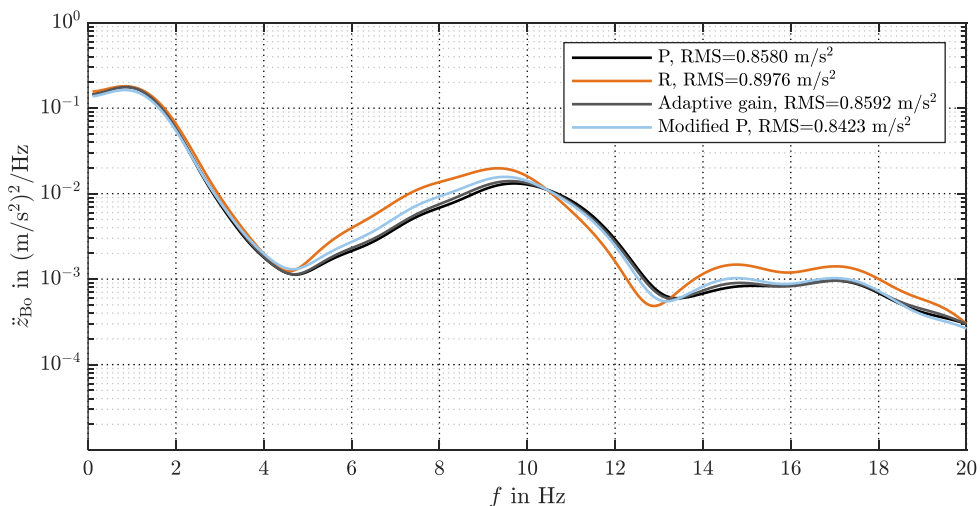
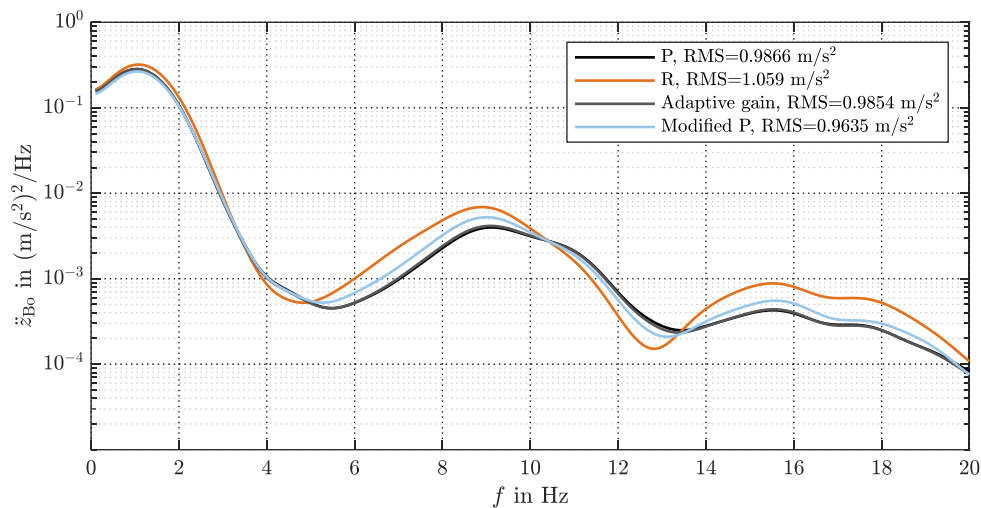
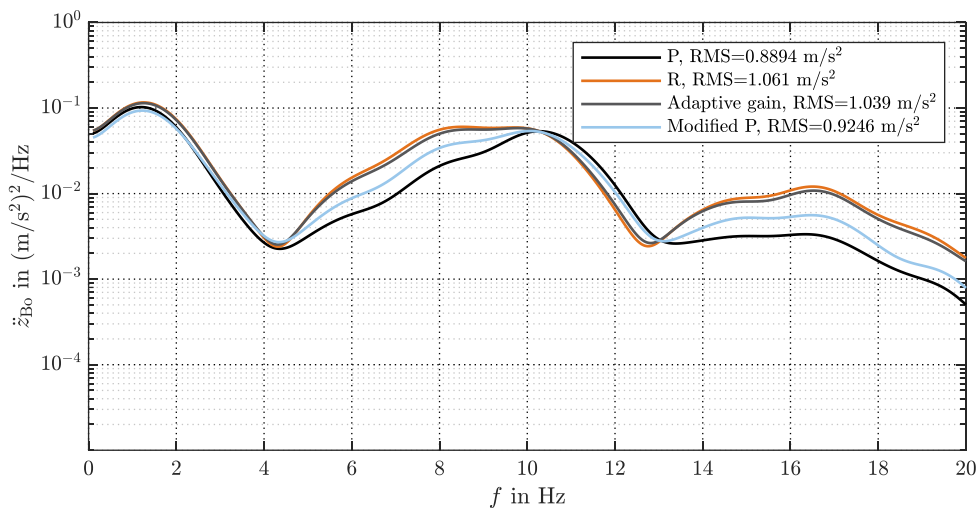


Figure 4.38: MnF, \ddot{z}_{B_0} , 100 km/h

Figure 4.39: FnP, \ddot{z}_{Bo} , 100 km/hFigure 4.40: A-C-A-C, \ddot{z}_{Bo} , 100 km/h

4.7.3 Pitch

The body mode of pitch shows low RMS values for both stochastic road profiles (Figure 4.41, 4.42) and higher values for the artificially generated one (Figure 4.43), especially if compared to the other body modes. For the MnF input, the lowest RMS value is obtained with the R controller, which shows the lowest dynamic behaviour in terms of PSD, in the frequency range from 2 Hz to 8 Hz and from 13 to 20 Hz. For the FnP input, the most comfortable RMS value is reached with the modified P controller, followed by the adaptive gain. In this case, the R controller, reaches the minimum PSD value in the ranges between 4 to 8 Hz, and 13 to 20 Hz. For the A-C-A-C profile, the lowest RMS value is reached with the P controller which shows the minimum PSD from 4 to 15 Hz.

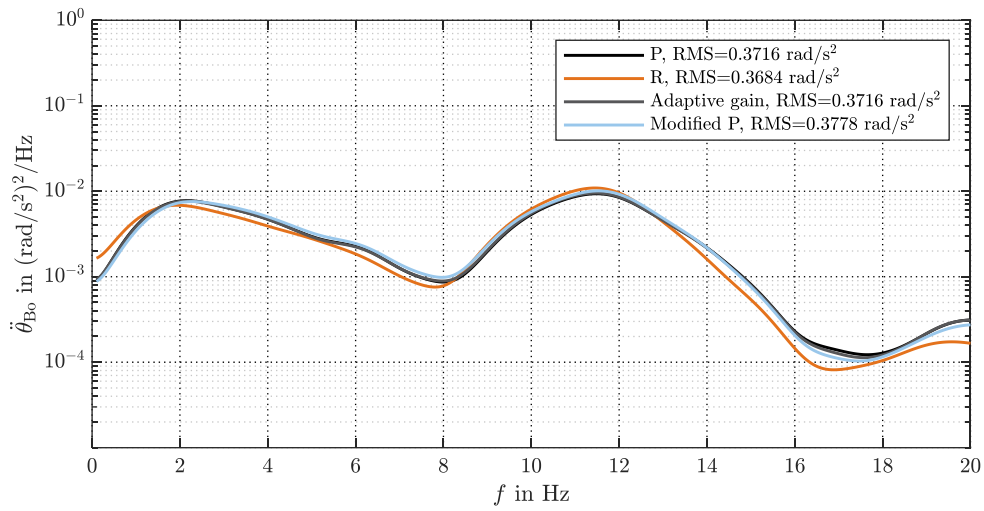


Figure 4.41: MnF, $\ddot{\theta}_{Bo}$, 100 km/h

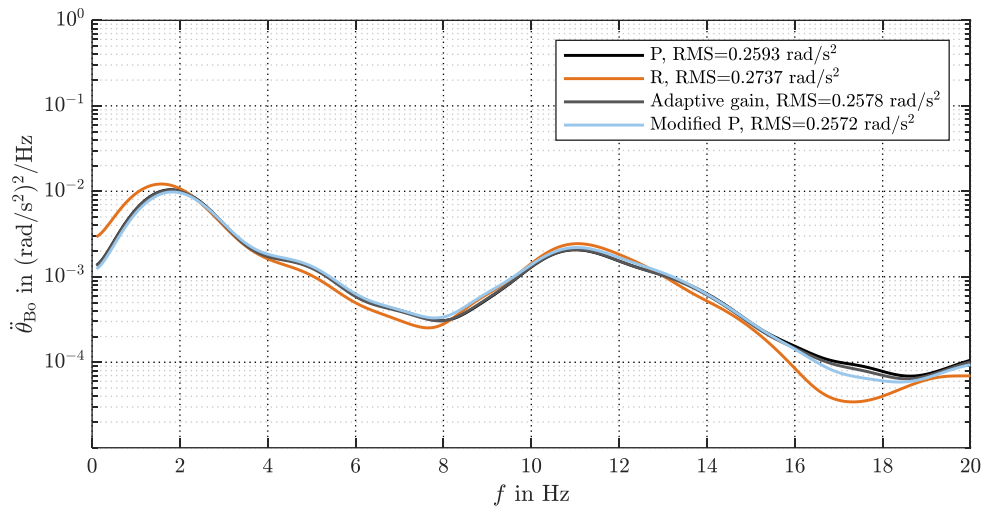


Figure 4.42: FnP, $\ddot{\theta}_{Bo}$, 100 km/h

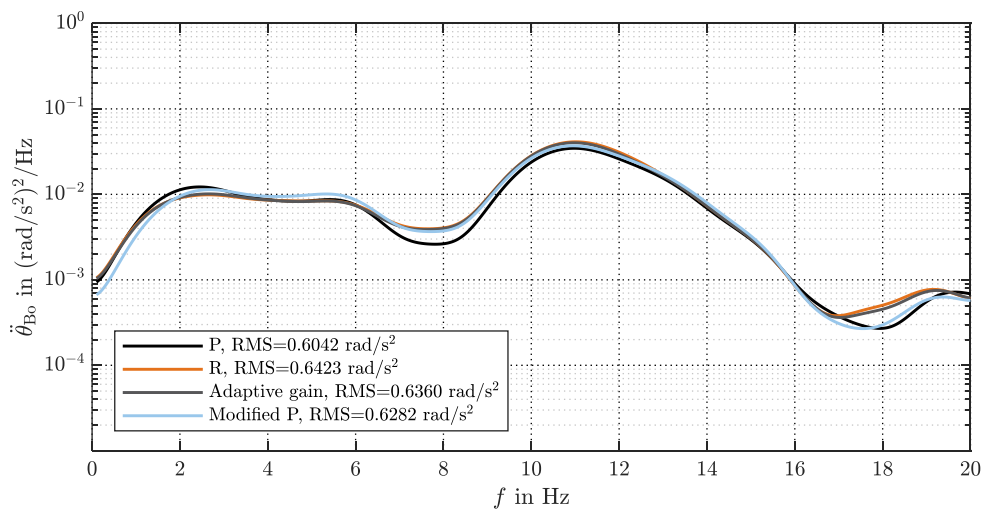


Figure 4.43: A-C-A-C, $\ddot{\theta}_{Bo}$, 100 km/h

4.7.4 Roll

The body eigenmode of roll is the one displaying the major differences between the controllers at the body eigenfrequency. For both stochastic road inputs, in the frequency range between 5 and 13 Hz, the dynamic behaviour of the body is almost the same for all four controlling logics (Figure 4.44, 4.45). From 13 Hz to 20 Hz the largest peaks in terms of PSD can be found for the R controller. A lowering in the PSD peak at the body eigenfrequency, at around 2 Hz, is seen with the P controller, the modified P controller or the adaptive gain. For both MnF and FnP inputs, the lowest RMS value is reached with the modified P controller. The same applies for the A-C-A-C profile, where the lowest PSD values are reached with both P and modified P controllers, while the R and the adaptive gain, show a similar behaviour in the entire frequency range considered.

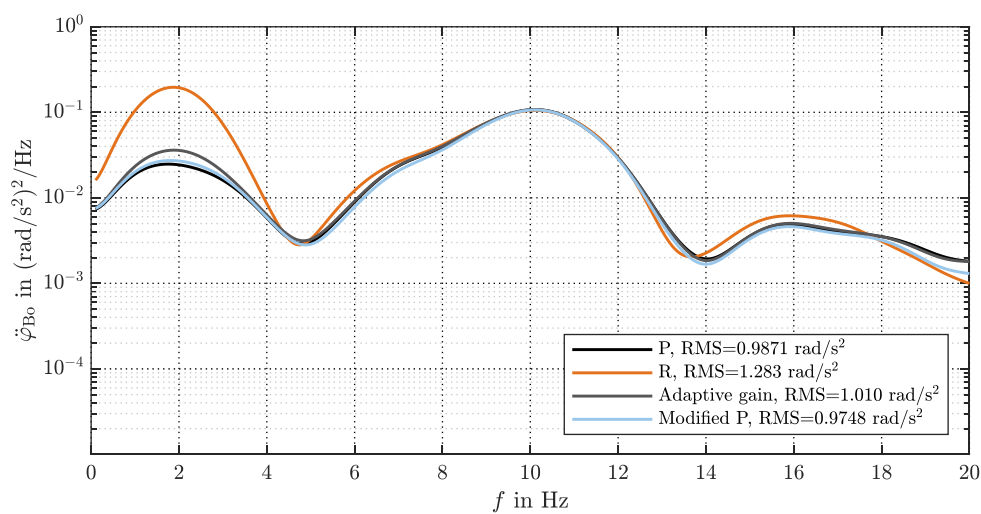


Figure 4.44: MnF, $\ddot{\varphi}_{Bo}$, 100 km/h

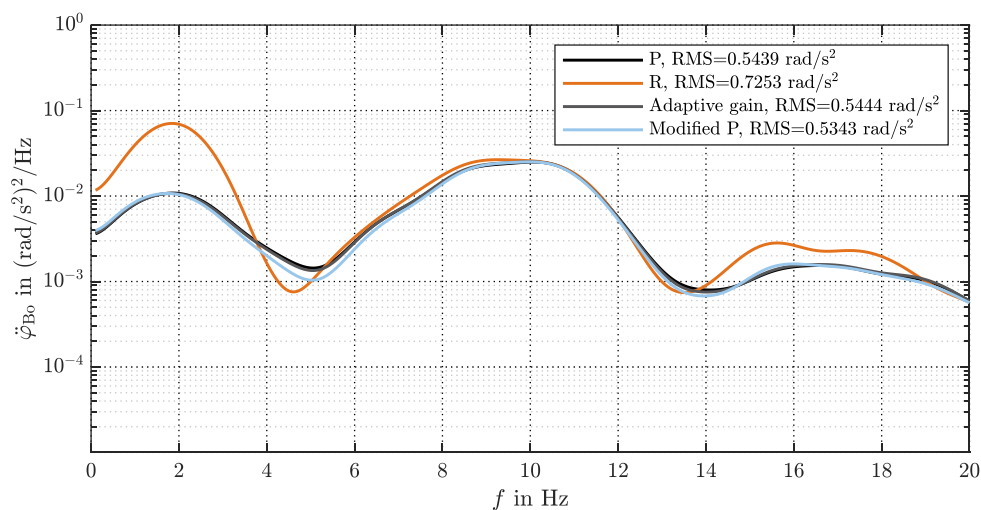


Figure 4.45: FnP, $\ddot{\varphi}_{Bo}$, 100 km/h

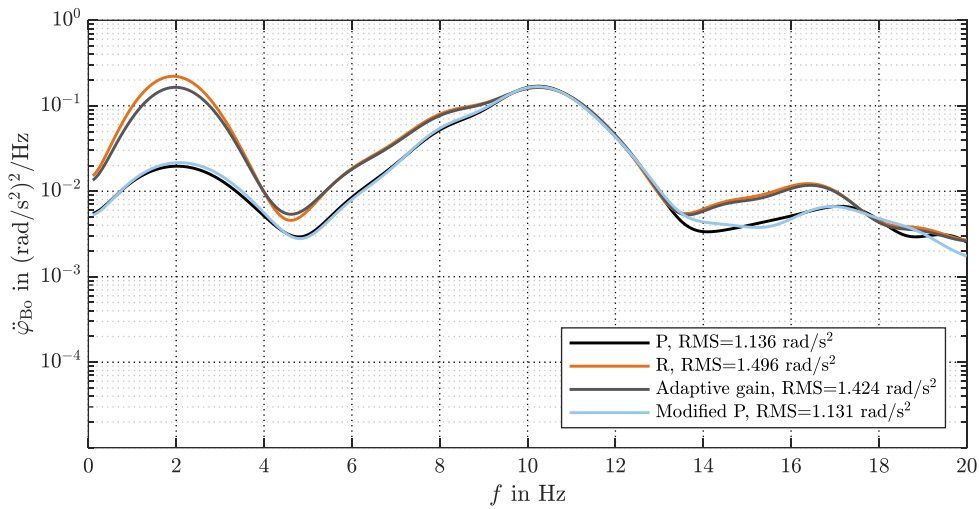


Figure 4.46: A-C-A-C, $\dot{\phi}_{B_0}, 100 \text{ km/h}$

4.7.5 Overall comfort perception

The overall acceleration value for comfort perception, a_{ISO} is computed for the simulations shown in the previous sections. The assumptions for the estimation of a_{ISO} have already been explained in Section 2.4.1. Tables 4.1, 4.2 and 4.3 summarise the results for the road inputs of MnF, FnP and A-C-A-C, respectively.

Table 4.1: a_{ISO} in m/s^2 for MnF

P	R	Adaptive Gain	Modified P
0.5718	0.7809	0.5863	0.5824

Table 4.2: a_{ISO} in m/s^2 for FnP

P	R	Adaptive Gain	Modified P
0.5419	0.6532	0.5417	0.5364

Table 4.3: a_{ISO} in m/s^2 for A-C-A-C

P	R	Adaptive Gain	Modified P
0.7393	1.016	0.9671	0.7919

For both MnF and A-C-A-C profiles, the lowest values for a_{ISO} are obtained with the pure P controller, followed by the modified P controller and the adaptive gain. For the FnP road input, the best comfort is achieved with the modified P controller and with the adaptive gain, immediately followed by the pure P controller. In whole three cases, the highest a_{ISO} , is reached with the pure R controller.

4.7.6 Dynamic wheel loads

Dynamic wheel loads are computed offline with Eq. (2.51). The mean of the PSD of the dynamic loads between the four wheels is calculated to have only one reference signal to use in order to compare the different controllers. The RMS value displayed for each configuration is the mean of the RMS of the signals on the four wheels. In the frequency range from 12 to 20 Hz, no significant changes are displayed between the four controllers. The main differences between the logics can be found at the body and wheel eigenfrequencies and in general, in the range between 0.1 to 12 Hz. The R controller is the one displaying the lowest RMS for both MnF and A-C-A-C (Figure 4.47, 4.49). For the FnP profile, the lowest RMS is reached with the modified P controller (Figure 4.48).

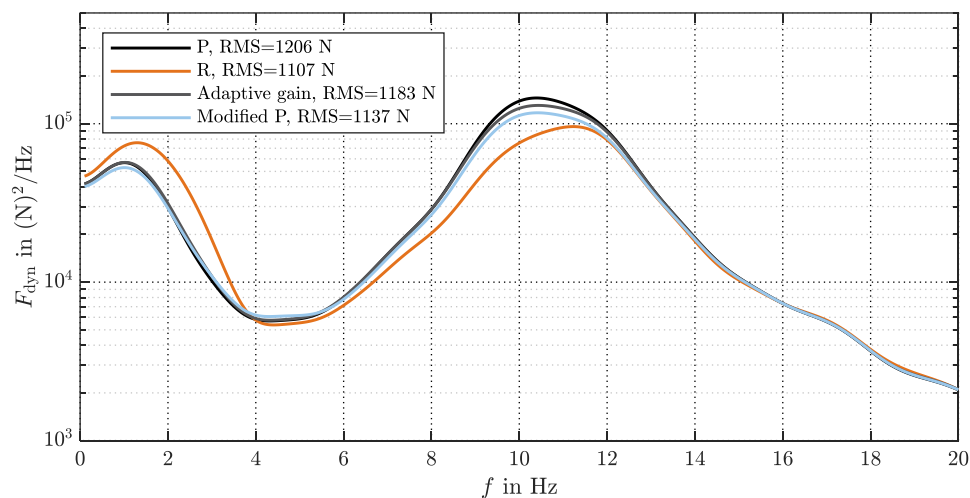


Figure 4.47: MnF, F_{dyn} , 100 km/h

The coordination logic displays a similar behaviour to the pure P controller for both MnF and FnP. This happens because for the two inputs, the RMS values of the dynamic wheel loads tend not to exceed the defined threshold, which, for these simulations, was set to the 35% of the static wheel loads. For the artificially generated profile A-C-A-C, the peak of the PSD at the wheel eigenfrequency is lowered with respect to the one obtained with the pure P controller for every other configuration.

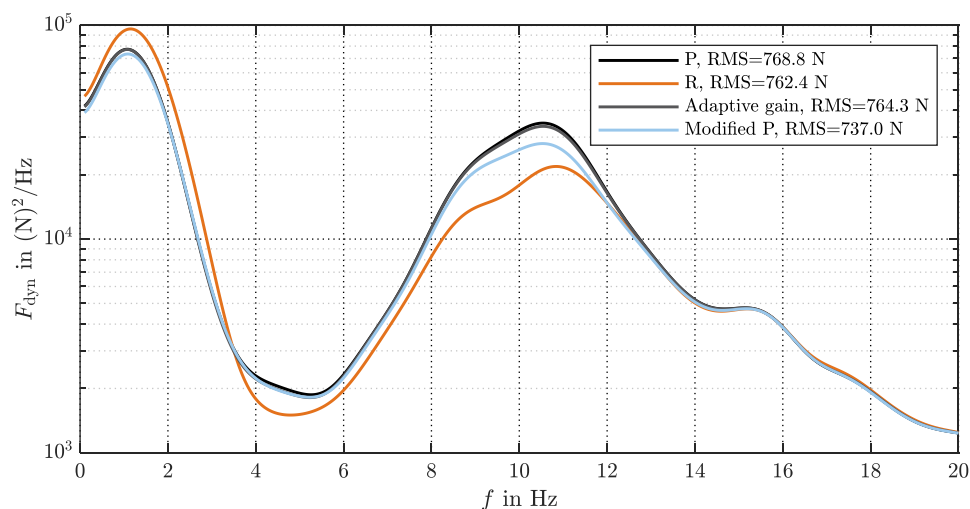


Figure 4.48: FnP, F_{dyn} , 100 km/h

At the wheel eigenfrequency, the PSD for the modified P controller, lies in all three case between the pure P and the pure R, which is the one displaying the lowest value. At the body eigenfrequency, the modified P presents a similar behaviour to the pure P, managing to lower the peak reached with the pure R.

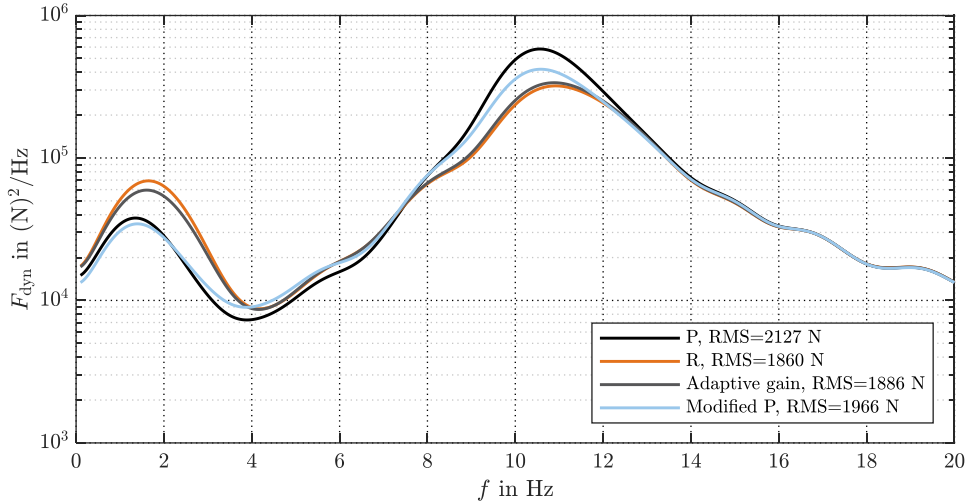
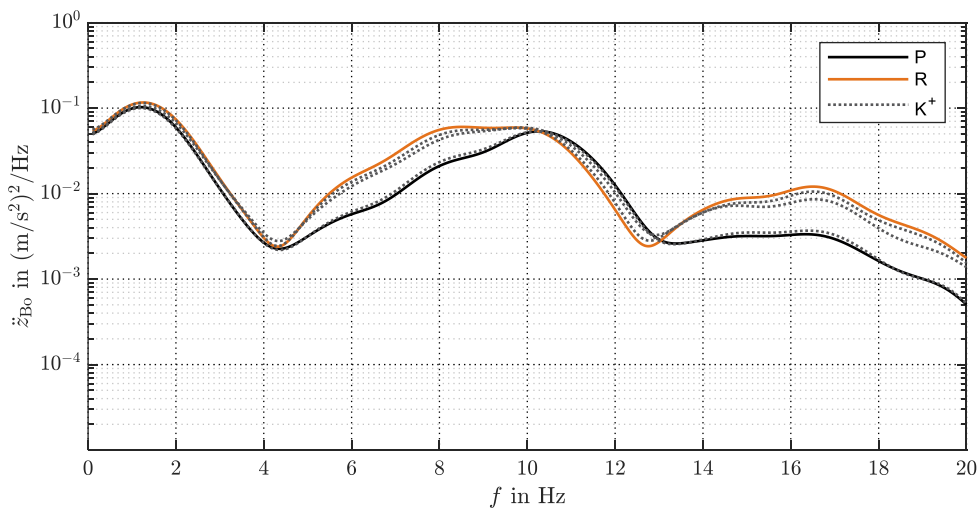


Figure 4.49: A-C-A-C, F_{dyn} , 100 km/h

4.7.7 Thresholds tuning potential

The coordination logic displays the advantage of being easily tuneable by simply changing the values of the thresholds described in Section 4.5. The A-C-A-C profile is used in both semi-active (Figure 4.50) and active configurations (Figure 4.51). The threshold k was changed and set, for both front and rear of the vehicle to 30%, 50% and 70%. The higher k , the closer the overall vehicle dynamics response to the pure P controller. It is shown from the simulation results, that the coordination logic always lies between the dynamic behaviour of the vehicle with the pure P and R controllers but it can be adjusted towards the one or the other depending on the desired dynamics. The most appreciable differences in the tuning of the coordination logic can be observed in both semi-active and active configurations at the body eigenfrequency for the body acceleration in roll mode and at the body and wheel eigenfrequencies for the dynamic wheel load.



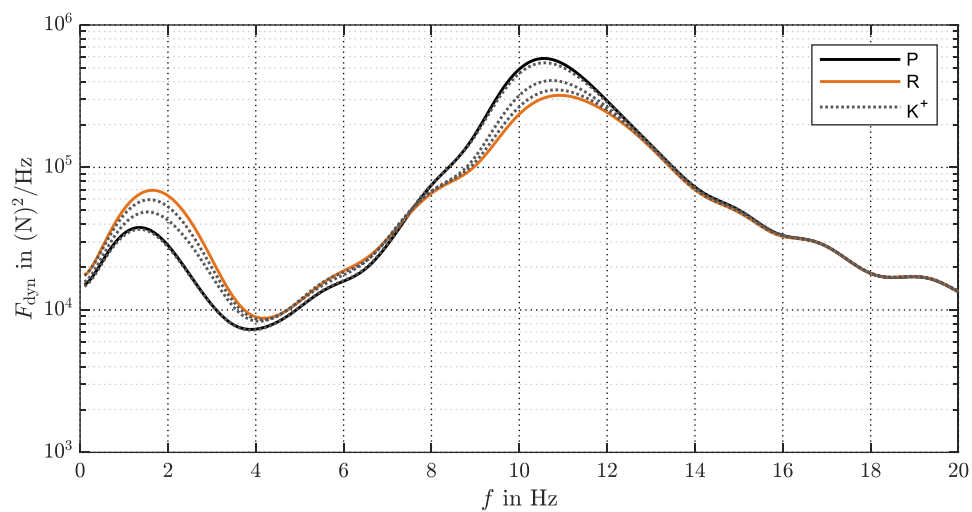
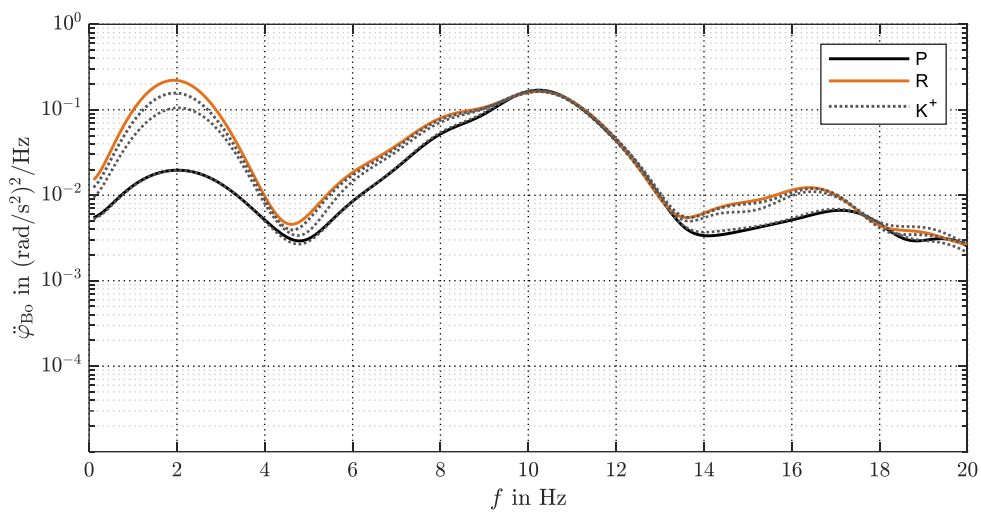
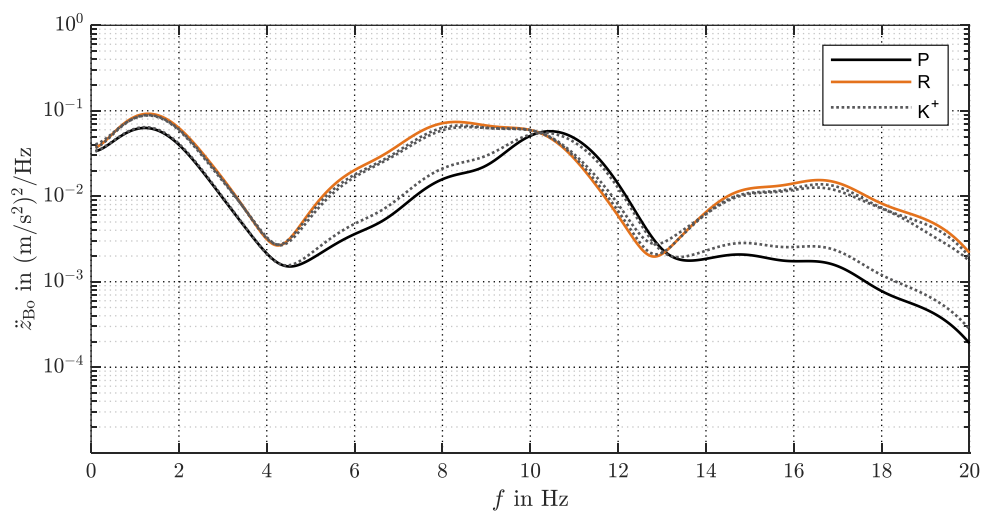


Figure 4.50: A-C-A-C, from top: \ddot{z}_{Bo} , $\ddot{\varphi}_{Bo}$, F_{dyn} for semi-active suspensions, 100 km/h



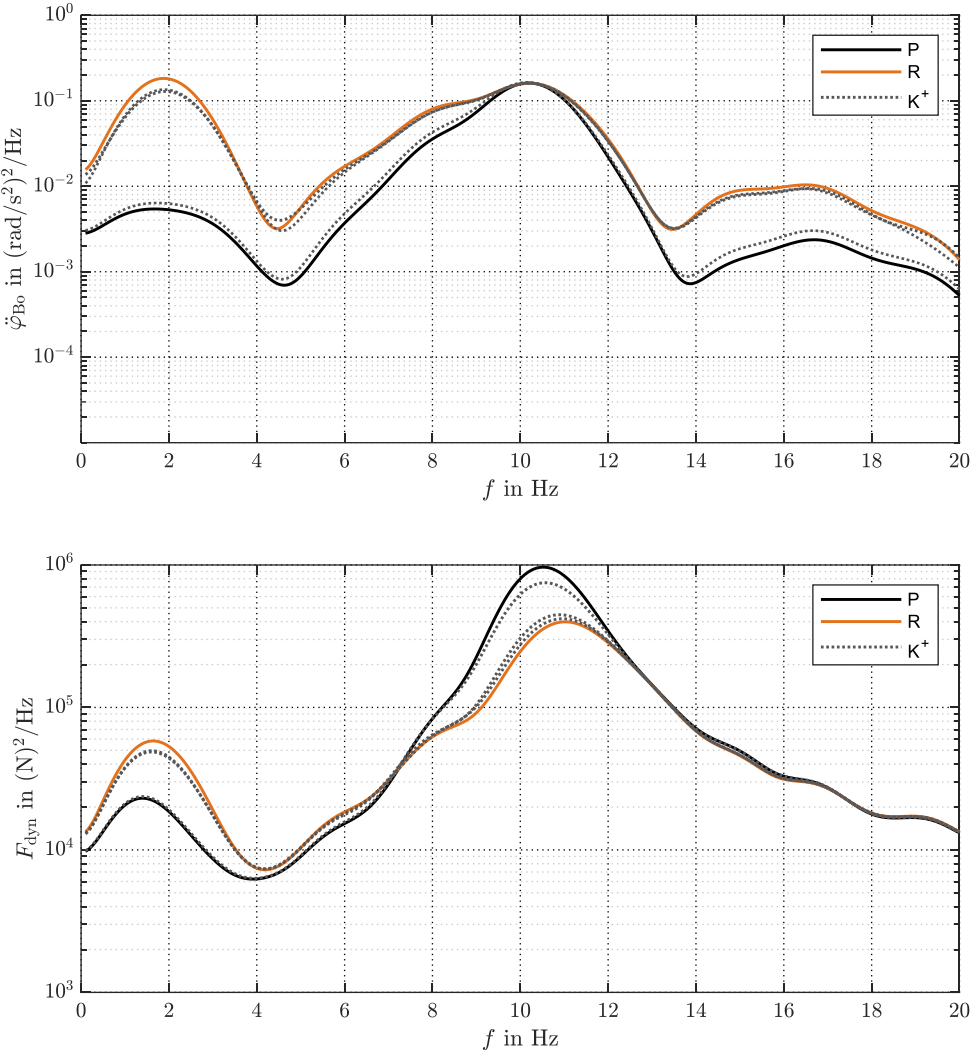


Figure 4.51: A-C-A-C, from top: \ddot{z}_{B_0} , $\ddot{\varphi}_{B_0}$, F_{dyn} for active suspensions, 100 km/h

5 Results

The following chapter contains the results of the work, according to the method described in Chapter 4. Firstly, the experimental setup for real life tests (Section 5.1) as well as the measurements processing (Section 5.2) are displayed. Several analysis are conducted: experimental tests with pure P and R controllers (Section 5.3), a comparison with the full vehicle model (Section 5.4) and tests results with the modified P controller and the coordination logic (Section 5.5). A sensitivity analysis on the parameter α_i for the modified P controller is carried out (Section 5.6). Finally, results for the adaptive gain of the coordination logic are shown for different vehicle speeds (Section 5.7).

5.1 Experimental setup

The vertical vehicle dynamics department of the industrial partner uses a specific development environment (BACE) with limited available libraries. Such an environment can be found in MatLab, version R2015B. A reimplementations of the developed logic is needed in order to assure compatibility with the vehicle in the subsequent testing phases. The BACE environment provides well-defined rules which are followed in order to obtain a stable and consistent C-Code generation from the Simulink model. Matrix and vectors multiplications are not allowed, constants need to be defined directly in the model as numerical values. Signals need to have a “single” precision and all operations must be performed with discrete resolution methods and fixed step size. Parameters as well as signals are defined in separate files with their own extension (*.json*). In order to measure a signal, the Simulink property “*Signal name must resolve to Simulink signal object*” must be activated. The ECU has limited memory resources and therefore the software cannot exceed in computational time, RAM or disk space. Changes to the logic are made in order to reduce the computational effort and to reconstruct some unavailable blocks in the BACE library as the *moving RMS* block or the *Spectrum Estimator* block. The overall principles of the logic are maintained. Further explanations on this are given in Appendix J. The coordination logic as well as the modified version of the P controller are implemented in the industrial partner model regarding vertical vehicle dynamics control. Such model provides the estimation of the vehicle states in terms of accelerations in heave, pitch and roll as well as the corresponding velocities. The series vertical vehicle dynamics controller is also active. In order to exclude its presence, disabling switches are used.

Models are saved in Git which allows multiple users to locally work on the same projects. A master is available and copies of it can be made as branches to work freely and independently of the master. For the scope of this thesis a new branch has been created, where the developed logic is added. A code generation in the hexadecimal system to transfer the logic to the vehicle ECU is performed. Final creation of the software version as well as the transfer of the latter to the ECU require specific permissions from the company. The help of an expert is needed for this

process. Several attempts have been made before obtaining a running software because of memory allocation problems to the ECU unit. These can usually depend on the definition of floating parameters and signals or on the computational effort required when, for example, buffering and saving some values online.

The test vehicle is a 7 series (G12, long version) BMW AG sedan which displays standard sensors. Further explanations on the suspension setup are given in Appendix G. In order to perform test measurements, additional sensors are mounted in the vehicle. An Automotive Dynamic Motion Analyzer (ADMA) is installed on top of the vehicle with measurements referring to the vehicle centre of gravity, and acquired at a sampling rate of 100 Hz. The basic principle of ADMA entails three gyroscopes, recording the rotational motion in three space dimensions and three accelerometers, to record linear movements. Signals are processed via an extended Kalman Filter. Potential sensors drift is corrected by using a Global Navigation Satellite System like GPS. Some of the measured signals are the acceleration of the body in vertical direction (heave motion) as well as roll and pitch rates which are available in °/s and consequently converted in rad/s. The corresponding accelerations are not available as measurements and therefore are derived with the following:

$$\frac{\partial f(x_0)}{\partial x} = \frac{f(x_0 + h) - f(x_0)}{h} \quad (5.1)$$

Both signals from the inertial and vehicle reference frame are recorded. The latter considers the vertical direction always perpendicular to the ground. Four accelerometers are also mounted on each of the four wheels and they measure the accelerations of the wheels in all three space directions, acquired at a sampling rate of 100 Hz. The processed signals are the wheels accelerations in vertical direction. All the measured signals are recorded with CANape by Vector on a portable computer by means of an eight-channel multi-input analog measurement module. Further explanations on the mounted sensors and acquisition modules are given in Appendix H.

5.2 Measurements processing

At the beginning, driving tests are conducted in different Munich areas in order to validate the setup of the sensors. The BMW test track in Aschheim (48° 13' 14.8" N, 11° 43' 15.7" O) is initially chosen. The road is driven by with constant speed of 80 km/h. Tests are conducted by either using the P or the R controller separately. Measurements signals are processed and observations are made. A comparison between recorded signals and estimated ones from a reference estimator from BMW is conducted. Furthermore, an analysis on dynamic wheel loads estimation reliability is performed. The parametrization for both P and R controller of Appendix F is used and it is addressed in the following as, respectively, "Optimal P" and "Optimal R". For the R controller, two extreme values in terms of damping ratios (percentage of critical damping) are used and namely $D_i = 0.05$ and $D_i = 2$ with $i \in \{z_{B_0}, \theta_{B_0}, \varphi_{B_0}, t_{B_0}\}$. The test track is driven on from a reference point A to a reference point B (AB) and in the opposite direction (BA). Table 5.1 summarizes the number of attempts of measurements for the BMW test track in Aschheim, for each configuration of the controllers.

Table 5.1: Number of tests measurements in Aschheim

	Optimal R	Optimal P	R, $D_i = 0.05$	R, $D_i = 2$
AB	3	2	3	3
BA	3	2	3	3

The RMS values of the acceleration in heave direction, of the roll and pitch rates and of the accelerations of the four wheels, all considered in the vehicle reference frame, are calculated for each test. Their mean value is computed among the available measurements on the same path and with the same controller configuration. The same applies for their coefficient of variation. The latter, c_v is equal to the ratio of the standard deviation σ to the mean μ :

$$c_v = \frac{\sigma}{\mu} \quad (5.2)$$

The higher the coefficient of variation, the more uncertain the measurements. The standard deviation and signals mean value are computed as it follows:

$$\sigma = \sqrt{\frac{1}{n} \sum_{i=1}^n (x_k - \mu)^2} \quad (5.3)$$

$$\mu = \frac{1}{n} \sum_{k=1}^n x_k \quad (5.4)$$

Tables 5.2 and 5.3 present the mean value between the available attempts, of the RMS of the measured signals as well as their coefficient of variation for section AB.

Table 5.2: μ for section AB

Signals	Optimal R	Optimal P	R, $D_i = 0.05$	R, $D_i = 2$
\ddot{z}_{B_0} , m/s ²	1.32	1.10	1.19	1.99
$\ddot{z}_{w,fr}$, m/s ²	20.9	23.0	22.0	19.0
$\ddot{z}_{w,fl}$, m/s ²	0.870	0.532	0.652	0.888
$\ddot{z}_{w,rl}$, m/s ²	14.7	14.0	15.3	13.8
$\ddot{z}_{w,rr}$, m/s ²	18.6	19.0	17.9	15.9
$\dot{\theta}_{B_0}$, rad/s	$35.2 \cdot 10^{-3}$	$29.9 \cdot 10^{-3}$	$31.7 \cdot 10^{-3}$	$38.4 \cdot 10^{-3}$
$\dot{\varphi}_{B_0}$, rad/s	$59.1 \cdot 10^{-3}$	$55.7 \cdot 10^{-3}$	$58.1 \cdot 10^{-3}$	$57.4 \cdot 10^{-3}$

Table 5.3: c_v for section AB

Signals	Optimal R	Optimal P	R, $D_i = 0.05$	R, $D_i = 2$
\ddot{z}_{Bo}	$12.8 \cdot 10^{-3}$	$10.1 \cdot 10^{-3}$	$86.0 \cdot 10^{-4}$	$28.0 \cdot 10^{-3}$
$\ddot{z}_{w,fr}$	$14.5 \cdot 10^{-3}$	$36.3 \cdot 10^{-3}$	$29.0 \cdot 10^{-4}$	$52.0 \cdot 10^{-4}$
$\ddot{z}_{w,fl}$	0.165	$11.6 \cdot 10^{-3}$	$70.7 \cdot 10^{-3}$	0.166
$\ddot{z}_{w,rl}$	$29.0 \cdot 10^{-3}$	$30.0 \cdot 10^{-3}$	$27.0 \cdot 10^{-3}$	$35.0 \cdot 10^{-3}$
$\ddot{z}_{w,rr}$	$15.6 \cdot 10^{-3}$	$47.1 \cdot 10^{-3}$	$48.0 \cdot 10^{-4}$	$10.6 \cdot 10^{-3}$
$\dot{\theta}_{Bo}$	$96.0 \cdot 10^{-4}$	$19.4 \cdot 10^{-3}$	$12.0 \cdot 10^{-4}$	$18.9 \cdot 10^{-3}$
$\dot{\phi}_{Bo}$	$17.0 \cdot 10^{-4}$	$47.0 \cdot 10^{-4}$	$42.7 \cdot 10^{-3}$	$38.0 \cdot 10^{-4}$

The same procedure was performed for section BA (Appendix I). The RMS values listed in the tables are obtained from raw signals. From the analysis of the tables, it can be observed that the coefficient of variation lies between 10^{-3} and 10^{-2} for all the signals. The only exception is represented by the acceleration of the front left wheel which displays a mean RMS value significantly distant from the other wheels. This can be the result of a mounting error or of the detachment of the accelerometer from the initial position of mounting. Consequently accelerations signals of the front left wheel as well as the correspondant dynamic wheel loads are not considered for further analysis. Results are shown in the frequency domain. All recorded signals are treated with the following procedure:

1. Filtering of the raw signal with a lowpass filter with cut-off frequency of 18 Hz.
2. Alignment of the available measurement attempts of the same type. For this purpose the MatLab function *finddelay* is used and a manual code is written to obtain the realignment.
3. Cutting of the available realigned signals according to the shortest signal length.
4. Computation of the power spectral density with Welch's method of averaged periodograms, with rectangular window of 0.5 s of width if not differently specified, for each of the signals available for one simulation setup, in the frequency range from 0.1 Hz to 20 Hz.
5. Averaging of the computed PSD according to the number of available measurements.
6. Plot in the frequency domain with a smoothing average filter with 10 samples of span.

When it comes to dynamic wheel loads, they are computed with the following:

$$F_{dyn,ij} = m_{Bo,ij} \ddot{z}_{Bo,ij} + m_{w,ij} \ddot{z}_{w,ij} \quad (5.5)$$

where $i \in \{f, r\}, j \in \{r, l\}$ and where the accelerations signals $\ddot{z}_{Bo,ij}$ and $\ddot{z}_{w,ij}$ are taken from the sensors and are further processed with steps 1, 2 and 3. From step 4, the same procedure is applied to dynamic wheel loads. In Section 5.5, rather than considering the dynamic wheel load on each of the four wheels, an average value is derived from the front right wheel and the rear

wheels and it is addressed as F_{dyn} . This is obtained by processing the acceleration signals from the sensors with steps 1,2 and 3. Afterwards, Eq. (5.5) is used to obtain a dynamic wheel load on each of the 3 wheels considered. Eq. (5.4) is applied where x_k is the power spectral density of $F_{\text{dyn},ij}$ and k goes from 1 to n , where the latter corresponds to the number of wheels considered and it is equal to 3. The so-obtained mean value on a single measurement file, is further treated between the available set of measurements with steps 5 and 6. In Section 5.5, RMS values of the signals are displayed. They are the mean of the RMS values of the signals for each available measurements treated with steps 1, 2 and 3. The RMS of F_{dyn} , is computed as it follows:

$$\text{RMS}(F_{\text{dyn}}) = \frac{1}{n} \sum_{k=1}^n \text{RMS}(F_{\text{dyn},ij})_k \quad (5.6)$$

Where $\text{RMS}(F_{\text{dyn},ij})$ is previously averaged on the number of available measurements. Appendix I shows an example of how raw signals have been treated, according to the described procedure.

A comparison between a reference estimator from BMW and the experimental sensor setup is performed for some of the signals of interest. The extremely underdamped configuration for the R controller is used as an example. It must be considered that, when referring synthetically to “ADMA” for dynamic wheel loads, the latter are calculated, and not directly measured, by taking into account both vertical body acceleration from ADMA as well as wheels vertical accelerations from the accelerometers, and therefore, the reference is to the whole sensor setup. Angular rates and accelerations for pitch and roll are displayed, respectively, with reference to the same y-axis scale. Vertical acceleration on the contrary, is shown on a different scale because it is, in the majority of the test setups, an order of magnitude higher.

It can be observed that the reference estimator slightly overestimates the acceleration of the body in heave, at the body eigenfrequency and the latter it is shifted towards lower frequencies if compared to the measured signal. In the frequency range from 2 Hz to 12, they present almost the same behaviour. The wheel eigenfrequency is slightly underestimated with respect to measurements (Figure 5.1). The acceleration in pitch mode, at the body eigenfrequency around 2 Hz is slightly overestimated with respect to the measurements. The effect of the filter eliminates higher frequencies vibrations that could occur due to other phenomena (Figure 5.2). The acceleration in roll eigenmode displays the major differences between the signals in the whole frequency range of interest (Figure 5.3). Roll and pitch rates presents a similar behaviour between the reference estimator and ADMA respectively from 8 to 20 Hz and from 4 to 20 Hz. At the body eigenfrequency the estimator overestimates the pitch rate. Viceversa, the roll rate is significantly underestimated in comparison to the measurements (Figure 5.4, 5.5).

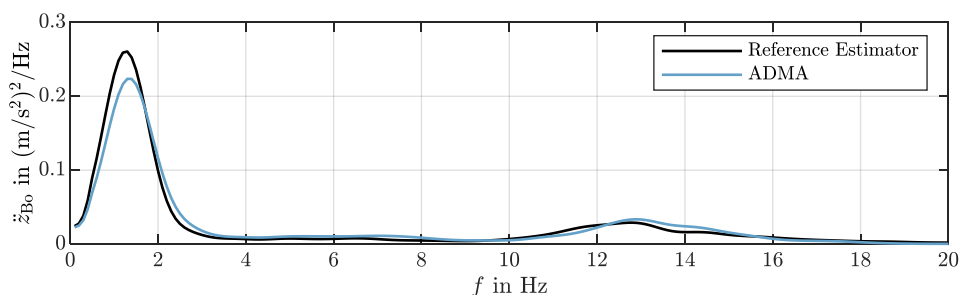


Figure 5.1: \ddot{z}_{B_0} for R, $D_i = 0.05$

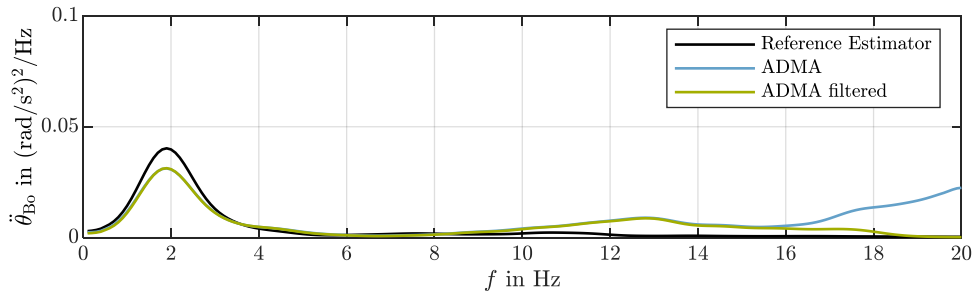


Figure 5.2: $\ddot{\theta}_{B_0}$ for R, $D_i = 0.05$

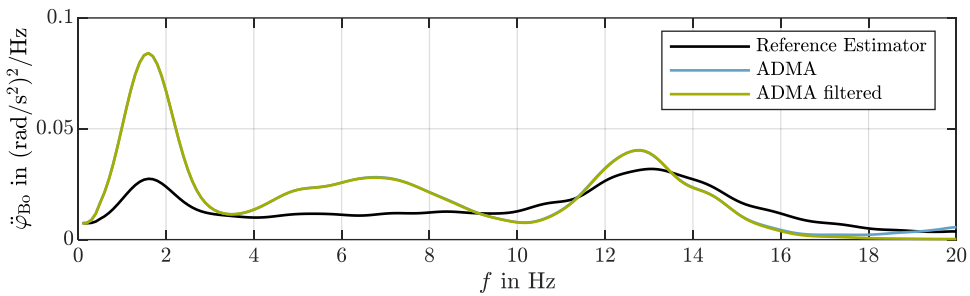


Figure 5.3: $\dot{\varphi}_{B_0}$ for R, $D_i = 0.05$

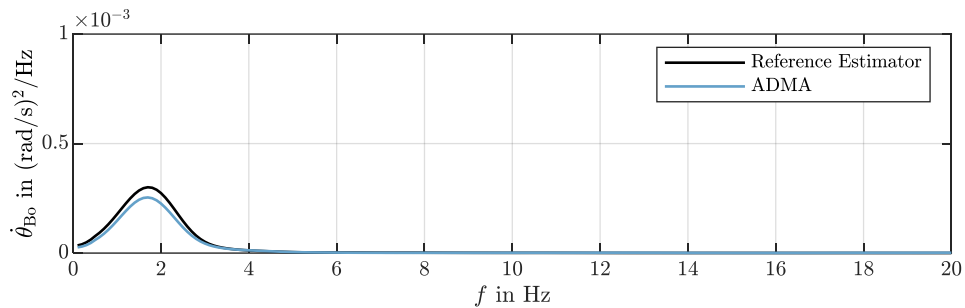


Figure 5.4: $\ddot{\theta}_{B_0}$ for R, $D_i = 0.05$

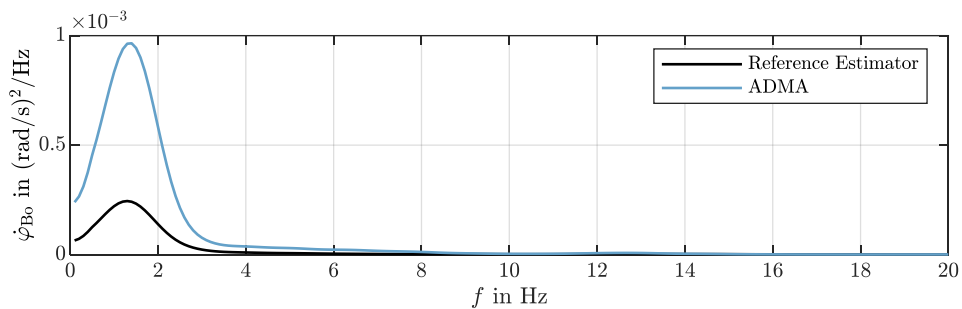
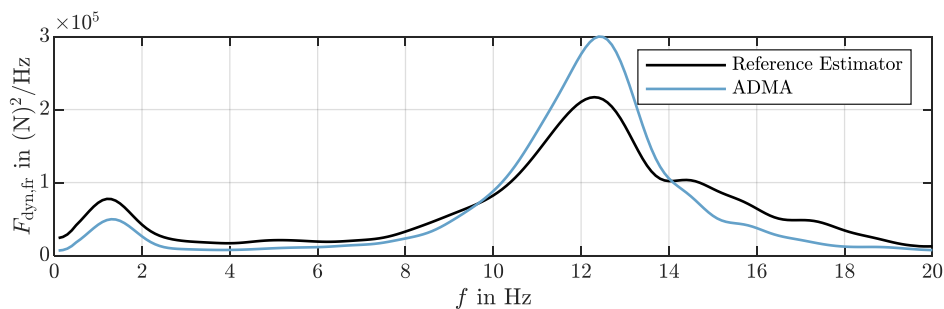
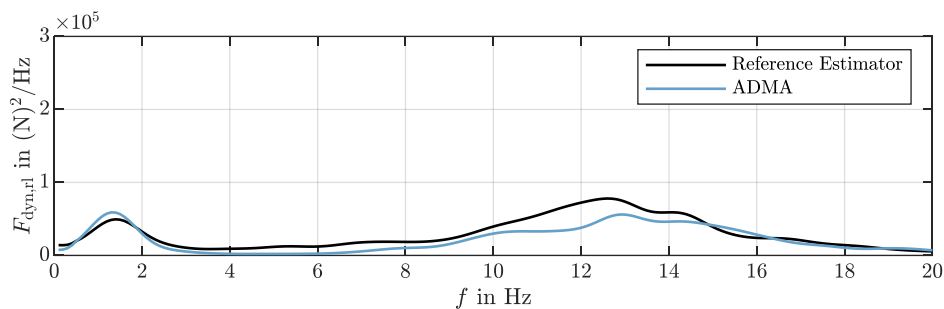
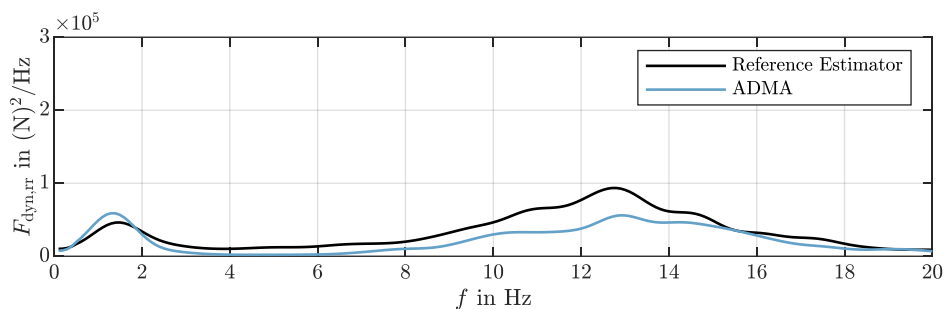
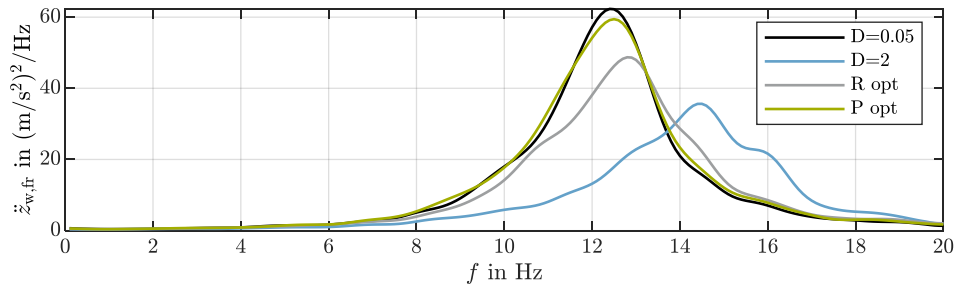
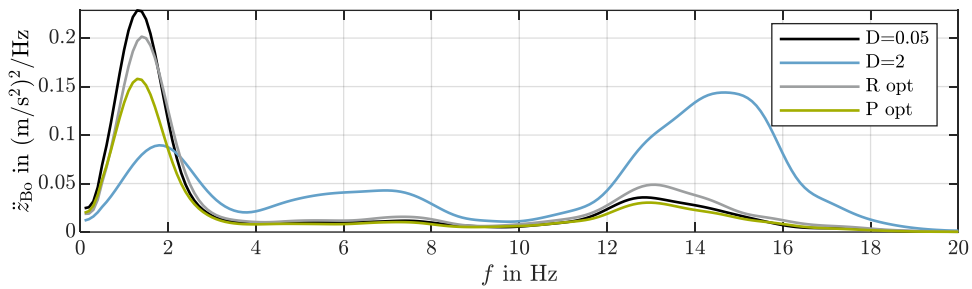
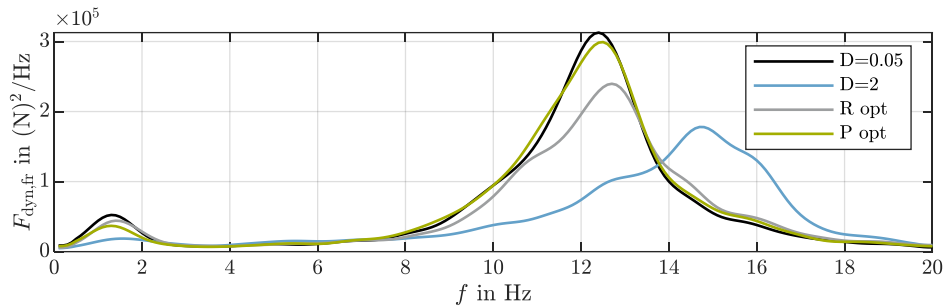


Figure 5.5: $\dot{\varphi}_{B_0}$ for R, $D_i = 0.05$

Dynamics wheel loads estimated by the BMW logic are compared to the ones derived from ADMA and accelerometers measurements, applying the procedure which has been described previously. The first one takes into account estimated wheels accelerations and the suspension forces, also considering the contribution of anti-roll bars. For the front right wheel, the estimator overcomes the measurements until 9 Hz and from 14 to 20 Hz. At the wheel eigenfrequency, at around 12 Hz, measurements show a greater peak (Figure 5.6). For the rear of the vehicle, ADMA displays a lower PSD for the dynamic wheel load except at the body eigenfrequency. The wheel eigenfrequency is slightly shifted towards greater frequencies (Figure 5.7, 5.8).

Figure 5.6: $F_{\text{dyn,fr}}$ for R, $D_i = 0.05$ Figure 5.7: $F_{\text{dyn,ri}}$ for R, $D_i = 0.05$ Figure 5.8: $F_{\text{dyn,rr}}$ for R, $D_i = 0.05$

The different configurations for the R controller and the one for the P controller are also compared in the following. Only direct measurements results are shown. The front right wheel acceleration shows a reduction of the peak at the wheel eigenfrequency with the R controller with the optimal parametrization and in the overdamped case. The latter presents a shift of the eigenfrequency towards higher frequencies (Figure 5.9). The acceleration of the body as well as the dynamic wheel load display, with the R controller, the theoretical expected behaviour of a passive suspension with different damping ratios [2, p. 1120], [13, p. 257]. A small damping coefficient entails higher accelerations at the body eigenfrequency but lower ones between the frequency range from the body bounce to the wheel hop. An opposite behaviour can be observed in the overdamped configuration (Figure 5.10). Figure 5.11 shows the dynamic wheel load for the front right wheel obtained from measurements. Increasing damping causes a shift towards higher values of the wheel eigenfrequency. Pure P controller reduces the PSD of the acceleration of the body at around 1 Hz (Figure 5.10) but shows an high peak at the wheel eigenfrequency for the dynamic wheel load (Figure 5.11).

Figure 5.9: $\ddot{z}_{w,fr}$ Figure 5.10: \ddot{z}_{Bo} Figure 5.11: $F_{dyn,fr}$

The initial measurement processing phase allowed to validate the sensor setup in the estimation of the desired quantities, highlighting anomalies as the one for the front left wheel. Eq. (4.11) is proved to be accurate in the estimation of dynamic wheel loads with the measured signals and despite its derivation from a quarter car model. A comparison between the measured signals and the estimated ones from a reference estimator has shown that the latter possesses limited accuracy. Nevertheless, some of the estimated signals have been used in the coordination logic as the velocity in heave mode, pitch and roll rates as accuracy in the estimation is not the main requirement in the coordination but an efficient detection of changes in different driving conditions.

5.3 Experimental results with P and R controllers

A new set of driving tests is organised. The aim is to experimentally observe the main differences in the behaviour of the signals of interest, when using the pure P and R controllers. Tests have been performed with the optimized parametrization of Appendix F in a comfort perspective. The area around Pulling and Freising (48° 21' 44.9" N, 11° 42' 11.7" O) is selected. Two tracks are chosen in the specific, the FnP, as addressed in this work, whose measurements of the height

levels are available and a second one, nearby the first, which is driven from a point C to a point D (CD) with constant speed of 70 km/h. The same analysis of Section 5.2 on the RMS mean values and coefficients of variation has been carried out and it is included in Appendix I. Only some of the directly measured signals are displayed in this section. At first, an analysis on the CD path is performed.

It can be observed that the acceleration of the body as well as the roll and pitch rates, display a lower PSD in the whole frequency range considered, using the pure P controller (Figure 5.12, 5.13, 5.14). The peaks displayed with the pure R controller are not significantly higher because of the optimization in comfort perspective.

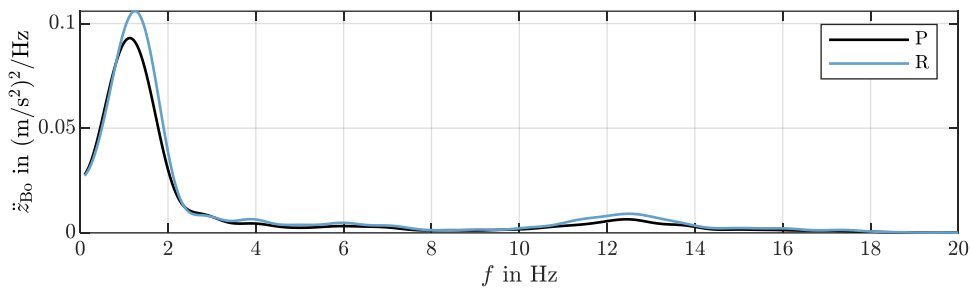


Figure 5.12: \ddot{z}_{B_0} , CD

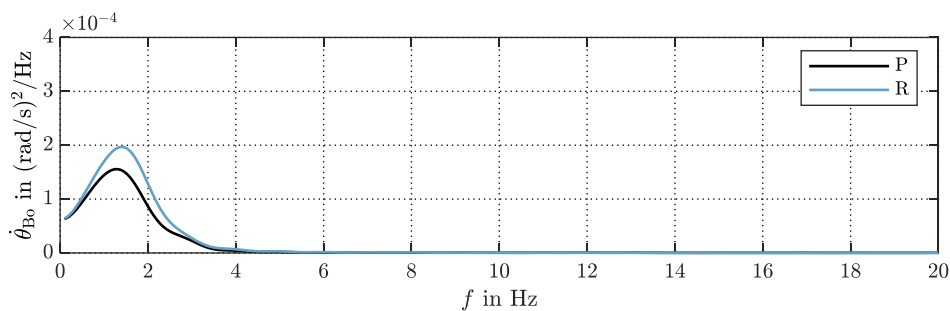


Figure 5.13: $\dot{\theta}_{B_0}$, CD

When it comes to the dynamic wheel load on the other hand, the R controller shows a lower PSD at the wheel eigenfrequency while the opposite happens at the body eigenfrequency. This is consequence of the observations that have been already pointed out in the design of the controller, as the extended Skyhook law does not limit the wheel excitation.

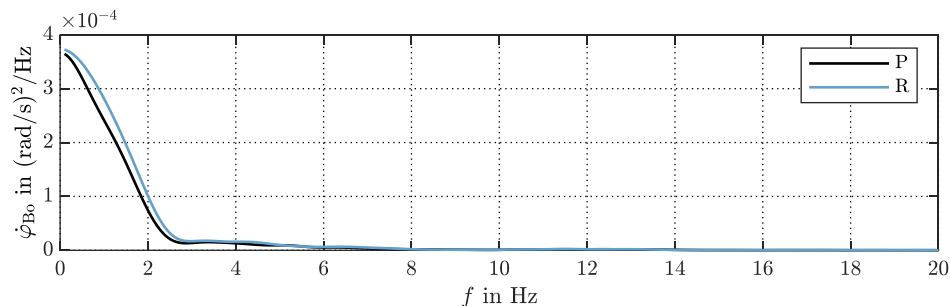


Figure 5.14: $\dot{\phi}_{B_0}$, CD

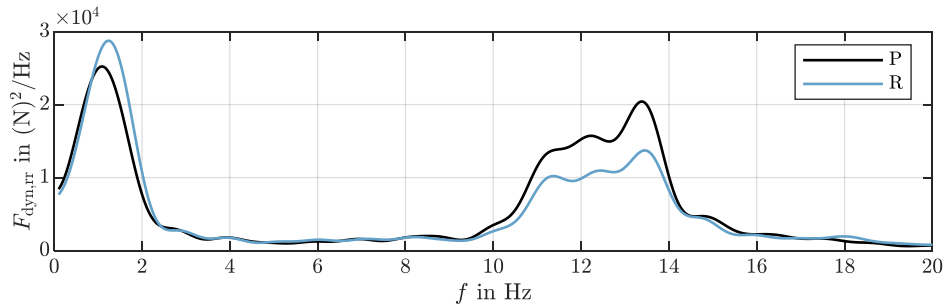


Figure 5.15: $F_{\text{dyn,rr}}$, CD

Results for the FnP profile are shown as it follows. The track is driven by with constant speed of 100 km/h. The observations made for the CD track in terms of acceleration and body rates are valid. The PSD of the acceleration in heave mode, is an order of magnitude higher, compared to the previous test track (Figure 5.16, 5.17, 5.18). From the latter and considering the analysis of the dynamic wheel loads, it can be seen that this track, presents a high content of low frequency disturbance. The two controllers presents approximately the same behaviour in the range that goes from 6 to 20 Hz while at the body eigenfrequency, the P controller shows a better dynamic behaviour (Figure 5.19).

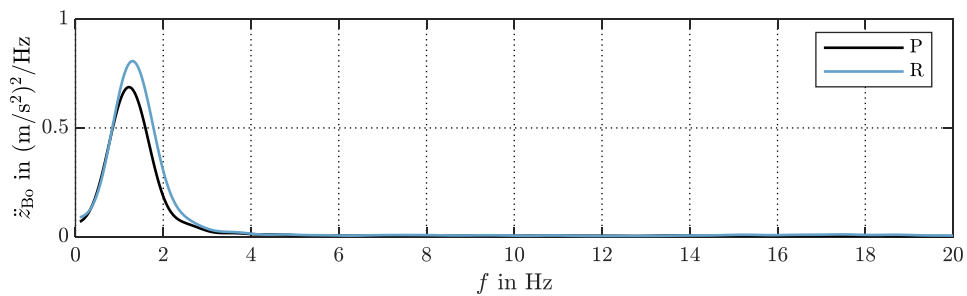


Figure 5.16: \ddot{z}_{B_0} , FnP

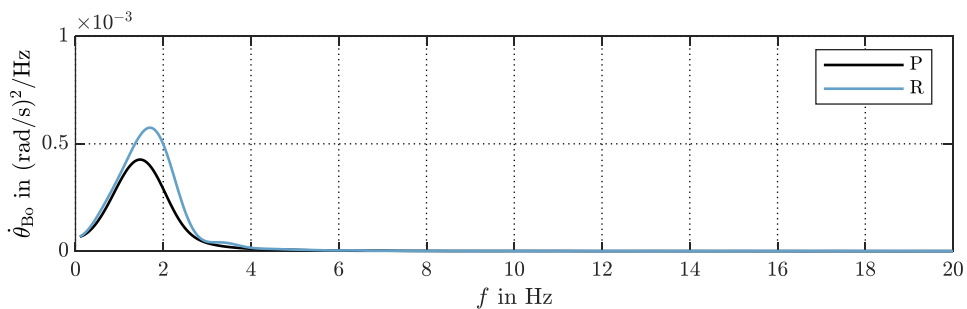


Figure 5.17: $\dot{\theta}_{B_0}$, FnP

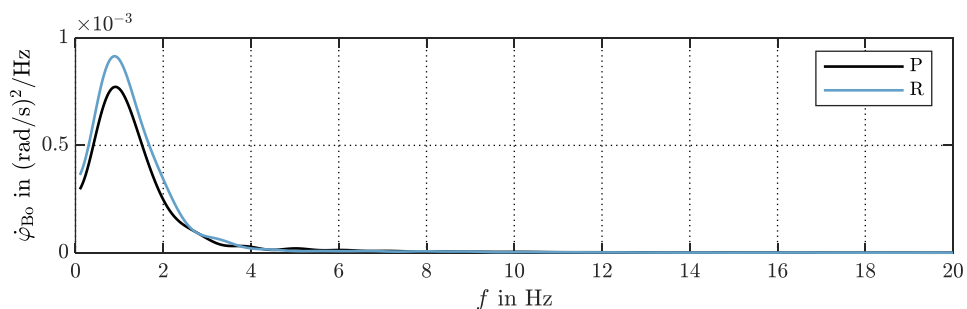
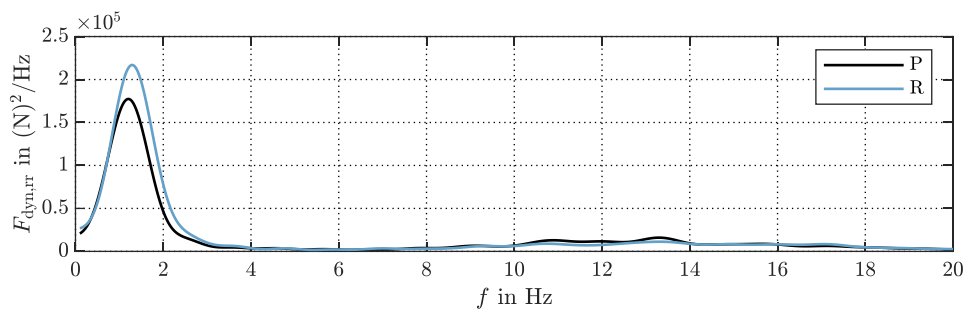
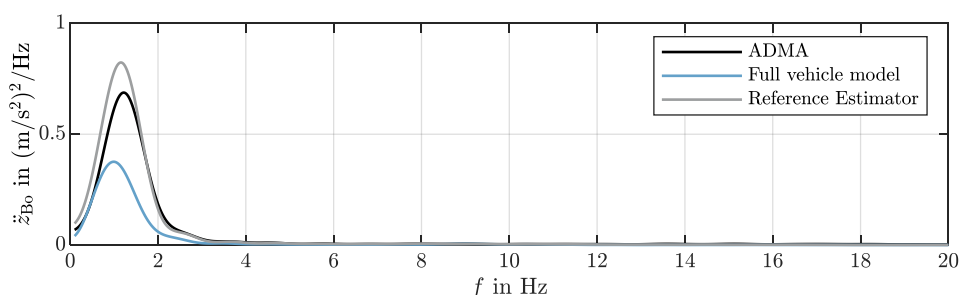
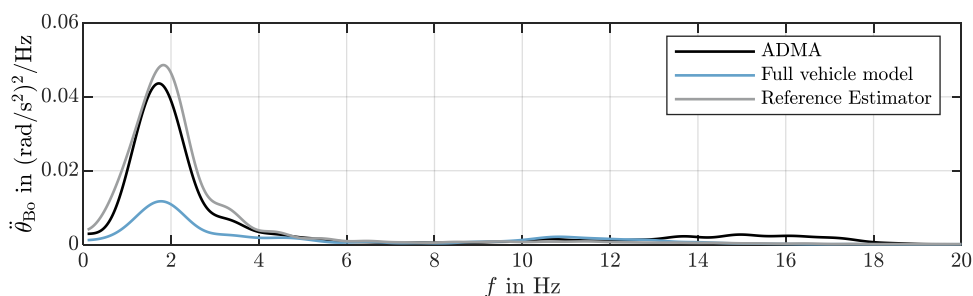


Figure 5.18: ϕ_{B_0} , FnP

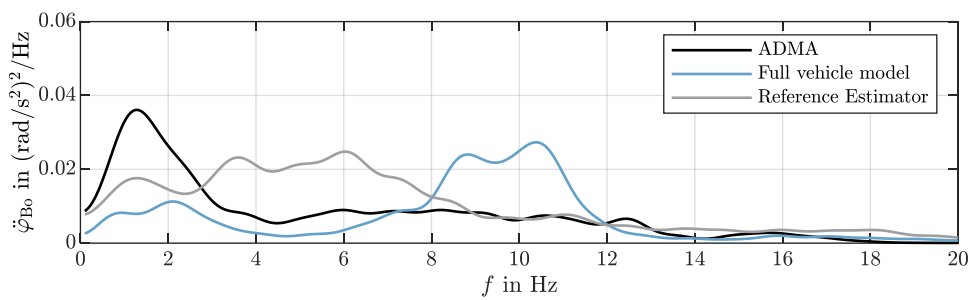
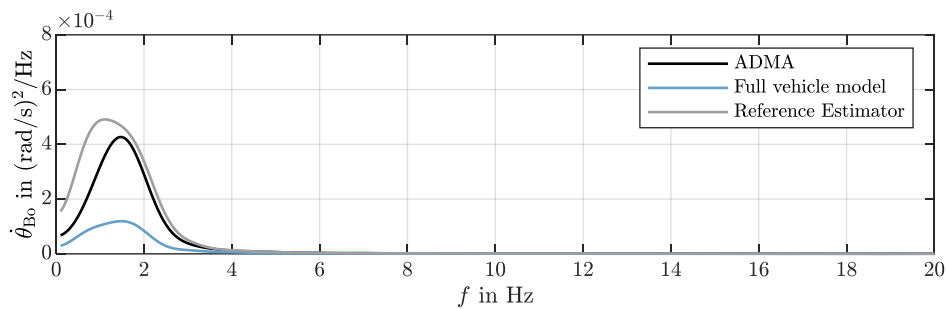
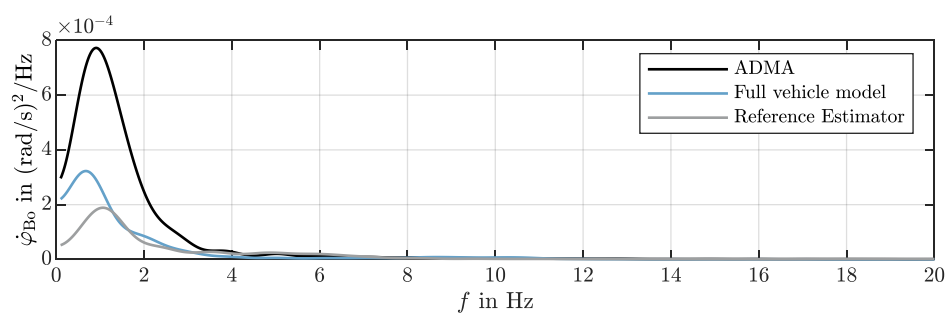
Figure 5.19: $F_{\text{dyn,rr}}$, FnP

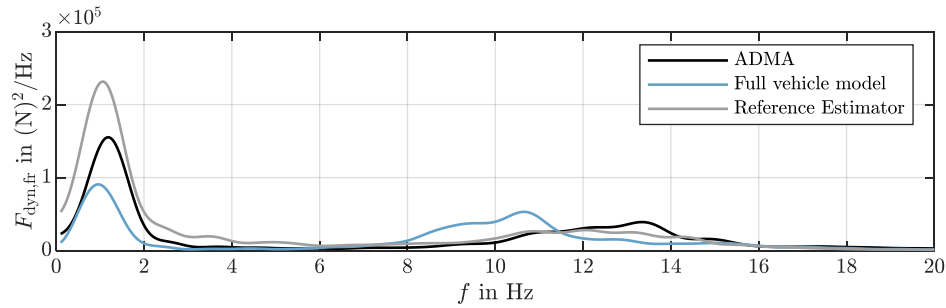
5.4 Comparison with the full vehicle model

In this section, a comparison between the measured signals, the estimates from the reference estimator and the simulated ones with the full vehicle model of Section 2.3 is performed. The first two are taken from the tests on the FnP profile, driven by with constant speed of 100 km/h. The measured and estimated signals are acquired with CANape with a sampling rate of 100 Hz. On the other hand, the simulation model uses a fixed time step resolver with a sampling rate of 10^5 Hz. The PSD of both measured and simulated signals is computed with Welch's method of averaged periodograms with a rectangular window of 1 s and 50 % of overlap. Such a comparison is carried out as the method has been developed in reference to the full vehicle model, but in order to produce a running software testable in the car, estimated signals have to be used. Signals from ADMA are used as a reference of what is truthfully occurring in the vehicle. Both configurations with optimal P and optimal R controllers, in comfort sense, are analysed. For what concerns the P controller, at the body eigenfrequency, the reference estimator is the one displaying the highest values in terms of vertical body acceleration (Figure 5.20), pitch acceleration (Figure 5.21) and pitch rate (Figure 5.23), followed by the measured values and the ones from the full vehicle model.

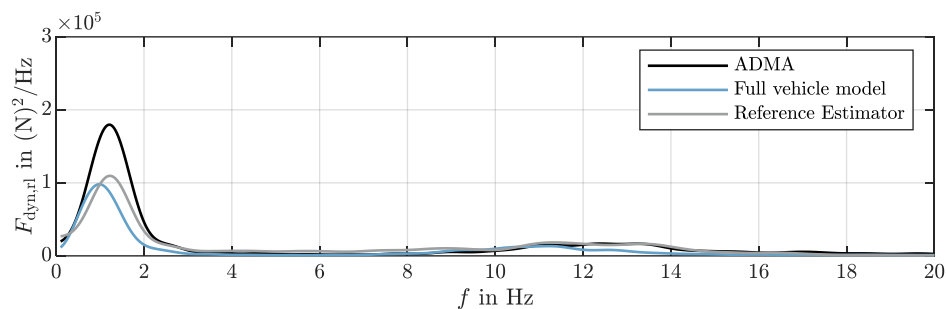
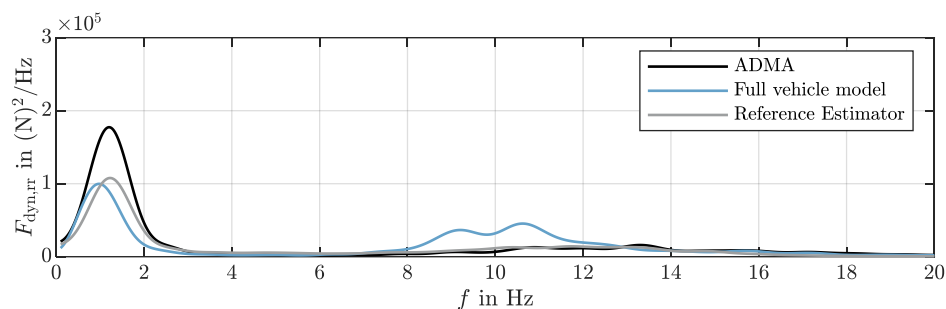
Figure 5.20: \ddot{z}_{B_0} , FnP, P controllerFigure 5.21: $\ddot{\theta}_{B_0}$, FnP, P controller

The roll angular acceleration displays an almost constant PSD from 0.1 to 10 Hz with the reference estimator, while it shows two peaks at the body and wheel eigenfrequency for both ADMA and the full vehicle model, where the latter shows a higher PSD around 10 Hz, compared to the measurements, and an opposite behaviour at around 2 Hz (Figure 5.22). Roll rate is underestimated by both the full vehicle model and the reference estimator (Figure 5.24). Dynamic wheel loads are characterised by a low PSD content at the wheel eigenfrequency as already observed in the previous section, which is overestimated by the full vehicle model and shifted towards lower frequencies. This is due to the simplifying assumptions that have been made for the full vehicle model. At the body eigenfrequency, for the front axle, a similar relationship between the models to the one observed for the vertical acceleration, is observed (Figure 5.25). On the rear axle at 1 Hz, both full vehicle model and reference estimator, underestimates the maximum peak reached with the measured signals (Figure 5.26, 5.27).

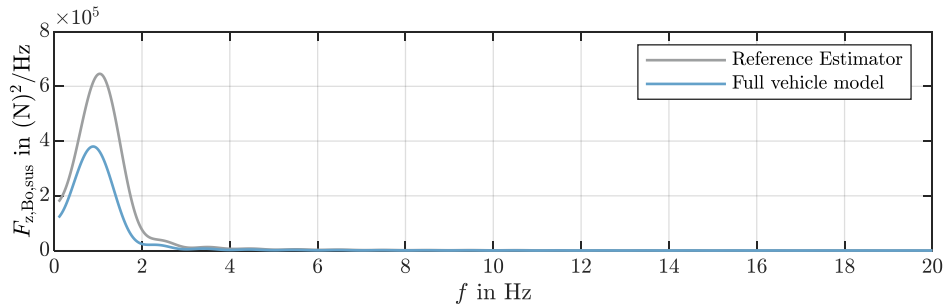
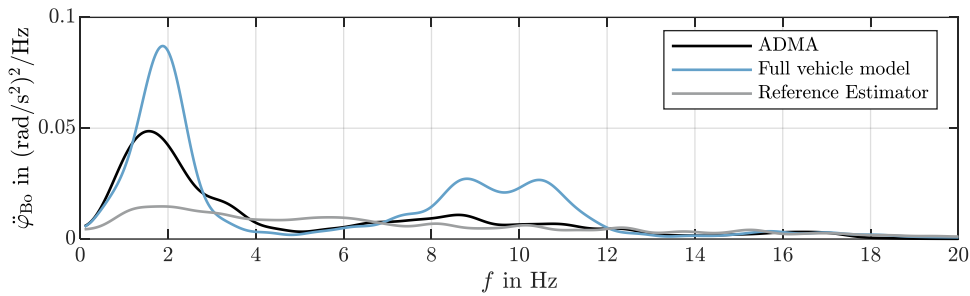
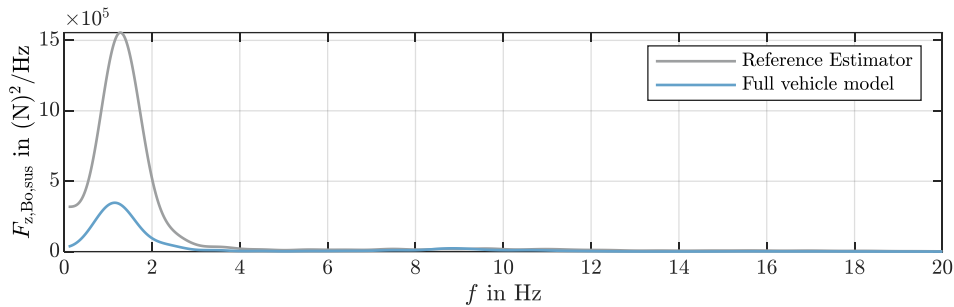
Figure 5.22: $\dot{\varphi}_{B_0}$, FnP, P controllerFigure 5.23: $\dot{\theta}_{B_0}$, FnP, P controllerFigure 5.24: $\dot{\varphi}_{B_0}$, FnP, P controller

Figure 5.25: $F_{\text{dyn,fr}}$, FnP, P controller

The same observations can be made for the pure R controller. Differences are found with the angular roll acceleration which displays at both body and wheels eigenfrequencies, an overestimation of its PSD with the full vehicle model with respect to the measurements (Figure 5.29).

Figure 5.26: $F_{\text{dyn,rl}}$, FnP, P controllerFigure 5.27: $F_{\text{dyn,rr}}$, FnP, P controller

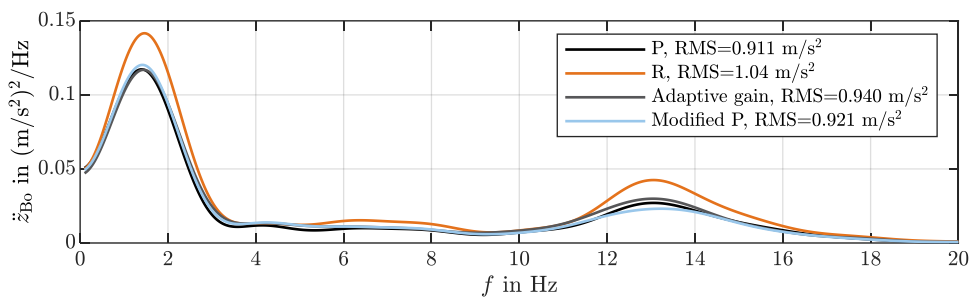
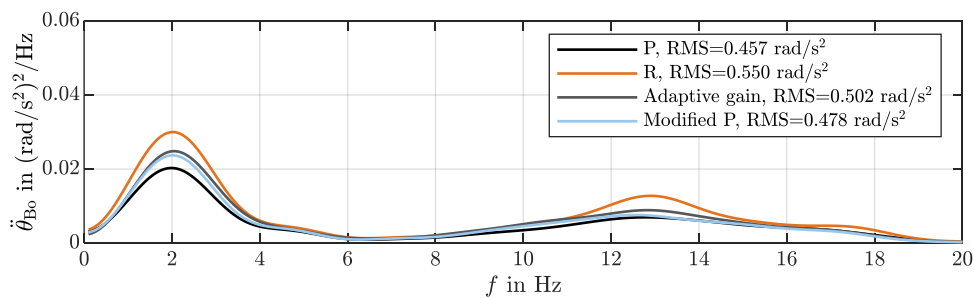
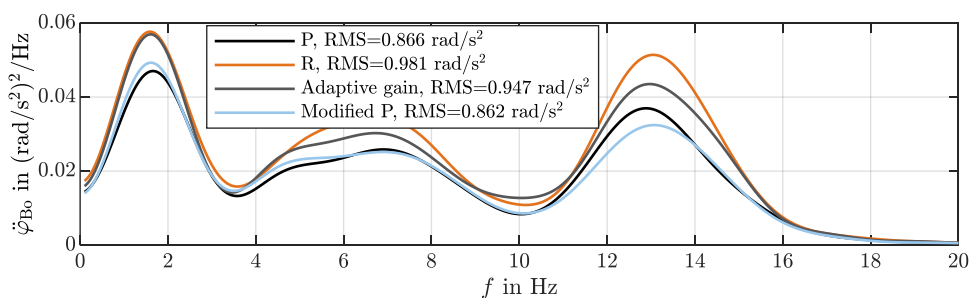
The desired suspension force from the control unit in the eigenmode of heave, respectively from P and R controllers, shows that with the latter, it is not null at the wheel eigenfrequency even if it is significantly smaller with respect to the PSD peak at lower frequencies (Figure 5.30). It is equal to zero for the pure P controller that as already stated, does not control the higher frequency range (Figure 5.28). When it comes to the desired suspension force in heave or moments in pitch, roll and twist, the “Reference Estimator” does not provide an actual estimation as these signals are directly computed in the controller block of the model, using the estimated kinematic signals.

Figure 5.28: $F_{z,Bo,sus}$, FnP, P controllerFigure 5.29: $\dot{\varphi}_{Bo}$, FnP, R controllerFigure 5.30: $F_{z,Bo,sus}$, FnP, R controller

5.5 Experimental results with modified P controller and coordination logic

In the previous sections, a comparison between the pure P and R controllers, as well as an analysis on a reference estimator, the sensor setup and the full vehicle model have been performed. From this preliminary considerations, further experimental tests have been made in order to evaluate the modified P controller and the coordination logic. In the following, measured signals are displayed, as the acceleration of the body in heave, as well as the derived angular roll and pitch accelerations according to Eq. (5.1). Dynamic wheel loads are also computed as described in Section 5.2. Both modified P controller and the coordination logic with its adaptive gain, are compared to pure P and R controllers which are used as reference. Controllers parametrization is shown in Appendix F. RMS values are obtained as described in Section 5.2. Firstly, results from test tracks AB and BA are shown. Both roads sections are driven by with constant speed of 80 km/h. Figure 31 shows the vertical acceleration of the body for test track AB. It displays a similar behaviour when activating the pure P, the modified P and the coordination logic from 0.1 to 10 Hz. At the wheel eigenfrequency, the modified P controller entails a reduction

in the PSD peak with respect to the pure P controller. The R controller displays the highest PSD in the whole frequency range. The lowest RMS value is obtained with the P controller followed by the modified P. The same is valid for the pitch angular acceleration of the body. The modified P and the coordination logic lie between the pure P and the pure R at the body eigenfrequency. At the wheel eigenfrequency, the modified P and the pure P display a comparable behaviour (Figure 5.32). The roll acceleration of the body, displays a similar behaviour for the coordination logic and the R controller from 0.1 to 4 Hz. From 4 Hz to 20 Hz, the coordination logic entails a lower PSD with respect to the R controller. The lowest PSD is obtained respectively with the pure P controller in the intervals of 0.1-2 Hz, 3.5-6 Hz and with the modified P controller in the complementary frequency ranges. The lowest RMS value is obtained with the modified P controller.

Figure 5.31: $\ddot{z}_{B_0, AB}$ Figure 5.32: $\ddot{\theta}_{B_0, AB}$ Figure 5.33: $\ddot{\phi}_{B_0, AB}$

When it comes to dynamic wheel loads, both the adaptive gain and the modified P controller manage to lower the peak of the R controller at approximately 1 Hz. At the wheel eigenfrequency, the lowest PSD is reached with any of the controllers except for the pure P, but there is a shift in the wheel eigenfrequency value. The lowest RMS values is reached with the modified P controller (Figure 5.34).

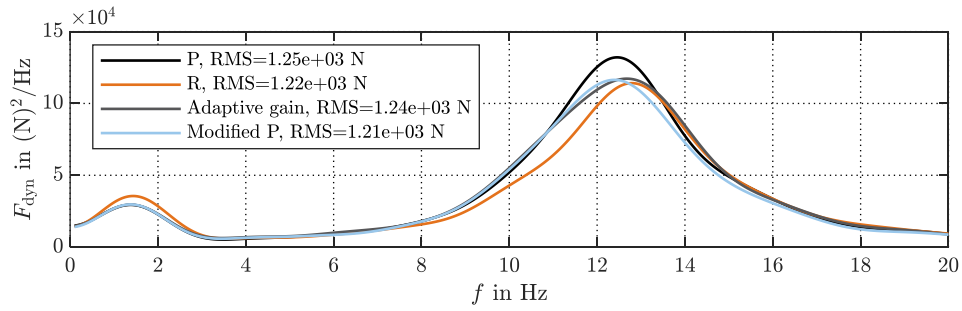


Figure 5.34: F_{dyn} , AB

Figure 5.35 shows the adaptive gain behaviour in the time domain. The coordination detects changes in the driving conditions, weighting the two controllers differently during the test measurements.

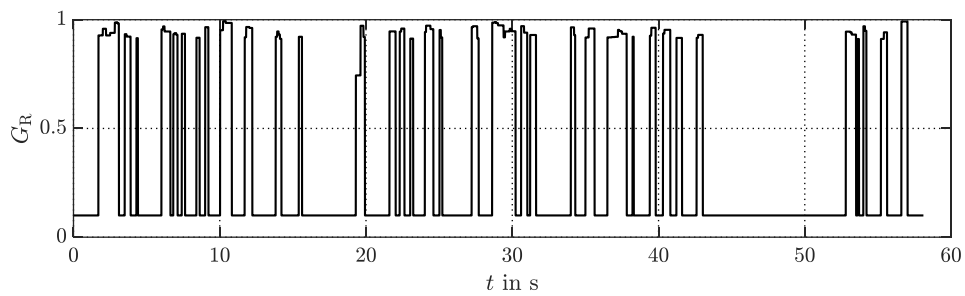


Figure 5.35: G_R , AB

Similar observations can be made for test track BA, for both vertical and pitch accelerations (Figure 5.36, 5.37).

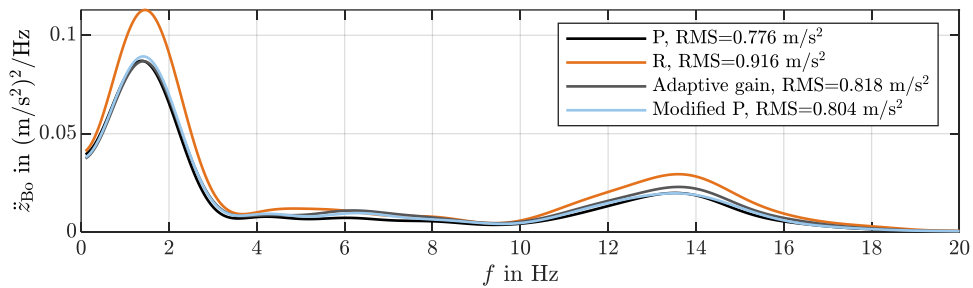


Figure 5.36: \ddot{z}_{B_0} , BA

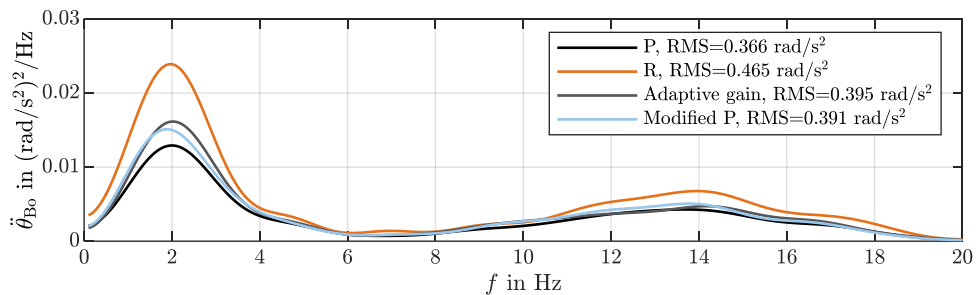
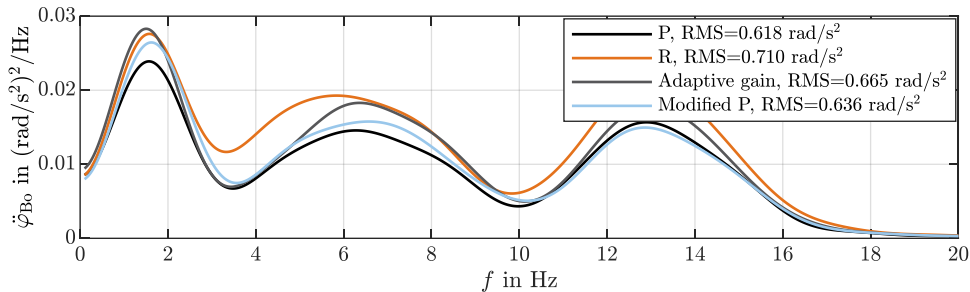
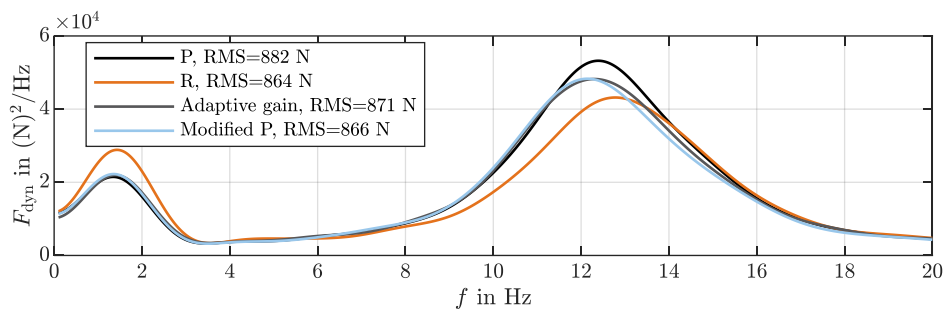
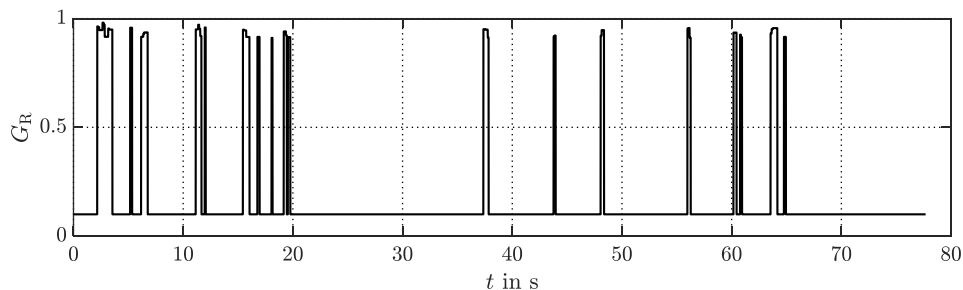


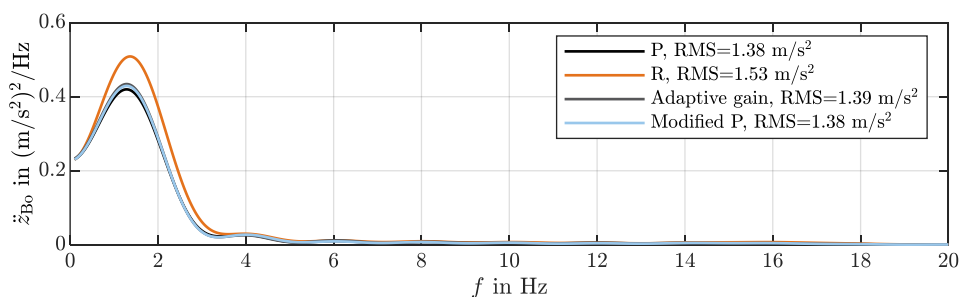
Figure 5.37: $\ddot{\theta}_{B_0}$, BA

The lowest RMS for roll acceleration is obtained with the pure P controller (Figure 5.38). When it comes to dynamic wheel loads, both the modified P controller and the coordination logic display

a dynamic behaviour which lies between the pure R and pure P and the lowest RMS values are reached with the R controller and the modified P (Figure 5.39). Figure 5.40 shows the adaptive gain trend, which, compared to the AB section, tends to privilege the usage of the P controller. This is due to higher dynamic wheel loads in the AB test track.

Figure 5.38: $\dot{\varphi}_{Bo}$, BAFigure 5.39: F_{dyn} , BAFigure 5.40: G_R , BA

Test track FnP is driven by with constant speed of 100 km/h. Vertical acceleration of the body displays a similar behaviour with all controllers except for the R, which presents the highest RMS value. The lowest RMS is reached with the modified P controller and the pure P (Figure 5.41).

Figure 5.41: \ddot{z}_{Bo} , FnP

The lowest RMS is obtained with the coordination logic for both pitch and roll body accelerations (Figure 5.42, 5.43). The latter shows, at the body eigenfrequency, the major differences between the controller, and the PSD maximum is progressively lowered when switching from the R controller, to the modified P, the adaptive gain and the P controller. The coordination logic entails the most comfortable behaviour in the frequency range between 4 Hz and 8 Hz (Figure 5.43). Figure 5.44 shows the behaviour of dynamic wheel loads. For this particular test track, as already observed, the low frequency solicitations are prevalent and this entails a lower PSD for the P controller at the body eigenfrequency. The highest frequency content is recognised by the coordination logic that weighs the R controller until the 90% of the overall controlling force in specific sections of the road (Figure 5.45). This results in the lowest RMS for dynamic wheel loads (Figure 5.44).

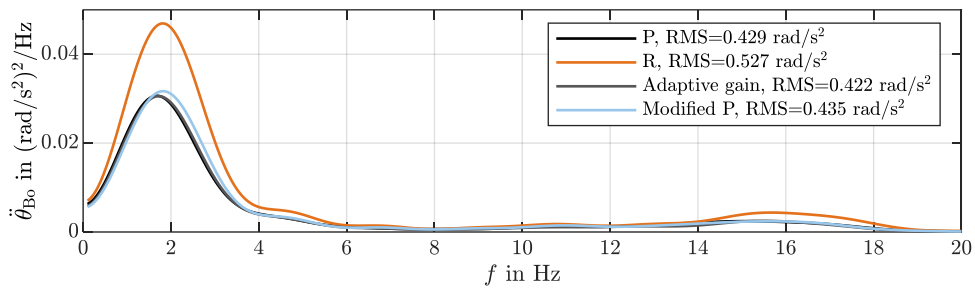


Figure 5.42: $\ddot{\theta}_{Bo}$, FnP

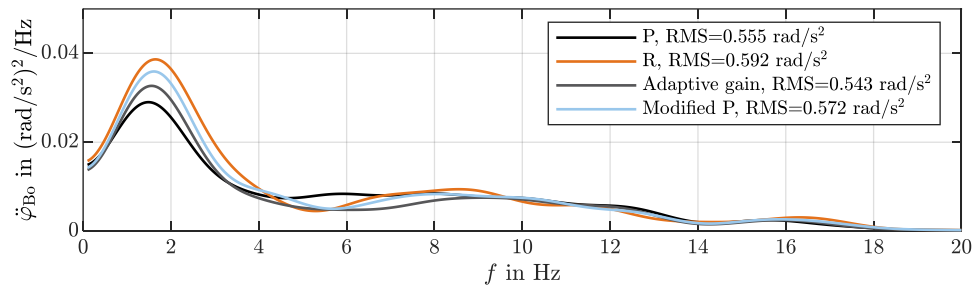


Figure 5.43: $\ddot{\phi}_{Bo}$, FnP

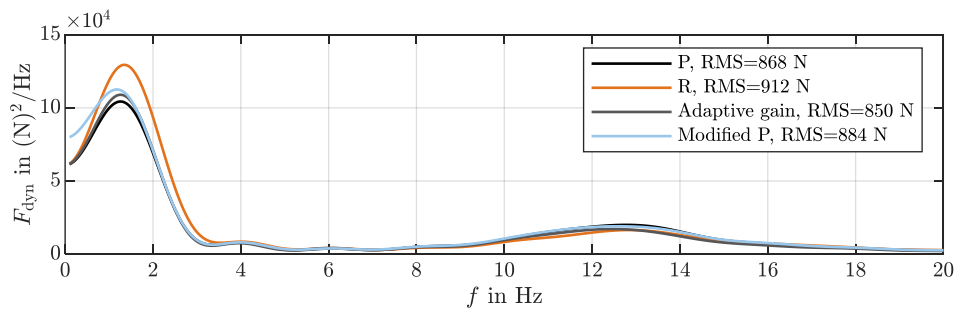


Figure 5.44: F_{dyn} , FnP

Tests have been conducted on track CD which is driven by with constant speed of 70 km/h. It is an A roughness road with only three sections displaying an higher roughness class. These can be perceived by the vehicle occupants during the tests phases and they are recognized by the coordination logic (Figure 5.50). The modified P controller shows the lowest PSD for the vertical acceleration of the body in the whole frequency range considered, followed by the P controller, the adaptive gain, and the more uncomfortable R controller (Figure 5.46).

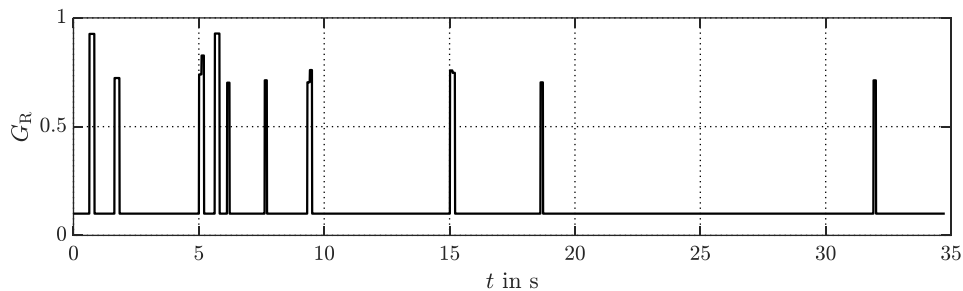


Figure 5.45: G_R , FnP

For pitch angular acceleration, at the body eigenfrequency, the lowest PSD is obtained with the P controller. On the contrary, at the wheel eigenfrequency, the modified P controller shows the lowest values (Figure 5.47). When it comes to roll acceleration, the minimum RMS value is obtained with the pure P controller, followed by the coordination logic. The latter shows a similar behaviour to the pure P controller at the wheel eigenfrequency and to the R controller between 3 and 8 Hz. The highest PSD at 13 Hz is reached with the modified P controller.

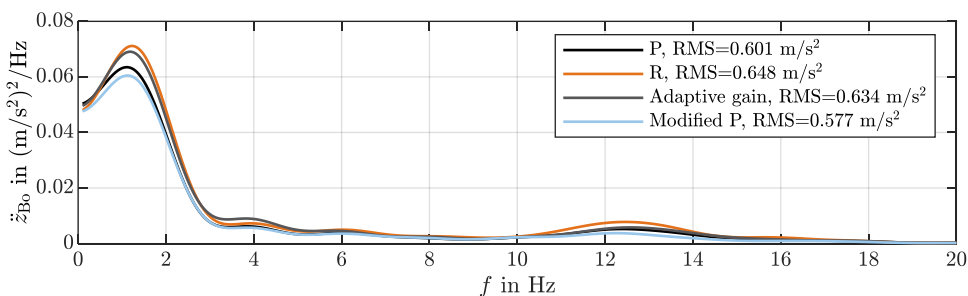


Figure 5.46: \ddot{z}_{B_0} , CD

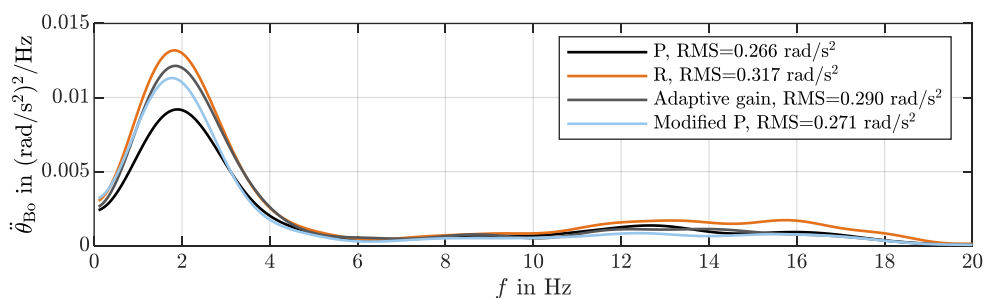


Figure 5.47: $\ddot{\theta}_{B_0}$, CD

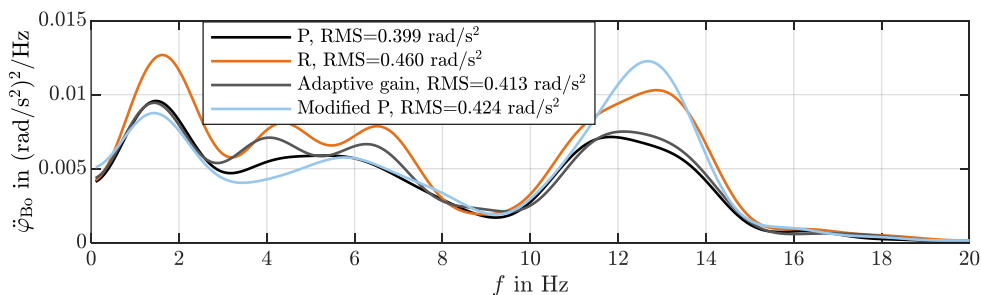


Figure 5.48: $\ddot{\phi}_{B_0}$, CD

The lowest PSD for dynamic wheel loads is reached with the coordination logic at the wheel eigenfrequency and at the body eigenfrequency, with the modified P controller. The latter shows

the highest PSD between the controllers from 6 to 15 Hz, as well as the highest RMS value. The lowest RMS is reached with the coordination logic.

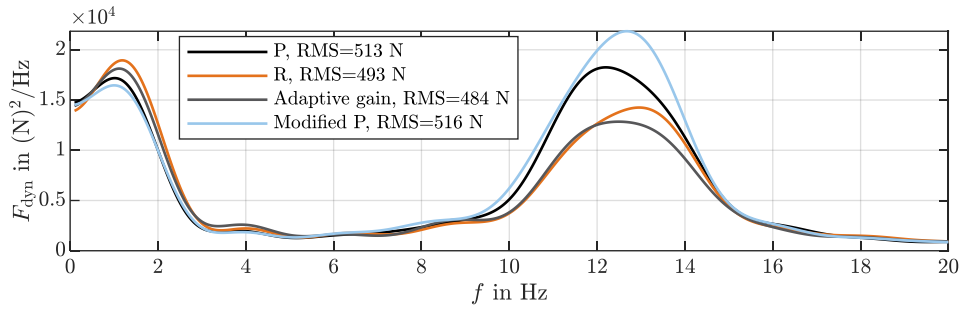


Figure 5.49: $F_{\text{dyn, CD}}$

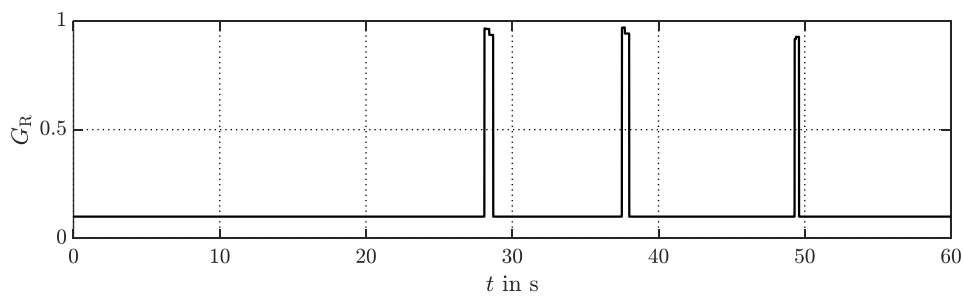


Figure 5.50: G_R, CD

5.6 Sensitivity analysis on modified P controller

An analysis on the parameter α_i , with $i \in \{h, p, r, t\}$, is conducted. The chosen test tracks are the FnP and section CD. For each controller configuration, two measurements are made on the same track (Appendix I). The set of optimised parameters for the modified P controller is taken as a reference (Appendix F, Table F.4, F.5). These α_i and $K_{p,\alpha}$ values have been obtained with an optimization procedure using the MnF profile as a simulated input to the full vehicle model. In these tests, the parameter $K_{p,\alpha}$ is not changed. According to Eq. (4.30), when $\alpha_i = 0$, the pure P controller is obtained with its skyhook logic extended to the vehicle modes. In this analysis, with respect to the optimal values, for each test, only one α_i value is changed. This is done because the vehicle modes are not completely decoupled and a change in some parameters for one body mode can affect the others. This is due, for example, to the different spring stiffnesses for the front and rear axles, to the position of the centre of gravity which is not in the exact middle of the wheelbase or to the loads distribution in the vehicle, due to its occupants. The set of values, chosen for this analysis are:

- $\alpha_h = [0.1, 0.5, 0.7, 0.9]$
- $\alpha_p = [0.3, 0.5, 0.7, 0.9]$
- $\alpha_r = [0.1, 0.3, 0.5, 0.7, 0.9]$
- $\alpha_t = [0.1, 0.5, 0.7, 0.9]$

The reason for the differences in the chosen values for the four modes, depends on their optimal values. For example, α_t is equal to 0.3 according to the optimization and therefore this value,

has already been tested previously. Each body mode is tested with 4 different α values except for the body mode of roll, which is analysed with 5, as its optimised version was found to be $\alpha_r = 0$, which corresponds to pure skyhook in the vehicle rolling.

Results for this analysis are shown in the following. The RMS of the accelerations of the body for the modes of heave, pitch and roll, as well as of dynamic wheel loads are displayed. The available experimental values have been interpolated with linear segments to provide an easier graphic interpretation. The dashed orange line represents, for each plot, the RMS of the variable in analysis, with optimal α_i . The region below this line represents a possible improvement of the optimal solution. This needs to be compared with the RMS of the other signals. The RMS of the measured signals, derived as described in Section 5.2, is a representative value of their level of vibration and therefore it must be minimized for both accelerations and dynamic wheel loads.

Figure 5.51, 5.52, 5.53 and 5.54 show the results for the FnP test track. From the analysis of the RMS of the acceleration of the body in heave, it can be observed that the lowest RMS can be reached by using $\alpha_h = 0.1$ (Figure 5.51). This choice would entail a decrease of the RMS of the acceleration for both pitch and roll (Figure 5.52, 5.53). It would also provide the lowest RMS for the dynamic wheel load of 839 N with respect to 884 N of the optimal configuration. This can be explained as the FnP mainly solicitates the low frequency ranges, where the body eigenfrequency is located and therefore, lowering α_h from the optimal value of 0.3786 to 0.1, would mean weighting less the suspensions velocities and getting closer to a pure P controller configuration for the heave mode. The value $\alpha_r = 0.5$ would lower the RMS for the accelerations in heave and pitch and of the dynamic wheel load, but would cause an increase of the RMS of the roll acceleration. The same happens for other combinations.

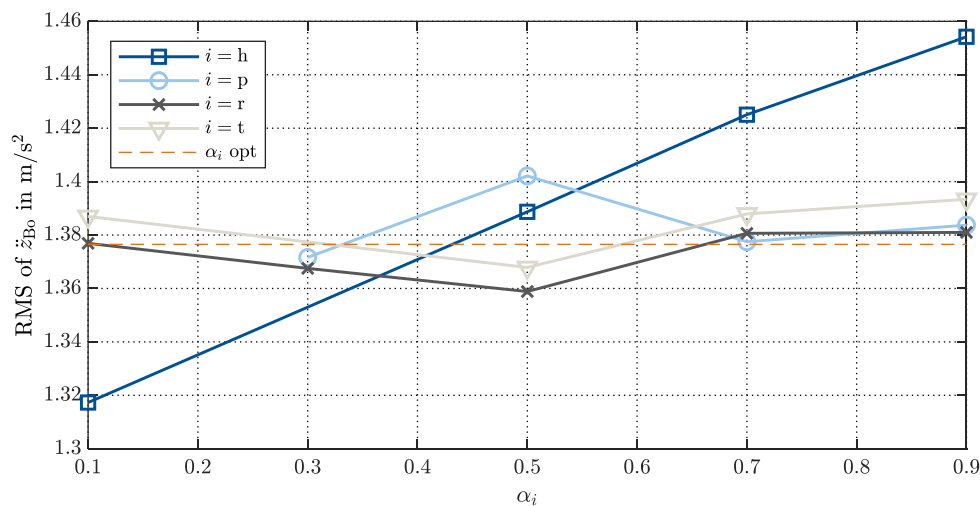


Figure 5.51: RMS of \ddot{z}_{B_0} , FnP

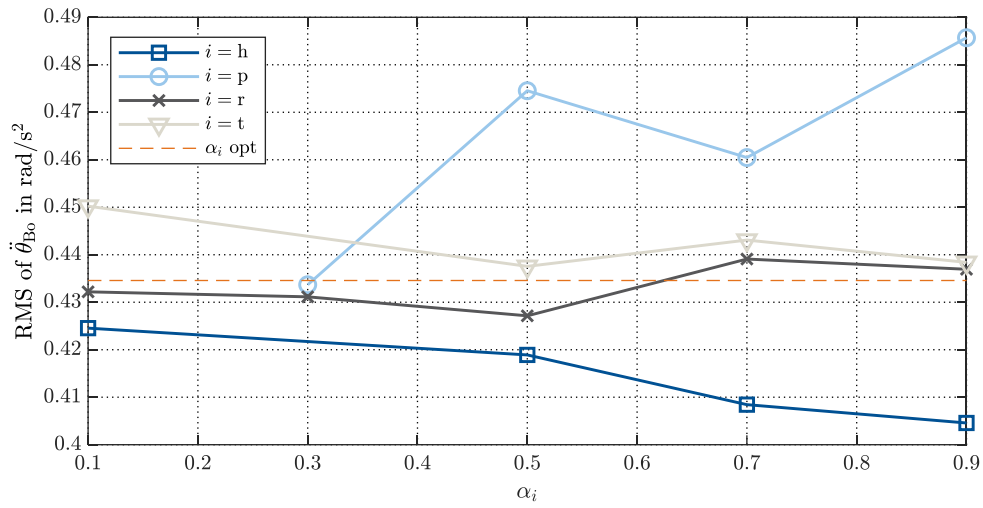


Figure 5.52: RMS of $\ddot{\theta}_{B_0}$, FnP

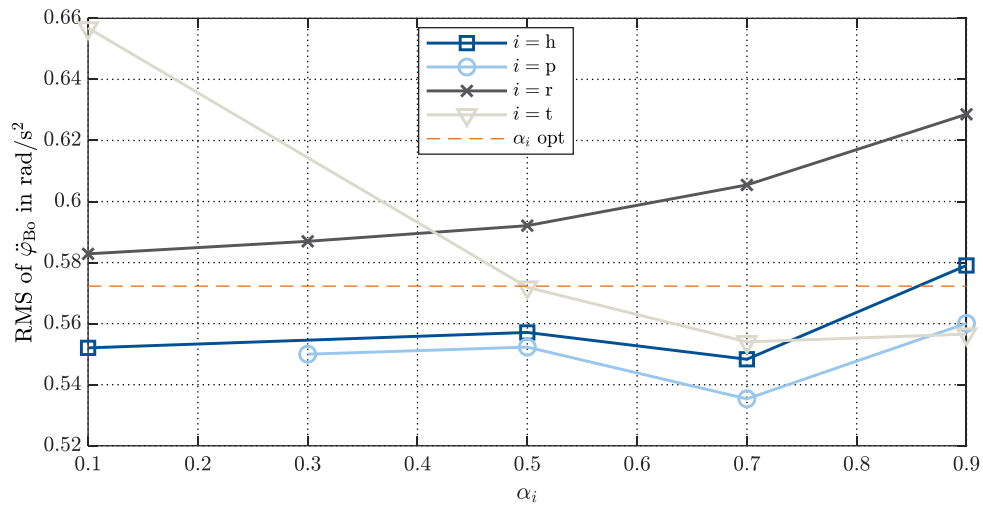


Figure 5.53: RMS of $\ddot{\varphi}_{B_0}$, FnP

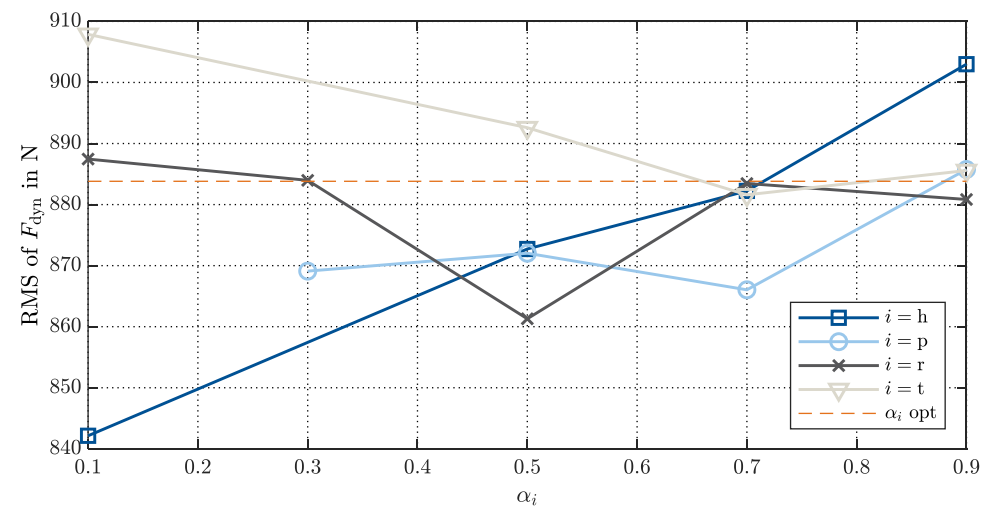


Figure 5.54: RMS of F_{dyn} , FnP

The analysis conducted on the path CD, show different results. For both the accelerations of the body in heave and pitch, there is no convenience in changing α_i (Figure 5.55, 5.56). This effect is especially relevant in the first case, since the optimal RMS is equal to 0.577 m/s² with respect to the other configurations where it lies between 0.609 and 0.640 m/s² (Figure 5.56). The RMS of the angular acceleration of roll, could be improved from the optimal 0.424 rad/s² to a minimum of 0.398 rad/s², with $\alpha_p = 0.7$ (Figure 5.57). The latter would increase the RMS of \ddot{z}_{B_0} to 0.634 m/s² and of $\ddot{\theta}_{B_0}$ to 0.295 rad/s² from 0.271 rad/s². At the same time, it would lower the RMS of the dynamic wheel loads from 516 N to 493 N (Figure 5.58). The lowest one is reached with $\alpha_r = 0.9$ and it is equal to 471 N but this choice would increase the RMS of all three accelerations signals.

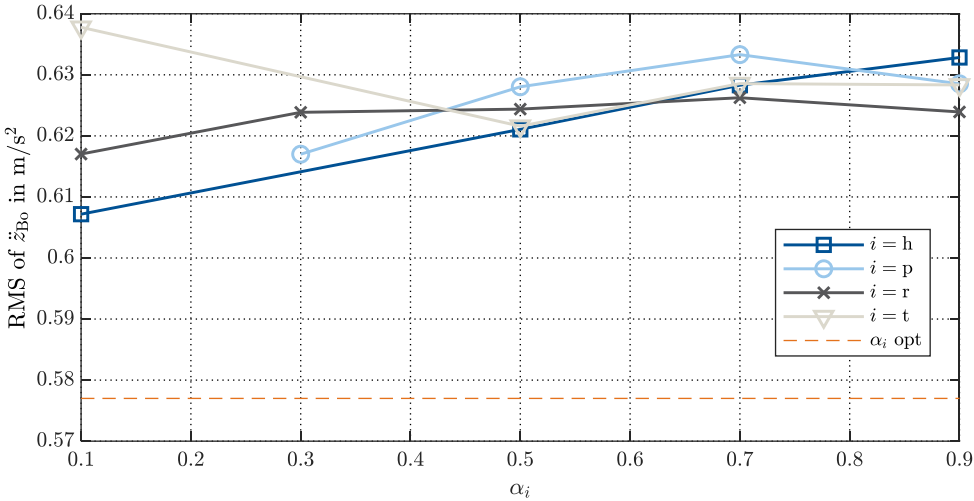


Figure 5.55: RMS of \ddot{z}_{B_0} , CD

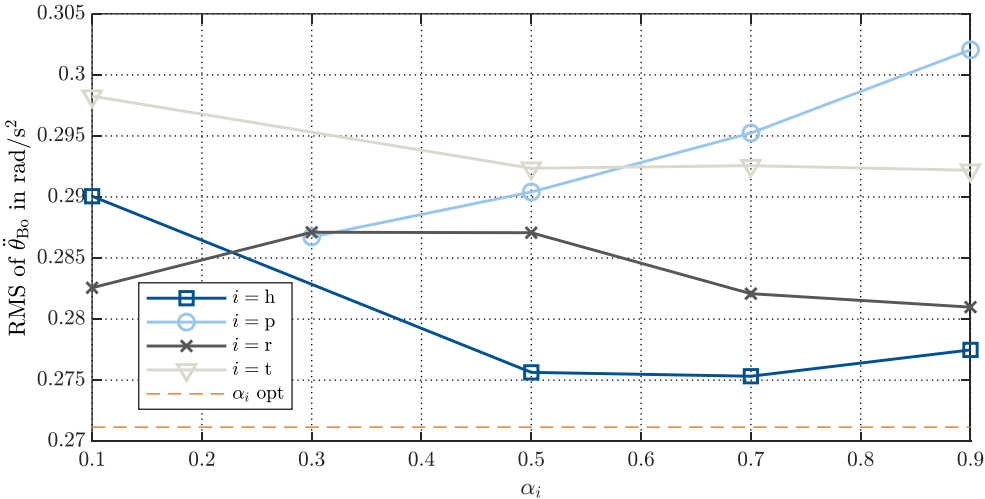


Figure 5.56: RMS of $\ddot{\theta}_{B_0}$, CD

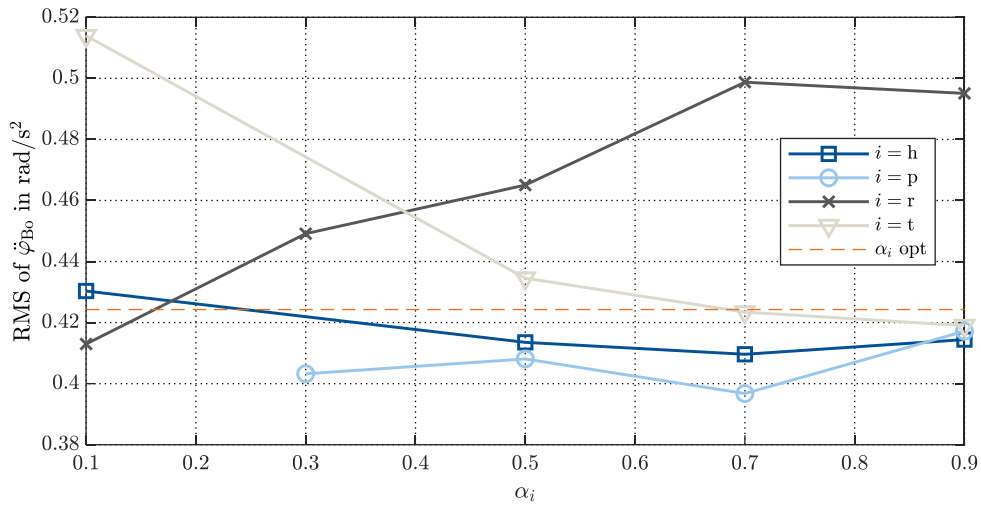


Figure 5.57: RMS of $\ddot{\varphi}_{B0}$, CD

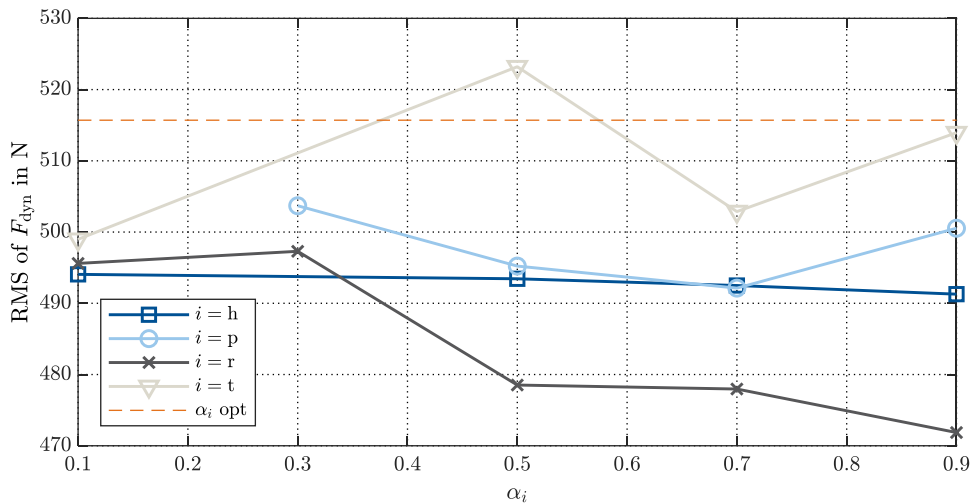


Figure 5.58: RMS of F_{dyn} , CD

5.7 Coordination logic at different speeds

An analysis on the coordination logic is conducted by driving at different constant vehicle speeds on the same road sections. Test tracks AB and BA are selected for this analysis and driven by at 20, 40, 60, 80 and 100 km/h. In the following, the synthetic a_{ISO} value is shown for each velocity and road section (Table 5.4). The behaviour of the resulting adaptive gain is also displayed (Figure 5.59, 5.60). From the tests results and subsequent post-processing to calculate a_{ISO} , it can be observed that, increasing the vehicle speeds results in a less comfortable perception from the vehicle occupants. Furthermore, section BA is more comfortable than section AB. Both test tracks can be categorized between classes B and C, according to [36]. The same observations can be made analysing Figure 5.59 and Figure 5.60. For every vehicle speed, section BA displays a lower mean value for the adaptive gain. This is a consequence of higher dynamic wheel loads for section AB where the coordination logic acts to weight more the R controller. Despite the quality of the roads, lowering the vehicle speed leads to a more comfortable feeling for the passengers and to lower loads on the wheels. Consequently the adaptive gain G_R

approaches to lower values. Section AB present a higher number of shifts of the adaptive gain towards the R controller as a consequence of a worse road roughness (Figure 5.59).

Table 5.4: a_{ISO} in m/s^2 for AB and BA

	20 km/h	40 km/h	60 km/h	80 km/h	100 km/h
AB	0.337	0.547	0.755	0.953	1.11
BA	0.276	0.444	0.627	0.796	0.895

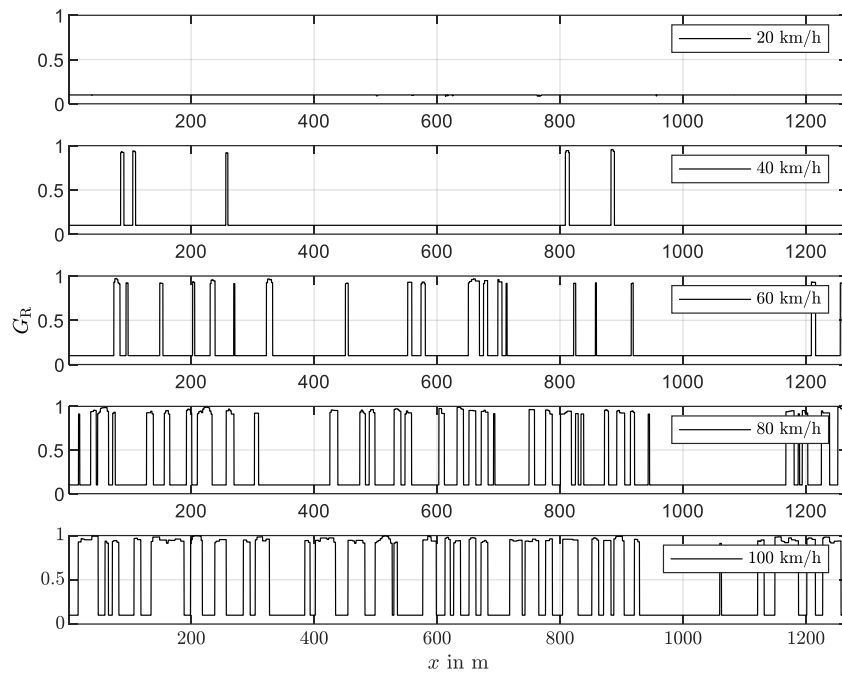


Figure 5.59: G_R at different speeds, AB

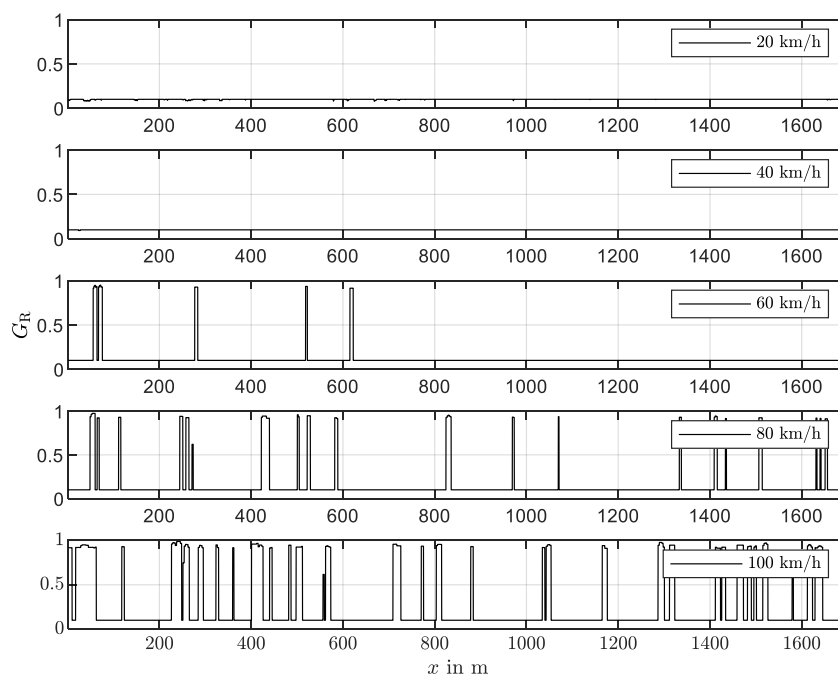


Figure 5.60: G_R at different speeds, BA

6 Discussion

In the following, a discussion of the results is presented. Reference to the initial aim of the work is made (Section 1.1). At the beginning of the experimental phase of this work, attention was put on the validation of the sensors equipment. ADMA and accelerometers measurements were compared with the estimated signals from a reference estimator, since the input signals to the controller block would have been the estimated ones. A general overestimation of the kinematic signals can be observed, with exception for the roll mode, which displays a significantly different behaviour with respect to the measured one. Dynamic wheel loads have been compared as well, showing an overall similar trend in the frequency domain. The experimental tests conducted in the test vehicle were performed at first, to verify the behaviour of the pure P and R controllers in real life scenarios. Results confirmed the expectations on the two controllers: the pure P controller, with respect to the R, entails lower accelerations of the body since it is derived from the skyhook principle, but higher peaks at the wheel eigenfrequency in the dynamic wheel loads. In test tracks as the FnP, where the low frequency range is the one presenting the worst dynamic behaviour, the two controllers act similarly at the wheel eigenfrequency. A comparison with the full vehicle model was also performed showing that the latter generally underestimates the state space variables. Its limited accuracy with respect to real life tests depends on the simplifying hypothesis including the one of linearity. Additionally, semi-active suspensions properties are considered via lookup tables but the modelling of the actuators and the servo-valves with their dynamic properties is neglected. It is anyway an useful mean, especially in a preliminary developing phase, because it allows to perform Model in the Loop tests and to iteratively improve the logic according to simulation results.

When it comes to tests with the modified P controller, the latter generally shows an improved dynamic behaviour with respect to the R controller in the body accelerations. For what concerns dynamic wheel loads, it displays a better behaviour in the low frequency range with respect to the R controller and in the high frequency range compared to the pure P controller. Exceptions to this behaviour are found with the CD track, where the modified P controller shows, for roll acceleration in the frequency range from 0.1 to 9 Hz, the lowest PSD and in the range from 9 to 20 Hz, the worst dynamic behaviour. This can be solved by increasing α_r from 0, which corresponds to pure skyhook control, to 0.1 (Figure 5.57). The same happens with the dynamic wheel load, where the dynamic behaviour with the modified P controller becomes the worst between the controllers at the wheel eigenfrequency, with a PSD peak which is almost two times to lowest ones. The sensitivity analysis showed that there is a great potential in lowering the RMS of the dynamic wheel load on the CD path. This can be achieved by increasing α_r to the highest possible value. An optimal compromise, not to affect significantly the other signals, is $\alpha_r = 0.1$ that would lower as well, the roll angular acceleration. The overall promising behaviour of the modified P controller was already observed in the simulations results (Section 4.7), even though the influence of the controllers in both angular pitch acceleration and at the body eigenfrequency in

vertical acceleration is not comparable to the experimental one, since in simulations, there is no appreciable difference between the controllers in these two cases.

For what concerns the coordination logic, initial expectations were that it would have represented a compromise between the pure P and the pure R controllers, in order to solve the conflict between ride comfort and road-holding. According to experimental tests, this goal has been achieved. The dynamic behaviour of the signals of interest generally lies between the pure P and the pure R controllers. Exception to this, is found in the BA path in the roll angular acceleration at the body eigenfrequency, where the coordination logic overcomes the R controller's peak. This can be solved via a different parametrization for the single controllers. On the other hand, in the CD path, it shows the best dynamic behaviour at the wheel eigenfrequency.

Results for the adaptive gain with the stochastic input of FnP in the simulation model (Figure 4.35), showed a significantly different behaviour with respect to experimental tests (Figure 5.45). In the first case, the P controller is weighed as a 90% of the overall controlling force while in second one, the coordination logic detects some bumps, weighing more the R controller. This is due to an underestimation of dynamic wheel loads in simulation with respect to real life scenarios. A significant result accomplished with the coordination logic is the gain behaviour with respect to the vehicle speed (Figure 5.59, 5.60). The gain manages to adapt itself to the velocity of the vehicle. At 20 km/h the more comfortable P controller is mainly used. With an increase in the vehicle speed, the gain progressively detects bumps until 100 km/h, where the R controller is the most present in the overall control force. This results in a controller that changes with the speed, without the latter being an input to the control law.

A weakness of the developed method, is a delay in the coordination logic and namely in the estimation of the adaptive gain. This depends on the number of samples stored for the online estimation of the variables as well as on the sample rate. At the same time, it does not affect the stability of the system since it does not introduce any delay in the control forces but only in the coordination. Furthermore, the developed logic has not been tested with speeds higher than 100 km/h and the influence of lateral and longitudinal dynamics has not been considered. In order to limit the memory allocation on the ECU, adjustments were made in the reimplementing of the logic in the company environment. Considering the limited amount of time available to perform experimental tests, fixed values for the thresholds in the coordination logic were chosen. Further details on this and on the stability of the system are given in Appendix J and Appendix K.

A positive aspect of this work, is the possibility of direct tuning of the body characteristics in the different modes, thanks to an overall modal approach. In order to limit dynamic wheel loads, a groundhook approach could have been considered rather than the R controller. This choice though, would have led to the implementation of the groundhook principle at the four vehicle corners and not at the body modes, resulting in a less immediate tuning of the parameters as it can be done with the logic developed in this work.

In order to perform additional analysis and considerations with the objective of further improving the vertical dynamics controller, additional time should have been spent in this work. Nevertheless, the initial aim of enhancing an existing controller in order to reduce the conflict between ride comfort and road-holding, has been achieved.

7 Summary and Outlook

The aim of this work was the improvement of an existing vertical vehicle dynamics controller in order to solve the conflict between ride comfort and road-holding. Initial simulations have been made and limits to the existing logic were identified. According to these, a research on the state of the art has been performed with a focus on the strategies to combine different controllers, on adaptive control systems as well as on suspensions oriented skyhook control. Criticism of the state of the art was carried out, leading to the scientific news value of this work. Its novelty is represented by two different approaches to control vertical vehicle dynamics: a coordination logic in terms of an adaptive gain, combining criteria for ride comfort, road-holding and suspension deflection and an extended skyhook control, with additional consideration of the suspensions velocities. Both approaches were tested at the beginning, with measured road displacements and were progressively and recursively improved with artificially generated inputs. Results have been evaluated in terms of perceived vehicle occupants comfort as well as in terms of resulting dynamic wheel loads. The developed logic was later implemented in the industrial partner development environment. Thanks to adjustments to the logic, experimental tests have been performed with an adequate post-processing of the measurements. Results have been showed and discussed, underlining both the limits and the potential of the logic.

Future research work can be developed. For what concerns the adaptive gain, at first, sensitivity analysis in the real vehicle should be performed by changing the coordination logic thresholds as it has been done in simulations. Further attention should be put in the parametrization of the pure P and R controllers since the set of optimal values was obtained having performed an optimization procedure in the simulation environment but real tests outcome has not been sufficiently tested. Furthermore, an analysis on the influence of the stiffness parameter in the R controller in terms of desired undamped body eigenfrequency should be carried out, since the focus has been on the damping term. The role of the delay in the coordination logic should be further exploited. This could include the substitution of the online estimation blocks with an immediate comparison of the signal of interest with a physical threshold. An analytical description of the stability of the coordination logic should also be considered.

A further development of the modified P controller could be made. This can include a logic to continuously change the α_i values in order to combine ride comfort and road-holding. This approach could entail an adaptive solution for the proportional damping rates as well. The overall controller should be tested at higher speeds, and it could be also modified taking into account aspects of the longitudinal and lateral dynamics, as well as some inputs from the driver.

List of figures

Figure 1.1:	Structure of the work	3
Figure 2.1:	Transfer function for vehicle passive configuration.....	8
Figure 2.2:	Transfer function for vehicle passive configuration with different damping rates	8
Figure 2.3:	Full vehicle model.....	9
Figure 2.4:	Vertical dynamics controller.....	20
Figure 2.5:	Skyhook principle on quarter car suspension.....	21
Figure 2.6:	State feedback controller.....	22
Figure 2.7:	Extended Skyhook controller with twist mode	24
Figure 2.8:	R controller	25
Figure 3.1:	Quarter car model with suspension oriented Skyhook controller	29
Figure 4.1:	Simulation model.....	34
Figure 4.2:	MnF, 100 km/h, Bandpass-filter 0.1-25 Hz.....	345
Figure 4.3:	FnP, 100 km/h, Bandpass-filter 0.1-25 Hz.....	345
Figure 4.4:	Single Obstacle, 30 km/h.....	346
Figure 4.5:	A-C-A-C profile, 100 km/h	346
Figure 4.6:	C profile, 80 km/h	347
Figure 4.7:	Garage, 20 km/h.....	347
Figure 4.8:	Garage, 20 km/h, \ddot{z}_{B0} with P and R controller	347
Figure 4.9:	Garage, 20 km/h, \ddot{z}_{B0} with P and R controller and a constraint in the suspension travel	38
Figure 4.10:	Quarter car model of semi-active suspensions	39
Figure 4.11:	Kalman filters overview.....	40
Figure 4.12:	Untuned Kalman filter simulation.....	41
Figure 4.13:	Tuned Kalman filter simulation	41
Figure 4.14:	Adaptive gain logic	43
Figure 4.15:	Switching condition.....	43
Figure 4.16:	$PS_{\ddot{z}_{B0},ISO,0-5\text{ Hz}}$	44

Figure 4.17:	Power spectrum online estimation at a certain time step	45
Figure 4.18:	G_{PS}	45
Figure 4.19:	Lookup table for G_{PS}	46
Figure 4.20:	x for A-C-A-C profile	46
Figure 4.21:	x for C-A-C-A profile	46
Figure 4.22:	$G_{Fdyn,max}$	47
Figure 4.23:	$G_{Fdyn,i,j}$	47
Figure 4.24:	$F_{dyn,check}$	48
Figure 4.25:	$G_{Fdyn,i,j}$	48
Figure 4.26:	G_R for garage simulation without $G_{sus,def}$	49
Figure 4.27:	G_R for garage simulation with $G_{sus,def}$	49
Figure 4.28:	$\widetilde{\Delta z}_{sus,i,j}$	49
Figure 4.29:	$G_{sus,def}$	50
Figure 4.30:	$G_{sus,def}$ logic	50
Figure 4.31:	$G_{sus,def}$	50
Figure 4.32:	G_R without gain correction	52
Figure 4.33:	G_R for A-C-A-C profile, 100 km/h	53
Figure 4.34:	G_R for MnF, 100 km/h	53
Figure 4.35:	G_R for FnP profile, 100 km/h	53
Figure 4.36:	G_R for C profile, 80 km/h	53
Figure 4.37:	G_R for single obstacle, 100 km/h	54
Figure 4.38:	MnF, \ddot{z}_{Bo} , 100 km/h	54
Figure 4.39:	FnP, \ddot{z}_{Bo} , 100 km/h	55
Figure 4.40:	A-C-A-C, \ddot{z}_{Bo} , 100 km/h	55
Figure 4.41:	MnF, $\ddot{\theta}_{Bo}$, 100 km/h	56
Figure 4.42:	FnP, $\ddot{\theta}_{Bo}$, 100 km/h	56
Figure 4.43:	A-C-A-C, $\ddot{\theta}_{Bo}$, 100 km/h	56
Figure 4.44:	MnF, $\ddot{\phi}_{Bo}$, 100 km/h	57
Figure 4.45:	FnP, $\ddot{\phi}_{Bo}$, 100 km/h	57
Figure 4.46:	A-C-A-C, $\ddot{\phi}_{Bo}$, 100 km/h	58
Figure 4.47:	MnF, F_{dyn} , 100 km/h	59
Figure 4.48:	FnP, F_{dyn} , 100 km/h	59

Figure 4.49:	A-C-A-C, F_{dyn} , 100 km/h	60
Figure 4.50:	A-C-A-C, from top: \ddot{z}_{Bo} , $\dot{\phi}_{\text{Bo}}$, F_{dyn} for semi-active suspensions, 100 km/h...	60
Figure 4.51:	A-C-A-C, from top: \ddot{z}_{Bo} , $\dot{\phi}_{\text{Bo}}$, F_{dyn} for active suspensions, 100 km/h.....	61
Figure 5.1:	\ddot{z}_{Bo} for R, $D_i = 0.05$	67
Figure 5.2:	$\ddot{\theta}_{\text{Bo}}$ for R, $D_i = 0.05$	68
Figure 5.3:	$\ddot{\phi}_{\text{Bo}}$ for R, $D_i = 0.05$	68
Figure 5.4:	$\dot{\theta}_{\text{Bo}}$ for R, $D_i = 0.05$	68
Figure 5.5:	$\dot{\phi}_{\text{Bo}}$ for R, $D_i = 0.05$	68
Figure 5.6:	$F_{\text{dyn,fr}}$ for R, $D_i = 0.05$	69
Figure 5.7:	$F_{\text{dyn,rl}}$ for R, $D_i = 0.05$	69
Figure 5.8:	$F_{\text{dyn,rr}}$ for R, $D_i = 0.05$	69
Figure 5.9:	$\ddot{z}_{\text{w,fr}}$	70
Figure 5.10:	\ddot{z}_{Bo}	70
Figure 5.11:	$F_{\text{dyn,fr}}$	70
Figure 5.12:	\ddot{z}_{Bo} , CD	71
Figure 5.13:	$\dot{\theta}_{\text{Bo}}$, CD.....	71
Figure 5.14:	$\dot{\phi}_{\text{Bo}}$, CD	71
Figure 5.15:	$F_{\text{dyn,rr}}$, CD	72
Figure 5.16:	\ddot{z}_{Bo} , FnP.....	72
Figure 5.17:	$\dot{\theta}_{\text{Bo}}$, FnP	72
Figure 5.18:	$\dot{\phi}_{\text{Bo}}$, FnP	72
Figure 5.19:	$F_{\text{dyn,rr}}$, FnP	73
Figure 5.20:	\ddot{z}_{Bo} , FnP, P controller.....	73
Figure 5.21:	$\ddot{\theta}_{\text{Bo}}$, FnP, P controller	73
Figure 5.22:	$\ddot{\phi}_{\text{Bo}}$, FnP, P controller	74
Figure 5.23:	$\dot{\theta}_{\text{Bo}}$, FnP, P controller	74
Figure 5.24:	$\dot{\phi}_{\text{Bo}}$, FnP, P controller	74
Figure 5.25:	$F_{\text{dyn,fr}}$, FnP, P controller	75
Figure 5.26:	$F_{\text{dyn,rl}}$, FnP, P controller	75
Figure 5.27:	$F_{\text{dyn,rr}}$, FnP, P controller	75
Figure 5.28:	$F_{z,\text{Bo},\text{sus}}$, FnP, P controller.....	76
Figure 5.29:	$\dot{\phi}_{\text{Bo}}$, FnP, R controller.....	76

List of figures

Figure 5.30:	$F_{z_{B0,sus}}$, FnP, R controller	76
Figure 5.31:	\ddot{z}_{B0} , AB	77
Figure 5.32:	$\ddot{\theta}_{B0}$, AB	77
Figure 5.33:	$\ddot{\phi}_{B0}$, AB.....	77
Figure 5.34:	F_{dyn} , AB.....	78
Figure 5.35:	G_R , AB.....	78
Figure 5.36:	\ddot{z}_{B0} , BA	78
Figure 5.37:	$\ddot{\theta}_{B0}$, BA	78
Figure 5.38:	$\ddot{\phi}_{B0}$, BA.....	79
Figure 5.39:	F_{dyn} , BA.....	79
Figure 5.40:	G_R , BA.....	79
Figure 5.41:	\ddot{z}_{B0} , FnP.....	79
Figure 5.42:	$\ddot{\theta}_{B0}$, FnP	80
Figure 5.43:	$\ddot{\phi}_{B0}$, FnP.....	80
Figure 5.44:	F_{dyn} , FnP	80
Figure 5.45:	G_R , FnP.....	81
Figure 5.46:	\ddot{z}_{B0} , CD	81
Figure 5.47:	$\ddot{\theta}_{B0}$, CD.....	81
Figure 5.48:	$\ddot{\phi}_{B0}$, CD	81
Figure 5.49:	F_{dyn} , CD	82
Figure 5.50:	G_R , CD	82
Figure 5.51:	RMS of \ddot{z}_{B0} , FnP.....	83
Figure 5.52:	RMS of $\ddot{\theta}_{B0}$, FnP.....	84
Figure 5.53:	RMS of $\ddot{\phi}_{B0}$, FnP	84
Figure 5.54:	RMS of F_{dyn} , FnP	84
Figure 5.55:	RMS of \ddot{z}_{B0} , CD	85
Figure 5.56:	RMS of $\ddot{\theta}_{B0}$, CD.....	85
Figure 5.57:	RMS of $\ddot{\phi}_{B0}$, CD	86
Figure 5.58:	RMS of F_{dyn} , CD.....	86
Figure 5.59:	G_R at different speeds, AB	87
Figure 5.60:	G_R at different speeds, BA	87
Figure B.1:	Quarter car model.....	xx

Figure D.1:	Scheme of the suspensions constraints model	xxii
Figure G.1:	Passive and Semi-Active suspensions	xxx
Figure G.2:	RMS of $\ddot{\theta}_{B0}$, CD	xxxii
Figure G.3:	$F_{u,fj}$	xxxii
Figure G.4:	$F_{u,rj}$	xxxii
Figure G.5:	Suspensions mounting	xxxiii
Figure G.6:	ZF CDC damper with external valve	xxxiii
Figure H.1:	ADMA reference frame	xxxv
Figure H.2:	BMW 7 series, G12	xxxv
Figure H.3:	ADMA	xxxv
Figure H.4:	FlexRay and IPETRONIK modules	xxxvi
Figure H.5:	Accelerometer's mounting	xxxvi
Figure H.6:	Overall sensors and electronic modules scheme	xxxvii
Figure I.1:	Raw signals	xxxviii
Figure I.2:	Processed signals in time with steps 1, 2 and 3	xxxviii
Figure I.3:	PSD of the signals, zoom on 0-5 Hz; step 4	xxxiv
Figure I.4:	Averaged and smoothed PSD of the signals, steps 5 and 6	xxxiv

List of tables

Table 2.1:	Suspension classification	6
Table 2.2:	Comfort perception	17
Table 4.1:	a_{ISO} in m/s^2 for MnF	58
Table 4.2;	a_{ISO} in m/s^2 for FnP	58
Table 4.3:	a_{ISO} in m/s^2 for A-C-A-C	58
Table 5.1:	Number of tests measurements in Aschheim.....	65
Table 5.2:	μ for section AB.....	65
Table 5.3:	c_v for section AB.....	66
Table 5.4:	a_{ISO} in m/s^2 for AB and BA	87
Table A.1:	Data sheet for the test vehicle	xvi
Table B.1:	Data test vehicle adapted to quarter car model.....	xviii
Table D.1:	Parameters for suspensions constraints model.....	xxiii
Table E.1:	Kalman Filter parameters	xxiv
Table E.2:	Test vehicle parametrization.....	xxvi
Table F.1:	Eigenfrequencies parametrization	xxviii
Table F.2:	Damping ratios D_i for R controller	xxviii
Table F.3:	K_P values for P controller in Ns/m	xxviii
Table F.4:	$K_{P,\alpha}$	xxix
Table F.5:	α_i values for P controller in Ns/m	xxix
Table I.1:	μ for section BA, Section 5.2	xxxix
Table I.2:	c_v for section BA, Section 5.2.....	xl
Table I.3:	Number of tests measurements in Freising/Pulling, Section 5.3	xl
Table I.4:	μ for section CD, Section 5.3.....	xl
Table I.5:	c_v for section CD, Section 5.3	xli
Table I.6:	μ for FnP, Section 5.3.....	xli
Table I.7:	c_v for FnP, Section 5.3.....	xli

List of tables

Table I.8:	Number of tests measurements in Aschheim, Section 5.4.....	xlii
Table I.9:	μ for section AB, Section 5.4	xlii
Table I.10:	c_v for section AB, Section 5.4.....	xlii
Table I.11:	μ for section BA, Section 5.4	xlii
Table I.12:	c_v for section BA, Section 5.4	xliii
Table I.13:	Number of tests measurements in Freising/Pulling, Section 5.4	xliii
Table I.14:	μ for section CD, Section 5.4.....	xliii
Table I.15:	c_v for section CD, Section 5.4	xliv
Table I.16:	μ for section FnP, Section 5.4	xliv
Table I.17:	c_v for section FnP, Section 5.4	xliv
Table I.18:	Number of tests measurements in Freising/Pulling, heave, Section 5.6	xliv
Table I.19:	Number of tests measurements in Freising/Pulling, pitch, Section 5.6.....	xliv
Table I.20:	Number of tests measurements in Freising/Pulling, roll, Section 5.6	xliv
Table I.21:	Number of tests measurements in Freising/Pulling, twist, Section 5.6.....	xliv
Table I.22:	μ for FnP, heave, Section 5.6.....	xliv
Table I.23:	c_v for FnP, heave, Section 5.6.....	xlvi
Table I.24:	μ for FnP, pitch, Section 5.6	xlvi
Table I.25:	c_v for FnP, pitch, Section 5.6.....	xlvi
Table I.26:	μ for FnP, roll, Section 5.6.....	xlvi
Table I.27:	c_v for FnP, roll, Section 5.6.....	xlvi
Table I.28:	μ for FnP, twist, Section 5.6.....	xlvi
Table I.29:	c_v for FnP, twist, Section 5.6	xlvi

References

- [1] SAE On-Road Automated Vehicle Standards Committee, "Definitions for terms related to on-road motor vehicle automated driving systems," *Society of Automotive Engineers (SAE): Troy, MI, USA*, no. 3016, pp. 1–16, 2014.
- [2] L. BalaMurugan and J. Jeyaraj, "An investigation on semi-active suspension damper and control strategies for vehicle ride comfort and road holding," *Proc. of the Institution of Mechanical Engineers, Part I: Journal of Systems and Control Engineering*, vol. 226, no. 8, pp. 1119–1129, 2012, doi: 10.1177/0959651812447520.
- [3] D. Karnopp, J. C. Michael, and R. Harwood, "Vibration control using semi-active force generators," *J. Eng. for Industry*, vol. 96, no. 2, pp. 619–626, 1974, doi: 10.1115/1.3438373.
- [4] M. Valášek and M. Novak, "Ground hook for semi-active damping of truck's suspension," *CTU Prague (Hg.) Proc. of CTU Workshop*, no. 96, pp. 467–468, 1996.
- [5] R. M. Yerge, P. D. Shendge, V. Paighan, and S. B. Phadke, "Design and implementation of a two objective active suspension using hybrid skyhook and groundhook strategy," *2017 2nd IEEE International Conference on Recent Trends in Electronics, Information & Communication Technology (RTEICT)*, pp. 968–972, 2017, doi: 10.1109/RTEICT.2017.8256742.
- [6] M. Valášek, M. Novak, Z. Šika, and O. Vaculin, "Extended GroundHook - New Concept of Semi-Active Control of Truck's Suspension," *Vehicle System Dynamics*, vol. 27, 5, 6, pp. 289–303, 1997.
- [7] S. Hegazy, H. Rahnejat, and K. Hussain, "Multi-body dynamics in full-vehicle handling analysis," *Proc. of the IMechE, Part K: Journal of Multi-body Dynamics*, vol. 213, no. 1, pp. 19–31, 1999, doi: 10.1243/1464419991544027.
- [8] P. Karle, "Entwurf und Analyse einer modalen Vertikaldynamikregelung für semiaktive und aktive Fahrwerke," M.S. thesis dissertation, Dept. Automot. Eng. TUM, Munich, 2019.
- [9] R. A. Williams, "Automotive active suspensions part 1: Basic principles," *Proceedings of the Institution of Mechanical Engineers, Part D: Journal of Automobile Engineering*, vol. 211, no. 6, pp. 415–426, 1997, doi: 10.1243/0954407971526551.
- [10] S. M. Savaresi, C. Poussot-Vassal, C. Spelta, O. Sename, and L. Dugard, *Semi-active suspension control design for vehicles*: Elsevier, 2010.
- [11] D. Fischer and R. Isermann, "Mechatronic semi-active and active vehicle suspensions," *Control engineering practice*, vol. 12, no. 11, pp. 1353–1367, 2004, doi: 10.1016/2003.08.003.
- [12] E. Galvagno, "Complementi di Meccanica del Veicolo ESERCITAZIONI: [PowerPoint slides]. Available: https://didattica.polito.it/pls/portal30/sviluppo.pagina_corso.main," 2019.

- [13] B. Jacobson, "Vehicle Dynamics Compendium for Course MMF062," *Chalmers University of Technology*, 2016.
- [14] T. Dahlberg, "Ride comfort and road holding of a 2-DOF vehicle travelling on a randomly profiled road," *Journal of Sound and Vibration*, vol. 58, no. 2, pp. 179–187, 1978, doi: 10.1016/S0022-460X(78)80073-X.
- [15] A. G. Thompson, "THE EFFECT OF TYRE DAMPING ON THE PERFORMANCE OF VIBRATION ABSORBERS IN AN ACTIVE SUSPENSION," *Journal of Sound and Vibration*, vol. 133, no. 3, pp. 457–465, 1989.
- [16] R. Penrose, "A generalized inverse for matrices," *Math. Proc. Camb. Phil. Soc.*, vol. 51, no. 3, pp. 406–413, 1955, doi: 10.1017/S0305004100030401.
- [17] O. Sename, "Modelling, analysis and control of linear systems using state space representations:[PowerPointslides].Available:http://gipsawwww.ampere.inpg.fr/~o.sename/docs/ME_uto.pdf," 2018.
- [18] E. Enders, G. Burkhard, F. Fent, M. Lienkamp, and D. Schramm, "Objectification methods for ride comfort," *Forsch Ingenieurwes*, vol. 83, no. 4, pp. 885–898, 2019, doi: 10.1007/s10010-019-00361-6.
- [19] ISO 2631-1., "2631-1: Mechanical vibration and shock-evaluation of human exposure to whole-body vibration-Part 1: General requirements," *Geneva, Switzerland: ISO*, 1997.
- [20] British Standards Institution, BS 6841, "Guide to measurement and evaluation of human exposure to whole-body mechanical vibration and repeated shock," 1987.
- [21] Richtlinie, VDI, 2057, "Einwirkung mechanischer Schwingungen auf den Menschen, Blatt 1 und 2. VDI-Gesellschaft Konstruktion und Entwicklung, Fachbereich Schwingungstechnik, VDI-Verlag, Düsseldorf," 1987.
- [22] VDI-Fachbereich Schwingungstechnik VDI-2057 - Einwirkung mechanischer Schwingungen auf den Menschen - Ganzkörper-Schwingungen, 2017.
- [23] I. Rericha, "Methoden zur objektiven Bewertung des Fahrkomforts," *Automob Ind*, vol. 31, no. 2, pp. 175–182, 1986.
- [24] S. Cucuz, "Schwingempfindung von PKW-Insassen. Auswirkung von stochastischen Unebenheiten und Einzelhindernissen der realen Fahrbahn," Doctoral dissertation, TU Braunschweig, Braunschweig.
- [25] M. Mitschke and B. Klingner, "Schwingungskomfort im Kraftfahrzeug. ATZ-Automobiltechnische Zeitschrift," vol. 100, no. 1, pp. 18–24, 1998.
- [26] S. A. E. Standard, "Vehicle Dynamics Terminology-SAE J670C," *SAE Handbook Supplement*.
- [27] N. J. Mansfield and S. Maeda, "Subjective ratings of whole-body vibration for single- and multi-axis motion," *The Journal of the Acoustical Society of America*, vol. 130, no. 6, pp. 3723–3728, 2011, doi: 10.1121/1.3654014.
- [28] M. J. Griffin, "Discomfort from feeling vehicle vibration," *Vehicle System Dynamics*, 45(7-8), vol. 45, no. 7,8, pp. 679–698, 2007.

- [29] L. Zhang, M. G. Helander, and C. G. Drury, "Identifying factors of comfort and discomfort in sitting," *Human factors*, vol. 38, no. 3, pp. 377–389, 1996, doi: 10.1518/001872096778701962.
- [30] M. G. Helander and L. Zhang, "Field studies of comfort and discomfort in sitting," *Ergonomics*, vol. 40, no. 9, pp. 895–915, 1997.
- [31] E. Enders, S. Vos, G. Burkhard, N. Munzinger, and D. Schramm, "Requirements on driving dynamics in autonomous driving with regard to motion and comfort," *18. Internationales Stuttgarter Symposium*, pp. 683–697.
- [32] E. Enders, G. Burkhard, T. Berger, and D. Schramm, "Objectifying Ride Comfort," *Forschung im Ingenieurwesen*, vol. 83, no. 4, pp. 885–898, 2019.
- [33] E. Enders, G. Burkhard, N. Munzinger, and D. Schramm, "Acquiring requirements on drive comfort by quantifying the accelerations affecting vehicle occupants," *AmE - Automotive meets Electronics*, VDE, pp. 1–6, 2018.
- [34] G. Koch, "Adaptive Control of Mechatronic Vehicle Suspension Systems," Doctoral dissertation, Technische Universität München, Munich, 2011.
- [35] M. Lienkamp, "Praktikum Kraftfahrzeugmess- und -versuchstechnik: Suspension and Damping," [PowerPoint slides], Faculty of Mechanical Engineering, Technical University of Munich, TUM, Munich, 2019.
- [36] ISO 8608, (2016), "Mechanical Vibration—Road Surface Profiles—Reporting of Measured Data," *BSI Standards Publication: London, UK*, 2016.
- [37] M. Agostinacchio, D. Ciampa, and S. Olita, "The vibrations induced by surface irregularities in road pavements – a Matlab® approach," *Eur. Transp. Res. Rev.*, vol. 6, no. 3, pp. 267–275, 2014, doi: 10.1007/s12544-013-0127-8.
- [38] M. H. Abolbashari and M. Shamel, "Simulation of typical road surface profiles using a pseudo random approach," presented at 19th Canadian Congr. of Applied Mechanics CANCAM 03, June 2003.
- [39] K. Bogsjö, "Coherence of road roughness in left and right wheel-path," *Vehicle System Dynamics*, vol. 46, sup1, pp. 599–609, 2008, doi: 10.1080/00423110802018289.
- [40] X. Liu, H. Wang, Y. Shan, and T. He, "Construction of road roughness in left and right wheel paths based on PSD and coherence function," *Mechanical Systems and Signal Processing*, vol. 60,61, pp. 668–677, 2015, doi: 10.1016/j.ymssp.2015.01.034.
- [41] E. Enders, P. Karle, G. Burkhard, D. Killian, and G. Bonelli, "Modal Vertical Vehicle Dynamics Control for Semi-Active and Active Suspension Systems: (not published yet)," *2020 Fifteenth International Conference on Ecological Vehicles and Renewable Energies (EVER)*, 2020.
- [42] D. A. Williams and P. G. Wright, "Wright, Williams et al. 1984 - The Application of Active Suspension," *U.S. Patent No. 4,625,993. Washington, DC: U.S. Patent and Trademark Office.*, 1986.
- [43] A. Unger, "Serientaugliche quadratisch optimale Regelung für semiaktive Pkw-Fahrwerke," Doctoral dissertation, Technische Universität München, Munich, 2012.

- [44] P. Barsaiyan and S. Purwar, "Comparison of state feedback controller design methods for MIMO systems," in *IEEE Int. Conf. on Power, Control and Embedded Systems, 2010*, pp. 1–6.
- [45] F. Braghin, S. Cinquemani, and F. Resta, "A new approach to the synthesis of modal control laws in active structural vibration control," *Journal of Vibration and Control*, vol. 19, no. 2, pp. 163–182, 2013, doi: 10.1177/1077546311430246.
- [46] F. Braghin, F. Resta, and E. Sabbioni, "A Modal Control for Active/Semi-Active Suspension Systems," presented at IEEE/ASME Int. Conf. on Advanced Intelligent Mechatronics. Zurich, Switzerland, Sep. 4 2007.
- [47] I. Kolmanovsky and N. H. McClamroch, "Switching between controllers to improve closed loop performance," in *Proceedings of the 2000 American 23/06/2000 - 30/06/2000, 2702-2703* vol.4.
- [48] T. F. Li and J. Fu, "Event-triggered control of switched linear systems," *Journal of the Franklin Institute*, vol. 354, no. 15, pp. 6451–6462, 2017, doi: 10.1016/j.franklin.2017.05.018.
- [49] T. T. Ma, "Multiple UPFC damping control scheme using ANN coordinated adaptive controllers," *Asian Journal of Control*, vol. 11, no. 5, pp. 489–502, 2009, doi: 10.1002/asjc.130.
- [50] A. B and M. Venkatakirthiga, "FPGA based co-ordinated controller for hybrid power systems," in *2016 IEEE 1st International Conference on Power Electronics, Intelligent Control and Energy Systems (ICPEICES)*, Delhi, India, Jul. 2016 - Jul. 2016, pp. 1–6.
- [51] M. A. Kumar and N. V. Srikanth, "An Adaptive Coordinated Control for an Offshore Wind Farm Connected VSC Based Multi-Terminal DC Transmission System," *Open Engineering*, vol. 5, no. 1, 2014, doi: 10.1515/eng-2015-0005.
- [52] L. G. C. Bautista and P. B. de Araujo, "Analysis of the influence of ipfc-pod and pss controllers coordinated tuning by an adaptive genetic algorithm with hyper-mutation," in *2018 Workshop on Communication Networks and Power Systems (WCNPS)*, Brasília, Nov. 2018 - Nov. 2018, pp. 1–5.
- [53] J. Han, S. K. Solanki, and J. Solanki, "Coordinated Predictive Control of a Wind/Battery Microgrid System," *IEEE J. Emerg. Sel. Topics Power Electron.*, vol. 1, no. 4, pp. 296–305, 2013, doi: 10.1109/JESTPE.2013.2282601.
- [54] M. A. Kumar, B. V. Kumar, and N. V. Srikanth, "ANFIS based coordinated control for an offshore wind farm connected VSC MTDC system," in *2014 Eighteenth National Power Systems Conference (NPSC)*, Guwahati, India, Dec. 2014 - Dec. 2014, pp. 1–6.
- [55] H. Termous, H. Shraim, R. Talj, C. Francis, and A. Charara, "Coordinated control strategies for active steering, differential braking and active suspension for vehicle stability, handling and safety improvement," *Vehicle System Dynamics*, vol. 57, no. 10, pp. 1494–1529, 2019, doi: 10.1080/00423114.2018.1521001.
- [56] X. Moreau, O. Altet, and A. Oustaloup, "The CRONE Suspension: Management of the Dilemma Comfort-Road Holding," *Nonlinear Dynamics*, vol. 38, 1, 4, pp. 461–484, 2004.
- [57] A. Rizzo, X. Moreau, A. Oustaloup, and V. Hernette, "A New CRONE Suspension: More Compact and More Efficient: Part 1," *Problematics and Specifications. In International Design Engineering Technical Conferences and Computers and Information in Engineering Conference*, no. 49019, pp. 1095–1102, 2009, doi: 10.1115/DETC2009-86783.

- [58] J. Na, Y. Huang, X. Wu, G. Gao, G. Herrmann, and J. Z. Jiang, "Active Adaptive Estimation and Control for Vehicle Suspensions With Prescribed Performance," *IEEE Trans. Contr. Syst. Technol.*, vol. 26, no. 6, pp. 2063–2077, 2018, doi: 10.1109/TCST.2017.2746060.
- [59] M. Soleymani and Montazeri-Gh, M., Amiryani, R., "Adaptive fuzzy controller for vehicle active suspension system based on traffic conditions," *Scientia Iranica*, vol. 19, no. 3, pp. 443–453, 2012, doi: 10.1016/j.scient.2012.03.002.
- [60] Y. Qin, J. J. Rath, C. Hu, C. Sentouh, and R. Wang, "Adaptive nonlinear active suspension control based on a robust road classifier with a modified super-twisting algorithm," *Nonlinear Dyn*, vol. 97, no. 4, pp. 2425–2442, 2019, doi: 10.1007/s11071-019-05138-8.
- [61] K. S. Hong and S. Park, "Road-frequency adaptive control for semi-active suspension systems," *Int. J. Control Autom. Syst.*, vol. 8, no. 5, pp. 1029–1038, 2010, doi: 10.1007/s12555-010-0512-1.
- [62] F. Gao, S. E. Li, D. Kum, and H. Zhang, "Synthesis of multiple model switching controllers using H theory for systems with large uncertainties," *Neurocomputing*, vol. 157, pp. 118–124, 2015, doi: 10.1016/j.neucom.2015.01.029.
- [63] M. Yamashita, K. Fujimori, K. Hayakawa, and H. Kimura, "Application of H_∞ Control to Active Suspension Systems," *IFAC Proceedings Volumes*, vol. 26, no. 2, pp. 87–90, 1993, doi: 10.1016/S1474-6670(17)48688-5.
- [64] J. Emura, S. Kakizaki, F. Yamaoka, and M. Nakamura, "Development of the Semi-Active Suspension System Based on the Sky-Hook Damper Theory," *SAE transactions, JOURNAL OF PASSENGER CARS*, vol. 103, no. 6, pp. 1110–1119, 1994.
- [65] D. Sanunier, O. Sename, and L. Dugard, "Comparison of Skyhook and H_∞ Control Applied on a Quarter-Car Suspension Model," *IFAC Proceedings Volumes*, vol. 34, no. 1, pp. 107–112, 2001, doi: 10.1016/S1474-6670(17)34385-9.
- [66] D. Sammier, O. Sename, and L. Dugard, "Skyhook and H_∞ Control of Semi-active Suspensions: Some Practical Aspects," *Vehicle System Dynamics*, vol. 39, no. 4, pp. 279–308, 2003, doi: 10.1076/vesd.39.4.279.14149.
- [67] M. Ahmadian, X. Song, and S. C. Southward, "No-jerk skyhook control methods for semi-active suspensions," *J. Vib. Acoust*, vol. 126, no. 4, pp. 580–584, 2004, doi: 10.1115/1.1805001.
- [68] A. Drivet, R. A. Ramírez-Mendoza, L. Flores, O. Sename, C. P. Vassal, and L. Dugard, "Virtual prototyping for vehicle dynamic modelling," *IFAC Proceedings Volumes*, vol. 39, no. 16, pp. 986–991, 2006, doi: 10.3182/20060912-3-DE-2911.00169.
- [69] D. Hrovat, "Survey of advanced suspension developments and related optimal control applications," *Automatica*, vol. 33, no. 10, pp. 1781–1817, 1997.
- [70] C. Poussot-Vassal, O. Sename, L. Dugard, R. Ramirez-Mendoza, and L. Flores, "OPTIMAL SKYHOOK CONTROL FOR SEMI-ACTIVE SUSPENSIONS," *IFAC Proceedings Volumes*, vol. 39, no. 16, pp. 608–613, 2006, doi: 10.3182/20060912-3-DE-2911.00106.
- [71] F. H. Besinger, D. Cebon, and D. J. Cole, "Force control of a semi-active damper. Vehicle System Dynamics," *Vehicle System Dynamics*, vol. 24, no. 9, pp. 695–723, 1995, doi: 10.1080/00423119508969115.

- [72] S. A. Abu Bakar, H. Jamaluddin, R. A. Rahman, P. M. Samin, and K. Hudha, "Vehicle ride performance with semi-active suspension system using modified skyhook algorithm and current generator model," *International journal of vehicle autonomous systems*, vol. 6, no. 3,4, pp. 197–221, 2008, doi: 10.1504/IJVAS.2008.023577.
- [73] L. Flores and R. A. Ramirez-Mendoza, "Extended Skyhook for Heave, Pitch and Roll in a Semiactive Suspension of a Full Vehicle Model," in *11th MINI conference on Vehicle 11th MINI conference on Vehicle System Dynamics, Identification and Anomalies, VSDIA, Budapest, Hungary, 2008*.
- [74] M. Sorli and G. Quaglia, *Meccatronica: LE BASI DELLA MECCATRONICA, STRUTTURA DEI DISPOSITIVI DI ATTUAZIONE CONTROLLATA, CARATTERISTICHE STATICHE E DINAMICHE DEGLI STRUMENTI*, Politecnico di Torino, Dipartimento di Meccanica. Torino: politeko, 2017.
- [75] P. Welch, "The Use of Fast Fourier Transform for the Estimation of Power Spectra: A Method Based on Time Averaging Over Short, Modified Periodograms," *IEEE Transactions on audio and electroacoustics*, vol. 15, no. 2, pp. 70–73, doi: 10.1109/TAU.1967.1161901.
- [76] H. Schmid, "How to use the FFT and Matlab's pwelch function for signal and noise simulations and measurements," *FHNW/IME*, pp. 2–13, 2012.
- [77] O. Lindgärde, "Kalman filtering in semi-active suspension control," *IFAC Proceedings Volumes*, vol. 35, no. 1, pp. 439–444, 2002.
- [78] H. Wang, T. Nagayama, and D. Su, "Estimation of dynamic tire force by measurement of vehicle body responses with numerical and experimental validation," *Mechanical Systems and Signal Processing*, no. 123, pp. 369–385, 2019, doi: 10.1016/j.ymssp.2019.01.017.
- [79] S. W. Kang, J. S. Kim, and G. W. Kim, "Road roughness estimation based on discrete Kalman filter with unknown input," *Vehicle System Dynamics*, vol. 57, no. 10, pp. 1530–1544, 2019.
- [80] M. Doumiati, A. Charara, A. Victorino, and D. Lechner, *Vehicle Dynamics Estimation Using Kalman Filtering : Experimental Validation*: John Wiley & Sons, 2012.
- [81] J. Lee, G. Jang, E. Muljadi, F. Blaabjerg, Z. Chen, and Y. C. Kang, "Stable Short-Term Frequency Support Using Adaptive Gains for a DFIG-Based Wind Power Plant," *IEEE Trans. Energy Convers.*, vol. 31, no. 3, pp. 1068–1079, 2016, doi: 10.1109/TEC.2016.2532366.
- [82] A. J. Accardi and R. V. Cox, "Core estimator and adaptive gains from signal to noise ratio in a hybrid speech enhancement system," *U.S. Patent Application*, no. 09/206,478, 2002.
- [83] M. Ahmed and F. Svaricek, "Adaptive robust gain scheduled control of vehicle semi-active suspension for improved ride comfort and road handling," in *2013 IEEE Int. Conf. 27/02/2013 - 01/03/2013*, pp. 376–381.
- [84] G. Welch and G. Bishop, "An Introduction to the Kalman Filter," *Department of Computer Science, University of North Carolina at Chapel Hill*, 1995.
- [85] E. Zanasi, "System Theory: [PowerPoint slides]. Available: http://www.dii.unimo.it/~zanasi/didattica/Teoria_dei_Sistemi/Luc_TDS_ING_2016_Stability_Analysis_of_Nonlinear_Systems.pdf," 2015.

Appendix

Appendix A	Model parametrization	xvi
Appendix B	Quarter car model	xviii
Appendix C	Model matrices	xxi
Appendix D	Suspensions constraint model in the garage simulation	xxii
Appendix E	Kalman Filter	xxiv
Appendix F	Controller parametrization	xxviii
Appendix G	Passive and Semi-Active suspensions.....	xxx
Appendix H	Sensor setup	xxxiv
Appendix I	Measurements processing.....	xxxviii
Appendix J	Implementation of the logic in the test vehicle	xlix
Appendix K	Controller stability	I

Appendix A Model parametrization

Table A.1 Data sheet for the test vehicle

Symbol	Value	Description
l_f	1.588 m	Distance from front axle and centre of gravity
l_r	1.621 m	Distance from rear axle and centre of gravity
l_{eng}	1.486 m	Distance from the engine mounting and the vehicle centre of gravity in x-direction
b_{eng}	0.6520 m	Distance from the engine mounting and the vehicle centre of gravity in y-direction
b_f	1.609 m	Front axle track width
b_r	1.637 m	Rear axle track width
$c_{Bo,fr} = c_{Bo,fl}$	$20.51 \cdot 10^3$ N/m	Suspension stiffness, front axle
$c_{Bo,rr} = c_{Bo,rl}$	$24.52 \cdot 10^3$ N/m	Suspension stiffness, rear axle
$c_{arb,f}$	$15.49 \cdot 10^3$ N/m	Anti-roll bar stiffness, front axle
$c_{arb,r}$	$25.86 \cdot 10^2$ N/m	Anti-roll bar stiffness, rear axle
$c_{T,f} = c_{T,r}$	$27.06 \cdot 10^4$ N/m	Tyre stiffness
c_{eng}	$6.000 \cdot 10^5$ N/m	Stiffness of the engine mounting
$d_{Bo,fr} = d_{Bo,fl}$	542.1 N s/m	Suspension damping coefficient, front axle
$d_{Bo,rr} = d_{Bo,rl}$	829.6 N s/m	Suspension damping coefficient, rear axle
d_{eng}	6000 N s/m	Damping of the engine mounting
m	2160 kg	Vehicle mass
m_{Bo}	1903 kg	Body mass
m_{eng}	300 kg	Engine mass
$m_{w,fr} = m_{w,fl}$	66.12 kg	Unsprung mass, front axle
$m_{w,rr} = m_{w,rl}$	62.43 kg	Unsprung mass, rear axle
$J_{eng,xx}$	54.4 kg m ²	Roll moment of inertia of the engine
$J_{Bo,t}$	991.2 kg m ²	Twist moment of inertia of the body
J_{xx}	543.5 kg m ²	Roll moment of inertia of the body

J_{yy}	3563 kg m ²	Pitch moment of inertia of the body
sus_{th}	0.1 m	Suspension deflection threshold to overcome to obtain $G_{sus,def}$
th_{def}	0.6	Threshold for the gain in suspension deflection
th_{dyn}	0.9	Threshold for G_{Fdyn}
th_{Fdyn}	$k_i F_{z_{w,ij,stat}}$ N	Threshold for dynamic wheel load
th_{PS}	0.1	Threshold for G_{PS}
th_{ratio}	0.9	Threshold for power spectrum estimation
th_{xdef}	0.1 m	Threshold for suspension deflection

Appendix B Quarter car model

Quarter car model, also known as quarter car suspension, is shown in Figure B.1. The system consists of m_{B_0} , sprung mass, m_w , unsprung mass, c_{B_0} , stiffness coefficient of the suspension, c_T , vertical stiffness of the wheel, d_{B_0} , damping coefficient of the suspension, d_T damping coefficient of the wheel. The latter is neglected as usually relatively low. The vertical displacements of the sprung and unsprung masses are respectively denoted by z_{B_0} and z_w , while z_{r_0} is the road excitation. This only model accounts for the mass movements on the vertical axis.

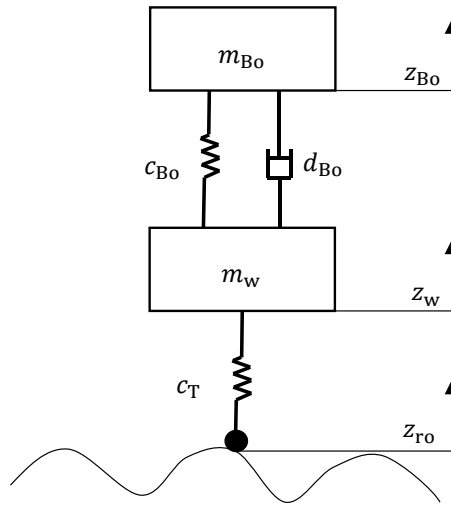


Figure B.1: Quarter car model

The equations of motions of this two degrees of freedom model are:

$$m_{B_0}\ddot{z}_{B_0} = -d_{B_0}(\dot{z}_{B_0} - \dot{z}_w) - c_{B_0}(z_{B_0} - z_w) \quad (\text{B.1})$$

$$m_w\ddot{z}_w = -d_{B_0}(\dot{z}_w - \dot{z}_{B_0}) - c_{B_0}(z_w - z_{B_0}) - c_T(z_w - z_{r_0}) \quad (\text{B.2})$$

and expressed in matrix form:

$$\mathbf{M}\ddot{\mathbf{q}} + \mathbf{D}\dot{\mathbf{q}} + \mathbf{K}\mathbf{q} = \mathbf{H}z_{r_0} \quad (\text{B.3})$$

with:

$$\mathbf{q} = \begin{Bmatrix} z_{B_0} \\ z_w \end{Bmatrix}, \quad (\text{B.4})$$

$$\mathbf{M} = \begin{bmatrix} m_{B_0} & 0 \\ 0 & m_w \end{bmatrix} \quad (\text{B.5})$$

$$\mathbf{D} = \begin{bmatrix} d_{B_0} & -d_{B_0} \\ -d_{B_0} & d_{B_0} \end{bmatrix} \quad (\text{B.6})$$

$$\mathbf{K} = \begin{bmatrix} c_{B_0} & -c_{B_0} \\ -c_{B_0} & c_{B_0} + c_T \end{bmatrix} \quad (\text{B.7})$$

$$\mathbf{H} = \begin{bmatrix} 0 \\ c_T \end{bmatrix} \quad (\text{B.8})$$

With respect to the vehicle datas, parameters in Table B.1 have been used:

Table B.1 Data test vehicle adapted to quarter car model		
Symbol	Value	Description
m_{B_0}	550.7 kg	Quarter of the sum of the engine mass and body mass
m_w	64.27 kg	Mean between front and rear tyres masses
d_{B_0}	685.9 N s/m	Mean between front and rear suspension damping coefficient
c_{B_0}	$22.52 \cdot 10^4$ N/m	Mean between front and rear suspension stiffness
c_T	$27.06 \cdot 10^4$ N/m	Mean between front and rear wheels stiffness
d_{opt}	$26.89 \cdot 10^4$ N s/m	Optimal damping coefficient
$0.5d_{opt}$	$1.345 \cdot 10^4$ N s/m	-
$1.25d_{opt}$	$3.362 \cdot 10^4$ N s/m	-
$2d_{opt}$	$5.379 \cdot 10^4$ N s/m	-

The vertical force transmitted to the ground, representing road-holding is F_z and it is calculated as it follows:

$$\mathbf{F}_z = -c_T(\mathbf{z}_w - \mathbf{z}_{ro}) \quad (\text{B.9})$$

The natural frequencies are computed: the lower frequency is equal to 0.9775 Hz and corresponds to the “bounce mode”, with both masses in phase, the higher frequency is equal to 10.75 Hz and it is called the “wheel hop mode”, where the masses are in counter-phase and the sprung mass is almost not moving [13, p. 245]. An optimal damping coefficient value can be calculated as to obtain an horizontal tangent in the first invariant point at low frequencies [12] (Figure 2.1).

$$d_{opt} = \sqrt{\frac{m_{B_0} c_{B_0} c_T + 2c_{B_0}}{2 c_{B_0}}} \quad (\text{B.10})$$

Usually damping coefficients are expressed via their damping ratio which is:

$$\zeta = \frac{d_{\text{Bo}}}{d_{\text{crit}}} \tag{B.11}$$

where:

$$d_{\text{crit}} = 2\sqrt{m_{\text{Bo}}c_{\text{Bo}}} \tag{B.12}$$

Appendix C Model matrices

Eq. (2.21) and Eq. (2.26) display the system stiffness matrix \mathbf{K}_{sys} and the system damping matrix \mathbf{D}_{sys} . Their formulation is based on the following:

$$\mathbf{K}_{w,w} = \mathbf{K}_T + \mathbf{K}_{\text{sus}} + \mathbf{K}_{\text{arb}} \quad (\text{C.1})$$

$$\mathbf{K}_{w,\text{Bo}} = (\mathbf{K}_{\text{sus}} + \mathbf{K}_{\text{arb}})\mathbf{T}^T \quad (\text{C.2})$$

$$\mathbf{K}_{\text{Bo},w} = \mathbf{T}(\mathbf{K}_{\text{sus}} + \mathbf{K}_{\text{arb}}) \quad (\text{C.3})$$

$$\mathbf{K}_{\text{Bo},\text{Bo}} = (\mathbf{T}(\mathbf{K}_{\text{sus}} + \mathbf{K}_{\text{arb}})\mathbf{T}^T + \mathbf{T}_{\text{eng}}\mathbf{K}_{\text{eng}}\mathbf{T}_{\text{eng}}^T) \quad (\text{C.4})$$

$$\mathbf{K}_{\text{Bo},\text{eng}} = \mathbf{T}_{\text{eng}}\mathbf{K}_{\text{eng}} \quad (\text{C.5})$$

$$\mathbf{K}_{\text{eng},\text{Bo}} = \mathbf{K}_{\text{eng}}\mathbf{T}_{\text{eng}}^T \quad (\text{C.6})$$

$$\mathbf{K}_{\text{eng},\text{eng}} = \mathbf{K}_{\text{eng}} \quad (\text{C.7})$$

$$\mathbf{D}_{w,w} = \mathbf{D}_T + \mathbf{D}_{\text{sus}} \quad (\text{C.8})$$

$$\mathbf{D}_{w,\text{Bo}} = \mathbf{D}_{\text{sus}}\mathbf{T}^T \quad (\text{C.9})$$

$$\mathbf{D}_{\text{Bo},w} = \mathbf{T}\mathbf{D}_{\text{sus}} \quad (\text{C.10})$$

$$\mathbf{D}_{\text{Bo},\text{Bo}} = \mathbf{T}\mathbf{D}_{\text{sus}}\mathbf{T}^T + \mathbf{T}_{\text{eng}}\mathbf{D}_{\text{eng}}\mathbf{T}_{\text{eng}}^T \quad (\text{C.11})$$

$$\mathbf{D}_{\text{Bo},\text{eng}} = \mathbf{T}_{\text{eng}}\mathbf{D}_{\text{eng}} \quad (\text{C.12})$$

$$\mathbf{D}_{\text{eng},\text{Bo}} = \mathbf{D}_{\text{eng}}\mathbf{T}_{\text{eng}}^T \quad (\text{C.13})$$

$$\mathbf{D}_{\text{eng},\text{eng}} = \mathbf{D}_{\text{eng}} \quad (\text{C.14})$$

The expression for the \mathbf{R} matrix of Eq. (2.86) is the following:

$$\mathbf{R} = [\mathbf{T}^{-1}\Delta\mathbf{K}^*\mathbf{T}^{-T} \quad -\mathbf{T}^{-1}\Delta\mathbf{K}^* \quad \mathbf{0} \quad \mathbf{T}^{-1}\Delta\mathbf{D}^*\mathbf{T}^{-T} \quad -\mathbf{T}^{-1}\Delta\mathbf{D}^* \quad \mathbf{0}] \quad (\text{C.15})$$

Eq. (C.15) can be also written as:

$$\mathbf{R} = \mathbf{T}^{-1}[\mathbf{K}^* - \hat{\mathbf{K}}_{\text{Bo}} \quad \mathbf{D}^* - \hat{\mathbf{D}}_{\text{Bo}}] \begin{bmatrix} \mathbf{T}^{-T} & -\mathbf{I}_4 & \mathbf{0}_{8 \times 2} & \mathbf{0}_4 & \mathbf{0}_4 \\ \mathbf{0}_4 & \mathbf{0}_4 & \mathbf{T}^{-T} & -\mathbf{I}_4 & \mathbf{0}_{8 \times 2} \end{bmatrix} \quad (\text{C.16})$$

Appendix D Suspensions constraints model in garage simulation

In order to analyse the differences between the P and the R controllers in scenarios as the garage road, a simple model to simulate a constraint in the suspension travel has been implemented (Figure D.1). The block receives as an input parameter, the suspension travel, $\Delta z_{sus,ij}$, calculated with the resolution of the state space equations and provides as an output, $\dot{x}_{add,ij}$ which is an acceleration vector which is added in the state space equation:

$$\dot{x} = \mathbf{Ax} + \mathbf{Bu} + \mathbf{Ez} + \sum \dot{x}_{add,ij} \quad (\text{D.1})$$

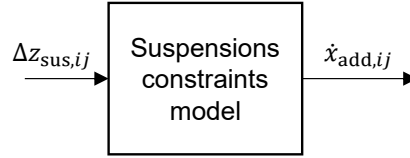


Figure D.1: Scheme of the suspensions constraints model

The idea is to gradually increase the stiffness suspension coefficient with an exponential function and calculate the difference between the corresponding increased stiffness force and the initial one. From the resulting force, the acceleration vector, $\dot{x}_{add,ij}$ can be finally obtained. The following equations apply for the model:

$$c_{Bo,add,ij} = \begin{cases} c_{Bo,ij} e^{[k_{ij}(\Delta z_{sus,ij} - \Delta z_{sus,c,ij} p_{ij}) - 1]} & \text{if } \Delta z_{sus,ij} > \Delta z_{sus,c+,ij} p_{ij} \\ c_{Bo,ij} e^{[-k_{ij}(\Delta z_{sus,ij} - \Delta z_{sus,c,ij} p_{ij}) - 1]} & \text{if } \Delta z_{sus,ij} < \Delta z_{sus,c-,ij} p_{ij} \end{cases} \quad (\text{D.2})$$

$$\mathbf{F}_{sus,add,ij} = \begin{bmatrix} 0 \\ 0 \\ 0 \\ F_{add,ij} \end{bmatrix} \quad (\text{D.3})$$

Where $F_{add,ij}$ is:

$$F_{add,ij} = c_{Bo,add,ij} (\Delta z_{sus,ij} - \Delta z_{sus,c,ij}) \quad (\text{D.4})$$

Finally $\dot{x}_{add,ij}$ is derived:

$$\dot{x}_{add,ij} = M_{sus} \begin{bmatrix} 0_{10 \times 1} \\ F_{add,ij} \\ -TF_{add,ij} \\ 0_{2 \times 1} \end{bmatrix} \quad (\text{D.5})$$

With M_{sus} :

$$M_{\text{sus}} = \begin{bmatrix} 0_{10 \times 20} \\ 0_{10 \times 10} & M_{\text{sys}}^{-1} \end{bmatrix} \quad (\text{D.6})$$

By adding to the state space equation an increasingly high acceleration vector, the suspension travel becomes restricted. This approach entails inevitable peaks in the accelerations of the body and therefore it is used only to investigate the differences between P and R controllers when introducing a constraint in the suspensions travel. Table (D.1) summarizes the mentioned variables:

Table D.1 Parameters for suspensions constraints model

Symbol	Description	Value
k_{fj}	Weighting factor for $\Delta z_{\text{sus},ij} - \Delta z_{\text{sus},c,ij} p_{ij}$, front axle	100
k_{rj}	Weighting factor for $\Delta z_{\text{sus},ij} - \Delta z_{\text{sus},c,ij} p_{ij}$, rear axle	100
p_{fj}	Percentage of $\Delta z_{\text{sus},c+,ij}$ and $\Delta z_{\text{sus},c-,ij}$, front axle	0.9
p_{rj}	Percentage of $\Delta z_{\text{sus},c+,ij}$ and $\Delta z_{\text{sus},c-,ij}$, rear axle	0.6
$\Delta z_{\text{sus},c+,ij}$	Maximum desired suspension travel	0.1 m
$\Delta z_{\text{sus},c-,ij}$	Minimum desired suspension travel	-0.1 m

Appendix E Kalman Filter

Kalman filtering is an algorithm that employs measurements conducted over time and containing noise and inaccuracies in order to estimate variables with a joint probability distribution. In simple terms, it is an iterative mathematical process to estimate the true values of some process variables. It is widely employed in signal processing and robotic motion planning. In Table E.1 there is an overview of the matrix format of the filter. In order to estimate the internal state for a linear and continuous time model, the following differential equations can be defined:

$$\dot{\mathbf{x}} = \mathbf{A}_k \mathbf{x} + \mathbf{B}_k \mathbf{u} + \mathbf{w} \quad (\text{E.1})$$

$$\mathbf{y} = \mathbf{C}_k \mathbf{x} + \mathbf{D}_k \mathbf{u} + \mathbf{v} \quad (\text{E.2})$$

Table E.1 Kalman Filter parameters

Symbol	Description
\mathbf{x}	State space vector $\in R^n$
\mathbf{A}_k	State-transition matrix, $n \times n$
\mathbf{u}	Control vector $\in R^l$
\mathbf{B}_k	Control-input matrix, $n \times l$
\mathbf{y}	Observation or measurement vector $\in R^m$
\mathbf{C}_k	Observation matrix, $m \times n$
\mathbf{D}_k	Control-input matrix for the measurement equation, $m \times l$
\mathbf{w}	Process noise
\mathbf{v}	Observation or measurement noise
\mathbf{Q}_k	Process noise covariance matrix
\mathbf{R}_k	Observation noise covariance matrix
\mathbf{P}	Error covariance matrix
\mathbf{K}	Kalman gain

Discrete-time Kalman filter transforms the linear and continuous formulation of Eq. (E.1) and Eq. (E.2) in a linear system where $j + 1$ indicates the following time-step with respect to j .

$$\mathbf{x}_{j+1} = \mathbf{A}_{k_j} \mathbf{x}_j + \mathbf{B}_{k_j} \mathbf{u}_j + \mathbf{w}_j \quad (\text{E.3})$$

$$\mathbf{y}_j = \mathbf{C}_{k_j} \mathbf{x}_j + \mathbf{D}_{k_j} \mathbf{u}_j + \mathbf{v}_j \quad (\text{E.4})$$

Kalman filter is a recursive filter which requires, for each iteration, the knowledge of the previous time-step estimate $\hat{\mathbf{x}}_{j-1}$ and the current observation \mathbf{y}_j . Being $\hat{\mathbf{x}}_j^-$, the a-priori estimation of the system state, based on the estimation at $j - 1$, and being $\hat{\mathbf{x}}_j$ the a-posteriori estimation of the system state based on the knowledge of \mathbf{y}_j , the estimated errors, a-priori and a-posteriori, can be respectively defined:

$$\mathbf{e}_j^- = \mathbf{x}_j - \hat{\mathbf{x}}_j^- \quad (\text{E.5})$$

$$\mathbf{e}_j = \mathbf{x}_j - \hat{\mathbf{x}}_j \quad (\text{E.6})$$

This errors can be associated to two error covariance matrices, respectively a-priori and a-posteriori as it follows:

$$\mathbf{P}_j^- = E[\mathbf{e}_j^- \mathbf{e}_j^{-T}] \quad (\text{E.7})$$

$$\mathbf{P}_j = E[\mathbf{e}_j \mathbf{e}_j^T] \quad (\text{E.8})$$

Where $E[\zeta]$, stands for the expected value of the general variable ζ . The aim of the Kalman filter is to minimize the a posteriori covariance matrix \mathbf{P}_j and to provide a method for the correct estimation of $\hat{\mathbf{x}}_j$ based on $\hat{\mathbf{x}}_j^-$ and \mathbf{y}_j . The following applies for the a-posteriori state:

$$\hat{\mathbf{x}}_j = \hat{\mathbf{x}}_j^- + \mathbf{K}_j(\mathbf{y}_j - \mathbf{C}_{k_j} \hat{\mathbf{x}}_j^-) \quad (\text{E.9})$$

The problem moves to the computation of the Kalman gain that multiplies the term $\mathbf{y}_j - \mathbf{C}_{k_j} \hat{\mathbf{x}}_j^-$, called "innovation". The process described by Eq. (E.9) can be summarised in two phases. At first, an a-priori estimation of both $\hat{\mathbf{x}}_j^-$ and \mathbf{P}_j^- by means of the following:

$$\hat{\mathbf{x}}_j^- = \mathbf{A}_k \hat{\mathbf{x}}_{j-1} + \mathbf{B}_k \mathbf{u}_j \quad (\text{E.10})$$

$$\mathbf{P}_j^- = \mathbf{A}_k \mathbf{P}_{j-1} \mathbf{A}_k^T + \mathbf{Q}_{k_j} \quad (\text{E.11})$$

Those two are the best estimates of the state vector and of the covariance at instant j . The second phase consists in calculating the Kalman gain with the following:

$$\mathbf{K}_j = \mathbf{P}_j^- \mathbf{C}_{k_j}^T \left(\mathbf{C}_{k_j} \mathbf{P}_j^- \mathbf{C}_{k_j}^T + \mathbf{R}_{k_j} \right)^{-1} \quad (\text{E.12})$$

By substituting Eq. (E. 11) in (E. 12), Eq. (E.10) and (E.12) in (E.9), the a-posteriori state is defined. With Eq. (E. 12), the a-posteriori estimation of the covariance matrix becomes:

$$\mathbf{P}_j = (\mathbf{I} - \mathbf{K}_j \mathbf{C}_{k_j}) \mathbf{P}_j^- \quad (\text{E.13})$$

Those equations can be translated in a more general form by means of:

$$\text{cov}(\mathbf{x}_j, \mathbf{y}_j) = \mathbf{P}_j^- \mathbf{C}_{k_j}^T \quad (\text{E.14})$$

$$\text{cov}(\mathbf{y}_j) = \mathbf{C}_{k_j} \mathbf{P}_j^- \mathbf{C}_{k_j}^T \quad (\text{E.15})$$

Eq. (E. 12) and (E. 13) become:

$$\mathbf{K}_j = \text{cov}(\mathbf{x}_j, \mathbf{y}_j) \left(\text{cov}(\mathbf{y}_j) + \mathbf{R}_{k_j} \right)^{-1} \quad (\text{E.16})$$

$$\mathbf{P}_j = \mathbf{P}_j^- - \mathbf{K}_j \text{cov}(\mathbf{x}_j, \mathbf{y}_j)^T \quad (\text{E.17})$$

The last formulation shows how the covariance matrix and the Kalman gain do not depend on the state, the observer or the innovation. It is important to notice that the variables \mathbf{w}_j and \mathbf{v}_j , which respectively represent the process noise and the measurement noise, present a null mean value meaning that $\bar{\mathbf{w}}_j = \bar{\mathbf{v}}_j = 0$. Process noise, \mathbf{w}_j is assumed to be taken from a zero mean multivariate normal distribution with covariance \mathbf{Q}_k , while the measurement noise \mathbf{v}_j is a zero mean Gaussian white noise with covariance \mathbf{R}_k . Further explanations on Kalman filter mathematical formulation can be found in [84]. With reference to Section 4.4, the following parametrization is used for the test vehicle:

Table E.2: Test vehicle parametrization

Variable	Value
$m_{1\text{fr}}$	480.6 kg
$m_{1\text{fl}}$	480.6 kg
$m_{1\text{rl}}$	470.9 kg
$m_{1\text{rr}}$	470.9 kg
$m_{2\text{fr}}$	66.12 kg
$m_{2\text{fl}}$	66.12 kg
$m_{2\text{rl}}$	62.43 kg
$m_{2\text{rr}}$	62.43 kg
$c_{1\text{fr}}$	542.1 N s/m
$c_{1\text{fl}}$	542.1 N s/m
$c_{1\text{rl}}$	829.6 N s/m
$c_{1\text{rr}}$	829.6 N s/m
$k_{1\text{fr}}$	$20.51 \cdot 10^3$ N/m
$k_{1\text{fl}}$	$20.51 \cdot 10^3$ N/m

k_{1rl}	$24.52 \cdot 10^3$ N/m
k_{1rr}	$24.52 \cdot 10^3$ N/m
k_{2fr}	$27.06 \cdot 10^4$ N/m
k_{2fl}	$27.06 \cdot 10^4$ N/m
k_{2rl}	$27.06 \cdot 10^4$ N/m
k_{2rr}	$27.06 \cdot 10^4$ N/m
w	10
v	10^{-4}

As explained in Section 4.4, in order to simulate a measurement process, a white Gaussian noise has been added to the computed measurement vector y via the state space equations for the full vehicle. The white noise power added to the y vector has been calculated as vdt_{sim} where dt_{sim} corresponds to the fixed simulation time step.

Appendix F Controllers parametrization

The controllers parametrization is described in this Appendix. The desired eigenfrequencies $f_{0,i}$, of the body, with $i \in \{z_{B0}, \theta_{B0}, \varphi_{B0}, t_{B0}\}$, in the directions of heave, pitch, roll and twist have been set to the following values for all simulations with the R controller and with the coordination logic, K^+ (Table F.1):

Table F.1: Eigenfrequencies parametrization
 $f_{0,i}$ in Hz

$f_{0,z_{B0}}$	$f_{0,\theta_{B0}}$	$f_{0,\varphi_{B0}}$	$f_{0,t_{B0}}$
1.095	1.285	1.966	1.456

The eigenfrequencies values, namely the desired stiffnesses in the body eigenmodes, have not been changed in this work. The focus has been put on the tuning of the damping ratios, for the R controller and the adaptive gain, for the proportional values K_P to the velocities of the body of the P controller, and to the $K_{P,\alpha}$ values and the α_i for the modified P controller. All of the mentioned parameters have been tuned in an optimal sense for comfort. The following optimization procedure has been performed. The *Response Optimizer App* from Simulink has been used. For each optimization, a *Design Variable Set* is chosen as the list of variables to optimize. The signals that are the objective of the optimization are chosen as well. An increasing number of signals or set variables clearly increases the computational effort and the optimization time. Finally, the signal property to be optimized is chosen. Independently of the signal, its moving RMS is always computed, with a window length of 2 s. The mean of the so obtained vector is therefore minimized.

All the simulation results shown in Chapter 4 and experimental tests in Chapter 5, are performed with the parameters displayed in Tables (F.2, F.3, F.4, F.5). All the resulting controller values have been obtained by optimizing the body accelerations signals in the mode of heave, pitch and roll with the stochastic road input of MnF. For the coordination logic, both P and R controller are parametrized with the values of their individual optimizations.

Table F.2: Damping ratios D_i for R controller

$D_{z_{B0}}$	$D_{\theta_{B0}}$	$D_{\varphi_{B0}}$	$D_{t_{B0}}$
0.3865	0.1327	0.2445	0.2774

Table F.3: K_P values for P controller in Ns/m

$K_{z_{B0}}$	$K_{\theta_{B0}}$	$K_{\varphi_{B0}}$	$K_{t_{B0}}$
$5.833 \cdot 10^3$	$1.631 \cdot 10^4$	$2.025 \cdot 10^4$	$2.194 \cdot 10^3$

Table F.4: $K_{P,\alpha}$ values for modified P controller in Ns/m

$K_{z_{B0},\alpha}$	$K_{\theta_{B0},\alpha}$	$K_{\varphi_{B0},\alpha}$	$K_{t_{B0},\alpha}$
$6.923 \cdot 10^3$	$1.462 \cdot 10^4$	$1.627 \cdot 10^4$	$2.514 \cdot 10^3$

Table F.5: α_i values for modified P controller in Ns/m

$\alpha_{z_{B0}}$	$\alpha_{\theta_{B0}}$	$\alpha_{\varphi_{B0}}$	$\alpha_{t_{B0}}$
0.3786	0.1587	0	0.3

In the R controller, the poles specification is implicit, meaning that the desired body stiffness and damping are tuned by actually choosing, respectively, the body undamped natural frequencies and damping ratios as they are of more immediate understanding for the user of the logic. The following applies to obtain the spring stiffness and damping rates for the R controller logic:

$$c_i = 4\pi^2 f_{0,i}^2 m_i \quad (\text{F.1})$$

$$d_i = 4\pi D_i f_{0,i} m_i \quad (\text{F.2})$$

If the system is underdamped ($D_i < 1$), the following equation applies for poles position:

$$p_{i,\pm} = -2\pi f_{0,i} \left(D_i \pm i \sqrt{1 - D_i^2} \right) \quad (\text{F.3})$$

Appendix G Passive and Semi-Active Suspensions

A comparison between the passive configuration and the semi-active one is performed by means of the simulation model in terms of dynamic wheel load. In the first case, Eq. (2.33) becomes:

$$\mathbf{F}_{\text{sus}} = -(\mathbf{D}_{\text{sus}}\Delta\dot{\mathbf{z}}_{\text{sus}} + \mathbf{K}_{\text{sus}}\Delta\mathbf{z}_{\text{sus}}) \quad (\text{G.1})$$

Simulations with the stochastic road input of MnF are performed with a vehicle speed of 100 km/h (Figure G.1). For the semi-active behaviour, the coordination logic has been used.

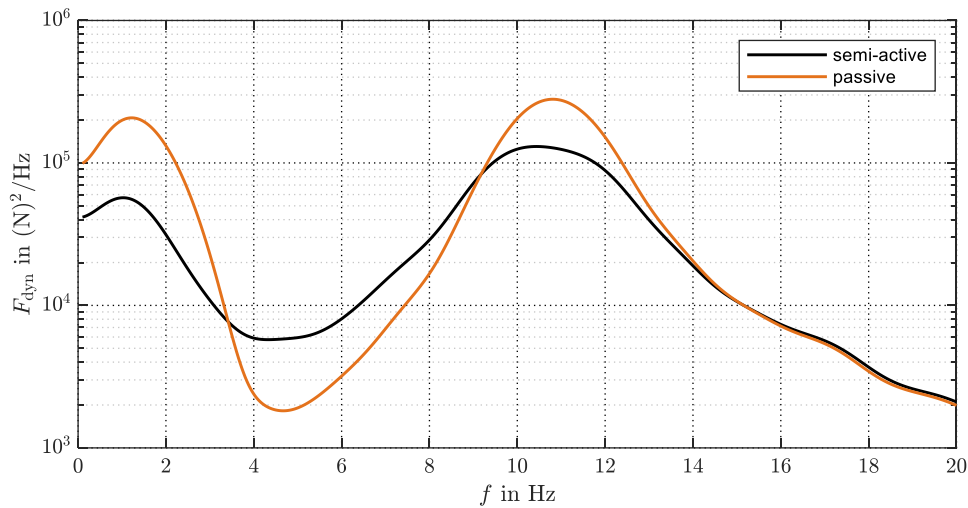


Figure G.1 : Passive and Semi-Active suspensions

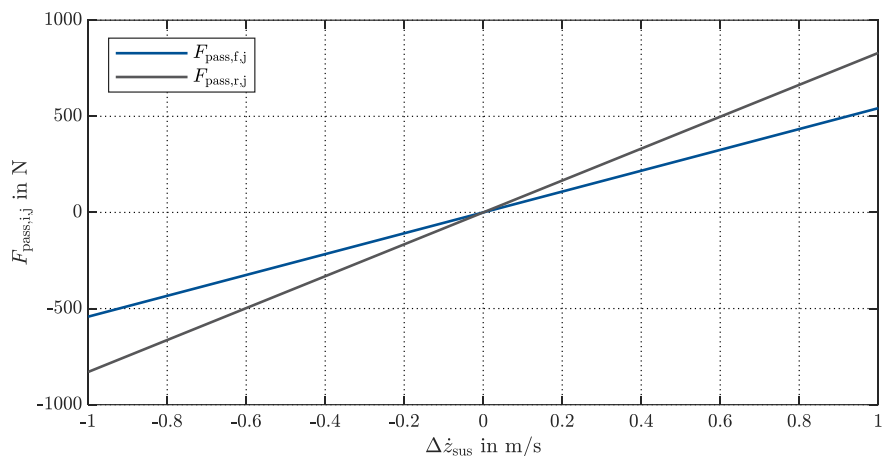
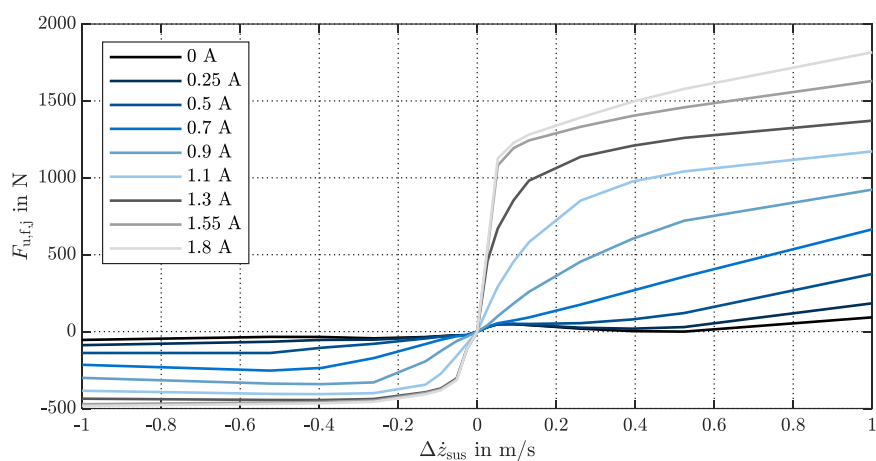
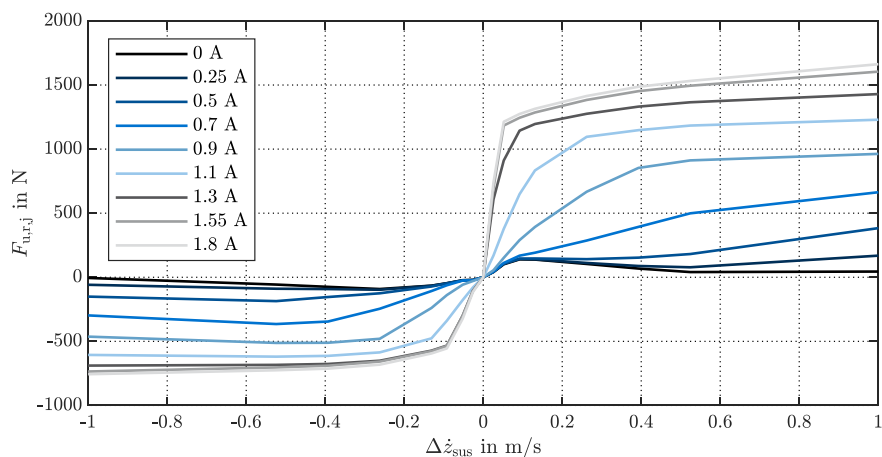
The two configurations display a similar behaviour in the frequency range between 14 Hz to 20 Hz. At 4 and 13 Hz, the passive configuration shows the lowest PSD value. Between 2 Hz and 9 Hz, it displays lower values with respect to the semi-active system. The latter results in a significant reduction of the peaks at the body and wheel eigenfrequencies, respectively around 1 Hz and 10 Hz. Considering Eq. (4.1), the following can be written:

$$F_{\text{pass},ij} = d_{\text{Bo},ij}\Delta\dot{z}_{\text{sus},ij} \quad (\text{G.2})$$

$$F_{\text{susp,d},ij} = F_{\text{pass},ij} + F_{u,ij} \quad (\text{G.3})$$

with $i \in \{f, r\}$, $j \in \{r, l\}$. The total force of the suspensions for the damping contribution, $F_{\text{susp,d},ij}$ can be split in two terms, the semi-active part $F_{u,ij}$ which is the controlled one, and the passive one $F_{\text{pass},ij}$. When the active configuration is chosen in the simulation model, the active term becomes unrestricted and can ideally assume any value. On the other hand, in the semi-active configuration, the real characteristic of the dampers is considered, depending on the control current and on the damper velocity. The dampers characteristics provided by the industrial partner are defined in a working range between -4 m/s and 4 m/s. This working range is restricted to -1

m/s and 1 m/s as the assumption of linearity for the passive component is made for such a range. The linear component is added to the non-linear one to obtain $F_{\text{susp},d,ij}$ (Figure G.2, G.3, G.4). The working range of the damper current, which controls the cross section of the actuator valve goes from 0 A to 1.8 A.

Figure G.2 : $F_{\text{pass},ij}$ Figure G.3 : $F_{u,fj}$ Figure G.4 : $F_{u,rj}$

As already stated in Sections 2.1 and 2.2, suspensions are one of the most relevant aspects in vertical vehicle dynamics and their main components are springs, dampers and ARBs. Usually, one couple of wheels, is equipped with two springs, two shock absorbers, four stops and an ARB. Between the springs types, one can mainly find: leaf springs, coil springs and air springs. Rubber springs and polyurethane elastomer ones are as well, other existing types. Leaf springs are also called elliptical or semi-elliptical and present an arc shape, at which middle point the axle is located. The ends of the arc are usually attached to the vehicle chassis. They are divided in longitudinal springs and transverse springs and can be multi/single layered or parabolic. They have been mainly implied in the 70s and are still used in heavy vehicles. They generally distribute the loads widely rather than to a single point as the coil springs. Coil springs display the simplest design and they are used on both front and rear axles. They show a linear characteristic in their whole working range. Air or gas springs have the advantage of guaranteeing that the body natural frequency remains unaltered with changes in the vehicle load. In the past, they have been mainly installed in buses and long-distance commercial vehicles. Air springs consist of a flexible bellow made of an elastomeric material, inflated with pressurised air. The latter is provided by compressors via some control valves. Air springs present a non-linear characteristic which is usually frequency-dependent in terms of stiffness. The bellow or rolling bellow entails an additional damping degree. Other possibilities are available, as the one used by Citroën called hydro-pneumatic springing (Section 3.1.3). Dampers or shock absorbers, in their passive form, need to represent a compromise between road holding and road comfort (Section 2.2). Adaptive dampers are able to switch from a lower to an higher damping ratio. Continuous damping control (CDC) provides any damping force which lies between the minimum and maximum damping rate. They are semi-active dampers, which means that they only have a dissipative effect and they can be magnetorheological, electrorheological or electromechanical. Their damping characteristics are non-linear. The first two types consist of a shock absorber filled with a magnetorheological or electrorheological fluid whose viscosity is controlled via a magnetic or electric field by varying, for example, the power of an electromagnet. Fluid viscosity increases with the intensity of the electromagnet. Electromechanical dampers consist of a shock absorber equipped with a solenoid-controlled valve, receiving a controlling signal in terms of current. Depending on the current and on the relative velocity between the chassis and the wheels (sprung and unsprung masses), a damping force is obtained. A common solution for damping adjustment consists of changing the flow area of the shock absorber throttle valve. The latter needs to have fast response speed and high control precision. Active dampers on the other hand, provide a force which is independent of the suspension speed and not purely dissipative usually by means of an electrical servopump. ARBs can be passive or active. The first ones rigidly connect two wheels of the same axle and their aim is to reduce body rolling during cornering as well as influencing the over- or understeering behaviour. At the same time they entail coupling of the wheels as road excitation on one, is transferred to the other. Active ARBs are usually designed to provide different roll stiffness in cornering. An important aspect of vehicle suspensions is the installation ratio of the spring/damper that relates the motion of the spring and the damper to the one of the wheel and tyre. Its most immediate form is expressed with Eq.(G.4) where $i \in \{f, r\}$.

$$i_i = \frac{\text{damper displacement}}{\text{wheel displacement}} \quad (\text{G.4})$$

The installation ratio can also be expressed as a result of a forces equilibrium according to Figure G.5.

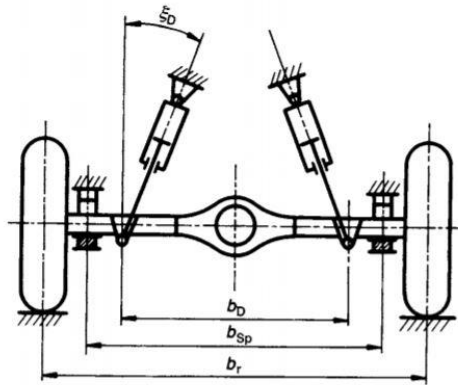


Figure G.5 : Suspensions mounting

The top of the shock absorber is fixed to the body or the frame and the bottom to a suspension link or the axle itself. The shock absorber should be mounted vertically but it can present an angle ξ_D . Assuming that $\cos \xi_D \approx 1$, the installation ratio can be written as:

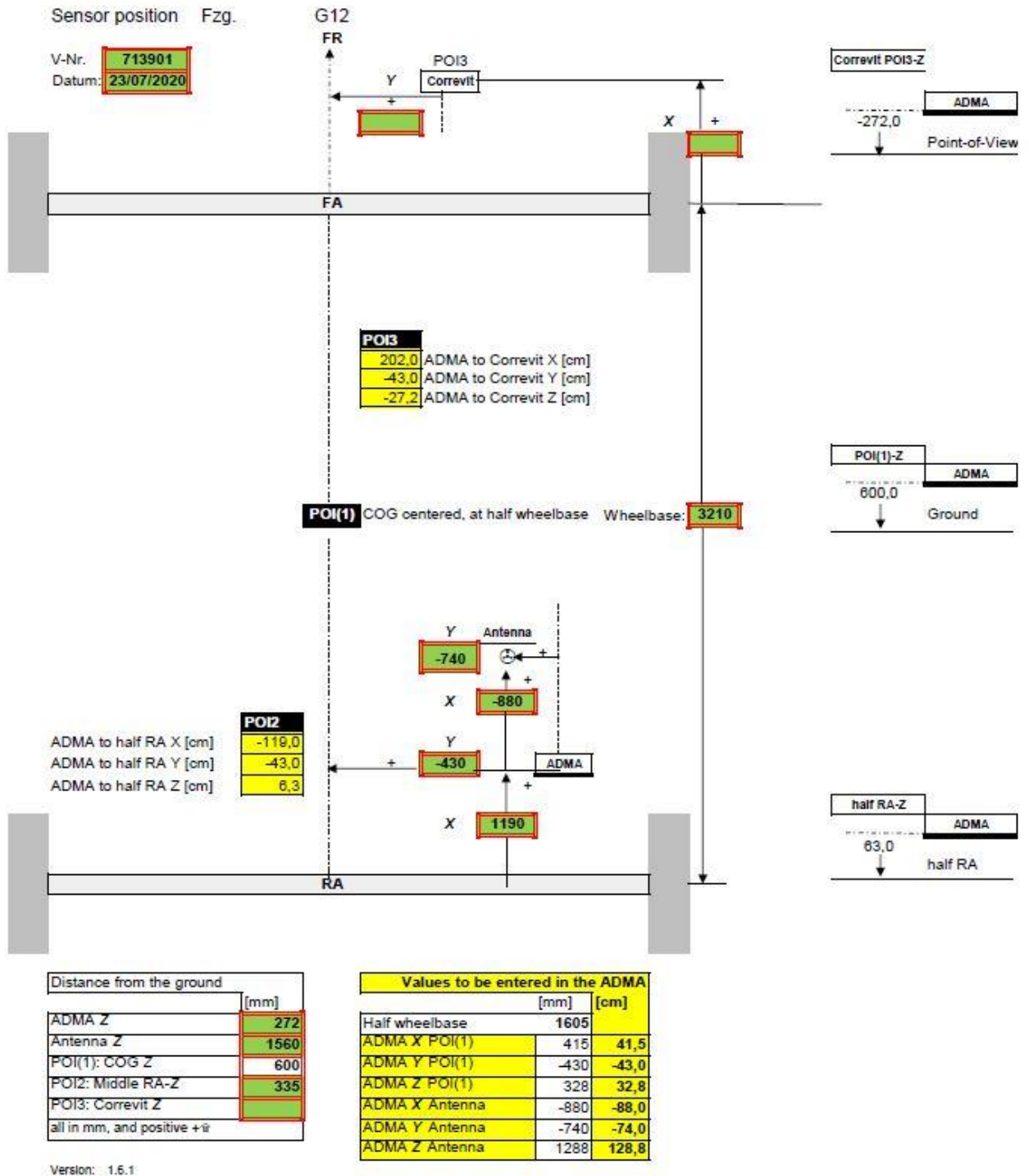
$$i_i = \frac{b_{SP}}{b_r} \quad (\text{G.5})$$

The luxury class sedan, BMW AG 7 series (G12, long version), which has been used for the experimental part in this work, is equipped with air springs, which are fed by an electrical air compressor, and by ZF continuously adjustable dampers which are controlled with the developed controlling logics. In series cars, they are thought to switch from an optimum damping or a sporty stiff one to a softer configuration, all according to the skyhook principle, where the vehicle superstructures can be adjusted independently of road conditions. In Figure G.6 there is an example of ZF CDC damper with external valve.



Figure G.6 : ZF CDC damper with external valve

Appendix H Sensor setup



As already stated in Section 5.1, ADMA stands for Automotive Dynamic Motion Analyzer and it refers to a Inertial Measurement Unit using Differential Global Positioning System. An inertial platform is equipped with three accelerometers measuring linear motions in all three directions

of movement. Three gyroscopes, mounted orthogonally, measure the rotational motions. From the available measurements, via an Extended Kalman Filter, location, spatial position and vehicle speed are derived with a precision of 1 cm. A Global Navigation Satellite System is used to compensate potential drifts in the sensors measurements. ADMA uses a CAN bus interface to output the data with an IPETRONIK module (Figure H.4). A FlexRay is used as an interface for some signals from the ECU (Figure H.6). Measurements are available in both an horizontal reference frame, represented in red (Figure H.1) and in a body-fixed one, represented in grey. The latter is the one effectively employed in the post processing of the measurements.

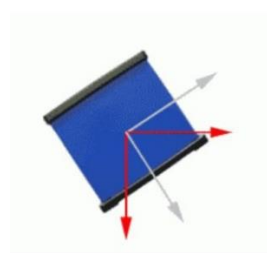


Figure H.1 : ADMA reference frame

Figure H.2 shows the test vehicle which has been used in this work. Figure H.3 displays ADMA sensor system.



Figure H.2 : BMW 7 series, G12



Figure H.3 : ADMA



Figure H.4 : FlexRay and IPETRONIK modules

Four Piezoelectric accelerometers from PCB Piezotronics have been mounted on the four wheels. In the specific, they have been fixed to the mounting bolts of the brake caliper (Figure H.5). They are fed by constant current conditioners and they provide low-impedance output signals. The mounting technique needs to be carefully analysed as it affects the high frequency performance of the sensors: this happens because, depending on the chosen technique, mass is added to the system and the mounting stiffness can be reduced. This phenomenon does not affect the frequency range up until 1000 Hz which means, considering the specific application, that the results are not dependent on the mounting, as the frequency range of interest is the one between 0 and 20 Hz.



Figure H.5 : Accelerometer's mounting

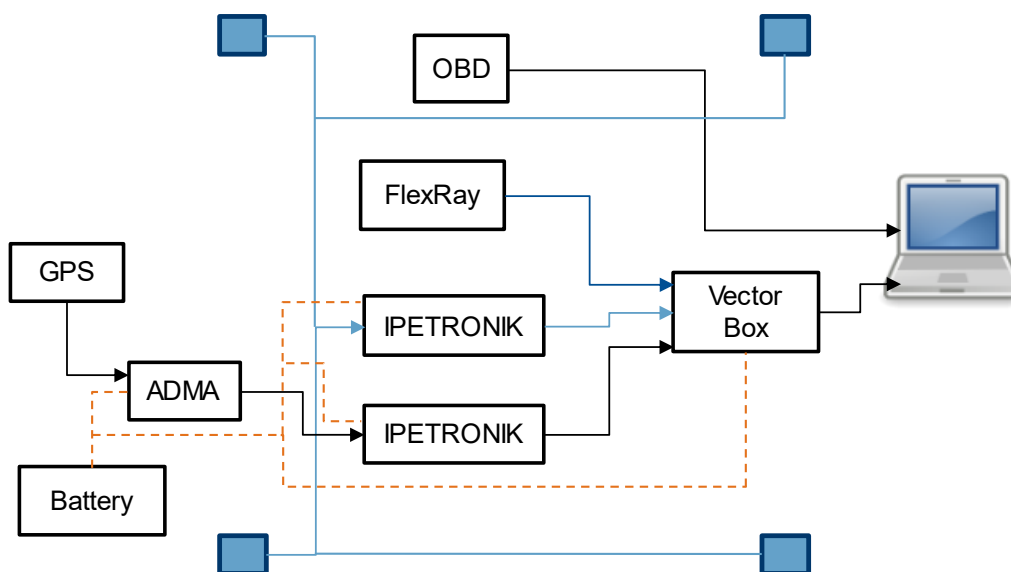


Figure H.6 : Overall sensors and electronic modules scheme

Appendix I Measurements processing

In the following, the analysis of the test measurements is performed as done in Section 5.2. An example of how signals have been processed in this work is shown. Four measurements are available for the FnP track for the pure optimal P controller, as listed in Table I.3. Figure I.1 shows the four raw signals of the roll angular rate of the body. As explained in Section 5.2, raw signals are filtered with a lowpass filter with 18 Hz as a cut-off frequency, realigned and cut according to the shortest signal length (Figure I.2).

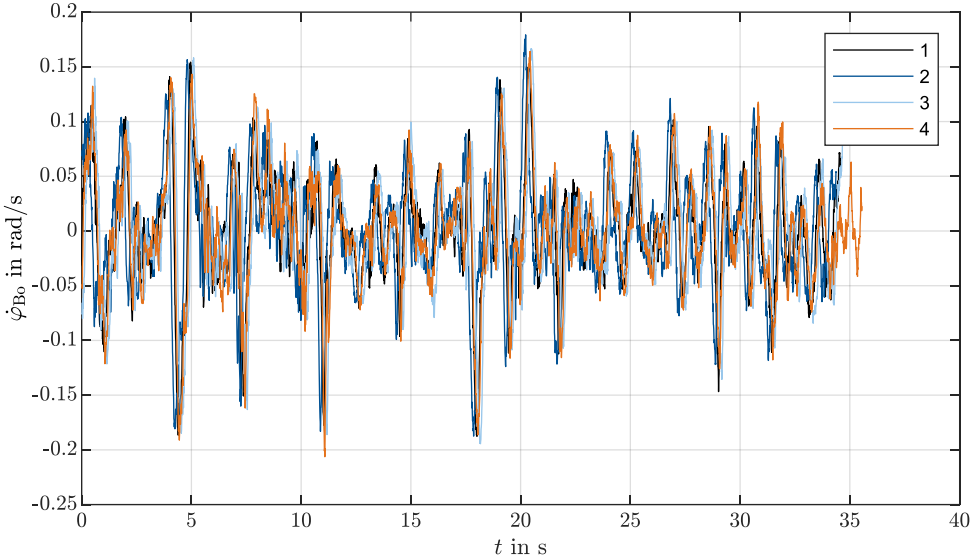


Figure I.1 : Raw signals

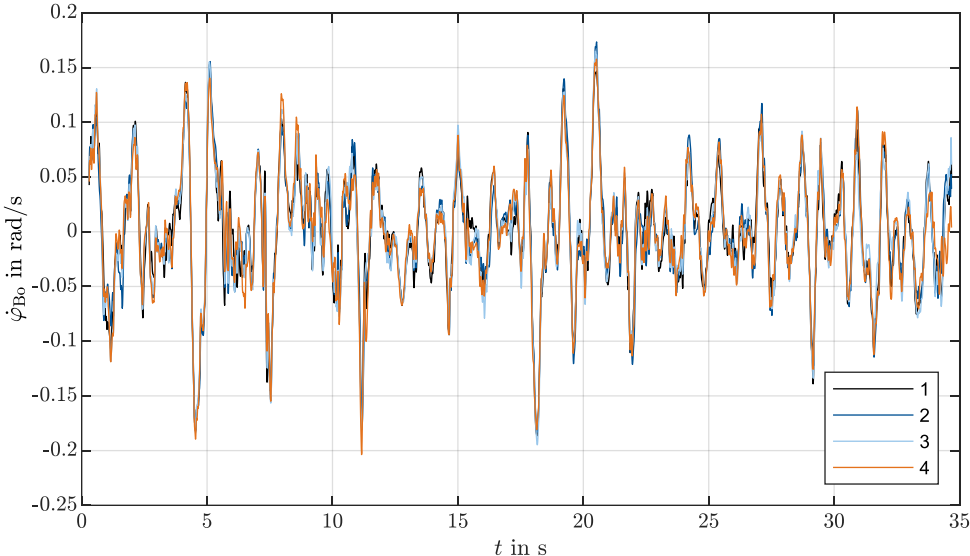


Figure I.2 : Processed signals in time with steps 1, 2 and 3

Figure I.3 displays the PSD with a focus on the range from 0 to 5 Hz of the signals as processed with steps 1, 2 and 3 of the procedure described in Section 5.2. Figure I.4 shows the final result consisting of an average of the PSD of the signals of Figure I.3 in the frequency domain and a subsequent smoothing with a moving average filter with 10 samples of span.

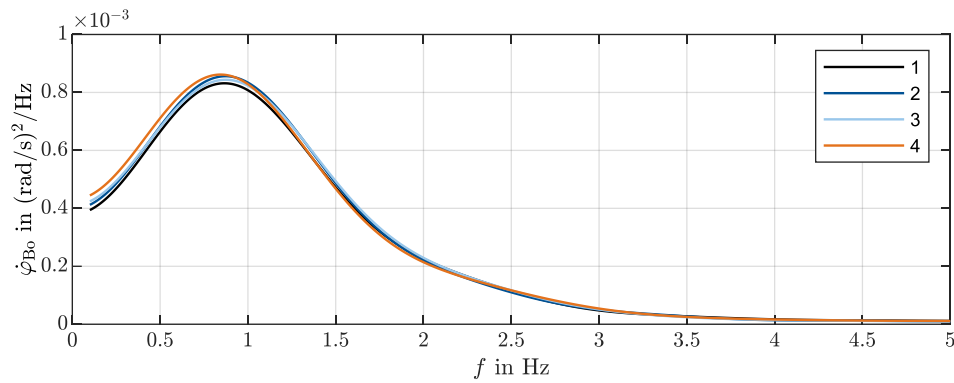


Figure I.3 : PSD of the signals, zoom on 0-5 Hz; step 4

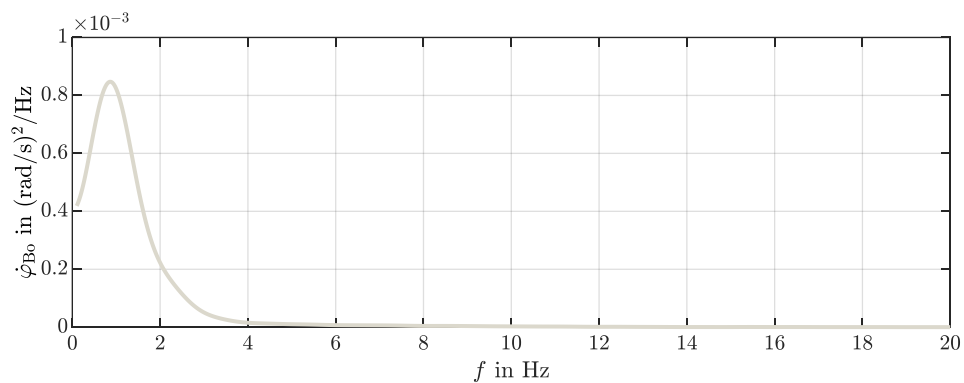


Figure I.4 : Averaged and smoothed PSD of the signals, steps 5 and 6

The following tables show an analysis of the raw signals in terms of mean of the RMS and coefficient of variation. It has been performed for all the available tests measurements.

Table I.1: μ for section BA, Section 5.2

Signals	Optimal R	Optimal P	R, $D_i = 0.05$	R, $D_i = 2$
\ddot{z}_{Bo} , m/s ²	1.13	0.924	1.06	1.84
$\ddot{z}_{w,fr}$, m/s ²	12.8	14.1	14.0	12.3
$\ddot{z}_{w,fl}$, m/s ²	0.706	0.466	0.648	0.667
$\ddot{z}_{w,rl}$, m/s ²	12.7	12.4	13.9	12.7
$\ddot{z}_{w,rr}$, m/s ²	10.9	11.1	10.9	10.3
$\dot{\theta}_{Bo}$, rad/s	$32.0 \cdot 10^{-3}$	$24.6 \cdot 10^{-3}$	$29.7 \cdot 10^{-3}$	$33.9 \cdot 10^{-3}$
$\dot{\phi}_{Bo}$, rad/s	$43.2 \cdot 10^{-3}$	$41.1 \cdot 10^{-3}$	$44.7 \cdot 10^{-3}$	$43.4 \cdot 10^{-3}$

Table I.2: c_v for section BA, Section 5.2

Signals	Optimal R	Optimal P	R, $D_i = 0.05$	R, $D_i = 2$
\ddot{z}_{Bo}	$11.7 \cdot 10^{-3}$	$46.0 \cdot 10^{-4}$	$27.4 \cdot 10^{-3}$	$94.0 \cdot 10^{-4}$
$\ddot{z}_{w,fr}$	$25.6 \cdot 10^{-3}$	$53.0 \cdot 10^{-4}$	$12.1 \cdot 10^{-3}$	$21.1 \cdot 10^{-3}$
$\ddot{z}_{w,fl}$	$15.7 \cdot 10^{-2}$	0.100	$41.3 \cdot 10^{-3}$	$77.4 \cdot 10^{-3}$
$\ddot{z}_{w,rl}$	$28.5 \cdot 10^{-3}$	$30.0 \cdot 10^{-3}$	$48.1 \cdot 10^{-3}$	$36.8 \cdot 10^{-3}$
$\ddot{z}_{w,rr}$	$15.6 \cdot 10^{-3}$	$49.0 \cdot 10^{-4}$	$10.8 \cdot 10^{-3}$	$19.4 \cdot 10^{-3}$
$\dot{\theta}_{Bo}$	$18.0 \cdot 10^{-4}$	$13.5 \cdot 10^{-3}$	$12.7 \cdot 10^{-3}$	$68.0 \cdot 10^{-4}$
$\dot{\varphi}_{Bo}$	$77.0 \cdot 10^{-4}$	$10.3 \cdot 10^{-3}$	$78.0 \cdot 10^{-4}$	$11.9 \cdot 10^{-3}$

Table I.3: Number of tests measurements in Freising/Pulling, Section 5.3

	Optimal R	Optimal P	R, $D_{t_{Bo}} = 0$	R, $D_{t_{Bo}} = 1$
CD	4	4	3	3
FnP	4	4	3	3

Table I.4: μ for section CD, Section 5.3

Signals	Optimal R	Optimal P	R, $D_{t_{Bo}} = 0$	R, $D_{t_{Bo}} = 1$
$\ddot{z}_{Bo}, \text{m/s}^2$	0.732	0.677	0.734	0.792
$\ddot{z}_{w,fr}, \text{m/s}^2$	7.51	8.05	7.46	7.02
$\ddot{z}_{w,fl}, \text{m/s}^2$	0.296	38.5	0.257	0.295
$\ddot{z}_{w,rl}, \text{m/s}^2$	5.01	5.26	5.01	5.18
$\ddot{z}_{w,rr}, \text{m/s}^2$	5.57	6.28	5.39	5.99
$\dot{\theta}_{Bo}, \text{rad/s}$	$27.4 \cdot 10^{-3}$	$24.9 \cdot 10^{-3}$	$27.7 \cdot 10^{-3}$	$27.5 \cdot 10^{-3}$
$\dot{\varphi}_{Bo}, \text{rad/s}$	$35.2 \cdot 10^{-3}$	$33.6 \cdot 10^{-3}$	$34.9 \cdot 10^{-3}$	$34.3 \cdot 10^{-3}$

Table I.5: c_v for section CD, Section 5.3

Signals	Optimal R	Optimal P	R, $D_{t_{Bo}} = 0$	R, $D_{t_{Bo}} = 1$
\ddot{z}_{Bo}	$26.8 \cdot 10^{-3}$	$21.6 \cdot 10^{-3}$	$13.3 \cdot 10^{-3}$	$25.9 \cdot 10^{-3}$
$\ddot{z}_{w,fr}$	$25.1 \cdot 10^{-3}$	$24.0 \cdot 10^{-3}$	$69.0 \cdot 10^{-4}$	$24.6 \cdot 10^{-3}$
$\ddot{z}_{w,fl}$	$44.5 \cdot 10^{-3}$	1.78	$43.6 \cdot 10^{-3}$	$26.4 \cdot 10^{-3}$
$\ddot{z}_{w,rl}$	$42.3 \cdot 10^{-3}$	$47.8 \cdot 10^{-3}$	$47.5 \cdot 10^{-3}$	$96.5 \cdot 10^{-3}$
$\ddot{z}_{w,rr}$	$33.5 \cdot 10^{-3}$	$18.2 \cdot 10^{-3}$	$17.9 \cdot 10^{-3}$	$19.4 \cdot 10^{-3}$
$\dot{\theta}_{Bo}$	$11.3 \cdot 10^{-3}$	$20.1 \cdot 10^{-3}$	$69.0 \cdot 10^{-4}$	$82.0 \cdot 10^{-4}$
$\dot{\phi}_{Bo}$	$16.5 \cdot 10^{-3}$	$78.0 \cdot 10^{-4}$	$80.0 \cdot 10^{-4}$	$24.3 \cdot 10^{-3}$

Table I.6: μ for FnP, Section 5.3

Signals	Optimal R	Optimal P	R, $D_{t_{Bo}} = 0$	R, $D_{t_{Bo}} = 1$
$\ddot{z}_{Bo}, \text{m/s}^2$	1.62	1.45	1.63	1.70
$\ddot{z}_{w,fr}, \text{m/s}^2$	9.17	9.60	8.94	9.95
$\ddot{z}_{w,fl}, \text{m/s}^2$	0.543	32.3	0.471	0.722
$\ddot{z}_{w,rl}, \text{m/s}^2$	7.15	7.59	7.34	8.20
$\ddot{z}_{w,rr}, \text{m/s}^2$	7.90	8.37	7.93	8.97
$\dot{\theta}_{Bo}, \text{rad/s}$	$45.7 \cdot 10^{-3}$	$38.7 \cdot 10^{-3}$	$46.0 \cdot 10^{-3}$	$47.3 \cdot 10^{-3}$
$\dot{\phi}_{Bo}, \text{rad/s}$	$56.4 \cdot 10^{-3}$	$52.2 \cdot 10^{-3}$	$54.3 \cdot 10^{-3}$	$56.1 \cdot 10^{-3}$

Table I.7: c_v for FnP, Section 5.3

Signals	Optimal R	Optimal P	R, $D_{t_{Bo}} = 0$	R, $D_{t_{Bo}} = 1$
\ddot{z}_{Bo}	$83.0 \cdot 10^{-4}$	$67.0 \cdot 10^{-4}$	$72.0 \cdot 10^{-4}$	$15.6 \cdot 10^{-3}$
$\ddot{z}_{w,fr}$	$41.7 \cdot 10^{-3}$	$46.5 \cdot 10^{-4}$	$15.5 \cdot 10^{-3}$	$61.0 \cdot 10^{-3}$
$\ddot{z}_{w,fl}$	$57.7 \cdot 10^{-3}$	1.46	0.156	0.355
$\ddot{z}_{w,rl}$	$23.7 \cdot 10^{-3}$	$25.3 \cdot 10^{-3}$	$78.4 \cdot 10^{-5}$	$22.2 \cdot 10^{-3}$
$\ddot{z}_{w,rr}$	$33.0 \cdot 10^{-3}$	$58.2 \cdot 10^{-3}$	$20.7 \cdot 10^{-3}$	$66.3 \cdot 10^{-3}$
$\dot{\theta}_{Bo}$	$95.0 \cdot 10^{-4}$	$34.2 \cdot 10^{-3}$	$49.0 \cdot 10^{-4}$	$15.8 \cdot 10^{-3}$
$\dot{\phi}_{Bo}$	$13.3 \cdot 10^{-3}$	$80.0 \cdot 10^{-4}$	$57.0 \cdot 10^{-4}$	$73.0 \cdot 10^{-4}$

Table I.8: Number of tests measurements in Aschheim, Section 5.4

	Coordination logic	Modified P
AB	4	4
BA	4	4

Table I.9: μ for section AB, Section 5.4

Signals	Coordination logic	Modified P
$\ddot{z}_{Bo}, m/s^2$	1.15	1.11
$\ddot{z}_{w,fr}, m/s^2$	20.7	21.1
$\ddot{z}_{w,fl}, m/s^2$	18.8	0.612
$\ddot{z}_{w,rl}, m/s^2$	13.3	13.5
$\ddot{z}_{w,rr}, m/s^2$	18.0	18.0
$\dot{\theta}_{Bo}, rad/s$	$30.7 \cdot 10^{-3}$	$29.9 \cdot 10^{-3}$
$\dot{\phi}_{Bo}, rad/s$	$57.0 \cdot 10^{-3}$	$56.3 \cdot 10^{-3}$

Table I.10: c_v for section AB, Section 5.4

Signals	Coordination logic	Modified P
\ddot{z}_{Bo}	$20.2 \cdot 10^{-3}$	$82.0 \cdot 10^{-4}$
$\ddot{z}_{w,fr}$	$19.1 \cdot 10^{-3}$	$23.5 \cdot 10^{-3}$
$\ddot{z}_{w,fl}$	$77.6 \cdot 10^{-3}$	0.165
$\ddot{z}_{w,rl}$	$28.6 \cdot 10^{-3}$	$12.5 \cdot 10^{-3}$
$\ddot{z}_{w,rr}$	$32.3 \cdot 10^{-3}$	$28.6 \cdot 10^{-3}$
$\dot{\theta}_{Bo}$	$18.6 \cdot 10^{-3}$	$34.9 \cdot 10^{-3}$
$\dot{\phi}_{Bo}$	$14.6 \cdot 10^{-3}$	$14.4 \cdot 10^{-3}$

Table I.11: μ for section BA, Section 5.4

Signals	Coordination logic	Modified P
$\ddot{z}_{Bo}, m/s^2$	0.972	0.964
$\ddot{z}_{w,fr}, m/s^2$	13.2	13.7

$\ddot{z}_{w,fl}$, m/s ²	16.8	0.581
$\ddot{z}_{w,rl}$, m/s ²	12.5	12.4
$\ddot{z}_{w,rr}$, m/s ²	10.8	10.7
$\dot{\theta}_{Bo}$, rad/s	$25.7 \cdot 10^{-3}$	$25.4 \cdot 10^{-3}$
$\dot{\phi}_{Bo}$, rad/s	$42.8 \cdot 10^{-3}$	$41.9 \cdot 10^{-3}$

Table I.12: c_v for section BA, Section 5.4

Signals	Coordination logic	Modified P
\ddot{z}_{Bo}	$12.6 \cdot 10^{-3}$	$10.2 \cdot 10^{-4}$
$\ddot{z}_{w,fr}$	$14.2 \cdot 10^{-3}$	$34.2 \cdot 10^{-4}$
$\ddot{z}_{w,fl}$	$52.2 \cdot 10^{-3}$	0.143
$\ddot{z}_{w,rl}$	$15.5 \cdot 10^{-3}$	$12.6 \cdot 10^{-3}$
$\ddot{z}_{w,rr}$	$11.3 \cdot 10^{-3}$	$24.6 \cdot 10^{-3}$
$\dot{\theta}_{Bo}$	$58.0 \cdot 10^{-4}$	$12.8 \cdot 10^{-3}$
$\dot{\phi}_{Bo}$	$16.0 \cdot 10^{-3}$	$18.3 \cdot 10^{-3}$

Table I.13: Number of tests measurements in Freising/Pulling, Section 5.4

	Coordination logic	Modified P
CD	2	4
FnP	2	4

Table I.14: μ for section CD, Section 5.4

Signals	Coordination logic	Modified P
\ddot{z}_{Bo} , m/s ²	0.704	0.684
$\ddot{z}_{w,fr}$, m/s ²	7.15	7.97
$\ddot{z}_{w,fl}$, m/s ²	25.8	0.294
$\ddot{z}_{w,rl}$, m/s ²	4.88	4.84
$\ddot{z}_{w,rr}$, m/s ²	5.41	6.23

$\dot{\theta}_{Bo}$, rad/s	$26.2 \cdot 10^{-3}$	$26.1 \cdot 10^{-3}$
$\dot{\varphi}_{Bo}$, rad/s	$34.0 \cdot 10^{-3}$	$34.2 \cdot 10^{-3}$

Table I.15: c_v for section CD, Section 5.4

Signals	Coordination logic	Modified P
\ddot{z}_{Bo}	$12.9 \cdot 10^{-3}$	$36.2 \cdot 10^{-3}$
$\ddot{z}_{w,fr}$	$86.0 \cdot 10^{-4}$	$53.3 \cdot 10^{-3}$
$\ddot{z}_{w,fl}$	1.39	$59.5 \cdot 10^{-3}$
$\ddot{z}_{w,rl}$	$63.0 \cdot 10^{-4}$	$89.2 \cdot 10^{-3}$
$\ddot{z}_{w,rr}$	$14.9 \cdot 10^{-3}$	$74.0 \cdot 10^{-3}$
$\dot{\theta}_{Bo}$	$10.0 \cdot 10^{-4}$	$36.3 \cdot 10^{-3}$
$\dot{\varphi}_{Bo}$	$88.0 \cdot 10^{-4}$	$23.9 \cdot 10^{-3}$

Table I.16: μ for section FnP, Section 5.4

Signals	Coordination logic	Modified P
\ddot{z}_{Bo} , m/s ²	1.46	1.43
$\ddot{z}_{w,fr}$, m/s ²	8.68	9.15
$\ddot{z}_{w,fl}$, m/s ²	3.91	0.582
$\ddot{z}_{w,rl}$, m/s ²	7.42	7.19
$\ddot{z}_{w,rr}$, m/s ²	7.74	7.86
$\dot{\theta}_{Bo}$, rad/s	$38.5 \cdot 10^{-3}$	$37.6 \cdot 10^{-3}$
$\dot{\varphi}_{Bo}$, rad/s	$52.8 \cdot 10^{-3}$	$53.2 \cdot 10^{-3}$

Table I.17: c_v for section FnP, Section 5.4

Signals	Coordination logic	Modified P
\ddot{z}_{Bo}	$26.0 \cdot 10^{-4}$	$14.2 \cdot 10^{-3}$
$\ddot{z}_{w,fr}$	$40.2 \cdot 10^{-3}$	$99.9 \cdot 10^{-3}$
$\ddot{z}_{w,fl}$	1.21	$73.5 \cdot 10^{-3}$
$\ddot{z}_{w,rl}$	$64.0 \cdot 10^{-4}$	$12.8 \cdot 10^{-3}$
$\ddot{z}_{w,rr}$	$32.4 \cdot 10^{-3}$	$60.3 \cdot 10^{-3}$

$\dot{\theta}_{Bo}$	$13.3 \cdot 10^{-3}$	$24.8 \cdot 10^{-3}$
$\dot{\varphi}_{Bo}$	$98.0 \cdot 10^{-4}$	$21.8 \cdot 10^{-3}$

Table I.18: Number of tests measurements in Freising/Pulling, heave, Section 5.6

	$\alpha_h = 0.1$	$\alpha_h = 0.5$	$\alpha_h = 0.7$	$\alpha_h = 0.9$
CD	2	2	2	2
FnP	2	2	2	2

Table I.19: Number of tests measurements in Freising/Pulling, pitch, Section 5.6

	$\alpha_p = 0.3$	$\alpha_p = 0.5$	$\alpha_p = 0.7$	$\alpha_p = 0.9$
CD	2	2	2	2
FnP	2	2	2	2

Table I.20: Number of tests measurements in Freising/Pulling, roll, Section 5.6

	$\alpha_r = 0.1$	$\alpha_r = 0.3$	$\alpha_r = 0.5$	$\alpha_r = 0.7$	$\alpha_r = 0.9$
CD	2	2	2	2	2
FnP	2	2	2	2	2

Table I.21: Number of tests measurements in Freising/Pulling, twist, Section 5.6

	$\alpha_t = 0.1$	$\alpha_t = 0.5$	$\alpha_t = 0.7$	$\alpha_t = 0.9$
CD	2	2	2	2
FnP	2	2	2	2

Table I.22: μ for FnP, heave, Section 5.6

Signals	$\alpha_h = 0.1$	$\alpha_h = 0.5$	$\alpha_h = 0.7$	$\alpha_h = 0.9$
$\ddot{z}_{Bo}, \text{ m/s}^2$	1.38	1.45	1.48	1.51
$\ddot{z}_{w,fr}, \text{ m/s}^2$	9.24	9.51	9.49	9.61
$\ddot{z}_{w,fl}, \text{ m/s}^2$	49.5	6.13	8.99	8.97
$\ddot{z}_{w,rl}, \text{ m/s}^2$	7.58	7.65	7.17	8.15
$\ddot{z}_{w,rr}, \text{ m/s}^2$	8.05	8.22	7.99	8.04

$\dot{\theta}_{Bo}, \text{rad/s}$	$37.0 \cdot 10^{-3}$	$36.4 \cdot 10^{-3}$	$35.8 \cdot 10^{-3}$	$34.5 \cdot 10^{-3}$
$\dot{\phi}_{Bo}, \text{rad/s}$	$52.4 \cdot 10^{-3}$	$53.5 \cdot 10^{-3}$	$54.0 \cdot 10^{-3}$	$52.3 \cdot 10^{-3}$

Table I.23: c_v for FnP, heave, Section 5.6

Signals	$\alpha_h = 0.1$	$\alpha_h = 0.5$	$\alpha_h = 0.7$	$\alpha_h = 0.9$
\ddot{z}_{Bo}	$65.0 \cdot 10^{-4}$	$28.0 \cdot 10^{-4}$	$77.0 \cdot 10^{-4}$	$11.7 \cdot 10^{-3}$
$\ddot{z}_{w,fr}$	$35.6 \cdot 10^{-3}$	$56.10 \cdot 10^{-3}$	$44.3 \cdot 10^{-3}$	$62.5 \cdot 10^{-3}$
$\ddot{z}_{w,fl}$	0.695	$78.2 \cdot 10^{-3}$	$31.3 \cdot 10^{-3}$	$33.6 \cdot 10^{-3}$
$\ddot{z}_{w,rl}$	$37.3 \cdot 10^{-3}$	$19.0 \cdot 10^{-4}$	$69.0 \cdot 10^{-4}$	0.152
$\ddot{z}_{w,rr}$	$52.9 \cdot 10^{-3}$	$72.8 \cdot 10^{-3}$	$47.9 \cdot 10^{-3}$	$44.2 \cdot 10^{-3}$
$\dot{\theta}_{Bo}$	$29.1 \cdot 10^{-3}$	$74.0 \cdot 10^{-4}$	$49.0 \cdot 10^{-4}$	$17.5 \cdot 10^{-3}$
$\dot{\phi}_{Bo}$	$62.0 \cdot 10^{-4}$	$15.7 \cdot 10^{-3}$	$57.0 \cdot 10^{-4}$	$17.0 \cdot 10^{-3}$

Table I.24: μ for FnP, pitch, Section 5.6

Signals	$\alpha_p = 0.3$	$\alpha_p = 0.5$	$\alpha_p = 0.7$	$\alpha_p = 0.9$
$\ddot{z}_{Bo}, \text{m/s}^2$	1.43	1.46	1.43	1.44
$\ddot{z}_{w,fr}, \text{m/s}^2$	9.66	9.36	9.36	9.80
$\ddot{z}_{w,fl}, \text{m/s}^2$	8.56	8.40	8.50	8.39
$\ddot{z}_{w,rl}, \text{m/s}^2$	7.43	7.48	7.60	7.60
$\ddot{z}_{w,rr}, \text{m/s}^2$	8.56	7.93	8.40	9.13
$\dot{\theta}_{Bo}, \text{rad/s}$	$38.1 \cdot 10^{-3}$	$41.8 \cdot 10^{-3}$	$40.0 \cdot 10^{-3}$	$43.1 \cdot 10^{-3}$
$\dot{\phi}_{Bo}, \text{rad/s}$	$53.6 \cdot 10^{-3}$	$53.5 \cdot 10^{-3}$	$51.9 \cdot 10^{-3}$	$53.0 \cdot 10^{-3}$

Table I.25: c_v for FnP, pitch, Section 5.6

Signals	$\alpha_p = 0.3$	$\alpha_p = 0.5$	$\alpha_p = 0.7$	$\alpha_p = 0.9$
\ddot{z}_{Bo}	$14.5 \cdot 10^{-3}$	$28.8 \cdot 10^{-3}$	$85.0 \cdot 10^{-4}$	$23.0 \cdot 10^{-4}$
$\ddot{z}_{w,fr}$	$96.0 \cdot 10^{-3}$	$84.3 \cdot 10^{-3}$	$76.8 \cdot 10^{-3}$	$27.7 \cdot 10^{-3}$
$\ddot{z}_{w,fl}$	$71.0 \cdot 10^{-4}$	$65.0 \cdot 10^{-4}$	$32.9 \cdot 10^{-3}$	$12.6 \cdot 10^{-3}$
$\ddot{z}_{w,rl}$	$97.0 \cdot 10^{-4}$	$34.0 \cdot 10^{-4}$	$47.0 \cdot 10^{-4}$	$64.0 \cdot 10^{-4}$

$\ddot{z}_{w,rr}$	$84.1 \cdot 10^{-3}$	$24.5 \cdot 10^{-3}$	$68.2 \cdot 10^{-3}$	$57.3 \cdot 10^{-3}$
$\dot{\theta}_{Bo}$	$22.5 \cdot 10^{-3}$	$86.3 \cdot 10^{-3}$	$20.1 \cdot 10^{-3}$	$78.0 \cdot 10^{-4}$
$\dot{\phi}_{Bo}$	$22.8 \cdot 10^{-3}$	$16.6 \cdot 10^{-3}$	$16.3 \cdot 10^{-3}$	$59.0 \cdot 10^{-4}$

Table I.26: μ for FnP, roll, Section 5.6

Signals	$\alpha_r = 0.1$	$\alpha_r = 0.3$	$\alpha_r = 0.5$	$\alpha_r = 0.7$	$\alpha_r = 0.9$
$\ddot{z}_{Bo}, \text{m/s}^2$	1.44	1.43	1.42	1.46	1.49
$\ddot{z}_{w,fr}, \text{m/s}^2$	10.3	10.1	9.28	9.59	9.07
$\ddot{z}_{w,fl}, \text{m/s}^2$	8.39	8.47	8.57	8.77	8.53
$\ddot{z}_{w,rl}, \text{m/s}^2$	7.25	7.31	7.48	7.71	8.07
$\ddot{z}_{w,rr}, \text{m/s}^2$	8.97	8.74	8.14	8.67	8.40
$\dot{\theta}_{Bo}, \text{rad/s}$	$38.2 \cdot 10^{-3}$	$37.8 \cdot 10^{-3}$	$37.1 \cdot 10^{-3}$	$37.5 \cdot 10^{-3}$	$37.3 \cdot 10^{-3}$
$\dot{\phi}_{Bo}, \text{rad/s}$	$53.2 \cdot 10^{-3}$	$53.9 \cdot 10^{-3}$	$52.7 \cdot 10^{-3}$	$52.9 \cdot 10^{-3}$	$51.7 \cdot 10^{-3}$

Table I.27: c_v for FnP, roll, Section 5.6

Signals	$\alpha_r = 0.1$	$\alpha_r = 0.3$	$\alpha_r = 0.5$	$\alpha_r = 0.7$	$\alpha_r = 0.9$
\ddot{z}_{Bo}	$68.0 \cdot 10^{-4}$	$87.0 \cdot 10^{-4}$	$17.4 \cdot 10^{-3}$	$11.3 \cdot 10^{-3}$	$10.4 \cdot 10^{-3}$
$\ddot{z}_{w,fr}$	$89.7 \cdot 10^{-3}$	$35.2 \cdot 10^{-3}$	0.123	$36.9 \cdot 10^{-3}$	$64.1 \cdot 10^{-3}$
$\ddot{z}_{w,fl}$	$43.6 \cdot 10^{-3}$	$16.4 \cdot 10^{-3}$	$13.9 \cdot 10^{-3}$	$72.0 \cdot 10^{-4}$	$15.0 \cdot 10^{-3}$
$\ddot{z}_{w,rl}$	$62.2 \cdot 10^{-3}$	$13.6 \cdot 10^{-3}$	$32.8 \cdot 10^{-3}$	$68.0 \cdot 10^{-4}$	$20.0 \cdot 10^{-3}$
$\ddot{z}_{w,rr}$	0.108	$29.1 \cdot 10^{-3}$	0.135	$28.2 \cdot 10^{-3}$	$95.0 \cdot 10^{-3}$
$\dot{\theta}_{Bo}$	$17.5 \cdot 10^{-3}$	$77.0 \cdot 10^{-4}$	$25.0 \cdot 10^{-3}$	$14.8 \cdot 10^{-3}$	$21.8 \cdot 10^{-3}$
$\dot{\phi}_{Bo}$	$11.0 \cdot 10^{-3}$	$13.4 \cdot 10^{-3}$	$71.0 \cdot 10^{-4}$	$34.0 \cdot 10^{-4}$	$19.6 \cdot 10^{-3}$

Table I.28: μ for FnP, twist, Section 5.6

Signals	$\alpha_t = 0.1$	$\alpha_t = 0.5$	$\alpha_t = 0.7$	$\alpha_t = 0.9$
$\ddot{z}_{Bo}, \text{m/s}^2$	1.50	1.43	1.45	1.45
$\ddot{z}_{w,fr}, \text{m/s}^2$	9.82	10.3	9.80	9.74

$\ddot{z}_{w,fl}$, m/s ²	8.86	8.48	8.54	8.85
$\ddot{z}_{w,rl}$, m/s ²	8.08	7.34	7.31	7.44
$\ddot{z}_{w,rr}$, m/s ²	9.19	9.08	8.71	8.59
$\dot{\theta}_{Bo}$, rad/s	$38.1 \cdot 10^{-3}$	$38.7 \cdot 10^{-3}$	$34.9 \cdot 10^{-3}$	$38.9 \cdot 10^{-3}$
$\dot{\varphi}_{Bo}$, rad/s	$53.2 \cdot 10^{-3}$	$54.6 \cdot 10^{-3}$	$53.1 \cdot 10^{-3}$	$53.1 \cdot 10^{-3}$

Table I.29: c_v for FnP, twist, Section 5.6

Signals	$\alpha_t = 0.1$	$\alpha_t = 0.5$	$\alpha_t = 0.7$	$\alpha_t = 0.9$
\ddot{z}_{Bo}	$25.0 \cdot 10^{-4}$	$76.0 \cdot 10^{-4}$	$44.0 \cdot 10^{-4}$	$10.0 \cdot 10^{-5}$
$\ddot{z}_{w,fr}$	$50.8 \cdot 10^{-3}$	0.103	$90.0 \cdot 10^{-4}$	$30.1 \cdot 10^{-3}$
$\ddot{z}_{w,fl}$	$75.0 \cdot 10^{-4}$	$47.1 \cdot 10^{-3}$	$38.4 \cdot 10^{-3}$	$58.2 \cdot 10^{-3}$
$\ddot{z}_{w,rl}$	$19.3 \cdot 10^{-3}$	$48.3 \cdot 10^{-3}$	$36.0 \cdot 10^{-3}$	$29.5 \cdot 10^{-3}$
$\ddot{z}_{w,rr}$	$32.4 \cdot 10^{-3}$	0.119	$13.4 \cdot 10^{-3}$	$17.1 \cdot 10^{-3}$
$\dot{\theta}_{Bo}$	$94.0 \cdot 10^{-4}$	$99.0 \cdot 10^{-4}$	$43.0 \cdot 10^{-4}$	$13.5 \cdot 10^{-3}$
$\dot{\varphi}_{Bo}$	$26.0 \cdot 10^{-4}$	$15.4 \cdot 10^{-3}$	$21.0 \cdot 10^{-4}$	$22.6 \cdot 10^{-3}$

Appendix J Implementation of the logic in the vehicle test

As stated in Section 5.1, a reimplementaion of the developed logic from the simulation model, to the BMW development environment was needed. This entailed two main difficulties:

1. The BACE, (BMW Autocoding Environment), only provided certain blocks with respect to the available Simulink libraries. This led to the necessity of rebuilding some of the blocks as the *moving RMS* one.
2. In the software creation phase, a maximum memory allocation was available with the implementation of the developed logic and therefore adjustments had to be made.

The modified P controller could be easily implemented in the new model paying attention to replace the vector-matrix multiplication with direct vector-constants multiplication and subsequent sum or subtraction of the equation terms. The coordination logic on the other hand, was modified to meet the memory requirements on the ECU. The adaptive gain law, was corrected as it follows:

$$G_R = \begin{cases} G_{PS} + G_{sus,def} & \text{if } F_{dyn,check} = 1 \wedge G_{PS} < G_{Fdyn,max} \\ 1 & \text{if } G_{PS} + G_{sus,def} > 1 \\ G_{Fdyn,max} & \text{else} \end{cases} \quad (J.1)$$

Where:

$$G_{PS} = 0.1 \quad (J.2)$$

The gain accounting for ride comfort was set to a constant value in order to avoid the implementation of the power spectrum online estimation, which would have required an excessive computational effort. During the simulations in the real vehicle, the gain was set to 0.1, but it could have been adjusted differently according to the desired dynamics. Lookup tables were substituted with simpler blocks to directly build the exponential law of Eq. (4.23). For the derivation of the gain accounting for dynamic wheel loads, the online calculation of an RMS value was required. Since the block was not available in the BACE library, the following procedure was used:

- Square of the signal
- Calculation of a fixed moving average with 127 samples
- Square root of the signal to obtain the moving RMS value

Furthermore, in the testing phase, the threshold for the acceptable dynamic wheel load is set to $k_i = 35\%$ of the static wheel load.

Appendix K Stability

A stability analysis of the full vehicle model, presented in Section 2.3 has been carried out in [8, xxi-xxiii]. It was focused on two stability aspects: with respect to an initial state or to an input variable, namely an input-output stability. The system was considered without the input vector ($\mathbf{u} = \mathbf{0}$), with $\dot{\mathbf{x}} = 0$ and starting from a stationary equilibrium point, an asymptotically stability criterion was applied. For a linear system, this corresponds to an analysis of the eigenvalues of the state system matrix \mathbf{A} . The eigenvalues need to have a negative real part in order to assure asymptotically stability. The same criterion applies to input-output stability, where the poles of the transfer matrix need to possess a real negative part in the complex plane. Asymptotically stability is proven analysing the eigenvalues of \mathbf{A} and, since the poles of the transfer matrix are included in the eigenvalues, input-output stability is confirmed as well. An additional analysis was carried out regarding the influence on the stability, of the feedback system in the calculation of the semi-active part of the four suspension forces. It is shown that, as soon as the suspension display a dissipative behaviour, namely they are semi-active and not fully active, they contribute in shifting the eigenvalues towards more negative real parts in the complex plane. An alternative analysis to the input-output stability for linear models, is the definition of a unique model transfer function, having performed Laplace transformations, and an analysis of its module and phase in a Bode diagram, in order to evaluate gain and phase margins. The full vehicle model adopted in this work, is the same as in [8] and therefore the same considerations applies when neglecting the input vector ($\mathbf{u} = \mathbf{0}$). An additional analysis should be performed when considering the coordination logic. Even though the resulting suspension forces are still dissipative and therefore they do not influence negatively the stability analysis, the calculation of the adaptive gain presents a non-linear procedure. When it comes to non-linear systems or subsystems, Lyapunov reduced criterion should be applied. It states that the stability analysis of an equilibrium point is performed by studying the stability of the corresponding linearized system in proximity of the equilibrium point [85]. An analytical stability analysis of the coordination logic has not been performed and can be object of further research. It has been proved in simulations and in experimental tests though, according to the stable response of the system.